

---

# DESIGN, CHARACTERISATION AND TESTING OF SU8 POLYMER BASED ELECTROTHERMAL MICROGRIPPERS

---



**Muaiyd H. M. Al-Zandi**

Submitted for the degree of Doctor of Philosophy

Heriot Watt University  
School of Engineering and Physical Sciences  
Institute of Sensors Signals and Systems  
June 2020

The copyright in this thesis is owned by the author. Any quotation from the thesis or use of any of the information contained in it must acknowledge this thesis as the source of the quotation or information.

## **ABSTRACT**

Microassembly systems are designed to combine micro-component parts with high accuracy. These micro-components are fabricated using different manufacturing processes in sizes of several micrometers. This technology is essential to produce miniaturised devices and equipment, especially those built from parts requiring different fabrication procedures. The most important task in microassembly systems is the manipulator, which should have the ability to handle and control micro-particles. Different techniques have been developed to carry out this task depending on the application, required accuracy, and cost. In this thesis, the most common methods are identified and briefly presented, and some advantages and disadvantages are outlined.

A microgripper is the most important device utilized to handle micro-objects with high accuracy. However, it is a device that can be used only in sequential microassembly techniques. It has the potential to become the most important tool in the field of micro-robotics, research and development, and assembly of parts with custom requirements. Different actuation mechanisms are employed to design microgrippers such as electromagnetic force, electrostatic force, piezoelectric effect, and electrothermal expansions. Also, different materials are used to fabricate these microgrippers, for example metals, silicon, and polymers such as SU-8.

To investigate the limitation and disadvantages of the conventional SU-8 electrothermal based microgrippers, different devices designed and fabricated at IMT, Romania, were studied. The results of these tests showed a small end-effector displacement and short cycling on/off (lifetime). In addition, the actuator part of these microgrippers was deformed after each operation, which results in reduced displacement and inconsistent openings at off state every time it was operated in a power ON/OFF cycle. One of these limitations was caused by the existence of conductors in arms of the end-effectors. These conductor designs have two disadvantages: firstly, it raises temperature in the arms and causing an expansion in the opposite direction of the desired displacement. Secondly, since the conductors pass through the hinges, they should be designed wide enough to reduce the conductor resistance as much as possible. Therefore, the wider the hinges are, the higher the in-plane stiffness and the less out of plane deflection. As a result, it increases the reaction force of the arm reducing the effect of deformation.

Based on these limitations a new actuator structure of L-shape was proposed to reduce the effects of these drawbacks. This actuator has no conductor in the hinges or the arms of the end-effectors which reduce limitation on the hinge width. . In addition, a further development of this actuator was proposed to increase the stiffness of the actuator by doubling its thickness compared with the other parts of the griper. The results of this actuator proved the improvement in performance and reduction of the actuator deformation.

This new actuator structure was used to design several different microgrippers with large displacement and suitable for a wide range of applications. Demonstrations of the capabilities of the microgrippers to be used in microassembly are presented.

In addition, a novel tri-directional microactuator is proposed in this thesis. This actuator's end-effector is capable of displacements in three different directions. This actuator was used with the other designs to develop a novel three-arm (three fingers) multidirectional microgripper.

To study the microgripper displacement as a function to the heater temperature, the TCR of the conductor layer of each device was measured. Because different configurations of conductor layers were studied, a significant effect of the metal layer structure on TCR was discovered. The TCR value of gold film is reduced significantly by adding the chromium layers below and about it which were used to improve the adhesion between the gold film and the SU layers.

In this thesis, a new method based on a robotic system was developed to characterise these microgrippers and to study the steady state, dynamic response, and reliability (lifetime cycling on/off). An electronic interface was developed and integrated to the robotic system to control and drive the microgrippers. This new system was necessary to carry out automated testing of the microgrippers with accurate and reliable results.

Four different new groups of microgrippers were designed and studied. The first group was indirectly actuated using an L-Shaped actuator and two different actuator widths. The initial opening was 120  $\mu\text{m}$  for both designs. The maximum displacement was about 140  $\mu\text{m}$  for both designs. However, the actuator in the wider heater width showed more stable behavior during the cycling and the dynamic tests.

The second group was based on direct actuation approach using the L-Shaped actuator. There were eight different designs based on this method with different heater conductor shape, actuator width, and arm thickness. The initial opening was 100  $\mu\text{m}$  and

there were different displacements for the eight designs. The study of these microgrippers proved that the actuator stiffness has a significant effect on the microgripper displacement. In addition, the shape of the heater conductor has less effect. The largest displacement achieved using this method of design was about 70  $\mu\text{m}$ .

The third group was designed for dual mode operation and has three different designs. The initial openings were 90  $\mu\text{m}$  and 250  $\mu\text{m}$ . The displacement was about 170  $\mu\text{m}$  in both modes. The last microgripper design was a tri-arm design for multi-mode operation.

The lifetime study of SU8 based microgrippers in this thesis was the first time such an investigation was carried out. The results of IMT designs showed that the larger is the displacement the less stable is the gripper design because of the high reaction force acting on the actuators. The L-shape based microgrippers had better performance and they did not break after more than 400 cycles. In addition, the studies of static displacement and dynamic response of different designed microgripper proved that better performance of the proposed actuator can be obtained by using double thickness for the actuator as compared to the arm thickness.



## **ACKNOWLEDGEMENTS**

First of all, I would like to thank my parents for the big support to get my dream true of finishing my PhD. Also, I would like to thank my wife and my son for the huge help and encouraging which without it, I would not finish my thesis.

My special thanks to my supervisor Dr. Wang for all his help and guidance during all of my PhD stages. Finally, I would like to thank Heriot-Watt University and the School of Engineering and Physics for offering me the opportunity to study for a PhD degree.

A special thanks to the IMT team specially to Dr Voicu and Dr Muller for there help to fabricate my microgrippers design.

## Research Thesis Submission

Please note this form should be bound into the submitted thesis.

Name:	Muaiyd Hameed Mohammed Al-Zandi		
School:	School of Engineering and Physics		
Version: <i>(i.e. First, Resubmission, Final)</i>	Final	Degree Sought:	PhD

### Declaration

In accordance with the appropriate regulations I hereby submit my thesis and I declare that:

1. The thesis embodies the results of my own work and has been composed by myself
2. Where appropriate, I have made acknowledgement of the work of others
3. The thesis is the correct version for submission and is the same version as any electronic versions submitted\*.
4. My thesis for the award referred to, deposited in the Heriot-Watt University Library, should be made available for loan or photocopying and be available via the Institutional Repository, subject to such conditions as the Librarian may require
5. I understand that as a student of the University I am required to abide by the Regulations of the University and to conform to its discipline.
6. I confirm that the thesis has been verified against plagiarism via an approved plagiarism detection application e.g. Turnitin.

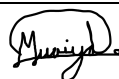
### ONLY for submissions including published works

Please note you are only required to complete the Inclusion of Published Works Form (page 2) if your thesis contains published works)

7. Where the thesis contains published outputs under Regulation 6 (9.1.2) or Regulation 43 (9) these are accompanied by a critical review which accurately describes my contribution to the research and, for multi-author outputs, a signed declaration indicating the contribution of each author (complete)
  8. Inclusion of published outputs under Regulation 6 (9.1.2) or Regulation 43 (9) shall not constitute plagiarism.
- \* Please note that it is the responsibility of the candidate to ensure that the correct version of the thesis is submitted.

Signature of Candidate:		Date:	10 February 2021
-------------------------	---	-------	------------------

### Submission

Submitted By <i>(name in capitals)</i> :	MUAIYD HAMEED MOHAMMED AL-ZANDI
Signature of Individual Submitting:	
Date Submitted:	10 February 2021

### For Completion in the Student Service Centre (SSC)

Limited Access	Requested	Yes	No	Approved	Yes	No
E-thesis Submitted (mandatory for final theses)						
Received in the SSC by <i>(name in capitals)</i> :				Date:		

## Inclusion of Published Works

Please note you are only required to complete the Inclusion of Published Works Form if your thesis contains published works under Regulation 6 (9.1.2)

### Declaration

This thesis contains one or more multi-author published works. In accordance with Regulation 6 (9.1.2) I hereby declare that the contributions of each author to these publications is as follows:

Citation details	e. g. Author 1 and Author 2, Title of paper, Title of Journal, X, XX-XX (20XX)
Author 1	Contribution....
Author 2	Contribution....
Signature:	
Date:	

Citation details	e. g. Author 1 and Author 2, Title of paper, Title of Journal, X, XX-XX (20XX)
Author 1	Contribution....
Author 2	Contribution....
Signature:	
Date:	

Citation details	e. g. Author 1 and Author 2, Title of paper, Title of Journal, X, XX-XX (20XX)
Author 1	Contribution....
Author 2	Contribution....
Signature:	
Date:	

Please included additional citations as required.

## TABLE OF CONTENTS

ABSTRACT.....	i
ACKNOWLEDGEMENTS .....	iv
TABLE OF CONTENTS .....	iv
LIST OF FIGURES .....	xi
LIST OF TABLES .....	xxxii
LIST OF PUBLICATIONS .....	xxxiii
Chapter 1 Introduction .....	1
1.1 Background .....	1
1.2 Objectives.....	2
1.3 Thesis Structure.....	3
Chapter 2 Literature Review .....	5
2.1 Microassembly Methods .....	5
2.1.1 Flip-Chip Microassembly Technique.....	5
2.1.2 Self-Assembly Methods .....	6
2.1.3 Robotics Systems .....	7
2.1.4 Piezoelectric Based Positioning .....	14
2.2 Actuation Principles - Contactless Micromanipulations.....	18
2.2.1 Photophoresis .....	18
2.2.2 Hydrogel Microgripper .....	20
2.2.3 Acoustic Manipulations .....	21
2.2.4 Air Flow Manipulation.....	23
2.2.5 Electrostatic Force Positioning .....	24
2.3 Actuation Principles – Single-End-effector Micromanipulator .....	25

2.3.1 Capillary Gripping .....	25
2.3.2 Vacuum Gripper.....	27
2.3.3 Van der Waals Forces .....	28
2.3.4 Cryogenic Grippers .....	29
2.3.5 Electrostatic End-effector.....	30
2.4 Actuation principles - Piezoelectric Microgrippers .....	32
2.4.1 Unimorph Piezoelectric Actuator.....	32
2.4.2 Bimorph Piezoelectric Actuator .....	32
2.4.3 Duo-bimorph Piezoelectric Actuator .....	33
2.4.4 Piezoelectric Microgrippers .....	33
2.5 Actuation Principles - Electrostatic Microgripper .....	34
2.5.1 Electrostatic Actuated Microgripper .....	34
2.5.2 Examples of Electrostatic Microgrippers:.....	36
2.5.3 Electromagnetic Microgripper .....	38
2.5.4 IPMC Actuated Microgripper .....	39
2.5.5 Example of IPMC Microgripper .....	41
2.6 Actuation Principles – Microgrippers with Integrated Electrothermal Actuator .....	42
2.6.1 Micro-Clamp Based Electrothermal Actuator: .....	42
2.6.2 Hot/Cold Arm Microgripper .....	43
2.7 SU-8 Electrothermally Actuated Microgripper.....	44
2.7.1 Chevron Actuator Style.....	45
2.7.2 Drawbacks of the Chevron Method .....	48
2.7.3 Hot-and-cold-arm actuators (normally closed) .....	48
2.8 Multi-Finger Micro-Cages gripper.....	53
2.9 Actuation Principles - Externally Actuated Microgripper .....	54
2.9.1 Pneumatically Actuated Microgripper .....	54
2.9.2 Voice Coil Actuated Microgripper.....	56

2.9.3 SMA Actuated Microgripper .....	57
2.9.4 Piezoelectric Actuator .....	59
2.9.5 Microgripper with Micrometer Screw .....	60
2.9.6 Disadvantages of Externally Actuated Microgrippers .....	61
2.10 Summary .....	62
2.10.1 Micromanipulation Methods .....	62
2.10.2 Materials Used in Microgripper Design.....	64
2.10.3 Fabrication Method for SU-8 Polymer .....	65
Chapter 3 Design, Simulation and Fabrication .....	67
3.1 Introduction .....	67
3.2 Actuation Design Principles.....	67
3.2.1 Displacement Force and Reaction Force.....	67
3.2.2 Displacement Amplification Ratio.....	69
3.2.3 Design History .....	70
3.2.4 L-Shaped Actuator Principle.....	71
3.3 One Mode Microgrippers .....	72
3.3.1 Design 1: Indirectly Actuated Microgripper .....	72
3.3.2 Design 2: Directly Actuated Microgripper .....	74
3.4 Dual Mode Microgripper .....	75
3.4.1 Design Concept .....	75
3.5 Tri-Directional Actuator Design .....	78
3.5.1 Design Principle .....	78
3.5.2 Design 4: Three-Armed Electrothermal Microgripper .....	78
3.6 IMT Designs .....	79
3.7 Fabrication.....	82
3.8 Modeling and Simulation.....	84
3.8.1 Simulation Method.....	84

3.8.2 Design 1- Indirectly Actuated Microgripper .....	87
3.8.3 Design 2- Direct Actuated Microgripper .....	89
3.8.4 Design 3 - Dual-Mode Microgripper .....	91
3.8.5 Tri-Directional Actuator.....	94
3.9 Summary .....	95
Chapter 4 TCR Measurements .....	97
4.1 Temperature Coefficient of Resistance (TCR) Measurement.....	97
4.1.1 TCR Measurement Methods .....	97
4.1.2 Closed Chamber Test Method.....	98
4.1.3 Water Bath based Test Method .....	99
4.1.4 Third TCR Measurement Method.....	100
4.2 Gripper Mounting and Connection .....	102
4.3 Results .....	104
4.3.1 TCRs of Cr/Au/Cr Film with Thickness 10 / 300 / 10 nm.....	104
4.3.2 TCRs of Cr/Au/Cr Film with Thickness 7/200/7 nm.....	109
4.3.3 TCRs of Gold with a thickness of 100 nm.....	110
4.4 Summery .....	112
Chapter 5 Characterisation and Measurement Methods .....	115
5.1 Introduction .....	115
5.2 Temperature Calculation Method .....	116
5.3 Displacement Measurements .....	118
5.3.1 Displacement Measurement on Zygo Metrology System.....	118
5.3.2 Displacement Measurement Using Percipio Chronogrip Robotic System .....	119
5.3.3 Measurement accuracy .....	122
5.4 Measurement of Dynamic Response Methods.....	123
5.4.1 Introduction .....	124
5.4.2 Interface Unit .....	125

5.4.1 Interface Unit Hardware Design .....	126
5.4.2 Interface Unit Schematic .....	127
5.4.3 Interface Unit Software .....	129
5.4.4 GUI Software .....	129
5.4.5 Robotic System Integration.....	131
5.4.6 Interface Unit Characterisation .....	135
5.4.7 Measurement Method.....	136
5.5 Method for Reliability Study .....	136
5.6 Summery .....	137
Chapter 6 Results, Analysis and Demonstration.....	138
6.1 Temperature and Displacement Measurements of IMT Designs.....	138
6.1.1 Design IMT-A.....	138
6.1.2 Design IMT-B & IMT-C.....	141
6.1.3 Design IMT-D.....	143
6.1.4 Design IMT-E .....	145
6.1.5 Design IMT-F (with Vertical Actuator).....	147
6.1.6 Design IMT-G and Design IMT-H .....	148
6.2 Temperature and Displacement Measurements of Heriot-Watt Designs.....	149
6.2.1 HWU-A: Indirect Actuator Based Microgripper Design .....	149
6.2.2 HWU-B: One Mode Microgripper.....	153
6.2.3 Design HWU-C: Dual-Mode L-Shaped Microgripper .....	158
6.2.4 Tri-directional electrothermal Microactuators .....	163
6.2.5 Three-arm Electrothermal Microgripper.....	166
6.3 Results of Dynamic Study.....	169
6.3.1 Design IMT-E .....	169
6.3.2 Design IMT-D.....	172
6.3.3 Design IMT-F .....	173



6.3.4 Design IMT-G.....	175
6.3.5 Design IMT-H.....	175
6.3.6 Dual-Mode L-Shaped Microgripper (Design HWU-C).....	176
6.4 Effect of Actuator Width and Thickness on Displacement.....	179
6.5 Results of Reliability Study .....	181
6.5.1 Design IMT-E ON/OFF Cycling Test.....	181
6.5.2 Design IMT-D ON/OFF Cycling Test .....	183
6.5.3 Design IMT-F Cycling Test.....	183
6.5.4 Design IMT-Z Cycling Test.....	185
6.5.5 Design IMT-V Cycling Test .....	186
6.5.6 Design HWU-B Cycling Test .....	189
6.6 Demonstration of Manipulation of Micro-objects .....	190
6.6.1 Manipulation Using Design IMT-E .....	191
6.6.2 Manipulation Using Design HWU-A and Design HWU-B.....	192
6.7 Microassembly Demonstration .....	193
6.7.1 PMMA Holder .....	193
6.7.2 3D Printed Holder .....	193
6.7.3 Microassembly Using Design HWU-C.....	196
6.8 Discussion .....	197
6.8.1 Temperature and Displacement Results.....	197
6.8.2 Dynamic Response Cycling Result.....	201
6.9 Summery .....	202
Chapter 7 Conclusions .....	206
7.1 Summary .....	206
7.1.1 Micromanipulation Method Selection.....	206
7.1.2 Design and simulation.....	207
7.1.3 Temperature Coefficient of Resistance Measurements.....	208

7.1.4 Demonstration .....	210
7.2 Contribution .....	210
7.3 Future Work .....	211
7.3.1 Tri-directional Actuator .....	211
7.3.2 Microgripper Structure Design .....	211
7.3.3 Dual-Mode Microgrippers .....	212
7.3.4 Limitations and proposed solutions .....	212
References .....	213
Appendix I Software Code.....	228
GUI Software (VC++) .....	228
Arduino Firmware (C).....	239
Header.h File .....	239
Main.c.....	240
Serial Management (Java Script) .....	243
Image Processing Management (Java Script) .....	244

## LIST OF FIGURES

Fig. 1.1 Size and scales [1].....	1
Fig. 2.1 (a) Optical image of a square ring with dimension of 2 mm and width of 200 $\mu\text{m}$ prior to flip-bonding. (b) Cross-section image of the assembled structure [12] .....	5
Fig. 2.2 Schematic of side view of hinges used in self-folded structure. The order of the metal layers defines the direction of folding [15] .....	6
Fig. 2.3 Video sequences of a cruciform folding and encapsulating a dyed 275- $\mu\text{m}$ glass bead [15].....	6
Fig. 2.4 TRING-Module 2 DOF robotic micromanipulator. This robot was based on piezoelectric material and Stick-slip actuation method (a) photograph for a set system (b) schematic showing the system components [24].....	10
Fig. 2.5 4 DOF Manipulator system [25].....	10
Fig. 2.6 A 6 DOF IRIS manipulator showing the 4 DOF base unit and the 2 DOF gripper unit [18] .....	11
Fig. 2.7 IRIS micro-assembly system [18] .....	12
Fig. 2.8 6 DOF assembly system (a and c) showing the rotation directions (b) focus photo on the working space (d and e) the end-effectors in different situation [26] .....	12
Fig. 2.9 Percipio-Robotics micromanipulation systems examples [29].....	13
Fig. 2.10 Stick and Slip Actuator, operation principle [22] .....	15
Fig. 2.11 An example of a linear actuator based on inchworm actuation method [34] ..	16
Fig. 2.12 Another example of linear actuation using the inchworm principle [35].....	16
Fig. 2.13 Cell phone camera module zooms based on inchworm linear motion [36]....	17
Fig. 2.14 Motion sequences: a belt clamps the rotor (2,5) while the opposite belt is released (3,6) and the clamped belt turns the rotor (1,4). Three sequences (clamp $\rightarrow$ release $\rightarrow$ turn) repeats. One complete cycle is composed of six sequences [37]. ..	17
Fig. 2.15 Assembly diagram of the precise rotary motor. (a) Exploded diagram; 1: rotor, 2: belt, 3: piezoelectric actuator, and 4: upper plate with flexure hinge levers. (b)	

Assembled; 1: piezo A, 2: piezo B, 3: piezo C, 4: piezo D, 5: adjusting screw, 6: pillar, and 7: base frame (lower plate) [26]. [37] .....	17
Fig. 2.16 Argon laser manipulator [38].....	18
Fig. 2.17 A cell manipulator system using the photophoresis [39].....	19
Fig. 2.18 (a) A <i>Bacillus subtilis</i> was captured by the optical tweezer. (b) <i>Bacillus subtilis</i> was patterned in circle. (c) A <i>Bacillus subtilis</i> was patterned in line [39] .....	20
Fig. 2.19 Proposed contact less microgripper actuated using magnetic field [42]. .....	20
Fig. 2.20 The proposition behind the operation of (a) the locomotion (b) gripping motion [42]. .....	21
Fig. 2.21 Acoustophoretic device compartmentalization [43] .....	21
Fig. 2.22 Device example used for separation technique [43] .....	21
Fig. 2.23 Ultra-sonic power is used to sort micro-size objects in a liquid [47] .....	22
Fig. 2.24 Injected air through a nozzle generates an air flow on the surface of the manipulator [21] .....	23
Fig. 2.25 Device layers of 2D manipulator using air flow [49] .....	24
Fig. 2.26 Two-dimensional positioning systems using electrostatic power [51].....	25
Fig. 2.27 (a) Side view: the capillary gripper is close to a micro-object with a liquid droplet at the end-effector (b) The liquid wets the micro-object (c) The surface tension pulls and centers the micro-object to the end-effector d) down view of the end-effector [52]. .....	26
Fig. 2.28 (a) Geometry of a liquid meniscus between a flat end-effector and a micro-sphere (b) The end effector approaches a micro-sphere (c) after the droplet of liquid wets the micro-sphere (d) pulling the micro-sphere by the surface tension [53] .....	26
Fig. 2.29 (1 – 4) Shows the voltage effect on the generated angle and how it has been used to grasp a micro-object. (a – b) Shows compression of a droplet shape with a voltage applied and a short circuit effect [54] .....	27
Fig. 2.30 Theory of vacuum microgripping where the vacuum generated in the nozzle is used to pick the micro-sphere and vibration is used for releasing [56].....	27
Fig. 2.31 Vacuum gripper (a) optical image after sputtering with gold (b) Cross-section [58] .....	27

Fig. 2.32 Principle of negative force generated by a micro-hole when it is cooled down after raising the temperature [59] .....	28
Fig. 2.33 Processes of using the Van der Waals forces to pick and release a micro-object [61] .....	29
Fig. 2.34 Microgripper tip using ice on an end-effector to implement pick and release tasks [62] .....	29
Fig. 2.35 Picking and releasing a microobject by the deposition / sublimation method [63] .....	30
Fig. 2.36 Using a charged end-effector to pick an object [64].....	30
Fig. 2.37 Planar concentric ring electrodes, layout and shape variants (a, b) are the different design. (c) Top view and (d) side view of the experimental photo [65]....	31
Fig. 2.38 Separated electrodes, bipolar electrostatic microgripper [7] .....	31
Fig. 2.39 A monomorph piezo-actuation principle [66] .....	32
Fig. 2.40 Bimorph piezo-actuation behavior and layers [67] .....	32
Fig. 2.41 Duo-bimorph actuator made of PMN-PT [69] .....	33
Fig. 2.42 Microgripper design based on piezoelectric cantilevers [70] .....	33
Fig. 2.43 FEMTO-ST 4 DOF microgripper fabricated using duo-bimorph piezo materials [6] .....	34
Fig. 2.44 Several commercially developed piezoelectric based microgrippers [6] .....	34
<i>Fig. 2.45 A simple micro-actuator is formed from two parallel plates [71].....</i>	<i>35</i>
Fig. 2.46 Microgripper actuated using electrostatic force [76].....	36
Fig. 2.47 Microgripper with embedded force sensor [77] .....	37
Fig. 2.48 Three states of electrostatically actuated microgripper arms during the manipulation processes. (a) The object is aligned and ready to pick. (b) higher force is applied than in (c) [77] .....	37
Fig. 2.49 A dual axis MEMS microgripper with built-in force and position sensor [78] .....	37
Fig. 2.50 Electromagnetics actuated microgripper [79].....	38
Fig. 2.51 Electromagnetic microgripper [80].....	38

Fig. 2.52 IPMC transduction mechanisms. IPMC actuator with (a) Cu–Pt-coated and (b) regular platinum. Sensor of platinum coat showing the effect of bending on the atom's intensity and the change in the resistivity (c) unbent (d) bent [81] .....	40
Fig. 2.53 IPMC microgripper which one arm is actuated and the other is used as sensor [83] .....	41
Fig. 2.54 Electro-thermal micro-clamp [89] .....	43
Fig. 2.55 Hot/cold arms electrothermal based on Poly-Si microgripper normally closed (a) the design structure (b) the deflection magnified by 10 (c) mesh for FEA of the microgripper model (d) the electrical potential distribution [90] .....	43
Fig. 2.56 Hot/cold arms electrothermal based on Poly-Si microgripper normally opened [91] .....	44
Fig. 2.57 Bent beam actuating microgripper [92] .....	45
Fig. 2.58 Microgripper for nano-manipulation [93] .....	46
Fig. 2.59 SU-8 microgripper [94] .....	47
Fig. 2.60 SU-8 microgripper actuated using chevron actuator [95, 96] .....	47
Fig. 2.61 Hot/cold arm based design microgripper [98] .....	48
Fig. 2.62 Hot/cold arms microgripper with an extension arm [99] .....	49
Fig. 2.63 Hot/cold arms microgripper [100] .....	50
Fig. 2.64 Three heating beam microgripper [102] .....	51
Fig. 2.65 Three beam working principle [102] .....	51
Fig. 2.66 Hybrid designed microgripper using silicon and SU-8 as structural materials [103] .....	52
Fig. 2.67 Hot/cold arms microgripper [104, 105] .....	52
Fig. 2.68 Deflection with current for different microgripper thickness [105] .....	53
Fig. 2.69 Optical photograph of the microcage (a) no power applied (b) less than 9 W applied; the angle is about 80° [106] .....	53
Fig. 2.70 SU8/DLC micro-cages with L of (a) 20 $\mu\text{m}$ , (b) 30 $\mu\text{m}$ , (c) 40 $\mu\text{m}$ , and (d) 50 $\mu\text{m}$ [106] .....	54

Fig. 2.71 Simplest microcage based on pneumatic actuation. When a pressure is applied on the membrane, it pushes the two arms [107] .....	55
Fig. 2.72 PMMA microgripper design and dimensions [108] .....	55
Fig. 2.73 Syringe based microgripper. The microgripper is actuated by the force that is generated because of the pressure due to the syringe movements [108].....	55
Fig. 2.74 Microgripper designed using SU-8 and driven pneumatically [109] .....	56
Fig. 2.75 Electromagnetic actuated microgripper. The figure shows the dimension, components, and the actuation method [114].....	57
Fig. 2.76 An SMA microgripper with a strain gauges to measure the force on the flexible hinge [116] .....	58
Fig. 2.77 An SMA microgripper with integrated strain gauges to sense the force [117] .....	58
Fig. 2.78 SU-8 microgripper actuated using SMA (a) the actuation method (b) the assembled microgripper [118].....	59
Fig. 2.79 Externally actuated microgripper using piezoelectric (a) the microgripper structure (b) the microgripper parts (c) the assembled microgripper [119] .....	59
Fig. 2.80 Piezo actuated SU-8 microgripper [120] .....	60
Fig. 2.81 An optical guide microgripper [121] .....	60
Fig. 2.82 Microgripper diagram showing the components [123] .....	61
Fig. 3.1 Beam deflection when a force (F) is applied at the distance a from the base to generate the deflection ( $\delta$ ) at the edge of the beam.....	68
Fig. 3.2 Effect of the compression force exceeding the critical force on a beam shape when the tangent edge is (a) free point (b) fixed point .....	68
Fig. 3.3 Three selected of different design based on the U-shape actuator .....	71
Fig. 3.4 Proposed L-Shape actuator structure and showing the details of the parts .....	71
Fig. 3.5 A proposed design for a microgripper based on the L-shaped actuation method and isolated actuator with interface stages. The L-Shape actuator part is detailed in Fig. 3.7 and the end-effectors arm is detailed in Fig. 3.6.....	72
Fig. 3.6 Details of one microgripper arm design showing the interface part and the end effector.....	73

Fig. 3.7 L-Shape actuator used to design the interfaced microgrippers.....	74
Fig. 3.8 Directly actuated microgripper based on the L-shape actuator. The heaters' conductors were designed in different shapes linear (a & b) and meander (c & d). Also, the actuator is in different width (a & c) 210 $\mu\text{m}$ and (b & d) 100 $\mu\text{m}$ .....	74
Fig. 3.9 Bi-directional actuator principal (a) actuated to deflect the endeffector to left, (b) deflection to right, (c) labelled actuator structure Design 3: Dual Mode Microgripper .....	76
Fig. 3.10 Two different designs of dual-mode microgripper based on bi-directional actuator (a) design 1 with line shaped micro-actuator (b) design 2 with meander shaped micro-actuator .....	77
Fig. 3.11 Tri-directional actuator design, the arrows show the effect of each actuator on the movement of the arm.....	77
Fig. 3.12 Schematic layout of the three-armed microgripper showing the heaters and conductor lines (yellow) and the SU8 based structure (blue).....	79
Fig. 3.13 Layout of the optimised three-armed microgripper showing the absence of the heaters h3 and h4.....	79
Fig. 3.14 Microgrippers by IMT design group 1. All these microgrippers were designed and fabricated by IMT except Design E which was designed in Italy and fabricated by IMT. The images are not to scale and the microgripper designs are in different sizes. Designs A and D were designed in two different sizes. ....	80
Fig. 3.15 Optical microscope image showing the dimensions of design (A - C) the large groups which was measured using the Zygo metrology system .....	80
Fig. 3.16 Optical microscope image showing the dimensions of design (D) the large groups which was measured using a Zygo metrology system. ....	81
Fig. 3.17 Optical microscope image showing the dimensions of design (E) and the measurement was taken using Zygo metrology system .....	81
Fig. 3.18 Microgripper based on V-shaped actuator.....	82
Fig. 3.19 Schematic of the cross-section of the microgripper's arms showing the SU-8 and the metallic layers (not to scale) .....	83
Fig. 3.20 Fabricated Heriot-Watt designs (a) Directly actuated microgripper with heart configuration of 7nm / 200 nm / 7nm (Cr/Au/Cr) (b) Multi-degree of freedom	



microgripper with same heater configurations (c) Bi-directional microgripper with heart configuration of 100 nm of gold.....	83
Fig. 3.21 Fabrication processes chart.....	84
Fig. 3.22 Models of the COMSOL Multiphysics simulation to study the dual-mode microgripper design.....	86
Fig. 3.23 Young's modulus and Poisson's ratio for SU-8 as a function of temperature change, generated by COMSOL using the interpolation function and five data points The properties of the SU-8 and gold are shown in Table 3-3 and Table 3-4 respectively. The Young's modulus and Poisson's ratio of the SU-8 were assumed to be temperature dependent, as shown in Fig. 3.23, using data from the literature [130], [131] and [132]. The graphs were produced in the COMSOL model using the built-in interpolation function and 5 data points for each curve. Results and Discussion .	86
Fig. 3.24 Temperature distribution and arm deflection of the interfaced microgripper using COMSOL multiphysics simulation model .....	87
Fig. 3.25 Displacement as a function of current result from the COMSOL modulation of the interfaced microgripper .....	87
Fig. 3.26 Temperature as a function of current result from the COMSOL modulation of the interfaced microgripper .....	87
Fig. 3.27 Displacement as a function of Temperature result from the COMSOL modulation of the interfaced microgripper.....	88
Fig. 3.28 Displacement as a function of temperature compression between different fixed values of Young modules with the variable one which this study was based on.....	89
Fig. 3.29 Displacement as a function of current compression between different fixed values of Young modules with the variable one which this study was based on.....	89
Fig. 3.30 Modelling result showing the temperature distribution and deflection of the direct actuated microgripper (a) with actuator width of 90 $\mu\text{m}$ and current of 11 mA (b) with actuator width of 200 $\mu\text{m}$ and current of 10 mA .....	89
Fig. 3.31 Temperature as a function of current result from the COMSOL modulation of the direct actuated microgripper with two different actuator widths .....	90
Fig. 3.32 Displacement as a function of current results from the COMSOL modulation of the direct actuated microgripper with two different actuator widths .....	90

Fig. 3.33 Displacement as a function of the average heater temperature from the COMSOL modulation of the direct actuated microgripper with two different actuator widths .....	90
Fig. 3.34 Temperature distribution and arm deflection caused by applying a current of 10 mA on (a) heater 1 (b) heater 2 .....	91
Fig. 3.35 Stress in the hinges when 10 mA current was applied on (a) heater 1 (b) heater 2 .....	91
Fig. 3.36 Simulation results of one arm showing the displacement and temperture as a function to the applied current for heater 1 and in closing mode .....	92
Fig. 3.37 Simulation results of one arm showing the displacement and temperture as a function of the applied current for heater 2 and in opening mode .....	92
Fig. 3.38 Displacement of the end effector in opening mode as a function of heater 1 average temperature.....	92
Fig. 3.39 Displacement of the end effector in closing mode as a function of heater 2 average temperature.....	93
Fig. 3.40 Effect of an increase in the actuator temperature on the actuator's pliability causing deformation. The opening mode and heater (2)'s average temperature is about (a) 110 °C (b) 190 °C and the closing mode when heater (1)'s average temperature is about (c) 100 °C (d) 180 °C. The deflection was scaled 1:7 to make it easy for observation. ....	93
Fig. 3.41 Simulation results of the tri-directional actuator. (a) and (d) deformation and temperature distribution when heater h4 is operated, (b) and (e) deformation and temperature distribution when heater h3 is operated, (c) and (f) deformation and temperature distribution when heaters h5 and h6 are used. ....	94
Fig. 3.42 Simulation results of the tri-directional actuator showing the average temperature in each actuator when they are in operation as a function of applied voltage .....	94
Fig. 3.43 Simulation results of the tri-directional actuator showing the displacement of the beam tip when each heater is operated as a function of applied voltage.....	95
Fig. 4.1 Equipment setup used to carry out the TCR measurements for the first method using a chamber.....	99

Fig. 4.2 Using distilled water to raise the temperature of the microgripper .....	100
Fig. 4.3 The microgripper was glued onto glass sheets and connected using copper tape and conductive adhesive (a) A camera photograph of this method showing all the component (b) the microgripper focused under the microscope (c) extra zoom of the microgripper .....	101
Fig. 4.4 Three methods were used to heat up the microgrippers. Thermocouple was used to measure the temperature. (a and b) the glass was placed on the hot plate without any interface while in (c) a block of Aluminium was used to stabilise the temperature by adding more mass to the glass sheet.....	101
Fig. 4.5 The first electrical connection method which was used to connect the three arms of the microgripper (a) Whole system showing the microgripper, copper tape strips, and PCB (b) The microwires glued on the microgripper pads and soldered on the copper strips on the other side (c) tiny wires used to connect the copper strips to the PCB .....	102
Fig. 4.6 Second connection method used to connect the microgripper pads to carry out the required tests. (a) Image was taken using a photographic camera showing all the components. Images b& c were taken using an optical microscope showing the connection between the copper strip and the pads under focus.....	103
Fig. 4.7 The second method of electrical connection used to set up the 2 DOF microgripper .....	103
Fig. 4.8 The third method used to connect the multi-degree of freedom microgripper. (a) Whole PCB shows the microgripper and the electrical pads. (b) Zooming in the microgripper to show the conductive paste connecting the microgripper pads to the PCB traces. ....	104
Fig. 4.9 Result of the resistance as a function of temperature for design A sample 1 two tests and one test for the second sample. The left vertical access is the resistance of sample (1) while the right is for sample (2). ....	105
Fig. 4.10 Microgripper design B TCR measurements on two different samples and methods. The left vertical axis is for sample (1) and the right is for sample (2)....	105
Fig. 4.11 Experiment results of TCR measurement using microgripper design C .....	106
Fig. 4.12 Result of testing H1 and H2 using the third method (a) .....	107

Fig. 4.13 Result of testing H1 using the third method (a & b).....	107
Fig. 4.14 Results of testing sample H1 using the cooling method.....	107
Fig. 4.15 Testing design D using each heater separately and in parallel connection. The left axis shows the single heater resistance while the right is for the parallel.....	108
Fig. 4.16 Results of testing design E which has two heaters. The left vertical axis shows the resistance of the single heater test while the right axis shows the resistance of the parallel connection. ....	108
Fig. 4.17 Resistance as a function of temperature for the directly actuated microgrippers with two different heater shapes. The left vertical axis is for the meander heater while the right axis is for the linear heater resistance value.....	109
Fig. 4.18 Resistance as a function to temperature for the directly actuated microgrippers with meander heater .....	110
Fig. 4.19 TCR measurement of the multi-degree of freedom microgripper .....	110
Fig. 4.20 Results of heater resistance as a function of temperature of the bi-directional microgripper .....	111
Fig. 4.21 TCR measurement result of the V-shaped based small size.....	111
Fig. 4.22 TCR measurement result of the V-shaped based large size.....	112
Fig. 5.1 Circuit diagram for the connection of the microgripper to measure the voltage and current then to use them to calculate the resistance.....	117
Fig. 5.2 Setup of the zygo metrology system. (a) shows the whole system and the test setup whereby on the left is the power supply and two multimeters to measure the voltage and the current, in the middle is the optic part, and on the left is the control and monitor part. (b) shows the microscope glass sheet carrying the microgripper and it fixed on the system stage using a tape. (c) shows the monitor and the user interface running and showing a result of one of the measurements. ....	117
Fig. 5.3 Screenshot from the Zygo user interface software showing one of the parts under test. (a) shows the microgripper part under observation, the line is the slicing tool and shows the result on (c). (b) shows the inspector's result.....	118
Fig. 5.4 Chronogrip robotic system setup to measure the displacements showing (a) the used power supply and (b) the used multimeters to measure the current and voltage (c) microgripper on the system's hexapod stage and the used microscope objective	

which is connected to a camera, a thermometer was also used to measure the test environment temperature (d) the tracking software user interface, the red area is the searching area while the green rectangle is the area of interest. ....	120
Fig. 5.5 Screen shot from the control computer of the Chronogrip robotic system showing the direct measurement technique. The left of the screen shows the image of the end-effectors taken from the microscope and overlapped with rulers to carry out the measurements. On the right of the screen is the user interface to control the robot and calibrate the ruler.....	121
Fig. 5.6 User interface software in the Chronogrip Robotic System which was developed in order to carry out the characterisation of the microgrippers .....	121
Fig. 5.7 Testing and verifying the pixel size by moving an edge of the actuator several micrometers and measuring the displacement in pixels. (a & b) is the measurement in pixels multiplied by the factor in (d) while (c) shows the movement control of the hexapod and (e) the displacement measurement using the tracking software.....	122
Fig. 5.8 Two different readings for same device and same conditions.....	123
Fig. 5.9 Design (a) testing pictures were taken by Zygo system to measure the displacement.....	123
Fig. 5.10 Block diagram of the interface Unit .....	125
Fig. 5.11 Top view of the designed interface unite which was used to study the dynamic behavior of the microgrippers and their reliability by cycling the microgrippers ON/OFF one hundred times .....	126
Fig. 5.12 Schematic of the designed interface unite to take the measurements.....	126
Fig. 5.13 Main power supply based on an AC transformer with dual 6V output and 240V input. Large capacitors were used to smooth the rectified AC voltage by the bridge diodes then regulators were used to regulate the output voltages. ....	127
Fig. 5.14 Flow chart showing the process in the Arduino microcontroller dev. Board .....	128
Fig. 5.15 UI used to control and configure the system measurements. ....	128
Fig. 5.16 UI state machine showing the flow of the states in this program.....	130
Fig. 5.17 Example of running the cycling test on one of the microgrippers (a) shows the video processing track function interface (b & c) the video processing Java software	

and the result respectively (d & e) the Arduino Java control and the raw data from the ADCs respectively (f) the video processing UI run the FastCV lib (g) C# UI (e) serial communication control module .....	132
Fig. 5.18 Flow chart shows the Java software structure of communication with the microscope through the video processing lib to send commands and fetch results	133
Fig. 5.19 Flow chart shows the Java software structure of communication with the Arduino to send commands and acquire results .....	134
Fig. 5.20 Arduino output delay after receiving the serial commands where the blue signal represents the UART and the yellow signal represents the microgripper voltage ..	135
Fig. 5.21 Microgripper voltage rising when the DAC was powered .....	135
Fig. 6.1 Pictures taken by the Chronogrip robotic system to carry out the displacement measurement using the integrated vision processing software. The two pictures were taken on different applied voltages and show the traced area in the green square..	139
Fig. 6.2 Comparison of displacement results as a function of the applied current from the two measurement systems on design (A) .....	139
Fig. 6.3 Comparison of displacement results as a function of the applied voltage from the two measurement systems on design (A) .....	139
Fig. 6.4 Comparison of displacement results as a function of the applied current from the two measurement systems on design (A) .....	140
Fig. 6.5 Design (a) average heater temperature as a function of the applied current...	140
Fig. 6.6 Horizontal displacement of each end-effectors .....	141
Fig. 6.7 Images taken using the Zygo system for design (B) and showing the end-effectors in different situations.....	141
Fig. 6.8 Robotic measurement of design (B). The two pairs of images show the end effectors with and without an applied voltage. The green area is the tracking part to measure the change in the position. The red area is the search area of the tracked part .....	142
Fig. 6.9 Design (C) when it was tested using the robotic systems.....	142
Fig. 6.10 Displacement and heater average temperature measurements of design (B and C) as a function of the applied voltage measured using Zygo and robotic system .	142

Fig. 6.11 Two different expansion effects in these microgrippers on the end-effector displacements. The first expansion comes from the cold arm (THE1) while the other comes from the actuator (THE2). The first expansion has the effect of closing operation while the second has the effect of opening operation on these microgrippers. As a result, the final displacement is the difference between the two effects .....	143
Fig. 6.12 Displacement measurements of design D using the Zygo system in different applied voltages .....	144
Fig. 6.13 Displacement measurements of design (D) using the image processing on the robotic system.....	144
Fig. 6.14 Displacement and temperature as a function of the applied voltage for design D measured using the two testing methods .....	144
Fig. 6.15 Displacement and temperature as a function of the average heater temperature for design D .....	145
Fig. 6.16 End-effectors horizontal displacement measured using the robotic system .	145
Fig. 6.17 Zygo measurement of design E .....	145
Fig. 6.18 Robotic measurement of three points simultaneously on two conditions - when the microgripper was off and while a 650 mV was applied .....	146
Fig. 6.19 Robotic test of design (E) displacement result at three points as a function of the applied voltage.....	146
Fig. 6.20 Zygo test of design (E) ) displacement result at three points as a function of the applied current.....	146
Fig. 6.21 IMT design with vertical microheater (a) is with off power (b) with applied voltage of 550 mV (c) picture from the robotic system showing the microgripper in the two previous conditions.....	147
Fig. 6.22 Displacement and temperature as a function of the applied voltage for design F using the robotic system.....	147
Fig. 6.23 Displacement and temperature as a function of the current passed for design F using the robotic system .....	148
Fig. 6.24 Optical images of the fabricated IMT developed design A actuated using (a) V-shaped actuator (b) Z-shaped actuator.....	148

Fig. 6.25 Design V and Z microgripper test results of displacement and temperature as a function of the applied voltage .....	149
Fig. 6.26 Design V and Z microgripper test results of displacement and temperature as a function of the applied current .....	149
Fig. 6.27 (a & c) Interfaced actuator microgripper with two actuator width (b & d) are the interface part between the actuator and the arms .....	150
Fig. 6.28 Interfaced actuator microgripper displacement measurement using the robotic method (a) 0 V is applied (b) 1.2 V is applied .....	150
Fig. 6.29 Displacement as a function of the applied voltage obtained using the robotic system. D150 and D500 refers to the actuator width 150 $\mu\text{m}$ and 500 $\mu\text{m}$ respectively. This chart shows the displacement result of the first cycle and the cycles after that. ....	151
Fig. 6.30 Displacement as a function of the applied current obtained using the robotic system. D150 and D500 refers to the actuator width 150 $\mu\text{m}$ and 500 $\mu\text{m}$ respectively. This chart shows the displacement result of first cycle and the cycles after that....	152
Fig. 6.31 Displacement as a function of the average heater temperature measured using the heater TCR and the resistance obtained using the robotic system. D150 and D500 refers to the actuator width 150 $\mu\text{m}$ and 500 $\mu\text{m}$ respectively. This chart shows the displacement result of first cycle and the cycles after that. ....	152
Fig. 6.32 Heater average temperature as a function of the applied current obtained using the robotic system. D150 and D500 refers to the actuator width 150 $\mu\text{m}$ and 500 $\mu\text{m}$ respectively. This chart shows the heater temperature result of first cycle and the cycles after that.....	152
Fig. 6.33 Cold arm expansion as a function of the applied current obtained using the robotic system. D150 and D500 refers to the actuator width 150 $\mu\text{m}$ and 500 $\mu\text{m}$ respectively. This chart shows the expansion result of the first cycle and the cycles after that.....	153
Fig. 6.34 1 DOF direct actuated microgripper optical images for two different actuator widths of meander heater (M) design (a) actuator width is 210 $\mu\text{m}$ and (b) is 100 $\mu\text{m}$ . ....	154
Fig. 6.35 Directly actuated microgripper optical images for two different actuator widths of linear heater (L) design (a) heater width is 210 $\mu\text{m}$ and (b) is 100 $\mu\text{m}$ .....	154



Fig. 6.36 1 DOF direct actuated microgripper using the robotic method showing two test conditions .....	154
Fig. 6.37 Measuring the opening of 1 DOF direct actuated microgripper using the robotic system.....	155
Fig. 6.38 Displacement and temperature as a function of the applied current for a linear shaped heater with a width of 100 $\mu\text{m}$ for both designs of arm with single layer and double layers.....	155
Fig. 6.39 Displacement and temperature as a function of the applied current for a linear shaped heater with actuator width of 210 $\mu\text{m}$ for both designs of arm with single layer and double layers .....	155
Fig. 6.40 Displacement and temperature as a function of the applied current for meander shaped heater with actuator width of 100 $\mu\text{m}$ for both designs of arm with single layer and double layers .....	155
Fig. 6.41 Displacement and temperature as a function of the applied current for a meander shaped heater with actuator width of 210 $\mu\text{m}$ for both designs of arm with single layer and double layers .....	156
Fig. 6.42 Displacement result of the four microgripper variants with actuator width of 100 $\mu\text{m}$ as a function of the average heater temperature for the microgrippers .....	156
Fig. 6.43 Displacement result of the four microgripper variants with actuator width of 210 $\mu\text{m}$ as a function of the average heater temperature for the microgrippers .....	156
Fig. 6.44 Displacement compression of the result of the best two microgripper designs as a function of the average heater temperature .....	158
Fig. 6.45 Displacement result of the best two microgripper designs as a function of the applied current.....	158
Fig. 6.46 Optical microscope images for the microgrippers (a) design 1 with opening 60 $\mu\text{m}$ (b) design 1 with opening 250 $\mu\text{m}$ (c) design 2 with opening 90 $\mu\text{m}$ .....	159
Fig. 6.47 Screen shots of displacement measurement based on vision tracking method. The microgripper design 2 is under test and the images were taken on three occasions. (a) and (b) 13 mW applied on heaters and the microgripper is in closing mode, (c) and (d) both heaters are off, (e) and (f) 18 mW was applied on heaters and the microgripper is in opening mode.....	160

Fig. 6.48 Microscopic photo of design 1 with 60 $\mu\text{m}$ initial opening. (a) closing mode when power is applied on heaters, (b) no power applied (c) opening mode when power is applied on the heaters.) .....	160
Fig. 6.49 Closing mode displacement and temperature measurements as a function of the current passed in both designs .....	161
Fig. 6.50 Opening mode displacement and temperature measurements as a function of the current passed in both designs .....	161
Fig. 6.51 Both opening and closing mode displacement measurements as a function of the average heater temperature .....	161
Fig. 6.52 Closing mode heater (1) average temperature to the applied power .....	162
Fig. 6.53 Opening mode heater (2) average temperature to the applied power .....	162
Fig. 6.54 Tri-directional electrothermal microactuators optimised by using only two actuators instead of four .....	163
Fig. 6.55 Tri-directional actuator displacement measurement by running both heaters 3 (right and left) (a) is the first image before applying power, the two images are for two tracking requests so two results obtained to increase the accuracy (b) after applying about 41 mA and about 10 $\mu\text{m}$ of longitudinal displacement .....	164
Fig. 6.56 Displacement result of applying power on heater (1 & 2) in the first design of the tri-directional actuator .....	164
Fig. 6.57 Displacement result of applying power on each heater in the optimised design .....	165
Fig. 6.58 Displacement as a function of the average heater temperature for both designs to actuate the arm to the side direction .....	165
Fig. 6.59 Longitudinal displacement of design 1 when the two H3 are powered design 2 when both heaters are powered as a function of the applied current. The two designs are identical in their longitudinal displacement because they are based on the same dimension .....	165
Fig. 6.60 Tri-End-effector microgrippers (a) Design 1 with eight actuators (b) Optimised design (design 2) using six actuators only .....	166
Fig. 6.61 Tri-arms microgripper in displacement measurement in six different situations where (a) closing mode (b) no power applied (c) opening mode. These results from	

the operation of the dual-mode actuator (d) tri-directional actuator (H3 in design 1 or the left heater in design 2) activated (e) tri-directional actuator (H4 in design 1 or the right heater in design 2) activated (f) tri-directional actuator (H5 & H6) activated	167
Fig. 6.62 Three-arm microgrippers displacement as a function of the average heater temperature for the main arms.....	167
Fig. 6.63 Displacement as a function of temperature for the middle arm for design (1) by powering the heaters (H3) and (H4) for right and left displacements.....	167
Fig. 6.64 Displacement as a function of temperature for the middle arm for design (2) by powering the left heater (H5) and the right heater (H5) for right and left displacements .....	168
Fig. 6.65 Displacement as a function of temperature for the middle arm for design 1 by powering both heaters (H5) to achieve longitudinal displacement .....	168
Fig. 6.66 Displacement as a function of temperature for the middle arm for design (2) by powering both heaters (H5) to achieve longitudinal displacement .....	168
Fig. 6.67 Dynamic study of displacement as a function of time for both power ON and power OFF time of applied voltage of 670 mV on design 1-E .....	170
Fig. 6.68 Heater temperature and end-effectors displacement over 1 second sampled 60 times of applied voltage of 680 mV on design 1-E.....	170
Fig. 6.69 Dynamic study result of displacement as a function of time for both power ON and power OFF time of applied voltage of 670 mV on design 1-E focused on the first second of transaction .....	170
Fig. 6.70 Dynamic study of displacement as a function of time for power ON time of applied voltage of 560 mV, 620 mV, and 680 mV on design 1-E for 10 seconds..	171
Fig. 6.71 Dynamic study of displacement as a function of time for power ON time of applied voltage of 560 mV, 620 mV, and 680 mV on design 1-E for 3 seconds....	171
Fig. 6.72 Dynamic study of displacement as a function of time for power OFF time of applied voltage of 560 mV, 620 mV, and 680 mV on design 1-E for 10 seconds..	171
Fig. 6.73 Dynamic study of displacement as a function of time for power OFF time of applied voltage of 560 mV, 620 mV, and 680 mV on design 1-E for 2 seconds....	172
Fig. 6.74 Screen shoot of dynamic study of displacement of design 1-D.....	173

Fig. 6.75 Dynamic study of displacement as a function of time for power ON/OFF time for applied voltage of about 620 mV on design 1-D for 10 seconds.....	173
Fig. 6.76 Screen shot of dynamic study of displacement of design 1-F .....	174
Fig. 6.77 Dynamic study result of displacement as a function of time over 10 seconds for both power ON and power OFF time of applied voltage of 580 mV on design 1-F .....	174
Fig. 6.78 Dynamic study result of the first seconds for both powering ON and powering OFF time of applied voltage of 580 mV on design 1-F .....	174
Fig. 6.79 Dynamic study result of the first 10 seconds for both powering ON and powering OFF time of applied voltage of 430 mV on design 1-G.....	175
Fig. 6.80 Dynamic study result for both powering ON and powering OFF time of applied voltage of 400 mV on design 1-H .....	176
Fig. 6.81 Dynamic study result of the first 25 seconds for both powering ON and powering OFF time of applied voltage of 2V and 2.1V on opening mode for design 1 and design 2 respectively .....	176
Fig. 6.82 Dynamic study result of the first 25 seconds for both powering ON and powering OFF time of applied voltage of 2V and 2.1V on closing mode for design 1 and design 2 respectively .....	177
Fig. 6.83 Temperature and displacement measured as a function of time in closing mode for both designs over 1 second .....	178
Fig. 6.84 Temperature and displacement measured as a function of time in opening mode for both designs over 1 second .....	178
Fig. 6.85 One DOF direct actuated microgripper optical photo for two different actuator widths of linear heater (L) design (a) actuator width is 210 $\mu\text{m}$ and (b) is 100 $\mu\text{m}$	179
Fig. 6.86 Dynamic study result of the first 10 seconds for both powering ON and powering OFF time of applied voltage of about 700 mV on design L100. The heater average temperature was about 170 $^{\circ}\text{C}$ .....	180
Fig. 6.87 Dynamic study result of the first 10 seconds for both powering ON and powering OFF time of applied voltage of about 810 mV on design L210. The heater average temperature was about 160 $^{\circ}\text{C}$ .....	180

Fig. 6.88 Both dynamic responses of designs L210_S and L100_S with the heaters driven ON and OFF .....	181
Fig. 6.89 Cycling test of the design 1-E. The microgripper was powered ON/OFF for 10 seconds each. The voltage used was about 560 mV and the average heater temperature was about 150°C .....	182
Fig. 6.90 Microgripper group 1 design E (a) before the reliability study (b) after 250 cycles of ON/Off by applying about 670 mV .....	182
Fig. 6.91 Screen shot of cycling test of design 1-D .....	182
Fig. 6.92 Cycling test of design 1-D. The microgripper was powered ON/OFF for 10 seconds each. The voltage used was about 560 mV, the average heater temperature was about 150°C .....	183
Fig. 6.93 Screen shot of cycling test of design 1-D .....	184
Fig. 6.94 Cycling test of design 1-F. The microgripper was powered ON/OFF for 10 seconds each. The voltage used was about 500 mV and the maximum heater temperature was about 125 °C.....	184
Fig. 6.95 Cycling test of design 1-F. The microgripper was powered ON/OFF for 10 seconds each. The voltage used was about 580 mV and the heater maximum temperature was about 150 °C.....	184
Fig. 6.96 Optical image of Design 1-Fshowing deformed hinges after the 250 cycles of test .....	185
Fig. 6.97 Screen shot of cycling test of design 1-Z.....	185
Fig. 6.98 Cycling test of design 1-Z. The microgripper was powered ON/OFF for 10 seconds each. The voltage applied was about 300 mV and the heater maximum temperature was about 130 °C.....	186
Fig. 6.99 Deformation in the actuator shape and over heating on one beam of design 1-Z microgripper .....	186
Fig. 6.100 Deformation in the actuator shape and over heating on one beam of design 1-Z microgripper.....	186

Fig. 6.101 Cycling test of design 1-V. The microgripper was powered ON/OFF for 10 seconds each. The voltage applied was about 340 mV and the maximum heater temperature was about 150 °C.....	187
Fig. 6.102 (a) Not used microgripper's actuator (b) microgripper's actuator after 120 cycles showing structural changes in the actuator.....	187
Fig. 6.103 Another failure in design 1-Z after the cycling test.....	187
Fig. 6.104 Cycling test of design 1D-L100. The microgripper was powered ON/OFF for 10 seconds each. The voltage applied was about 700 mV and the maximum heater temperature was about 160°C.....	188
Fig. 6.105 Cycling test of design 1D-L210. The microgripper was powered ON/OFF for 10 seconds each. The voltage applied was about 830 mV and the maximum heater temperature was about 160°C.....	188
Fig. 6.106 Powering ON/OFF of designs L100_S and L210_S .....	188
Fig. 6.107 Displacement of designs L100_S and L210_S .....	189
Fig. 6.108 Robotic systems used for manipulation and testing.....	190
Fig. 6.109 Design 1-E mounted on the robotic arm to manipulate the gold micro-structure. These micro-objects were mounted on the head of a needle.....	191
Fig. 6.110 Design 1-E used to pick a micro-object.....	191
Fig. 6.111 Manipulation of micro glass beads using design 2-A_500 (the interfaced microgripper).....	192
Fig. 6.112 Manipulation of micro glass beads using design 2-B (the L210_S microgripper) to arrange four beads as an array.....	192
Fig. 6.113 Micro-vacuum gripper designed using a needle to manipulate the discs ...	194
Fig. 6.114 Manipulation of the disc from a flat position into the slots (top view) using vacuum micromanipulation .....	194
Fig. 6.115 Manipulation of the disc from a flat position into the slots (side view) using vacuum micromanipulation .....	194
Fig. 6.116 Result from the needle (vacuum gripper) handling (a) top view (b) side view .....	195
Fig. 6.117 Top view of manipulating a disc using design 2-C (2 DOF microgripper)	195

Fig. 6.118 Side view of manipulating a disc using design 2-C (2 DOF microgripper)	195
Fig. 6.119 Robotic system used to implement the assembly process .....	196
Fig. 6.120 Side view of the assembly processes (a) disc is in the slot (b) picking the disc and change the disc orientation (c and d), Moving the disc to position, (e) aligning the disc on the carbon fibre and curing the UV glue using, (f) releasing the disc .....	197
Fig. 6.121 Top view of the assembly processes, (a) disc is in the slot, (b and c) picking the disc and manipulating the disc orientation (d) Moving the disc to position, (e) aligning the disc on the carbon fibre and curing the glue using UV, (f) releasing the disc.....	197
Fig. 6.122 Simulation and experiment results of displacement of both arms as a function to the heater average temperature of Design HWU-A .....	198
Fig. 6.123 Simulation and experimental results of displacement in closing mode operation as a function of (a) temperature and (b) current for the Design HWU-C	199
Fig. 6.124 Simulation and experiment results of displacement of both arms in opening mode operation as a function of (a) temperature (b) current of the Design HWU-C .....	200
Fig. 6.125 Actuator deformation after each on/off cycle and its effect on the end-effectors shape .....	202

## LIST OF TABLES

Table 2-1 Summery of micromanipulators systems.....	14
Table 2-2 Two different materials with different diameters, and the results [48] .....	23
Table 2-3 Summery of the externally actuated microgrippers.....	61
Table 2-4 Contactless micromanipulation methods.....	63
Table 2-5 Single end-effector microgrippers .....	63
Table 2-6 Microgrippers with Jaws with Integrated Actuators.....	64
Table 2-7 Materials used for microgrippers design. ....	64
Table 2-8 The physical properties of SU-8 2000 and SU-8 3000 series photoresist materials [124, 125].....	65
Table 3-1 List of direct actuated (one mode) microgrippers.....	75
Table 3-2 Tri-Arm Microgripper .....	78
Table 3-3 Properties of the SU-8 layer .....	86
Table 3-4 Properties of the metal layer .....	86
Table 4-1 Summery of designs with heater configuration of 10 /300 / 10 nm of Chromium / Gold / Chromium respectively .....	112
Table 4-2 Summery of designs with heater configuration of 7 / 200 / 7 nm of Chromium / Gold / Chromium respectively .....	113
Table 4-3 Summery of designs with heater configuration of gold only with thickness of 100 nm.....	113
Table 5-1 Group one of IMT design microgrippers.....	115
Table 5-2 Microgrippers Designed at Heriot-Watt University .....	116
Table 6-1 Microgrippers with different actuators and arm parameters.....	179



## LIST OF PUBLICATIONS

1. Al-Zandi; Muaiyd, Wang; Changhai (2018) Design of a Novel Three Arm Electrothermal Microgripper with Multiple Degrees of Control, *Advanced Materials Letters* (2018) Vol: 9 Issue 10 pp: 692 - 695 DOI: 10.5185/amlett.2018.2072
2. Al-Zandi; Muaiyd H, Wang; Changhai, Voicu; Rodica, Muller, Raluca (2016) Measurement and Characterisation of Displacement and Temperature of Polymer Based Electrothermal Microgrippers, *Microsystem Technologies* (2018) Vol: 24 Issue 1 pp: 379 - 387 DOI:10.1007/s00542-017-3298-8
3. Al-Zandi, Muaiyd H; Wang, Changhai; Voicu, Rodica; Muller, Raluca (2016) Testing and Characterisation of Electrothermal Microgrippers with Embedded Microheaters, *Proc. in Design, Test, Integration & Packaging of MEMS/MOEMS (DTIP16)*, Budapest, Hungary, pp. 1-5 DOI: 10.1109/DTIP.2016.7514880.
4. Al-Zandi; Muaiyd, Wang; Changhai (2018) An Electrothermal Microgripper with Multiple Degrees of Control, *AMWC-2018* DOI: 10.5185/amwc.2018
5. Voicu, Rodica; Mueller, Raluca; Al-Zandi, Muaiyd; Wang; Changhai (2019) V-shaped and Z-shaped SU-8 Micro-Tweezers with In-plane Displacement for Micromanipulation DOI: 10.1109/MARSS.2019.8860941
6. Aurelio; Iamoni, Sonia; Voicu, Rodica; Mueller, Raluca; Al-Zandi, Muaiyd H; Wang; Changhai (2017) Design and experimental testing of an electro-thermal microgripper for cell manipulation, *Microsystem Technologies* DOI: 10.1007/s00542-017-3460-3
7. Voicu, Rodica; Tibeica1, Catalin; Mueller, Raluca; Al-Zandi, Muaiyd; Wang; Changhai (2017) Nonlinear numerical analysis and experimental testing for an electrothermal SU-8 microgripper with reduced out-of-plane displacement, *Journal of Physics: Conference Series*, Volume 922, conference 1, DOI: 10.1088/1742-6596/922/1/012006

# Chapter 1 Introduction

Currently, the industrial field experiences high demand for miniaturised devices to decrease the size of a product and increase its accuracy and productivity. These devices mostly contain parts manufactured using different processes. Therefore, the assembly of these parts requires a micrometer scale accuracy of manipulation and alignment. There are several methods to manipulate micro-objects such as contactless manipulation (using magnetic field, electrostatic forces etc.), one-finger grippers (using electrostatic forces, vacuum power, cryogenic end-effectors etc.), and microgrippers with dual end-effectors.

Although other methods rather than microgrippers have been successfully used in the microassembly field, they do not have the power of tweezers to manipulate micro-objects freely. With microgrippers, the alignment, orientation control and angle control are much easier, especially in the research and development field. Although there are several piezoelectric and silicon-based microgrippers, they are very expensive and lack flexibility because of their sizes. Therefore, a small, accurate, and low cost microgripper is essential.

## 1.1 Background

Micromanipulation refers to a series of processes applied on microscopic size particles. The working environment is known as “Micro-world” and it points to the range from submicrometric to several millimeters, as shown in Fig. 1.1. In the micro-world, the related physics is different and the larger partials which some attribute is inversely related to size. In addition, some of the negligible forces become significantly effective at the micro-size such as surface tension, electrostatic etc. This is known as “scale effect” and should be studied at the micro-scale itself [1, 2].

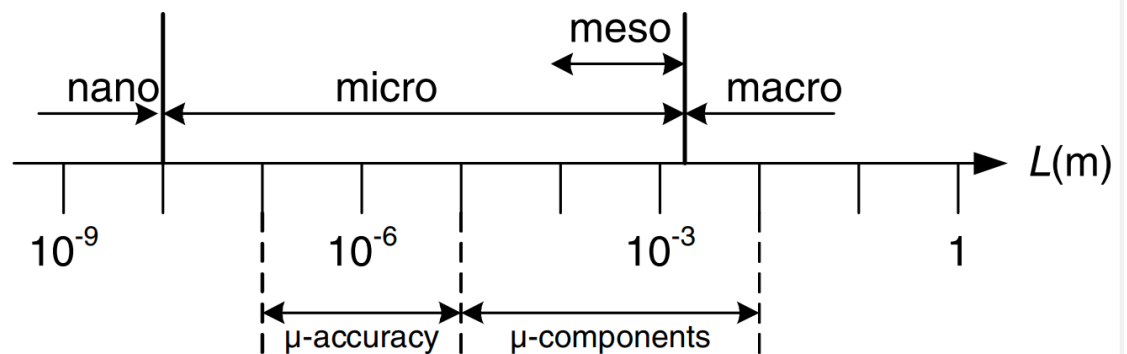


Fig. 1.1 Size and scales [1]

Recently, there has been high demand for miniaturised devices in many fields such as aerospace, biology, nuclear science etc. [3] in order to increase accuracy and functionality and to shrink the unit area [4, 5]. Such devices are built of hybrid pieces which come from different manufacturing methodologies and they cannot be fabricated on the same production line [6]. An example of such a device is a micro-electromechanical system (MEMS) which is based on multi-functional systems and requires components made from different fabrication processes [7].

The microassembly concept refers to the micromanipulation, alignment, and bonding processes. There are two main microassembly approaches. The first approach is based on the “self-assembly paradigm”, in which the surface effects are employed for alignment and positioning. The other approach is based on “microrobotic assembly”. Microrobotic is a microscale active structures which can generate a movement and to interact with other structures. Generally, these are attached with micro size microgrippers mainly down to about 10  $\mu\text{m}$ . In this method, miniaturised actuators and precise micromanipulators are used for the accurate assembly of micro-particles [2].

Actuators is a machine transfer an applied power to mechanical movement. For example, applying voltage on a piezoelectric material generate a mechanical displacement. It is the core of microassembly and micromanipulation systems.

Although, there are many systems in the market for mass and parallel production [8, 9, 10], they are not suitable for small production or prototyping. This is because of the high cost of setting up and modifying such systems and prototyping always requires modifications [11].

## **1.2 Objectives**

- To carry out a brief review of micromanipulation methods and the materials used in order to obtain the required understanding of existing technologies, challenges, and drawbacks, and to identify gaps to be filled.
- To employ COMSOL Multiphysics to determine the behavior of the newly designed microgrippers.
- To develop a robotic-based new measurement method to study the static and dynamic behavior of polymer microgrippers.
- To study in depth several electrothermal actuated microgrippers based on SU-8 material. This study includes the static, dynamic and the reliability (on/off) cycling).

The results of these tests will be used to develop a new actuator design and new microgripper structure.

- To design several microgrippers of large displacement value which are reliable for thousands of cycles.
- To demonstrate the advantages of the new design by highlighting the key features and show the ability to use these microgrippers in real world research and development applications.

### **1.3 Thesis Structure**

The thesis is structured as follows:

Chapter 1: Introduction. This chapter introduces the concept of microgrippers used in this thesis, sets out the scope of study and research, outlines the proposed contribution, and summaries the structure of the thesis.

Chapter 2: Literature Review.

Chapter 3: Design and Simulation. This chapter presents the design of the microgrippers based on an electrothermal actuation mechanism. These microgrippers are based on the SU-8 polymer material. COMSOL Multiphysics is used to study and improve the microgrippers to obtain the best and most effective design.

Chapter 4: TCR Measurements. This chapter presents the results of measurements of the temperature coefficient of resistance (TCR) of the microheaters in several different microgrippers. First of all, different measurement methods of TCR measurements were used to obtain accurate results of temperature related change of resistance for different metal layer configurations as the microheaters. . Two groups of microgrippers were studied in this chapter. The first group was designed and fabricated by IMT, Romania and the other group was designed at Heriot-Watt University in the UK.

Chapter 5: Characterisation and Measurement Methods. This chapter presents the control and measurement methods which were developed for characterisation and evaluation of the SU8 based electrothermal microgrippers. Two methods for measurement of static displacement were studied and compared using the Zygo metrology based system and a robotic system respectively. The design and construction of a custom electronic interface is described for measurement of dynamic responses, reliability study and lifetime of operation. A method and the associated processes for

demonstration of robotic microassembly using a microgripper developed in the thesis work is presented.

Chapter 6: Results, Analysis and Demonstration. This chapter presents the results of characterisation, measurement, evaluation and demonstration of application of electrothermal actuators. The results of displacement under steady state operation are shown and discussed. The results of dynamic responses in switch-on and switch-off operation are presented. The demonstration of application of the microgrippers for robotic microassembly is described in successful assembly of a copper foil disc on a carbon fibre rod.

Chapter 7: Conclusion. The contribution of this thesis is presented and some future work to develop the SU-8 electrothermally actuated microgrippers is proposed.

## Chapter 2 Literature Review

The steps in the microassembly of miniaturised devices are micromanipulation processes (picking, orientating, placing, and releasing) and bonding the parts together. Different methods are used to manipulate micro-particles depending on their sizes, stiffness, and the application. These methods are divided into two groups: contactless handling and contact handling. This chapter summaries the existing micromanipulation mechanisms and actuations techniques.

### 2.1 Microassembly Methods

In this section some of the well-known techniques used to implement microassembly are presented. Then, some of the most popular robotic-based manipulators are highlighted.

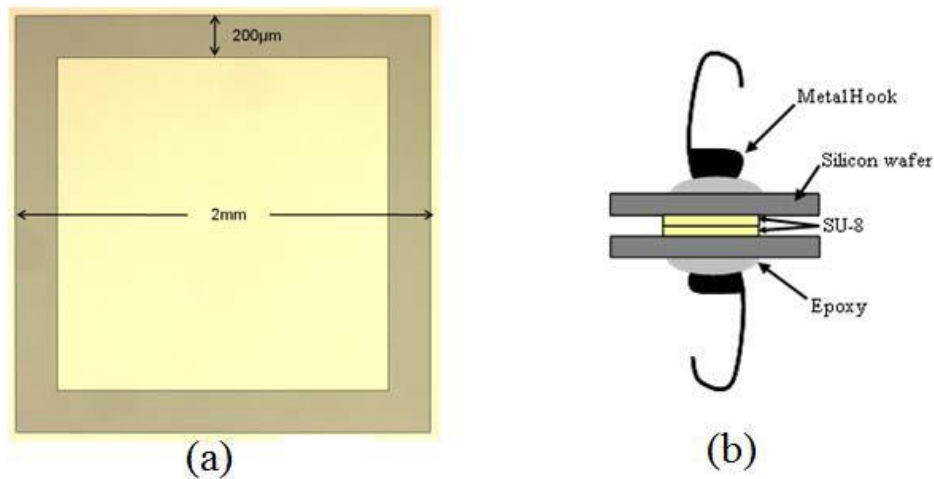


Fig. 2.1 (a) Optical image of a square ring with dimension of 2 mm and width of 200  $\mu\text{m}$  prior to flip-bonding. (b) Cross-section image of the assembled structure [12]

#### 2.1.1 Flip-Chip Microassembly Technique

A method was developed to assemble two arrays of parts using pressure and heat to bond them together. This method is used in the electronics field and MEMS application for parallel assembly based manufacturing when a multi-planar process is required, particularly when different fabrication processes are involved to make the parts. With this technology, there are three main steps. In the first step, the substrate was placed on bottom chuck (platform) and the chip is picked up and flipped by the upper chuck. The chip is then aligned to substrate with the corresponding bumps for electronic interconnections to the pads on the substrate. Finally, the bumps on the chip and the pads on the substrate are bonded by pressure and heat to make electronic connections between

the chip and the substrate. In MEMS packaging for encapsulation, different materials are used for the adhesive layer depending on the application, for example SU-8, as shown in Fig. 2.1 [13, 12].

### 2.1.2 Self-Assembly Methods

The surface tension-based folding process is employed to force some parts to behave in a certain way. The strategy is to implement a bilayer of thin film hinges made of chromium (Cr) and copper (Cu). Because of the mismatch in the coefficient of thermal expansion (CTE) of the layers, a residual stress is developed during the film deposition process such as thermal evaporation. This stress pulls or pushes the two sides of the hinges and generating an angle. The angle can be controlled by changing the thickness of each layer and the direction of the folding can be controlled by the order of the layers, as shown in Fig. 2.2. Fig. 2.3 shows an example of self-assembling a cube surrounding a glass bed [14, 15, 16, 17].

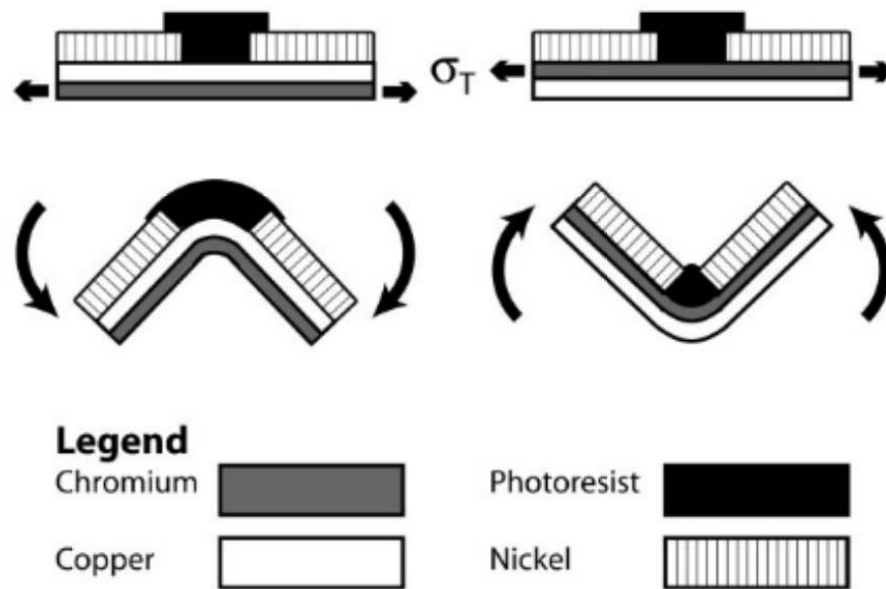


Fig. 2.2 Schematic of side view of hinges used in self-folded structure. The order of the metal layers defines the direction of folding [15]

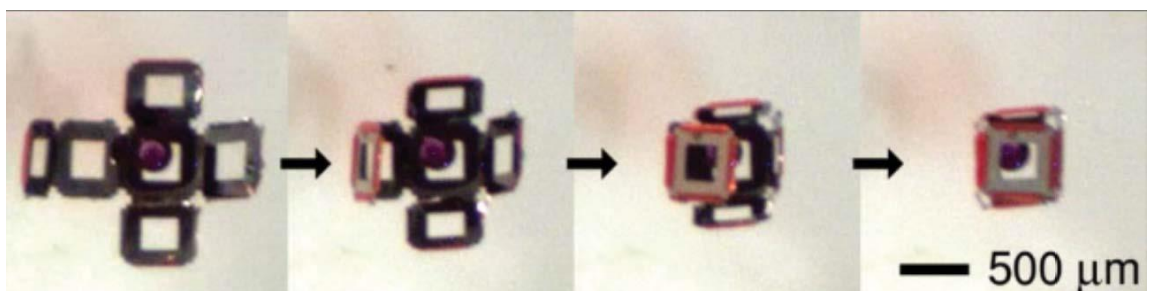


Fig. 2.3 Video sequences of a cruciform folding and encapsulating a dyed 275-μm glass bead [15]

### *2.1.3 Robotics Systems*

Robotics systems have merited the attention of academic and industrial researchers over the past 20 years. This field of studies covers the design, fabrication, and control of microassembly robotic systems. The importance of robotics in microassembly lies in the new generation of miniaturised devices containing parts from different manufacturing processes such as CMOS, MOEMS, LIGA, etc. Microassembly using robotics is the solution to overcoming such limitations.

An example product is the ‘Given Imaging’ camera capsule, which is assembled using this technology. This product is used in non-invasive surgery, whereby a patient swallows the device, and it sends images of the gastric system. Another example of such a device is developed by IRIS. This complex device contains sensors and actuators, and it is used in the field of ophthalmic surgery. Such devices need highly accurate technology to assemble and integrate the micro-components. The two previously mentioned technologies are not sufficient for this. Micro-assembly is simply handling, characterising, sorting, or/and positioning for a fully automated or semi-automated system.

There are several requirements for the micro-systems to achieve the target processes. First, the degree of freedom (DOF) which limits the flexibility of movement. Some systems come with six DOF such as Hexapod from Pi. The six DOF can be divided into a linear 3 axes (X-axis, Y-axis, and Z-axis) and an angular 3 axes ( $\alpha$  around Z-axis,  $\beta$  around Y-axis and  $\gamma$  around X-axis). Access to the workbench and implementation of the micro-assembly tasks should be easy and controllable. The vision feedback resolution is important for the right process to be accomplished [6, 18, 19, 20].

Micro-assembly systems can be divided into two categories depending on the methodology for operation. These are serial assembly and parallel assembly methodologies. In serial assembly, one task is done at a time in sequence until it is finished before the next one is started. In parallel assembly, the microassembly system relies on the known position of each element and they are processed together. In serial assembly, a more complex micro-device can be built while in parallel assembly, more devices can be produced.



Serial assembly can be divided into several categories:

- Master-slave system (Tele-Operation): this is a manually controlled system. It contains a basic element to do the assembly such as a gripper, a force sensor, or a microscope camera. The pick-release tasks are controlled by haptic input devices.
- Automatic assembly machines: these are pre-programmed to identify the position of the parts using cameras. These systems carry out repeated microassembly processes. Most of the new systems have six DOFs ( $x$ ,  $y$ ,  $z$ ,  $\gamma$ ,  $\beta$ , and  $\alpha$ ) which offer the flexibility to implement the tasks easily.
- Assembly by micro-robots: the assembly and manipulation tools are integrated in one microrobot. These types of systems do grasp, transportation, positioning and special processing steps like cutting, scratching, and bonding.
- Micro-factories: development of the microassembly and micromanipulation systems, for example in the field of automation, have become highly reconfigurable. A tabletop-sized microassembly system which is capable of automatically assembling a series of microproducts, is referred to as a micro-factory' [18]. Ideally, the micro-factory is installed in a clean and closed space like a cleanroom [18].

In operation process, microassembly is divided into a series of tasks:

- Identifying the object: First of all, the micro-system needs to identify an object and its position and move the end-effectors close to the object. This could be done manually or automatically using a vision system.
- Picking: This task could be implemented using a micro-gripper or any other tool which is capable of grasping objects. Some of these tools could have a force sensor which provides feedback to the control system in the robot. This sensor is used to detect the grasp event to stop applying more forces.
- Positioning: After the object has been grasped, the system should find the target position and move the object to the destination. The sensing method for achieving this task depends on the manipulation strategy. For example, in a linear accurate actuator, the steps are calculated from a reference point while in another system real image processing is used.
- Alignment of the target object to the destination.

- Placement (or release task): The picking force is gradually decreased to release the object on the target position. However, sometimes the gravity force is not enough to release micro-objects so additional forces are used for this purpose.
- Moving away: Ending the task by moving the end-effectors from the object to start a new task or end the job [6].

The closed-loop control is used in the micro-robotics field and in some actuators with sensors are embedded in them. These tiny sensors are not easy to control and install because of the complexity of integrating them into the tiny actuators. These reasons make the multi-degree of freedom micro-robotic systems difficult to manage [21].

The following are some examples of robotic micromanipulators:

#### A. TRING-Module

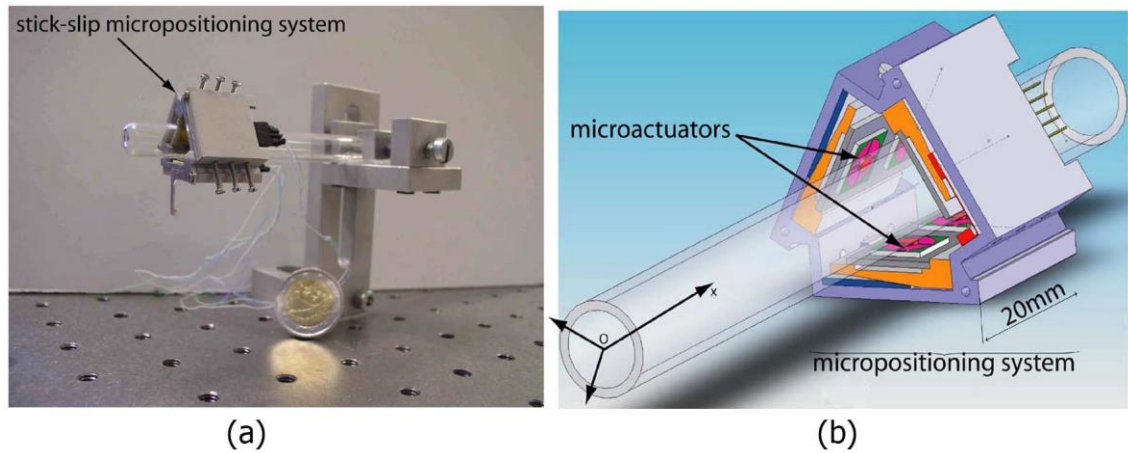
This system of micropositioning was developed in FEMTO-St Institute and dedicated to a microfactory station. The actuator part was based on piezoelectric and stick-slip principles with 2 DOF (linear and angular). A glass tube was supported from one edge and used as an axis for the Tring-module, as shown in Fig. 2.4.

TRING system specifications can be summarised as:

- This model has two DOF (degrees of freedom)  $Z$  and  $\gamma$  which are linear and angular.
- Linear resolution of 70 nm to 200 nm with a speed of 2 mm/s and workspace of more than 5 cm.
- Angular resolution of 17  $\mu\text{rad}$  - 44  $\mu\text{rad}$  with a speed of 2.4 rpm and 360° of available movement.
- This system has unlimited Stroke in both motions.
- This system has less degree of freedom, so it does not require a complicated control system.
- It works in scan mode by applying continuous voltage of saw-tooth wave with amplitude of  $\pm 150$  V and frequency of 10 kHz.
- The scanning displacement is linear related to the applied voltage.

To maintain the linear and angular movement, there are three pairs of contacts between the micro-systems and the glassy cylinder (spindle). Each actuator (from the six) has five electrodes used to control the motion, four for the saw-tooth signal and one as ground reference. The linear motion and angular motion are caused by applying a different control voltage. When applying a  $+V(t)$  on electrodes one and three and  $-V(t)$

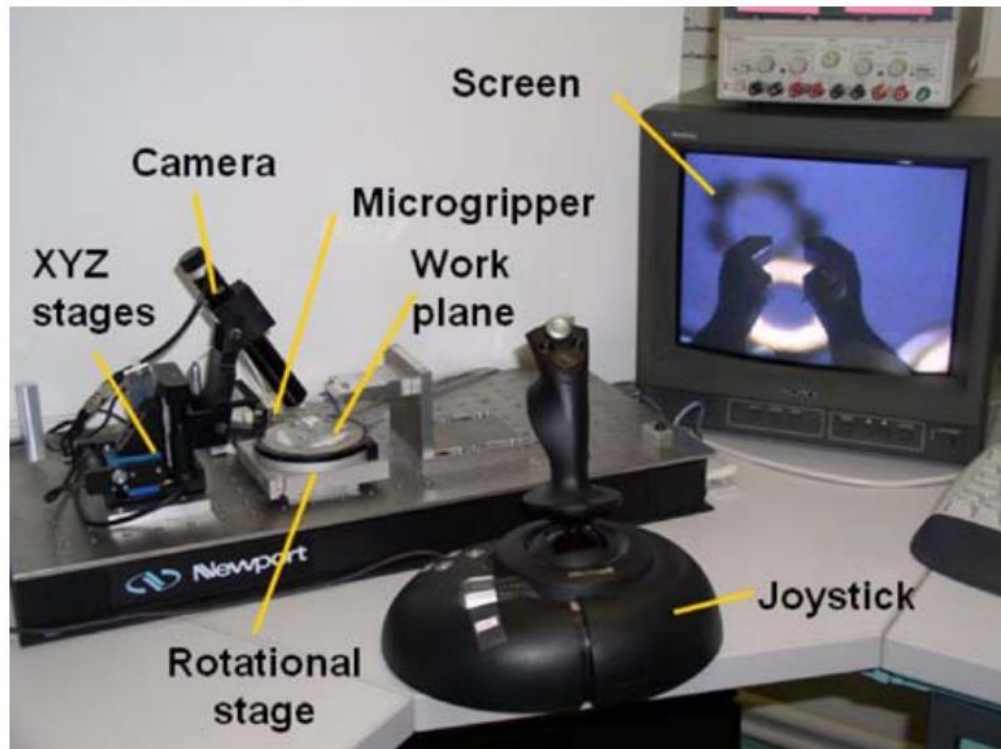
on electrodes - two and four, a linear motion is obtained. The angular motion is obtained by applying the  $+V(t)$  on electrodes - one and two, and  $V(t)$  on electrodes - three and four [19, 22, 23, 6].



*Fig. 2.4 TRING-Module 2 DOF robotic micromanipulator. This robot was based on piezoelectric material and Stick-slip actuation method (a) photograph for a set system (b) schematic showing the system components [24]*

#### B. Four DOF micromanipulator

This system is based on Physik Instrumente 3 DOF translation stage and a rotated stage as a work plane. The linear stage has 25 mm of stroke and the rotational has  $360^\circ$ . A SPI TIMM-400C camera was mounted at an angle of  $45^\circ$  for visual feedback. A joystick was used to control the system, as shown in Fig. 2.5 [25].



*Fig. 2.5 4 DOF Manipulator system [25]*

### C. IRIS Microassembly System

This system is based on a 6 DOF manipulator and is composed of 4 DOF units and 2 DOF gripper units. The base consists of a precise 3 DOF stage mounted on a precise rotational stage which rotates around the z-axis, as shown in Fig. 2.6. The resolution of the rotary actuator is  $0.001^\circ$  with infinite rotation, and the linear stage is  $1.4\text{ }\mu\text{m}$ . The working area is equipped with pneumatic and vacuum valves to fix the manipulated object on the stage. The gripper unit is composed of a rotational arm around the x-axis and y-axis and holds a microgripper at the end-effectors.

This system is designed to be controlled by a 3D input device control or using a task planner software which manage the axis's depending on a previous control command. The system's interface is based on Phantom® Omni™, which has a force feedback and position sensors based on potentiometers. There are two control interface modes. The first is GUI control mode which uses a normal mouse, and the functionalities are distributed on the mouse buttons. The second is a robotic control mode, where both input devices are used. This system uses three cameras to build a virtual environment which is the same as the real one.

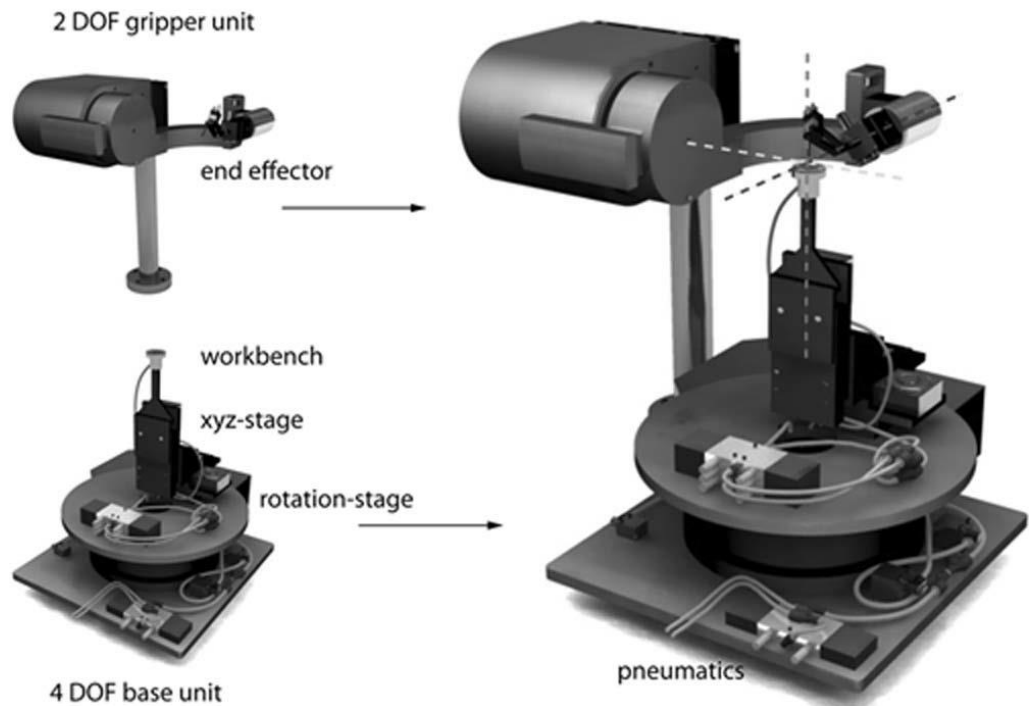


Fig. 2.6 A 6 DOF IRIS manipulator showing the 4 DOF base unit and the 2 DOF gripper unit [18]

All the motion commands are checked by the 'virtual reality control center' to verify whether these commands are applicable or not. Only the safe commands are passed to the real system; all others which could cause damage are blocked. After each motion, the

position sensors feed the visual computer to update the virtual environment with the new data. The disadvantage in this system design is the processing time which causes a delay in the execution of the commands and, therefore, slows applications [18].

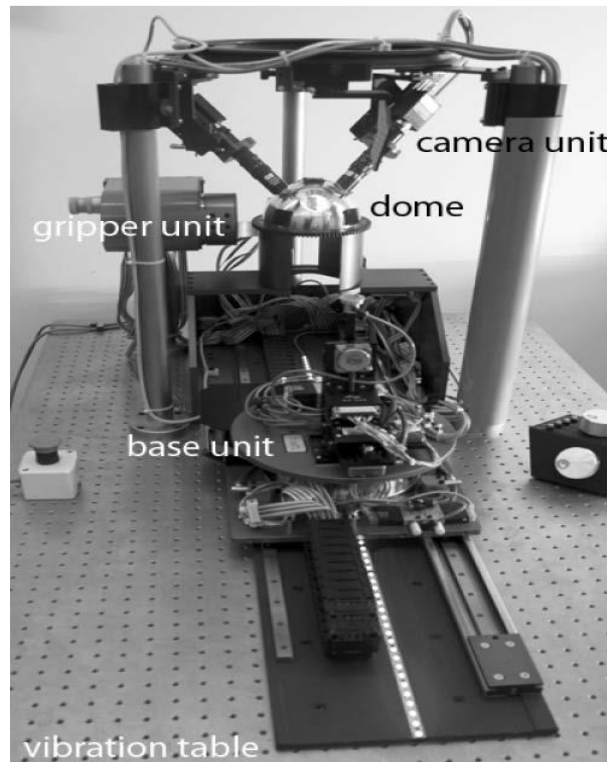


Fig. 2.7 IRIS micro-assembly system [18]

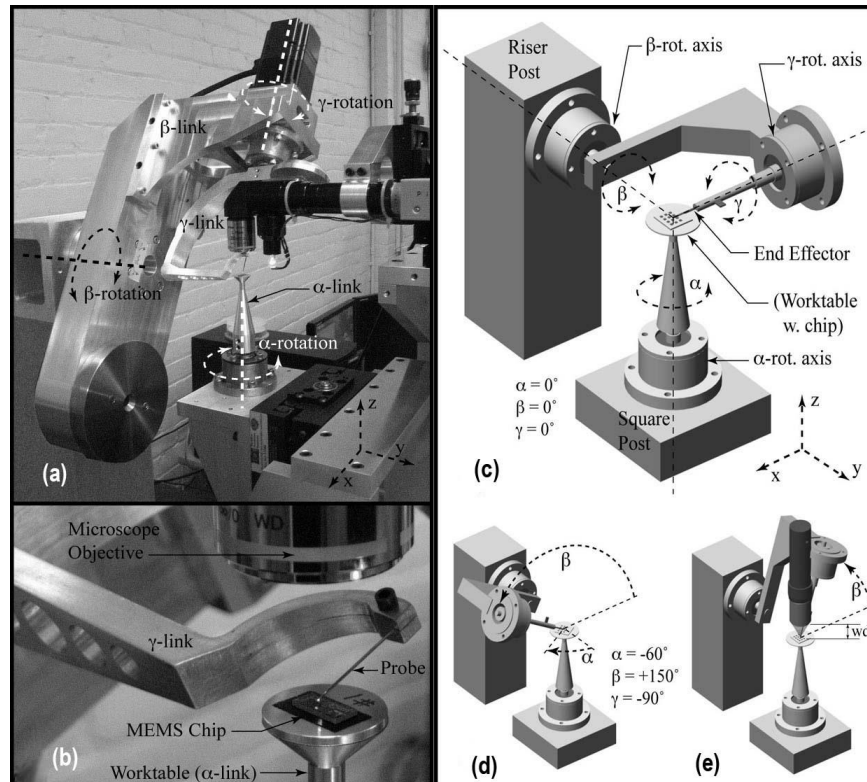


Fig. 2.8 6 DOF assembly system (a and c) showing the rotation directions (b) focus photo on the working space (d and e) the end-effectors in different situation [26]

#### D. Robot Rotational Links for Assembly System of Three-Dimensional MEMS

This system was developed to assemble MEMS devices with the ability of 3 rotation degrees of freedom ( $\alpha$ ,  $\beta$ , and  $\gamma$ ) and 3 translation axes (x, y, and z), as shown in Fig. 2.8. The workspace can rotate  $360^\circ$  while the end-effectors rotate only  $110^\circ$  and the end-effectors holder rotates  $180^\circ$ . One microscope with 0.8-micron optical resolution was mounted for vertical view [27, 28, 26].

#### E. Percipio-Robotics Systems

Percipio has developed several commercial semi-automated systems for micromanipulation and microassembly. The workplace of their systems is based on a 6 DOF hexapod or a rotation stage. Also, they are equipped with a robotic arm with 3 DOF based on brushless motors. To control the motion of both the robotic arm and the hexapod, a keyboard, joystick, or gamepad can be used. For user interface feedback, 2 cameras are used. Most of these systems are equipped with a 2 DOF piezoelectric-based microgripper. One of these systems is used in carrying out most of the research work described in this thesis [29].



*Fig. 2.9 Percipio-Robotics micromanipulation systems examples [29]*

A summary of the micromanipulator system examples is listed in Table 2-1. The system flexibility depends on the number of degrees of freedom (DOF) and the resolution

of the displacements of the system . However, the accurate assembly depends on the system displacement accuracy and repeatability.

*Table 2-1 Summery of micromanipulators systems*

Design	DOF	Resolution	Speed	Actuator method	Actuator materials
TRING-Module	2 (Z and $\gamma$ )	70 nm to 200 nm and 17 $\mu$ rad - 44 $\mu$ rad	2 mm/s for linear and 2.4 rpm for angular	stick-slip	piezoelectric
Four DOF micromanipulator	4 (X, Y, Z, AND $\theta$ )	0.1 $\mu$ m for the stage	-	-	-
IRIS Microassembly System	4 (X, Y, Z, AND $\theta$ )	1.4 $\mu$ m and 0.001°	-	electric motors	-
Robot Rotational Links	6 (X, Y, Z, $\alpha$ , $\beta$ , and $\gamma$ )	0.7 $\mu$ m and 0.036°	-	Stepper motors	-
Percipio-Robotics Systems	6 Hexapod 3 Robotic arms	0.36° and 0.5 $\mu$ m	400 °/s and 1300 mm/s 2000 mm/s	BLDC	-

#### *2.1.4 Piezoelectric Based Positioning*

More than a century ago, on the 2<sup>nd</sup> August 1880, brothers Jacques and Pierre Curie reported their discovery of electromechanical behavior. They showed conversion between the mechanical force and electrical force in some materials later became known as the piezoelectric effect. If a mechanical force is applied on these materials, such as quartz crystals, an electric field is generated, and when an electric field is applied on these materials, they generate a displacement. The displacement value depends on the amount of the electric field applied and the properties of the materials. Since the discovery, many applications and products have been developed by employing these materials such as transducers (for example speaker), sensors (for example force sensors) and actuators [30, 31]. Briefly, the following are some techniques used to design actuators using piezoelectric materials:

##### *A. Stick-slip actuators (SSA)*

Stick-slip points to two movable surfaces cycling between two states of movement and stop, as shown in Fig. 2.10. This method is widely used for nano-scale actuation resolution to microscale which in its application can be found in precise devices to a daily used device, for example, “fluid dynamics, acoustic effects in stringed musical instruments, static friction (stiction) in magnetic information storage systems, severe wear or ‘seizing’ of different materials of electric contacts and jerking of brakes” [32, 22]

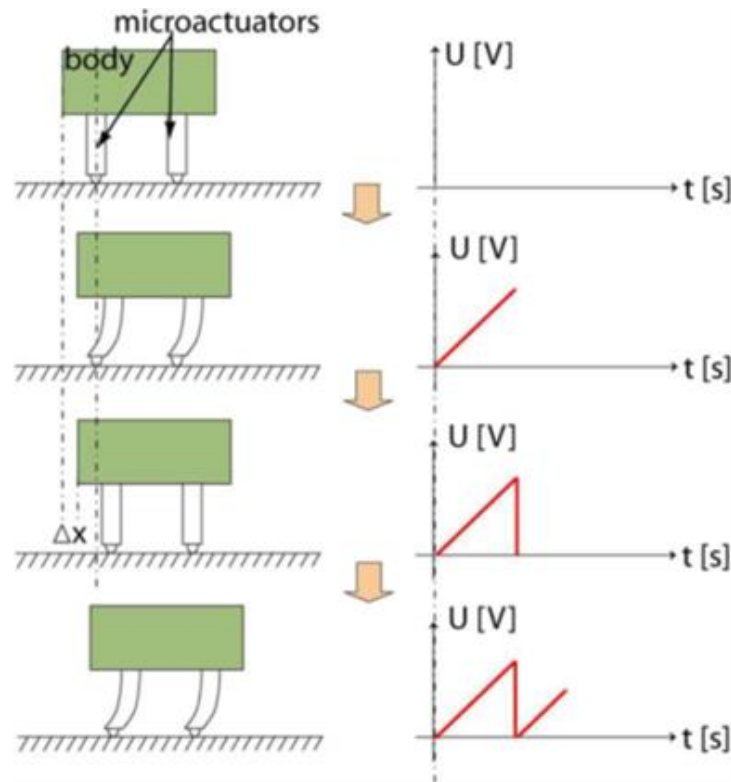


Fig. 2.10 Stick and Slip Actuator, operation principle [22]

This method was employed to design a nanomanipulator with nanometer resolution and several centimeters of workspace. These actuators operate in two modes: stepping mode and scanning mode. In the stepping mode, a saw-tooth voltage is applied on a piezo part. The electrical power is converted into a change in the shape of the microactuators. This deformation generates a step of movement with very low resolution. Then, it is followed by the scanning mode, in which the actuator is slowly moved until it is stopped in the final position. An example of 2 DOF linear and angular manipulator is presented in Fig. 2.4 [24].

The SSA was integrated to design a complex micromanipulator, a parallel kinematics actuated by three SSAs, each of them having 2-DOF. The platform has thus 6-DOF (3 translations and 3 rotations) [33]. The working volume is  $140 \text{ mm}^3$  and the structure volume is less than  $4 \text{ cm}^3$ . The maximum manipulated load was 100 mN. This actuator is mainly used for industrial micromanipulation of microscopy object assembly such as: optical and sensor microsystems, micro-factory (micromachining, micromanipulators, conveyors etc.), chemical and bio-engineering equipment [33].

#### B. Inchworm Motion Principle

This actuation / positioning method is based on three bi-stable piezoelectric actuators and is also known as inchworm motor. Two of these actuators are designed for clamping



and one is located for propulsion. Fig. 2.11 shows an example of a two directional inchworm linear actuator, in which the piezo actuators are powered in a sequence of 5 steps to generate a desired displacement. In this example, the mobile part moves up following these sequences. At the beginning, the lower actuator is powered. The produced expansion fixes the bottom part to the trunk, to keep the other two piezo parts free. Then, the middle actuator is activated. The generated expansion pushes the upper part up. Later, the upper actuator is activated and then the lower actuator is deactivated. This leaves the bottom part free of movement and fixes the upper part. Finally, the middle actuator is deactivated then the lower actuator is activated. By reversing these sequences, the direction of displacement is reversed too [34].

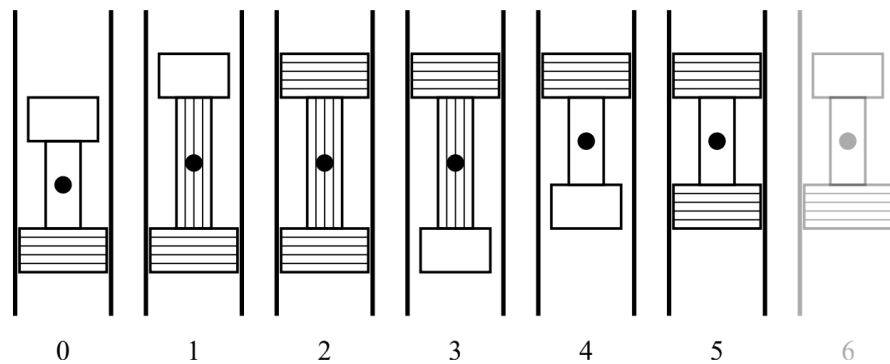


Fig. 2.11 An example of a linear actuator based on inchworm actuation method [34]

Another example of using this methodology of actuation is shown in Fig. 2.12. In this example, the mobile parts are two piezoelectric for clamping and the propulsion part is separated from them. The actuators are used to perform a linear shifting in six steps [35]

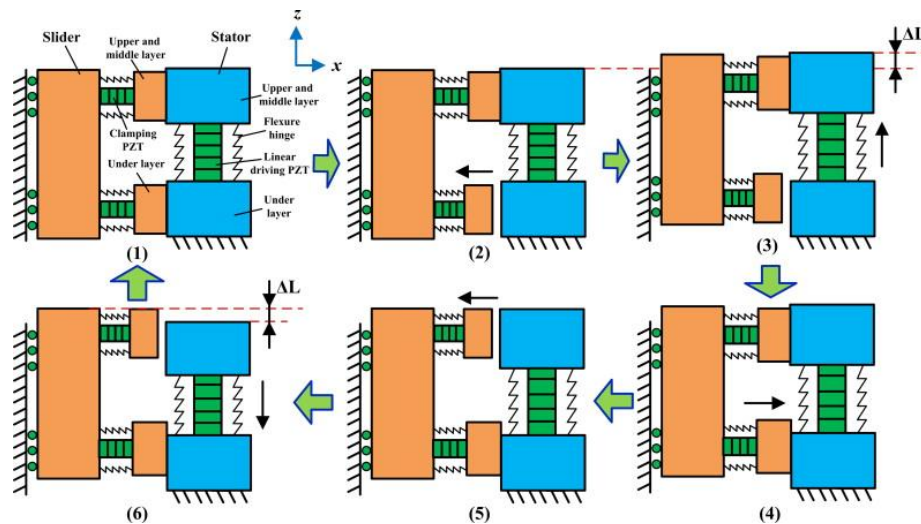


Fig. 2.12 Another example of linear actuation using the inchworm principle [35]

An example of application is shown in Fig. 2.13 The inchworm motion is used to control the lens position for zooming and auto focusing [36]. Fig. 2.14 shows an example of using the inchworm motion to generate a rotation motion with high resolution. The step size is only  $2.36 \mu\text{rad}$ . This method is based on four piezo actuators and two belts. Each belt is connected to two piezo actuators and each actuator is fixed from one side. The displacement is a sequence of three actions: clamp, release, and turn the rotary part [37].

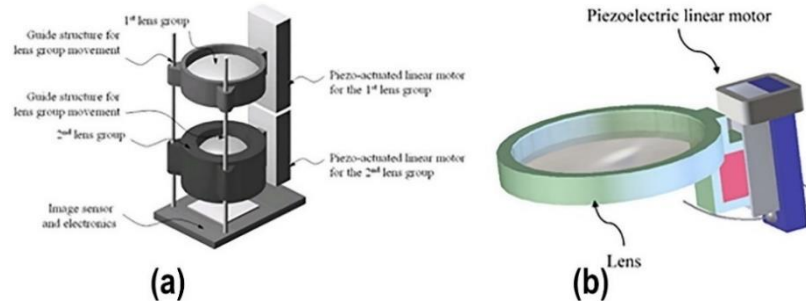


Fig. 2.13 Cell phone camera module zooms based on inchworm linear motion [36]

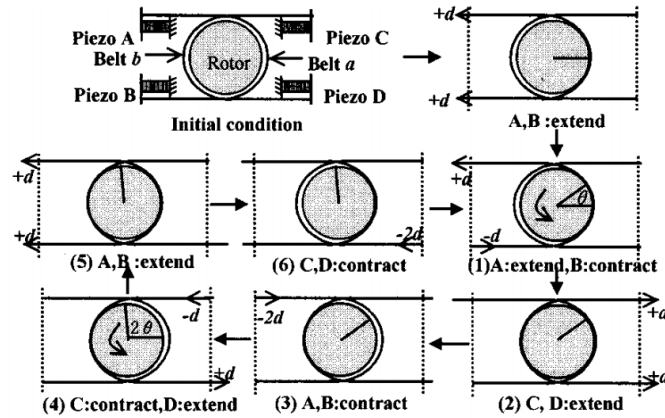


Fig. 2.14 Motion sequences: a belt clamps the rotor (2,5) while the opposite belt is released (3,6) and the clamped belt turns the rotor (1,4). Three sequences (clamp  $\rightarrow$  release  $\rightarrow$  turn) repeats. One complete cycle is composed of six sequences [37].

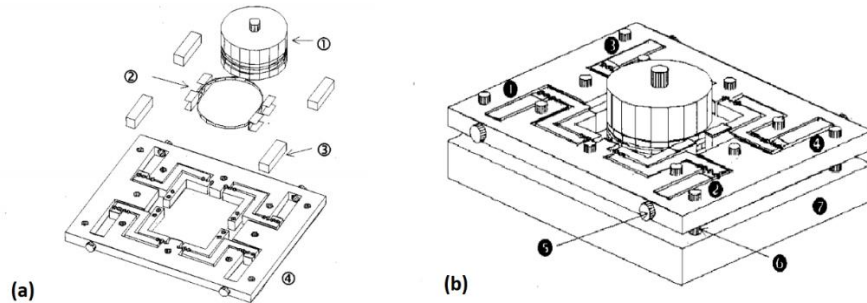


Fig. 2.15 Assembly diagram of the precise rotary motor. (a) Exploded diagram; 1: rotor, 2: belt, 3: piezoelectric actuator, and 4: upper plate with flexure hinge levers. (b) Assembled; 1: piezo A, 2: piezo B, 3: piezo C, 4: piezo D, 5: adjusting screw, 6: pillar, and 7: base frame (lower plate) [26]. [37]

## 2.2 Actuation Principles - Contactless Micromanipulations

Micromanipulation processes (pick, displacement, and release) are essential for microassembly and the maintenance work of micro-devices. Different methods are used to manipulate micro-particles depending on their sizes, stiffness, and the application. They are also subdivided into two groups: contactless handling and contact handling.

### 2.2.1 Photophoresis

Photophoresis is a phenomenon whereby a light causes microparticles to suspend in gas or liquid to displace. Because the light force is effective on the micro-objects, and it can be used for manipulation, measurements and positioning micro-objects. This was first reported in 1970 by Ashkin [38].

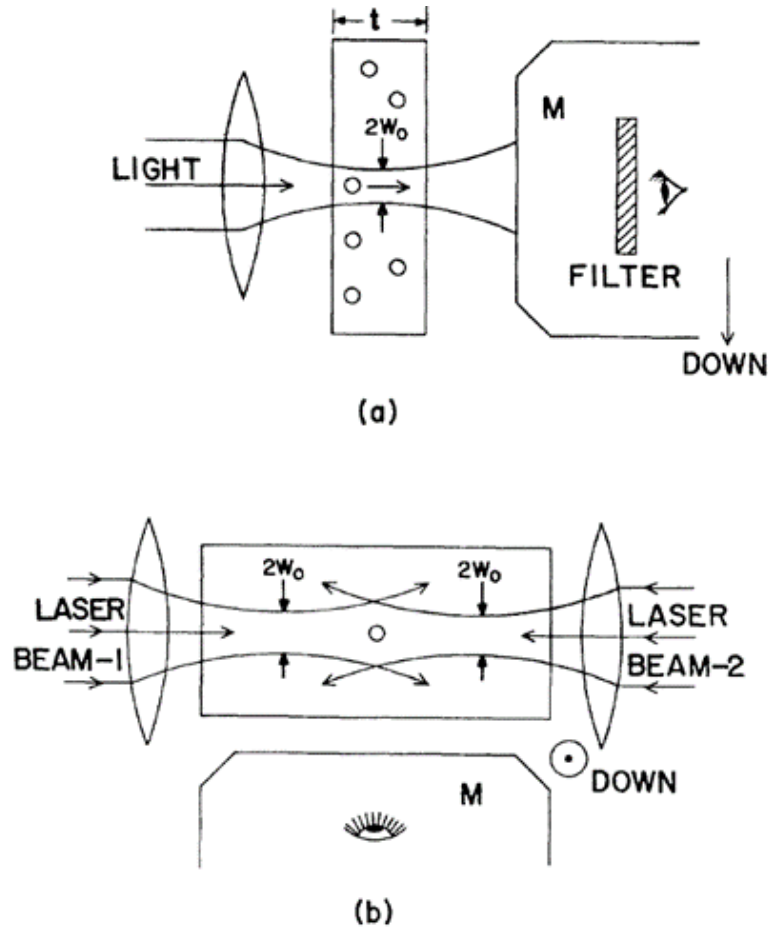


Fig. 2.16 Argon laser manipulator [38]

As shown in Fig. 2.16 (a), two experiments were done on a latex micro-sphere with 0.59, 1.31, and 2.68  $\mu\text{m}$  freely dispersed in water. In one case, an Argon laser in  $\text{TEM}_{00}$  mode with a radius ( $w_0$ ) of 6.2  $\mu\text{m}$  and ( $\lambda$ ) of 0.5145  $\mu\text{m}$  was passed through glass with a thickness of 120  $\mu\text{m}$  and focused on a single micro-particle in the center. In the other experiment it was found that a power of milliwatt was enough to manipulate and

accelerate the micro-sphere into the light direction. The acceleration was inversely proportional to the diameters of the micro-spheres. The second experiment shown in Fig. 2.16 (b) was on testing trapping of a micro-sphere in a position [38].

The light force was used as optical tweezers for live cell manipulation. For example, cells were sorted in microfluidic systems using optical force. Fig. 2.17 shows a system using a femtosecond laser with repetition rates of 1 – 1000 Hz, wavelength of 800 nm, and pulse width of 120 fs. This system was used to capture and manipulate *Bacillus subtilis* in a microchannel and then they were patterned, as shown in Fig. 2.18 [39].

This method in both previous examples proves the ability of light force to manipulate micro-objects and live cells. However, there are disadvantages in this approach. First of all, the size of the manipulated particles is limited by the laser beam width. Increasing the laser power increases the medium temperature which limits the possible application. In addition, this method can be applied only on suspended particles and the speed of the migration is accelerated slowly [40, 41].

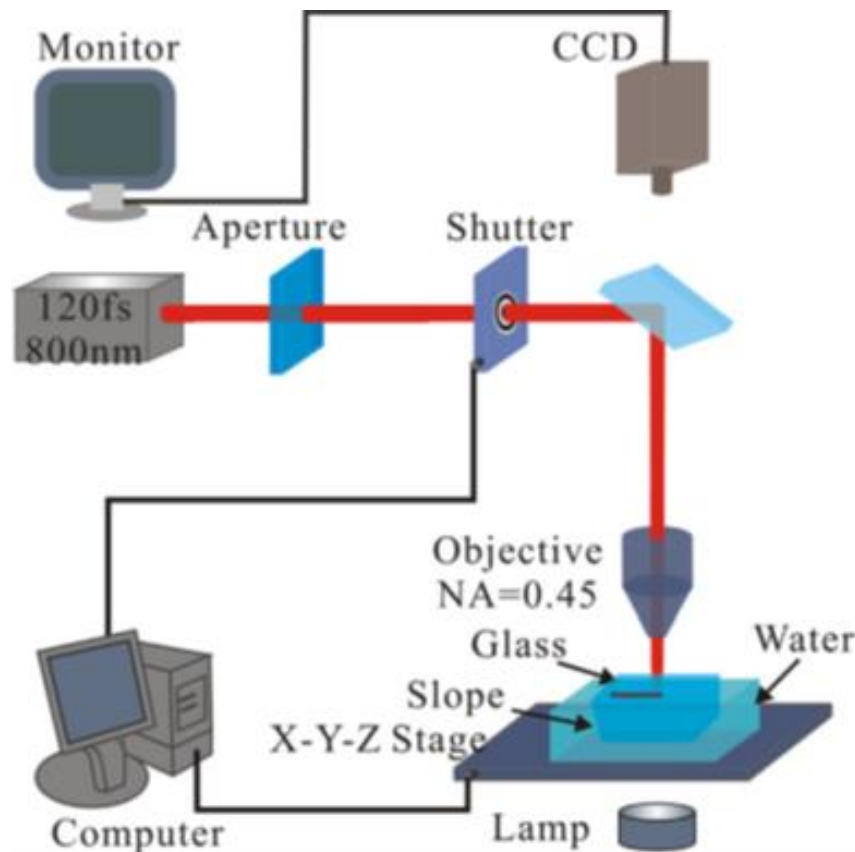


Fig. 2.17 A cell manipulator system using the photophoresis [39]

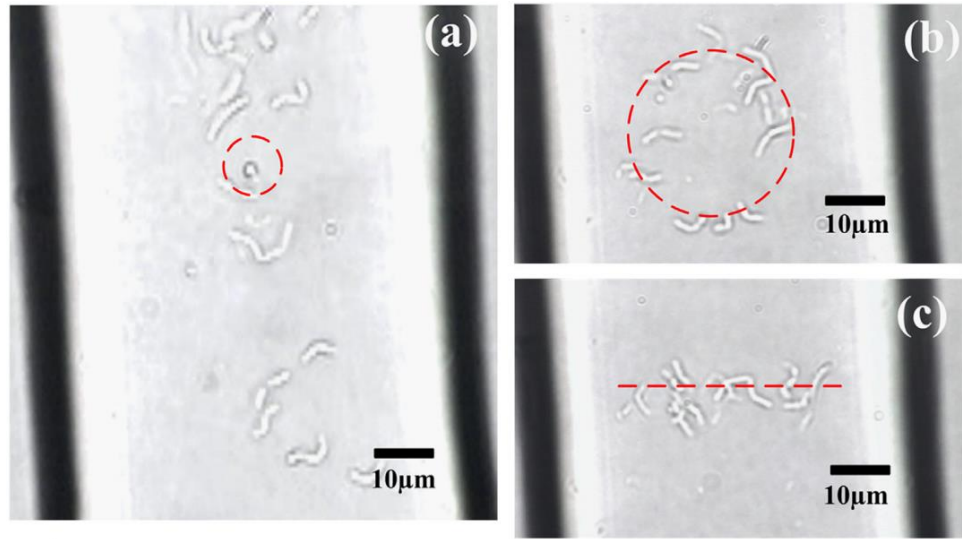


Fig. 2.18 (a) A *Bacillus subtilis* was captured by the optical tweezer. (b) *Bacillus subtilis* was patterned in circle. (c) A *Bacillus subtilis* was patterned in line [39]

### 2.2.2 Hydrogel Microgripper

A contactless microgripper was based on biocompatible hydrogel material. This microgripper was designed to propose a solution for cardiovascular diseases, potentially for intravascular therapy applications, as shown in Fig. 2.19. This microgripper was positioned in liquid using a direct current (DC) electromagnetic field, while the gripping was performed by an alternating current (AC) electromagnetic field [42].

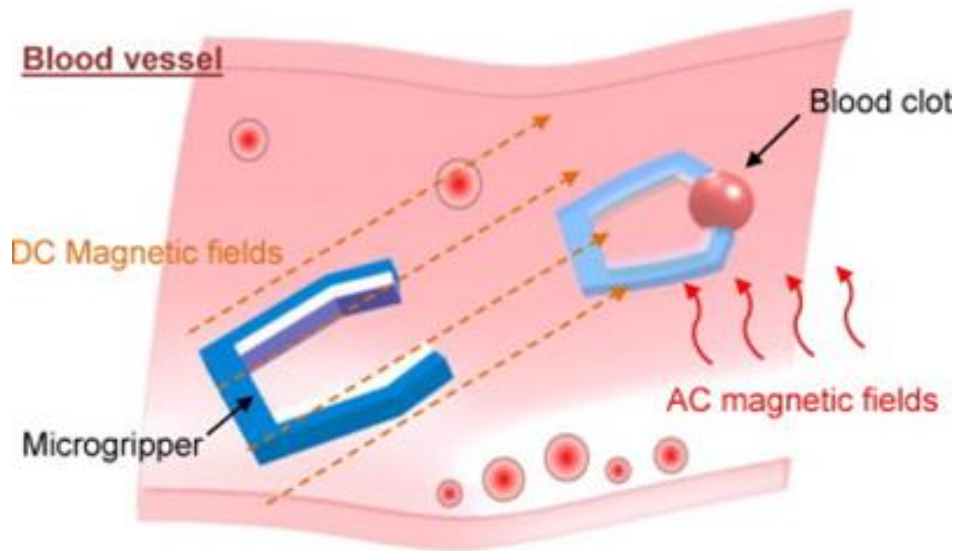


Fig. 2.19 Proposed contact less microgripper actuated using magnetic field [42].

The operational principles of this microgripper are shown in Fig. 2.20. The microgripper is made of hydrogel with distributed  $\text{Fe}_3\text{O}_4$  nanoparticles (NPs) and multiwall carbon nanotubes (MWCNTs). The applied magnetic field effects the distribution of nanoparticles then generates movement or rotation depending on the magnetic field direction, as shown in Fig. 2.20 (a). Two different crosslinked layers were

used to make up the microgripper. This leads to different responses to the magnetic field and generates the gripping motion, as shown in Fig. 2.20 (b) [42].

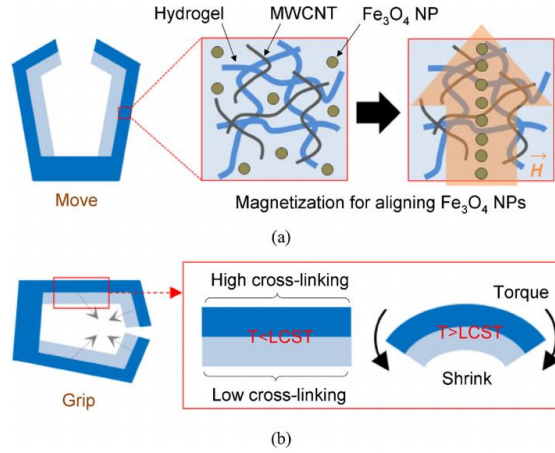


Fig. 2.20 The proposition behind the operation of (a) the locomotion (b) gripping motion [42].

The experiments on this microgripper were based on transparent containers made of PVC and PDMS while in reality there is no direct vision into the vessels. The maximum speed recorded was about 25 mm/min. Also, the gripping response time was too long, for example approximately 10 seconds were needed to get the microgripper fully closed.

### 2.2.3 Acoustic Manipulations

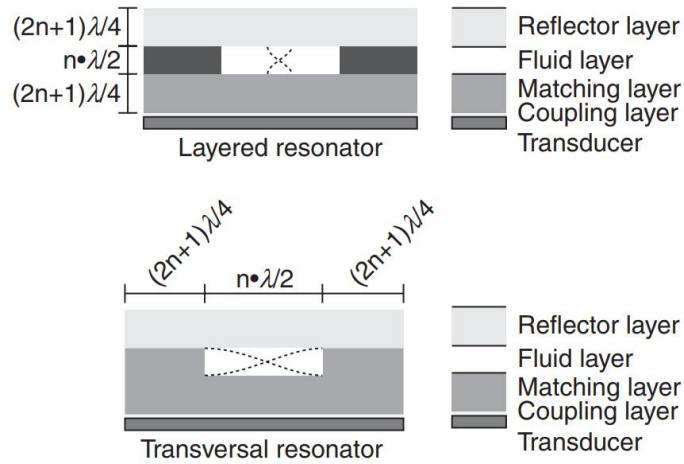


Fig. 2.21 Acoustophoretic device compartmentalization [43]

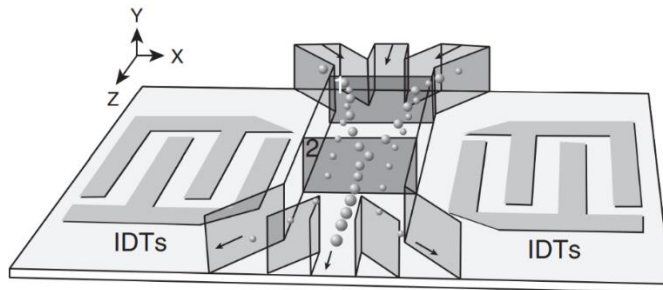


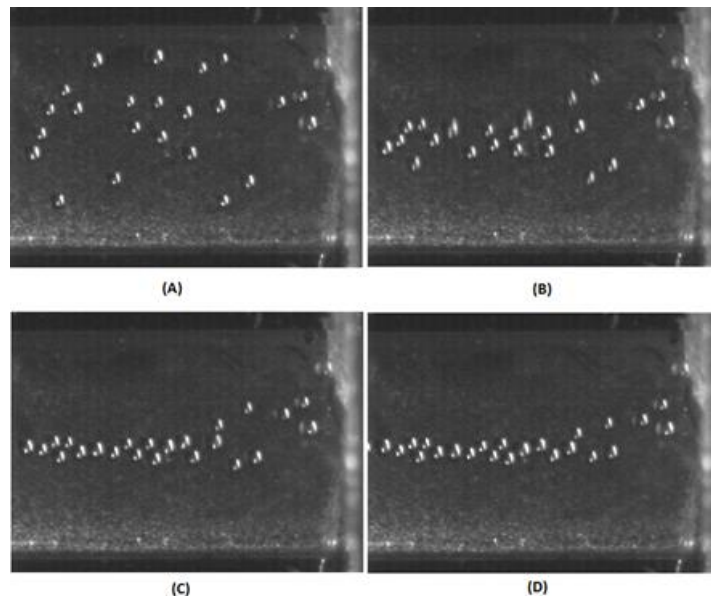
Fig. 2.22 Device example used for separation technique [43]



Ultrasonic standing wave (USW) based techniques are used for manipulating micro-objects suspended in fluid mediums. The commonly used resonator microsystems contain “layered, transversal, and surface acoustic wave (ASW)”. Fig. 2.21 shows schematics of such microsystems. Selecting the materials and the dimensions of the layers to fabricate these systems depends on the resonator type and the wavelength used. Fig. 2.22 shows a micro-fluidic device used to isolate micro-particles depending on its size. In this example, the larger particles positioned in the center line while the smaller particles are a bit further from the center. This behavior simplifies the classification of microparticles and forces them to flow in different channels [43, 44, 45, 46].

Another example of using ultra-sonic power is positioning of micro-objects in liquid using ultrasound waves force generated by an acoustic resonator to sort micro-particles in the desired way. In this example, two sources of ultrasounds with different frequencies and different power are used to position micro-objects in a straight line, as shown in Fig. 2.23 [47].

This method of positioning is suitable for grouping different sizes of microparticles. However, it is difficult to use it for a single particle manipulation. This is because microparticles of different sizes require different combinations of power values in order to achieve the desired repositioning, i.e. there is no standard setting that fits all applications.



*Fig. 2.23 Ultra-sonic power is used to sort micro-size objects in a liquid [47]*

#### 2.2.4 Air Flow Manipulation

Many fabrication processes need to handle fragile materials ‘such as silicon wafers, glass sheets, solar cell or flat foodstuffs’ [21] using the contactless method to keep these materials clean or safe from scratches. Contactless positioning technologies using the air flow force were developed as a solution to avoid damage that could be caused by contact manipulation. The fundamental mechanism behind this method is that when a strong vertical stream of air is injected out of an inlet, a horizontal air flow is generated, as shown in Fig. 2.24. The induced air flow levitates and transports micro-objects toward the nozzle on the generated air cushion [21].

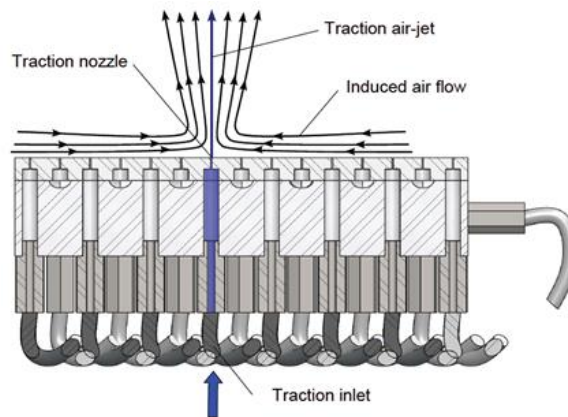


Fig. 2.24 Injected air through a nozzle generates an air flow on the surface of the manipulator [21]

A manipulator with an array of nozzles can be employed for accurate 1D [21] or 2D positioning [48]. Each nozzle is controlled by an independent solenoid valve. Running these valves in appropriate sequences displaces objects to the desire positions. A surface area of 120 mm by 120 mm was designed with an array of 225 solenoid valves each is 0.4 mm diameter [49]. The result of testing this system using two PID (proportional-integral-derivative) controllers is shown in Table 2-2.

	Pressure (kpa)	Mass (mg)	Velocity (m/s)	Diametre ( $\mu\text{m}$ )	Surface Flow ( $\text{mm}^2/\text{s}$ )
Traction	150	135	343	644	55. 92
Levitation	500	5. 82	38. 5	400	3. 895

Table 2-2 Two different materials with different diameters, and the results [48]

These results were with an error of 5% overshoot and a settling time of 1.5 seconds. A new test shows the possibility of using the same surface as a 3 DOF manipulator. The extra degree of freedom was in the ( $\alpha$ ) axis which is the orientation around the z-axis [21, 48, 49]. The setting of the manipulator depends on the shape and weight. Therefore, there is no common setting for all micro-objects.



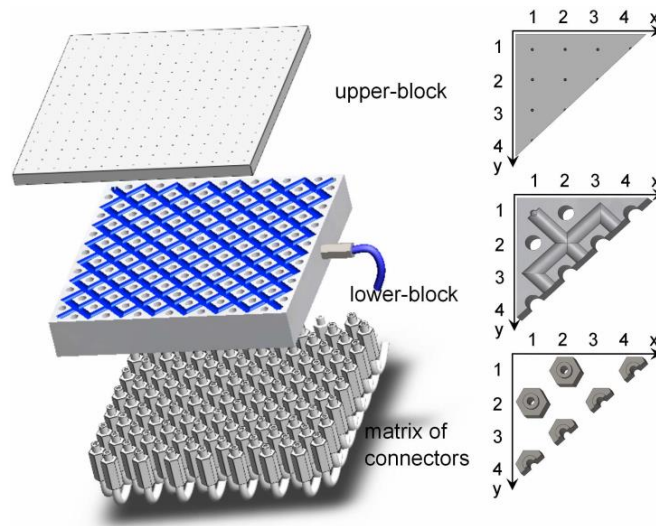


Fig. 2.25 Device layers of 2D manipulator using air flow [49]

### 2.2.5 Electrostatic Force Positioning

However, the electrostatic force is one of the unpleasant forces in the micromanipulation process because of its significant effect on small mass materials. It can be used to handle micro-objects if its force is directed properly (for more details, see section 2.3.5)). Ionizers can be used to change the charge on a handling arm or a surface to force an object to displace in the desired way. The electrostatic force is generated by adding or subtracting electrons by applying an electrical power on materials. The field distribution can be homogeneous or inhomogeneous depending on the properties of the handled material. For example, to manipulate conductor materials, a homogeneous electrostatic is used while inhomogeneous is used to manipulate insulator materials [50].

As shown in Fig. 2.26 the electrostatic force is used directly to position an object on a flat surface. By applying a high voltage on a series of electrodes, a micro-part can be manipulated. These electrodes are driven on and off electronically to control the movement of microparts to the desired position [51].

The positioning of an object using this method requires a large number of electrodes, and the resolution of the positioning depends on the separation between these electrodes. The voltage value used in this approach is very high and different voltages values are required depending on the object size and shape.

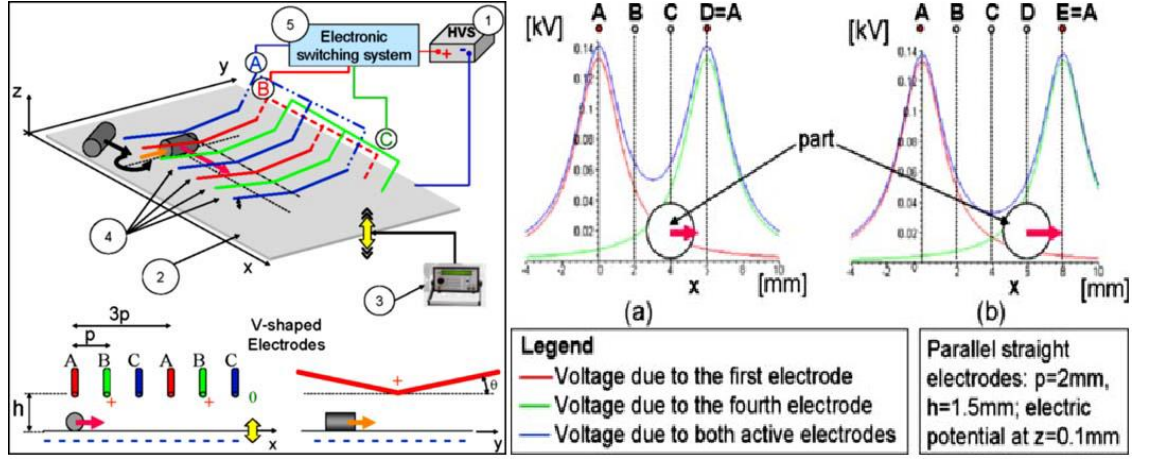


Fig. 2.26 Two-dimensional positioning systems using electrostatic power [51]

## 2.3 Actuation Principles – Single-End-effector Micromanipulator

This section will review the methods of manipulation using a single end-effector.

### 2.3.1 Capillary Gripping

This method of gripping is based on the surface tension of liquid. The picking principle behind this approach is illustrated in Fig. 2.27. The gripping arm is a hollow cylinder with a droplet of liquid at the end-effector. When the end-effector approaches a microobject, the liquid wets it and the surface tension pull the micro-object toward the end-effector. The attraction energy generated in this approach can be calculated using the following equation:

$$E = -2\gamma |G \cap C| \quad (2.1)$$

Where  $\gamma$  is the surface energy,  $G$  is the end-effector's area,  $C$  is the micro-object area, and  $|G \cap C|$  is the common area of the end-effector and the micro-object [52]. Another example is shown in Fig. 2.28. In this example, the surface tension and Laplacian forces were used to pick a micro-sphere. These two forces can be calculated using equation (2.2) and equation (2.3).

$$F_L = 2\gamma H \pi R_a^2 \quad (2.2)$$

$$F_T = 2\pi R_a \gamma \sin(\theta + \alpha) \quad (2.3)$$

Where:  $F_L$  is the Laplace force,  $F_T$  is the tension force,  $\gamma$  is the surface tension (for water  $\gamma \sim 72 \times 10^{-3} \text{ N/m}$ ) and  $H$  equals  $2(1/r_0 - 1/r_1)$ ,  $R_a$  is the radius of the circle formed between the object and the meniscus,  $\theta$  is the angle on the sphere at the interface with the liquid,  $x_a$  is the radius of the contact line between the plane and the meniscus, and  $r_0$  and  $r_1$  are the curvature radii of the meniscus [53]. This method suffers from the difficulty of releasing the micro-objects.

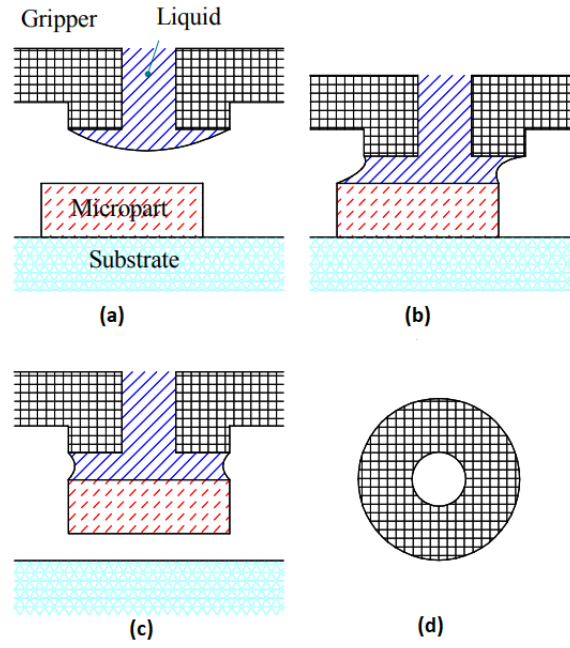


Fig. 2.27 (a) Side view: the capillary gripper is close to a micro-object with a liquid droplet at the end-effector (b) The liquid wets the micro-object (c) The surface tension pulls and centers the micro-object to the end-effector (d) down view of the end-effector [52].

As an improvement on the previous method, the electro-wetting on dielectric (EWOD) phenomenon is used. This approach is based on controlling the droplet contact angle on the surface of a microgripper end-effector using an applied voltage. Controlling the droplet angle leads to control of the lifting force (the attractive force) because the force is related directly to this angle of contact, as described in equation (2.4).

$$F = \frac{\gamma (\cos \theta_1 + \cos \theta_2) A}{d} \quad 2.4$$

Where  $\gamma$  is the surface tension of the liquid,  $\theta_1$  and  $\theta_2$  subsamples needed and they are the angles between the droplet and the surface and the micro-object respectively as shown in Fig. 2.28, and  $d$  is the distance between the gripping surface and the object through the droplet. An example of this gripping method is shown in Fig. 2.29 [54, 55].

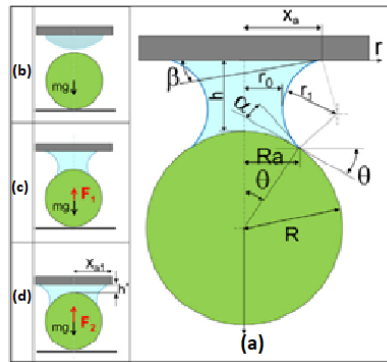


Fig. 2.28 (a) Geometry of a liquid meniscus between a flat end-effector and a micro-sphere (b) The end effector approaches a micro-sphere (c) after the droplet of liquid wets the micro-sphere (d) pulling the micro-sphere by the surface tension [53]

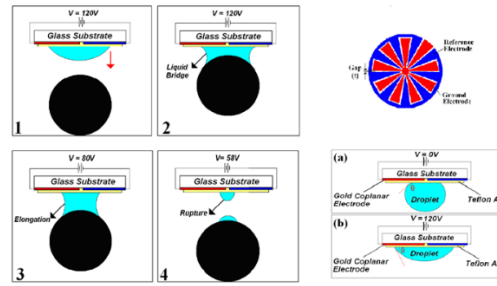


Fig. 2.29 (1 – 4) Shows the voltage effect on the generated angle and how it has been used to grasp a micro-object. (a – b) Shows compression of a droplet shape with a voltage applied and a short circuit effect [54]

### 2.3.2 Vacuum Gripper

The fundamental mechanism of this method is to generate pressure using a vacuum generator. Then the absorbing force pulls micro-objects. Fig. 2.30 shows the principle of this method. The negative air flow generates the picking force. Sometimes, the weight of the micro-objects is very small, so a positive air flow or vibration is required to release the micro-objects from the microgripper's end-effector. This method of manipulation can be used to pick micro-objects regardless size, shape and material [56, 57].

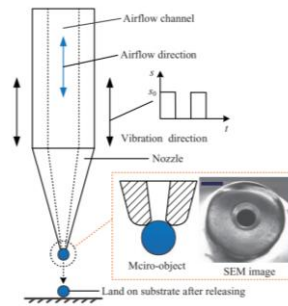


Fig. 2.30 Theory of vacuum microgripping where the vacuum generated in the nozzle is used to pick the micro-sphere and vibration is used for releasing [56]

An example is shown in Fig. 2.31, where a gripper tip made of glass is coupled to a glass pipette, which all are connected to the vacuum source by the polymer micro-loader. This microgripper was developed by IMFT (Vienna University of Technology) [58].

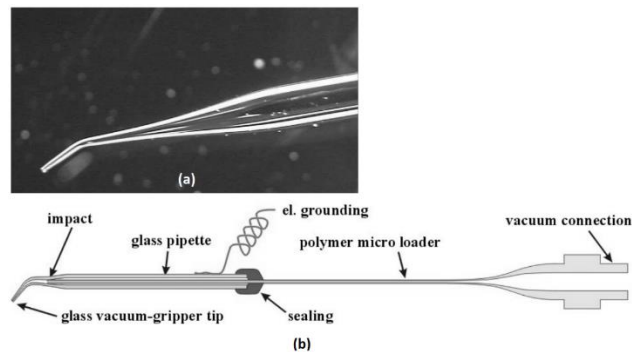


Fig. 2.31 Vacuum gripper (a) optical image after sputtering with gold (b) Cross-section [58]

Another vacuum method without using a vacuum motor is presented in Fig. 2.32. The end-effector has a micro-hole of about 10  $\mu\text{m}$ . This hole is used to pick a micro-object by producing a negative pressure. The pressure is generated by heating the end-effector. This causes an expansion of the air in the hole. Then, the end-effector touches the micro-object, and it is left for some time to reduce the temperature of the end-effector. This results in a negative pressure because the air in the holes cools. Then, the micro-object is stuck to the end-effector. To release the micro-object from the end-effector, the end-effector is heated again to equalize the pressure in the holes with the environment. Then, the micro-object is released by gravity. The generated force using this method can be calculated by equation (2.5).

$$F = S P_t \left(1 - \frac{T'}{T}\right) \quad 2.5$$

Where  $S$  is the contact area,  $P_t$  is the environment pressure,  $T$  is the environment temperature and  $T'$  is the temperature after heating [59].

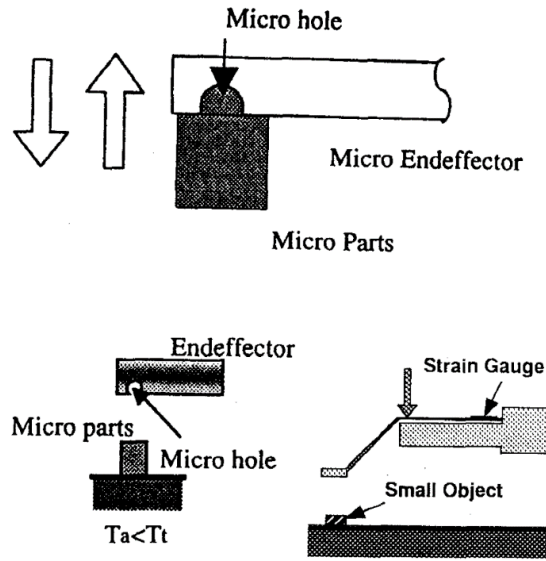


Fig. 2.32 Principle of negative force generated by a micro-hole when it is cooled down after raising the temperature [59]

### 2.3.3 Van der Waals Forces

This is one of the attractive forces which are considered as a dominant factor in micromanipulation. It acts among the atoms and it is not a chemical electronic bond. It is caused by ‘orientation effect, excitation effect, and dispersion effect’. [60]. The interactive energy between the atoms is enough in microscale objects (less than 100  $\mu\text{m}$ ) to override the gravity force. To use this force to pick an object, the gripping tip should have a greater attractive force than the object, with the substrate in addition to the force

caused by the object weight itself. The inverse is also correct for release. As shown in Fig. 2.33, a gripping tip with a rectangular shape is used to increase the contact area so the attractive force is increased. To release the object, the tip orientation is changed, and its contact angle is decreased so the contact area is decreased too. The decrease of the attractive force leads to the release of the microobject [60, 61].

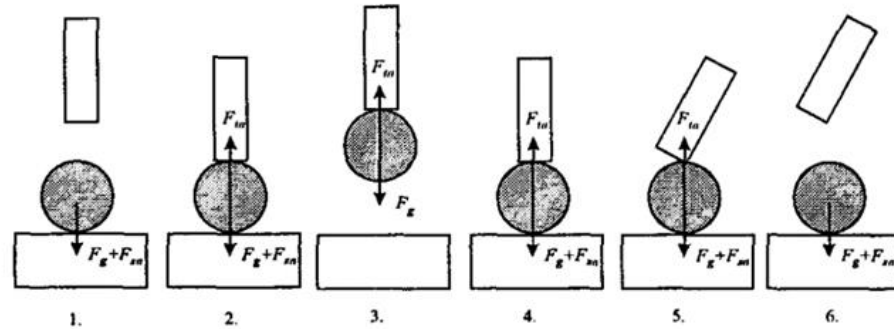


Fig. 2.33 Processes of using the Van der Waals forces to pick and release a micro-object [61]

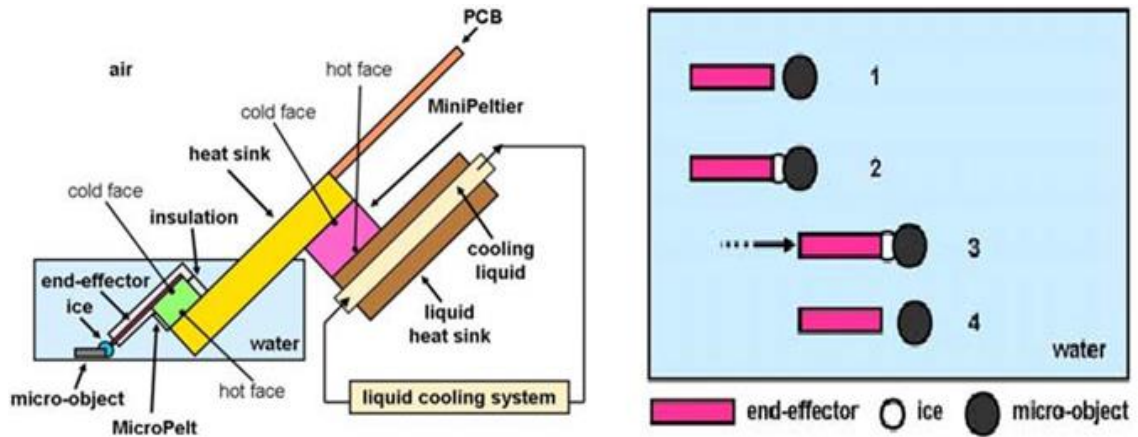


Fig. 2.34 Microgripper tip using ice on an end-effector to implement pick and release tasks [62]

### 2.3.4 Cryogenic Grippers

Typically, this method is used to handle micro-objects submerged in a liquid environment. This handling methodology is independent to the object's shape or dimension. As shown in Fig. 2.34, an end-effector tip based on the Peltier effect is used to pick micro-objects in liquid. The procedure of this method can be summarised as follows: when the end-effector is close enough to a microobject, the temperature of the end-effector is cooled down to approximately  $-10\text{ }^{\circ}\text{C}$ . This generates a tiny amount of ice on the tip of the end-effector. If the space between the end-effector and the micro-object is close enough, the ice fastens the micro-object to the end-effector. Then, the picked object can be manipulated to the desired destination. To release the object, the



end-effector is either heated up or left to equalize the temperature with the liquid and melt the ice [62].

A combination of the Van der Waals force and icing accumulated on a tip is employed to handle micro-objects. In this method, an end-effector is cooled down to  $-42^{\circ}\text{C}$  in the presence of water vapor. The very low temperature leads to the deposition of crystallized water on the tip. This increases the attractive force of the surface and sticks the microobject on the tip, as shown in Fig. 2.35 [63].

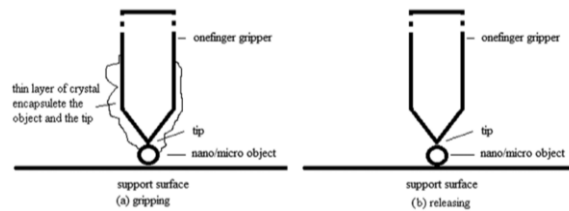


Fig. 2.35 Picking and releasing a microobject by the deposition / sublimation method [63]

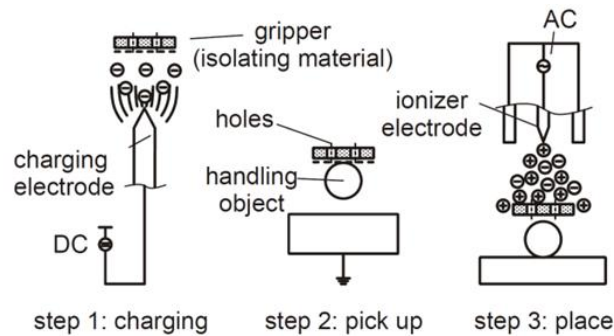


Fig. 2.36 Using a charged end-effector to pick an object [64].

### 2.3.5 Electrostatic End-effector

The electrostatic force can be used to handle a wide range of objects up to multi-millimeter size. It can be classified into unipolar and bipolar methods depending on the end-effector. The unipolar method uses the pin of a gripping electrode as an end-effector. Some designs have a flat end-effector instead of the tip depending on the manipulated shapes and sizes. The bipolar end-effector is a cylindrical capacitor. The unipolar method uses a DC power source to charge the unipolar electrode which is used to charge the gripping end-effector, as shown in Fig. 2.36. The gripping end-effector is made from insulating materials. To release the micro-object, an AC voltage is applied to discharge the end-effector [64].

Fig. 2.37 shows bipolar centering electrostatic microgrippers with different shapes, as numbered 1-5. The electrodes were made with deposited gold film of  $500\text{ }\mu\text{m}$  of thickness. The outer ring is connected to the ground. There are two working modes:

charging mode and discharging mode. The inner electrode is supplied with DC voltage to generate a strong electric field around the edge of the electrodes. This power is used to pick up micro-objects. In the releasing mode or discharging mode, a high AC voltage is applied to the inner electrode [65].

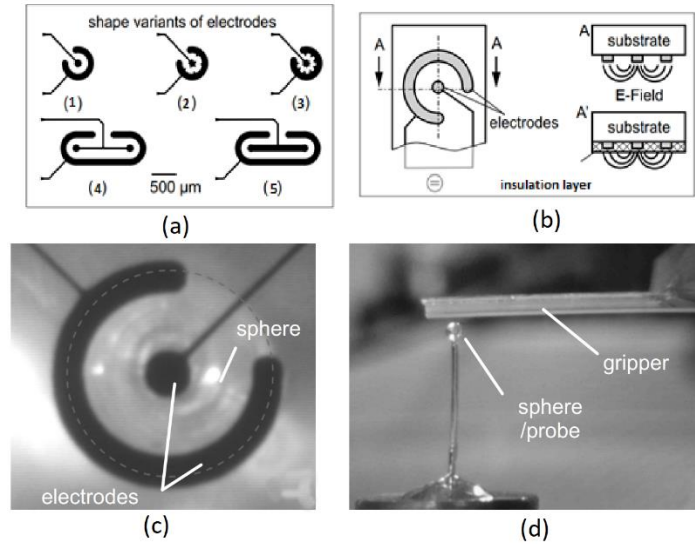


Fig. 2.37 Planar concentric ring electrodes, layout and shape variants (a, b) are the different design. (c) Top view and (d) side view of the experimental photo [65].

Another bipolar approach is presented in Fig. 2.38. This approach differs to the previous one by using one pole end-effector while the other pole is the substrate surface of the gripping device. A cross-shaped gripper is used as an end-effector to pick and release micro-objects. This electrode is fixed on a 150  $\mu\text{m}$  thick glass. A high voltage supply (HVS) is used to charge the end-effector and generate an electrostatic field. The generated field causes an attractive force which can be used to pick up micro-objects. The maximum force is generated in the cross section between the electrodes. The experimental tests prove that conductive objects can be manipulated using a voltage between 500 to 600 V, while the dielectric objects need about 1.5 kV. To release the objects, the electrode is shorted with the surfaces [7].

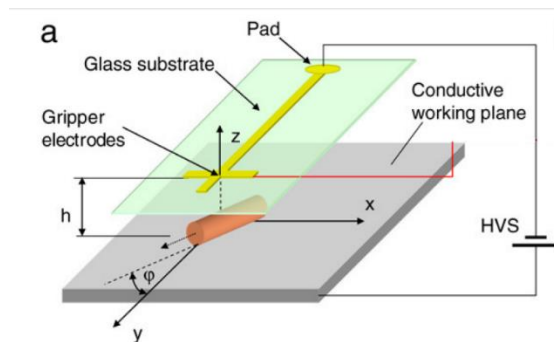


Fig. 2.38 Separated electrodes, bipolar electrostatic microgripper [7]



## 2.4 Actuation principles - Piezoelectric Microgrippers

This section will review the use of piezo materials as actuators to manipulate microgrippers.

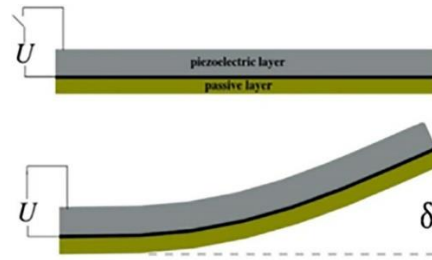


Fig. 2.39 A monomorph piezo-actuation principle [66]

### 2.4.1 Unimorph Piezoelectric Actuator

A unimorph or monomorph is simply a two-layer beam; one layer is active and made of piezoelectric materials, and the other is inactive and made of a non-piezoelectric material. When an electric field is applied on the active layer, it generates a deformation. An example is shown in Fig. 2.39. The active layer is made of a piezoelectric material and the other is a passive layer made of chromium, copper, or silicone. The applied voltage activates the piezoelectric layer and increases its length. The longitudinal length difference causes a deflection on the beam, and its value is proportional to the applied voltage [66].

### 2.4.2 Bimorph Piezoelectric Actuator

The bimorph actuator is a beam with two active layers of piezoelectric material. In some designs, it contains an inactive layer between the two active layers. While the monomorph is a 1 DOF, the bimorph is a 2 DOF actuator. Fig. 2.40 shows the basics of this actuator. There are three electrodes, one is common between the two layers and the other corresponds to each layer. There are three available configurations of this actuator. If one layer is activated, the actuator deforms to the opposite side, while if both layers are activated with same voltage, the actuator expands longitudinally [66, 67, 68].

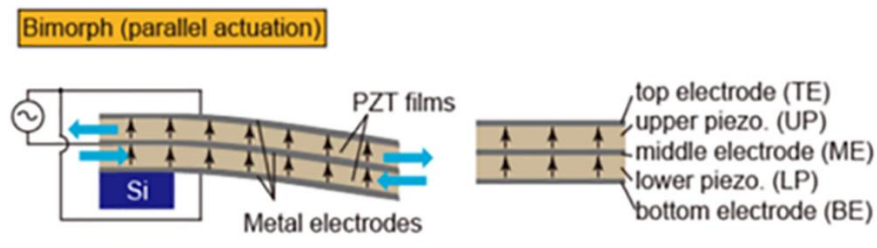


Fig. 2.40 Bimorph piezo-actuation behavior and layers [67]

### 2.4.3 Duo-bimorph Piezoelectric Actuator

This method was developed particularly for microgripper design application. The displacement result from this design is higher than in the other piezoelectric cantilever. It is made of two layers of piezo materials which are attached to each other just as in the ordinary bimorph piezo actuator, as shown in Fig. 2.41. As this cantilever is built with four piezo actuators, the design has five electrodes instead of three, as in the previous example. By applying voltage on these electrodes in different configurations, a multi degree of freedom can be achieved [69].

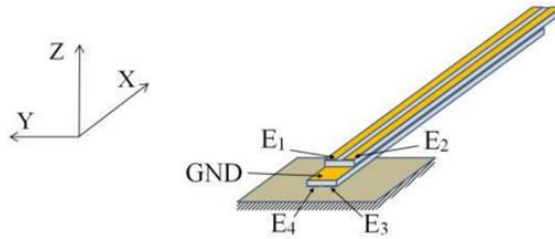


Fig. 2.41 Duo-bimorph actuator made of PMN-PT [69]

### 2.4.4 Piezoelectric Microgrippers

A microgripper is simply one or more cantilevers driven by actuators so a microgripper can be designed using any type of piezoelectric cantilever. Fig. 2.42 shows a microgripper based on unimorph piezoelectric cantilevers. The distinctive feature of this microgripper is that each of its arms is actuated independently [70].

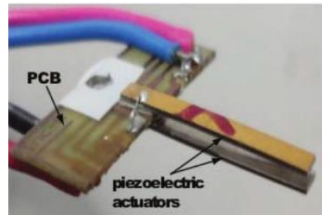


Fig. 2.42 Microgripper design based on piezoelectric cantilevers [70]

The MMOC (Micro-prehensile Micro-Robot on Chip) is a gripper with four degrees of freedom. This microgripper is designed by the duo-bimorph principle for piezoelectric cantilevers. Each arm is deflected into two directions. These offer flexibility of the end-effectors to align them to each other and with the manipulated micro-object. This microgripper is shown in Fig. 2.43 and it required a voltage of  $\pm 100$  V to drive the actuators. Each piezoelectric cantilever can deflect up to  $320\text{ }\mu\text{m}$  in the direction of opening and closing while it deflects up to  $200\text{ }\mu\text{m}$  in the up and down direction.

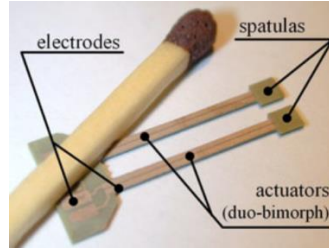


Fig. 2.43 FEMTO-ST 4 DOF microgripper fabricated using duo-bimorph piezo materials [6]

During the last decade different microgrippers have been designed and fabricated using piezoelectric materials. Each of them has been designed for a specific purpose and application. For example, the first microgripper concept was ‘Micro-robot on chip’, which was later developed to use a ‘plug-and-use micro-gripper’. They are combined in ‘LEMO® connector’. This version can be used to pick up objects of sizes of 100  $\mu\text{m}$  to 1 mm. One of the important developments is adding sensors to the microgrippers such as position and force sensors. Fig. 2.44 shows several commercially available microgrippers [6].

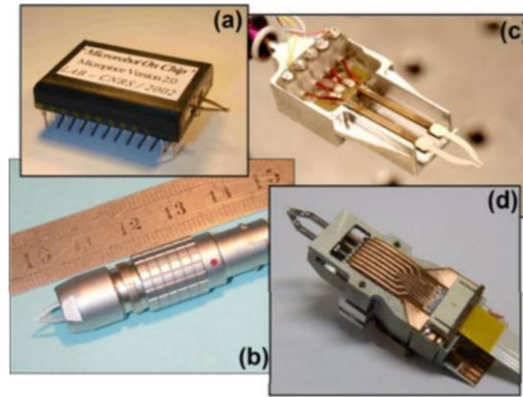


Fig. 2.44 Several commercially developed piezoelectric based microgrippers [6]

## 2.5 Actuation Principles - Electrostatic Microgripper

### 2.5.1 Electrostatic Actuated Microgripper

Any two parallel conductor plates charged with an opposite polarity generate an electrostatic attraction between them. Fig. 2.45 illustrates the effect of applying a voltage on two parallel conductor plates. An attractive force ( $F_{electric}$ ) is generated between them. If this force is higher than the spring force ( $F_{spring}$ ), the hung plate is displaced to equalize the forces. The electrostatic force between the two plates can be calculated using Coulomb’s law, as given by equation (2.6). Where  $K$  is a constant and its value in free space is  $9 \times 10^9 \text{ Nm}^2/\text{C}^2$ ,  $q_1$  and  $q_2$  are the amount of charge on each plate, and  $r$  is the distance between them.

$$F_{electric} = K \frac{q_1 q_2}{r^2} \quad 2.6$$

In addition,  $K$  can be calculated using equation (2.7), and  $q$  can be calculated using equation (2.8).

$$K = \frac{1}{4 \pi \epsilon} \quad 2.8$$

$$q = \frac{A V \epsilon}{d} \quad 2.9$$

Where  $A$  is the plate's common area,  $V$  is the voltage between the two plates,  $d$  is the distance, and  $\epsilon$  is the permittivity of the space between the two plates. Equation (2.7) shows a nonlinear relationship between the electrostatic force as a function to the applied voltage and the distance between the two plates. The spring force ( $F_{spring}$ ) can be measured using equation (2.9). Where ( $K_{spring}$ ) is the spring constant and  $d$  is the spring length change. The two force equations are used to find the equilibrium point and calculate the displacement [71, 72, 73].

$$F_{spring} = K_{spring} d \quad 2.10$$

All electrostatic actuators have a pull-in voltage threshold and the two plates become out of control if it is passed. The voltage value is equal to the required charge to generate a displacement of 1/3 of the total gap between the two plates. As a result, the voltage applied should not exceed the “pull-in voltage”. This threshold value can be found using equation 2.11).

$$V_{pi} = \sqrt{\frac{2 k d_0^3}{\epsilon A} \frac{3}{\sqrt{3}}} \quad 2.11$$

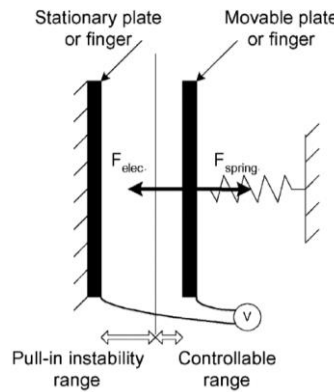


Fig. 2.45 A simple micro-actuator is formed from two parallel plates [71]

If the threshold level is passed, an extra force is generated, and the two plates are snapped together. This distance range of spacing is called pull-in instability range. The proposed solution to overcome this problem is to use a capacitor connected in series with the actuator. This acts as a voltage divider so when the two plates become closer the

capacitance increases. This results in a decrease in the voltage across the two plates. In other words, the added capacitor works passively to stabilize the actuator [74, 75].

The electrostatic actuator is employed to design many different microgrippers. Some of these designs are directly driven by the capacitor while others are driven indirectly.

### 2.5.2 Examples of Electrostatic Microgrippers:

- Simple Electrostatic Microgrippers

The first example is the simplest microgripper driven directly using a series of cantilevers as a comb, as shown in Fig. 2.46. When a voltage is applied on the microgripper, the comb charges and an attractive force is generated between the two sides which pulls the arms and displaces the end-effectors. The microgripper arms have three parts: first is a support cantilever with a length of 1.5 mm. The active part (the comb capacitor) is 400  $\mu\text{m}$  in length, and finally the end-effectors are 300  $\mu\text{m}$  [76].

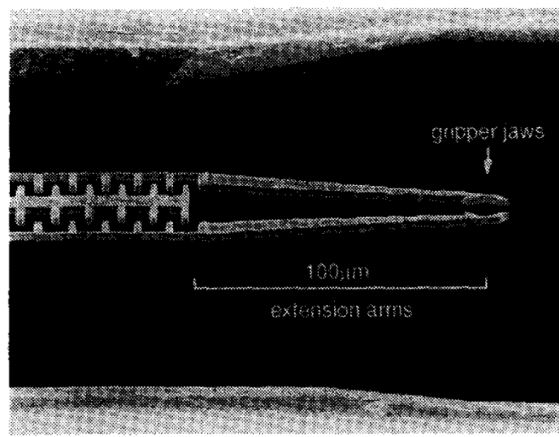


Fig. 2.46 Microgripper actuated using electrostatic force [76]

- Electrostatic Microgripper with integrated force sensor

The electrostatic actuation generates a high force compared to the size of the manipulated micro-objects, and most of the micro-objects are easily damaged. A force control is required to avoid any extreme force. A sensor is integrated in an electrostatically actuated microgripper. As shown in Fig. 2.47 and Fig. 2.48, one arm is used as a force sensor based on capacitor change and the other is actuated using the electrostatic force. When the sensing arm is deflected, the capacitor value decreases, and the force value can be calculated [77].

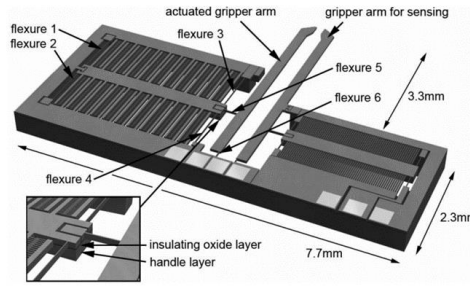


Fig. 2.47 Microgripper with embedded force sensor [77]

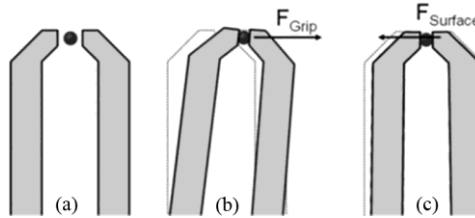


Fig. 2.48 Three states of electrostatically actuated microgripper arms during the manipulation processes. (a) The object is aligned and ready to pick. (b) higher force is applied than in (c) [77]

- Two DOF Electrostatic Microgrippers

A two DOF MEMS electrostatically actuated microgripper, as shown Fig. 2.49, is designed and fabricated by University of Macau in China. This microgripper is embedded with capacitive position and force sensors. Each jaw is controlled in two axes which gives flexibility of positioning. The microgripper shows a  $70\text{ }\mu\text{m}$  of displacement in x-axis and  $18\text{ }\mu\text{m}$  in y-axis with  $190\text{ }\mu\text{N}$  of force when a  $120\text{ V}$  of voltage is applied [78].

Although these microgrippers offer a high displacement and force at low temperature, they need a precise force sensor to avoid damaging the grasped objects. This is very difficult to achieve with the capacitive sensor because of the very small value in this size, which leads to high noise. In addition, the non-linear behavior complicates the control system. Also, they need a high operating voltage.

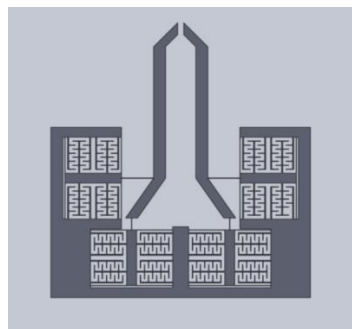


Fig. 2.49 A dual axis MEMS microgripper with built-in force and position sensor [78]

### 2.5.3 Electromagnetic Microgripper

In the previous section, the use of VCM to manipulate a microgripper was discussed. In this section, an embedded electromagnetic actuator is investigated. An example of a microgripper based on two permanent magnets and two coils is shown in Fig. 2.50. The magnets are fixed on the microgripper's arms and the two coils are fixed on the outer structure. When a voltage is applied to any of the coils, a magnetic field is produced, and it interacts with the magnetic field in two different ways (attraction and repulsion). Therefore, the end-effectors can be manipulated in both directions depending on the direction of the electric current. The results show a displacement of  $\pm 60 \mu\text{m}$  when a current of about  $\pm 200 \text{ mA}$  is applied to both coils [79].

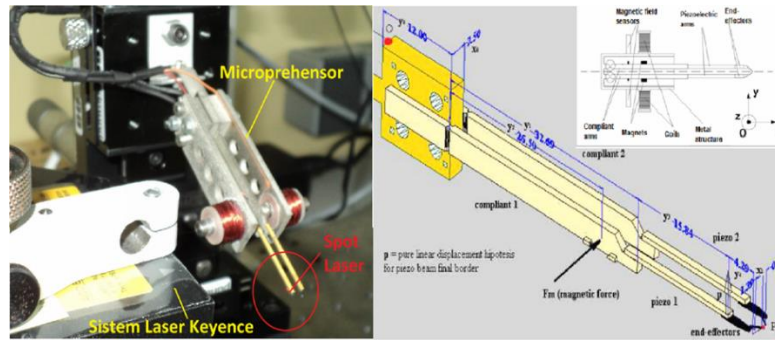


Fig. 2.50 Electromagnetics actuated microgripper [79]

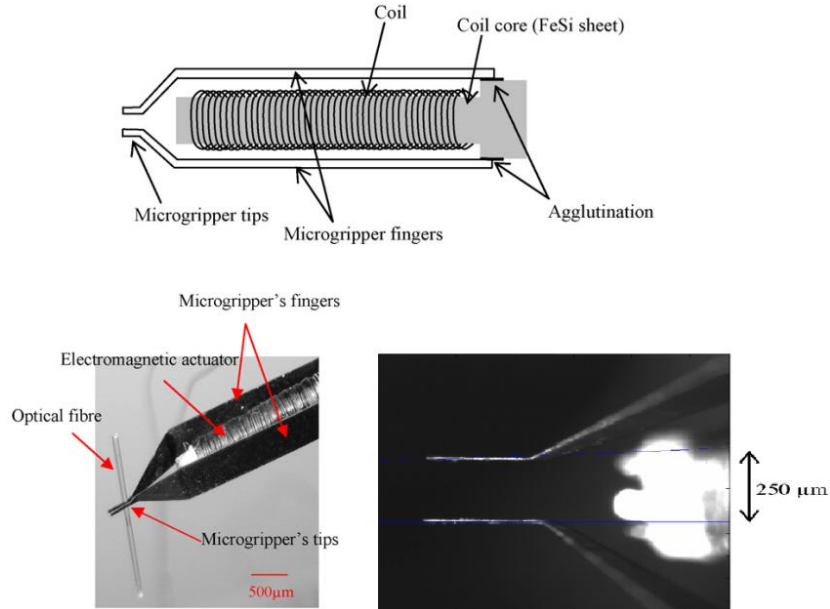


Fig. 2.51 Electromagnetic microgripper [80]

The previous designs are based on two different sources of magnetic field: electromagnetics and permanent magnets. Another method used to design a microgripper with embedded electromagnetics is shown in Fig. 2.51. This design is based on the use of an amorphous soft magnetic material like VITROVAC 7505 or Metglas and actuated

using an electromagnetic field generated using a coil around a FeSi sheet. The initial opening of the end-effector is 250  $\mu\text{m}$ . The applied voltage attracts both end-effectors and they are closer. The magnetic force generated by the coils' core can be calculated using equation (2.12):

$$F_{mag} = \frac{B_{air}^2 A_{core}}{4 u_o} = \frac{u_o (N I)^2 b t_c}{4 (d_{f-c} + t_g)^2} \quad 2.12$$

Where  $B_{air}$  is the magnetic flux density in the air gaps,  $A_{core}$  is the cross section area of the magnetic core,  $u_o$  is the permeability in the air,  $N$  is the number of windings,  $I$  is the applied current,  $b$  is the width,  $t_c$  is the thickness,  $d_{f-c}$  is the distance between the microgripper arm and the core, and  $t_g$  is the thickness of the glue layer between the microgripper's arms and core [80].

#### 2.5.4 IPMC Actuated Microgripper

Ionic polymer metal composites (IPMCs) are polymer materials such as Nafion, Teflon and Flemion and are made up of nanomaterials. The first IPMCs were innovated in 1992 by Shahinpoor's group. These materials have mechanoelectrical transduction mechanism properties and can be used to design actuators or sensors. Applying an electric field on IPMCs causes the migration of water molecules. This results in expansion on one side and shrinking on the other, depending on the direction of the electric field. This leads to deformation in the IPMCs materials. Forcing the IPMCs to deform causes ions to migrate to the other side and generate a small amount of electric field [81].

The actuation in IPMCs is illustrated in Fig. 2.52. When an electric field is applied on the electrodes, it causes an immigration of  $\text{Cu}^{2+}$  ions from the anode towards the cathode. These ions carry water to the cathode, and this leads to the IPMC bending toward the anode electrode. This effect can be reversed by changing the electric field polarity. The SMA force restores the deformation in the shape after turning off the applied electric field. The generated force is directly proportional to the thickness and width, while it is reversed proportionality with length. The force in can be measured using equation (2.13) where  $C_l$  is constant,  $w$  is the width,  $t$  is the thickness, and  $L$  is the length and the entire lengths unit in (mm).

$$F = C_l \frac{w t^2}{L} \quad 2.13$$

The stiffness of the actuator depends on the dimensions and the force applied on the actuator, as shown in equation (2.14).



$$Stiffness = E I = \frac{F L^3}{3 \delta} \quad 2.14$$

Where  $E$  is the Young's modulus,  $F$  is the applied force,  $L$  is the length,  $\delta$  is the deflection, and  $I$  is the momentum of inertia which could be calculated for the rectangular shape by using equation (2.15).

$$I = \frac{b h^3}{12} \quad 2.15$$

Where  $b$  is the width of the beam, and  $h$  is the thickness of the beam.

In addition, the different fabrication process has a different stiffness result. For example, if the Nafion film is pre-processed by hydration and ion exchange, its stiffness becomes higher [82].

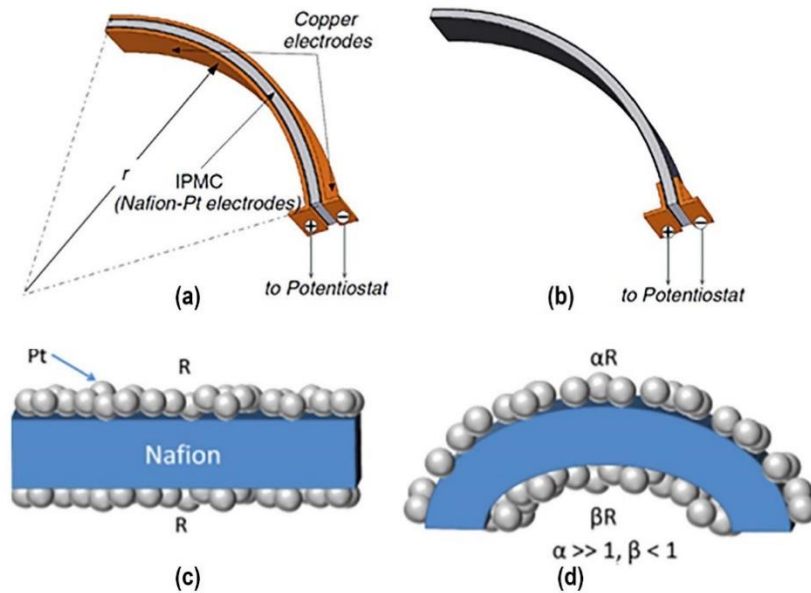


Fig. 2.52 IPMC transduction mechanisms. IPMC actuator with (a) Cu–Pt-coated and (b) regular platinum. Sensor of platinum coat showing the effect of bending on the atom's intensity and the change in the resistivity (c) unbent (d) bent [81]

The sensing property of IPMCs is shown in Fig. 2.52. It is clear in the convex side that the platinum atoms are redistributed and the intensity per area unit becomes less. This leads to a decrease in the resistance to drop sharply as expressed by the factor,  $\alpha$ . On the other hand, on the concave side, the atoms become closer than before. This leads to a decrease in the resistance but not in same proportion as the change on the other side [81].

The IPMC based materials result in different performance. For example, the Nafion based IPMCs respond in different ways comparing with the Flemion based IPMCs. When a small value of DC voltage is applied on the Nafion IPMC, it shows a fast and high

bending response toward the anode direction. Then, it goes back to the cathode direction slowly. When the voltage source is removed and the two electrodes are shorted, there is a fast deformation bending to the cathode direction then it slowly goes back to its original shape. The Flemion IPMCs act in a different way. When a DC voltage is applied on the electrodes, it bends in a very short time toward the anode direction and then it continues in same direction at a very slow speed before it stops. When the two electrodes are shorted, it goes back very fast (toward the cathode direction) then continues until it stops. The fast movement is about three quarters of its total displacement.

The sensor response as a voltage output can be calculated using equation (2.16). Each of the coefficients  $A$  and  $b$  are functions to the displacement and could be calculated using equation (2.17) and equation (2.18).  $\alpha$  and  $\beta$  are the slope and the y-intercept respectively which should be calculated practically [83].

$$V(\delta, t) = A(\delta)e^{-b(\delta)t} \quad 2.16$$

$$A(\delta) = \alpha_A \delta - \beta_A \quad 2.17$$

$$b(\delta) = \alpha_b \delta - \beta_b \quad 2.18$$

However, the actuation behavior of the IPMC depends on what it is based, and the cation form controls the way of responding too. For example, a Nafion based IPMC with large alkyl-ammonium cations (e.g. TBA<sup>+</sup>) [84] has a different actuation way. When a voltage is applied, the beam bends toward the anode but with a different speed. It starts very fast then the speeds goes down until it is stopped [82, 83, 84, 85].

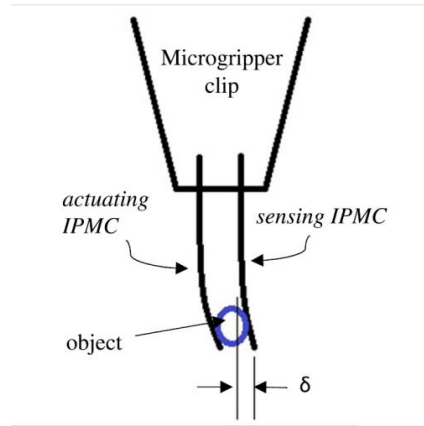


Fig. 2.53 IPMC microgripper which one arm is actuated and the other is used as sensor [83]

### 2.5.5 Example of IPMC Microgripper

Fig. 2.53 shows an example of a microgripper developed using IPMC materials. The actuation of the IPMC always needs a closed loop control system because of the behavior of these materials. One of the arms is designed as an actuator while the other is used as

a sensor. The length of the free arm is 15 mm. There is a zero-steady state error for displacement up to 250  $\mu\text{m}$ , while there is an error for larger displacement which can achieve up to 3mm. In addition, this error was maintained for a short time (up to 12 seconds). The reason behind that is how the actuator works and this called back relaxation phenomenon. [83].

## 2.6 Actuation Principles – Microgrippers with Integrated Electrothermal Actuator

The thermal actuation is a result of an expansion in an active part caused by an increment in its temperature which is based on the Joule heating effect. Joule heating or Ohmic heating or resistive heating is a concept which exhibits heat production in a conductor when a current is passed through it. The length of an actuator as a function to temperature is described by the equation (2.19), where  $L$  and  $L_o$  are the length and reference length at the reference temperature  $T_o$ ,  $\Delta T$  is the change in the temperature, and  $\alpha$  is the temperature coefficient of expansion at the reference temperature. Different materials can be used for heater fabrication, such as aluminum, copper, gold, and titanium [86].

$$L = L_o(1 + \alpha \Delta T) \quad 2.19$$

The resistivity of the heater material is expressed in equation (2.20), where  $\rho_{heater}$  is the resistivity of the heater film,  $\rho_{bulk}$  is the ideal resistivity of the material measured in bulk,  $\rho_{impurity}$  is the resistivity coming from the alloy impurity, and  $\rho_{thickness}$  is the resistivity coming from the thickness where the resistivity is increased when the thickness is decreased [87]. In addition, the temperature coefficient of the resistivity (TCR) is changed too in the thin film heater [88].

$$\rho_{heater} = \rho_{bulk} + \rho_{impurity} + \rho_{imperfection} + \rho_{thickness} \quad 2.10$$

### 2.6.1 Micro-Clamp Based Electrothermal Actuator:

Based on the electrothermal actuation method, a micro-clamp was designed and fabricated using silicon as the structure and aluminum as a heater. The length of the arms is 1.3 mm, the width is 60  $\mu\text{m}$  for the thin arm (hot arm) and 180  $\mu\text{m}$  for the wide arm (cold arm) with a thickness of 20  $\mu\text{m}$ , as shown in Fig. 2.54. When a current flow through the conductor layer, more heat is produced in the thinner part which causes an expansion in it. This leads to a displacement in the end-effectors. This design was developed

particularly to pick microparts of  $387\ \mu\text{m}$ ,  $387\ \mu\text{m}$ , and  $40\ \mu\text{m}$  in dimensions. The results of this microgripper show a  $20\ \mu\text{m}$  displacement when a voltage of  $20\ \text{V}$  is applied [89].

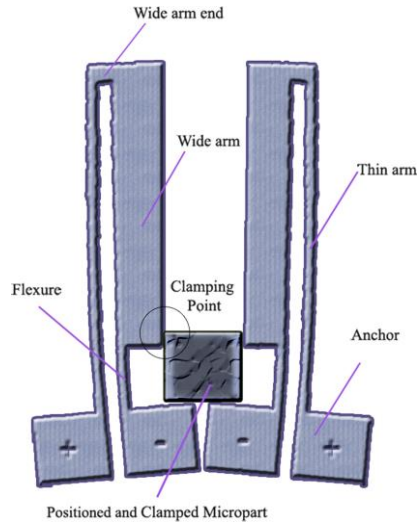


Fig. 2.54 Electro-thermal micro-clamp [89]

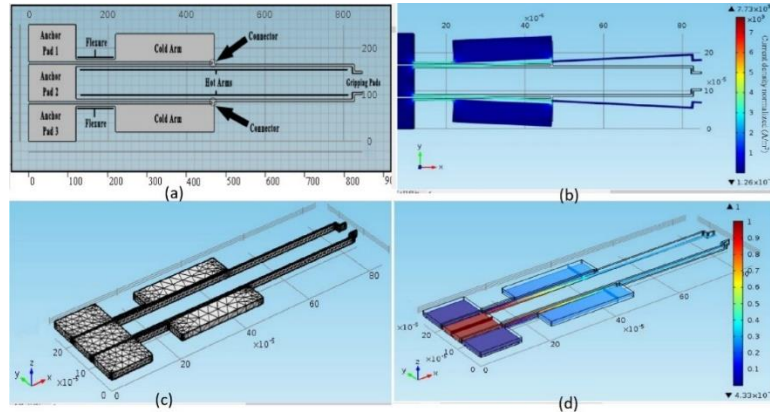


Fig. 2.55 Hot/cold arms electrothermal based on Poly-Si microgripper normally closed (a) the design structure (b) the deflection magnified by 10 (c) mesh for FEA of the microgripper model (d) the electrical potential distribution [90]

### 2.6.2 Hot/Cold Arm Microgripper

The hot/cold arms method is similar to the previous method and it is one of the two actuation methods used to design electrothermally actuated microgrippers. The conductor layer is mainly designed in two widths; one is narrower than the other to enable the heat to be produced in the actuator. Fig. 2.55 shows a microgripper designed using this approach. This microgripper was manufactured using poly-Si for the structure and gold as the conductor and heater layer. It is designed for normally closed operation and the opening is increased when it is actuated. The dimensions of the end-effectors (hot arms) are  $700\ \mu\text{m}$  in length,  $5\ \mu\text{m}$  in width, and  $15\ \mu\text{m}$  in thickness, while the dimensions of the cold arms are  $250\ \mu\text{m}$  in length,  $60\ \mu\text{m}$  in width, and  $15\ \mu\text{m}$  in thickness.

By applying a voltage to the conductor layer, heat is produced in the thinner arms and the expansion causes a deflection at the end-effectors. The initial opening is 40  $\mu\text{m}$  and it increases to about 100  $\mu\text{m}$  when a voltage of about 3 V is applied. These results are from FEM simulation using COMSOL Multiphysics [90].

Another simple hot/cold arm electrothermally actuated microgripper is fabricated using polysilicon and multi-user MEMS processes (PolyMUMPs). This microgripper is designed for normally open operation and the opening is decreased when it is actuated. The lengths of the arms are 207  $\mu\text{m}$  and 168  $\mu\text{m}$ , and the widths are 30  $\mu\text{m}$  and 70  $\mu\text{m}$  for the narrower and wider arms respectively. The initial displacement is 20  $\mu\text{m}$  and it decreases to about 10  $\mu\text{m}$  when a voltage of 14 V is applied. This microgripper is shown in Fig. 2.56 [91].

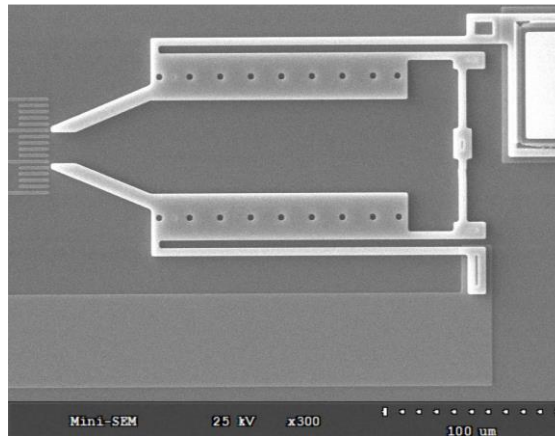


Fig. 2.56 Hot/cold arms electrothermal based on Poly-Si microgripper normally opened [91]

The poly-Si based microgrippers have a very high temperature of the actuator limits the possible application if the handled micro-objects are sensitive to high temperature. This is because the coefficient of temperature expansion (CTE) of the Poly-Si is low therefore the ratio of the temperature change to the length change is low too.

## 2.7 SU-8 Electrothermally Actuated Microgripper

The electrothermal actuators can be classified into three main groups depending on the actuator shape. First, the U-shaped actuator is based on hot and cold arms where the cold arm contains a wider conductor than the hot arm. The second type is the V-shaped actuator which is also known as the chevron electrothermal actuator. This actuator contains several beams connected in a V-shaped and there is a shuttle in the middle. When a current is applied, the narrower conductor generate heat. Then the actuator expands, and the shuttle is displaced accordingly. The third type is the Z-shaped actuator which is similar to the V-shaped operation methodology, but the actuators beams are Z-

shaped. The previous microgrippers could be classified into two main groups according to their operation mode. One of them is the normally open mode but is closed when it is actuated, and the other is in normally closed mode but it is opened when it is actuated.

### 2.7.1 Chevron Actuator Style

A microgripper is designed based on SU-8 and electrothermally actuated using a chevron style actuator and displacement amplification. The design dimensions are approximately 1.5 mm for the length and 20  $\mu\text{m}$  for the thickness. Fig. 2.57 shows that the bent beam actuator is generally a series of upside down V-shaped actuators. When a current is passed through the heater, the arms expand, and this results in a displacement on the base of the microgripper. The maximum achieved displacement on the end-effectors is about 9  $\mu\text{m}$  [92].

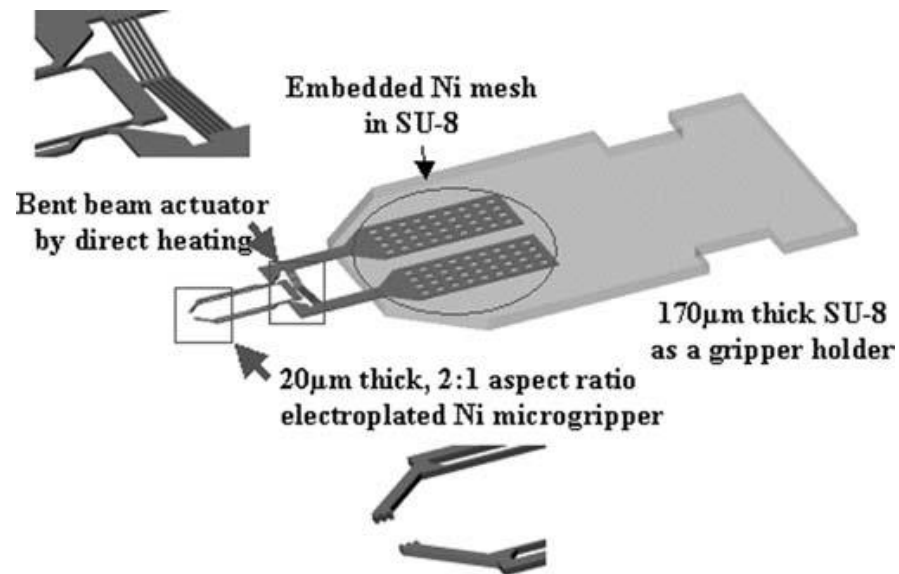


Fig. 2.57 Bent beam actuating microgripper [92]

Another design based on the V-shaped Chevron actuator is shown in Fig. 2.58 The thermal actuator is used to drive one arm of the microgripper while the other arm is fixed. The testing results show a maximum displacement of 2  $\mu\text{m}$  when a current of 8 mA is passed through the heater [93].

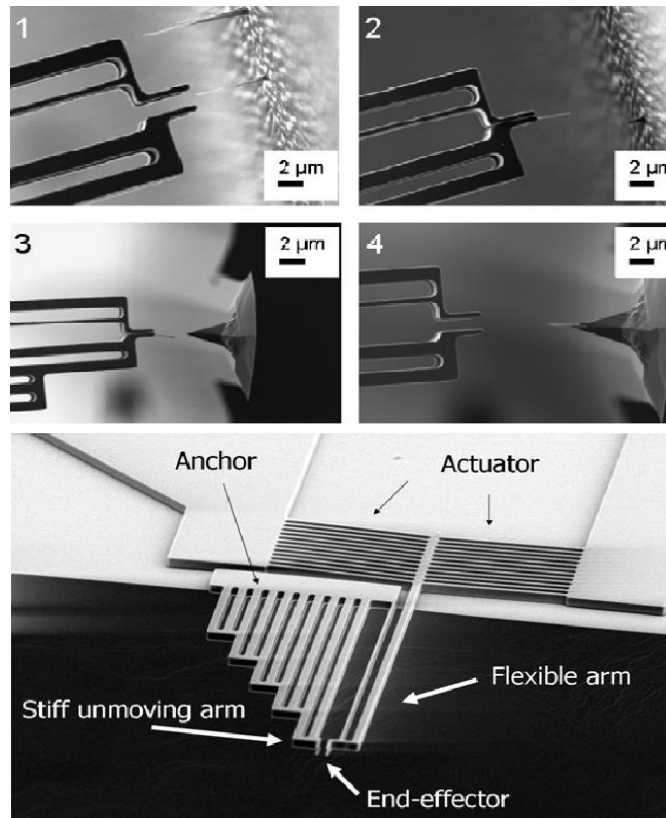


Fig. 2.58 Microgripper for nano-manipulation [93]

Another V-shaped actuator based SU-8 microgripper is shown in Fig. 2.59. The microgripper thickness is  $60\text{ }\mu\text{m}$  and the gold heater thickness is  $2\text{ }\mu\text{m}$ . The other dimensions are not provided. The microgripper displacement is  $10\text{ }\mu\text{m}$  in air and in PBS solution with only a  $7^{\circ}\text{C}$  and  $18^{\circ}\text{C}$  temperature change by applying a voltage  $0.17\text{ V}$  and  $0.7\text{ V}$  respectively. In addition, it is claimed that this gripper could be used to manipulate cells in a wide size range ( $15\text{ }\mu\text{m}$  -  $50\text{ }\mu\text{m}$ ) [94].

Fig. 2.60 shows the structure of two different microgrippers based on multi-stage moving amplification to get a larger displacement at a lower temperature. Both are based on the chevron electrothermal actuation method. The dimensions of the first one is  $1670\text{ }\mu\text{m}$  in overall length,  $1740\text{ }\mu\text{m}$  in overall width,  $45\text{ }\mu\text{m}$  in thickness, and the opening of the non-actuated end-effectors is  $100\text{ }\mu\text{m}$ . This microgripper is for normally open operation and it closes when a voltage is applied. The author claims the microgripper shows about  $68\text{ }\mu\text{m}$  of displacement when a voltage of about  $425\text{ mV}$  is applied and the temperature is raised to about  $78^{\circ}\text{C}$ . This microgripper decreases the gap between the jaws when a voltage is applied.

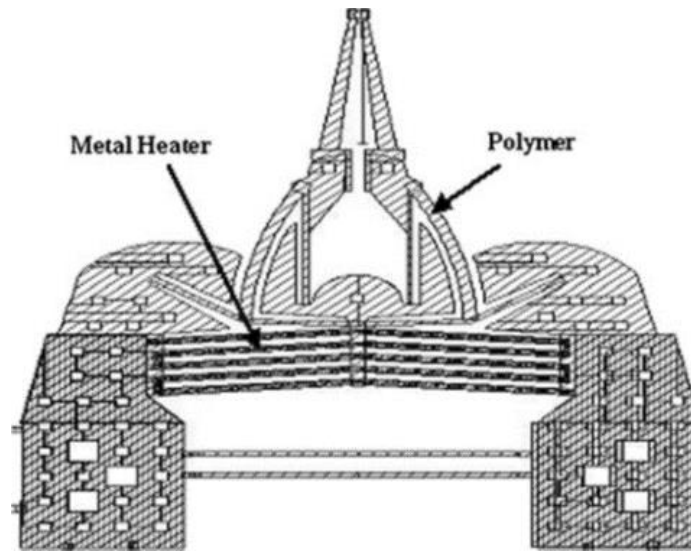


Fig. 2.59 SU-8 microgripper [94]

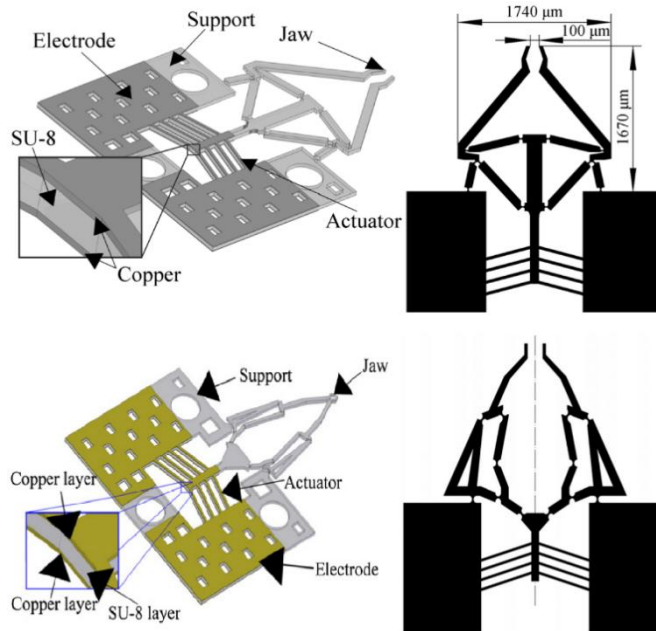


Fig. 2.60 SU-8 microgripper actuated using chevron actuator [95, 96]

For the second design, the dimensions are 1520  $\mu\text{m}$  in overall length, 1050  $\mu\text{m}$  in overall width, and 45  $\mu\text{m}$  thickness, and with an initial opening of 20  $\mu\text{m}$ . This microgripper is a normally closed design and it is opened when a voltage is applied. A displacement change of about 107  $\mu\text{m}$  is obtained when a voltage of 74 mV is applied and a change in temperature of about 45°C [95, 96, 97].

In this design, the temperature coefficient of the resistance (TCR) of the copper is used to estimate the temperature during the actuation process. However, the heater material is copper the temperature coefficient of the resistance is different in thin film to



the bulk value and sometimes is less by more than half. This leads to inaccurate temperature change measurement.

### 2.7.2 Drawbacks of the Chevron Method

In this type of actuation, there is a large amplification of the displacement. Several microns become tens of microns, especially when they are used to drive the microgripper indirectly such as the chain stage amplification. There is a limited angle of freedom in each hinge and the hinge is broken if the limit is passed. Even if the maximum allowed angle is not passed, it generates a high stress which could lead to low repeatability. In addition, these types of actuation cannot generate a large force on the end-effectors because the displacement and the force are inversely related. There are several designs using this method of actuation, as shown previously. The best design using this type of actuation is shown to be able to produce about 100  $\mu\text{m}$  of displacement.

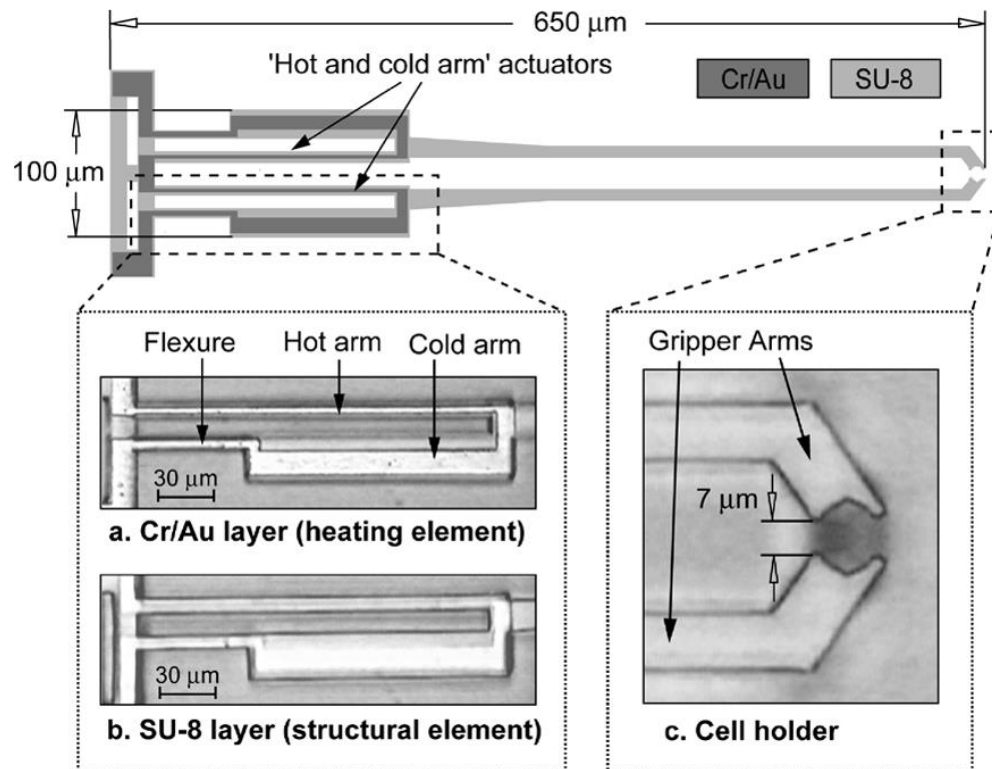


Fig. 2.61 Hot/cold arm based design microgripper [98]

### 2.7.3 Hot-and-cold-arm actuators (normally closed)

This design has been developed and used in many microgripper designs. In this design, both of the two arms include the metal heaters if the cold arm is wider than the hot arm. This result is that the hot arm has a higher temperature and generates a displacement due to expansion.

Fig. 2.61 shows a design developed at the University of California based on the hot and cold arm method. The microgripper dimensions are 650  $\mu\text{m}$  in length, 100  $\mu\text{m}$  in width, 20  $\mu\text{m}$  in thickness, and 7  $\mu\text{m}$  in the initial opening gap. Chromium and gold were used to make the connections and the heater. The experimental result shows a displacement change of about 12  $\mu\text{m}$  when a voltage of about 0.4 V is applied.

Fig. 2.62 shows another design which was developed at Durham University. The microgripper's dimensions are 3600  $\mu\text{m}$  in length where the actuator part is 2000  $\mu\text{m}$  and the extended arms are 1600  $\mu\text{m}$ . The device thickness is 100  $\mu\text{m}$  and the initial gap is 120  $\mu\text{m}$ . This design shows 300  $\mu\text{m}$  of displacement [99]. This design is suitable for manipulating micro-objects larger than 120  $\mu\text{m}$  in size. More details can also be found in [100].

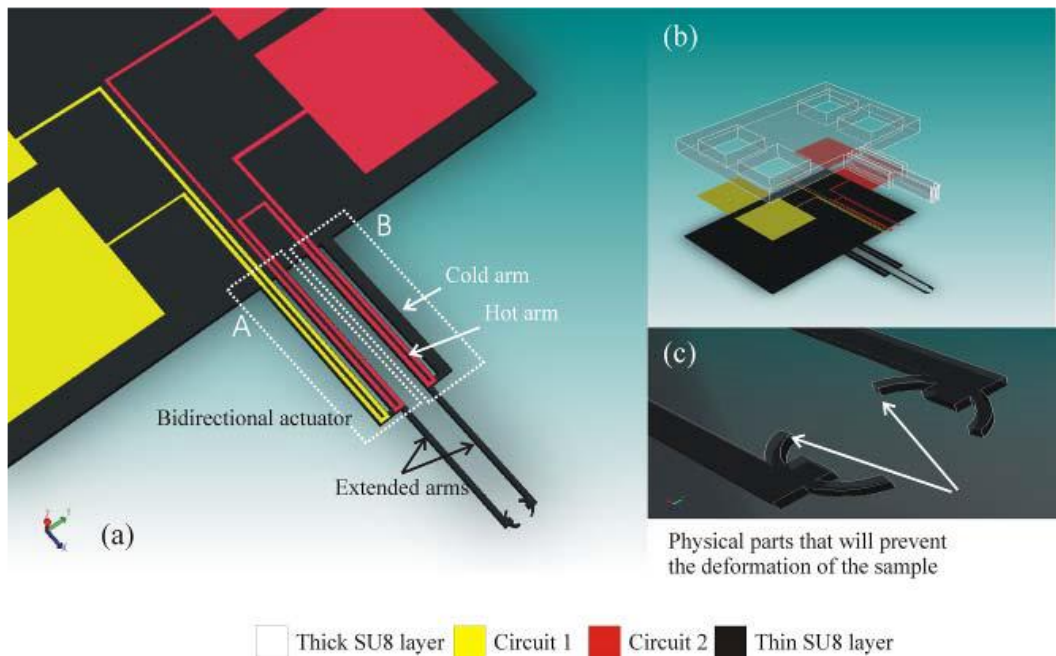


Fig. 2.62 Hot/cold arms microgripper with an extension arm [99]

Fig. 2.63 shows another design of SU-8 microgripper. This was designed based on the hot and cold arm method for the actuator. The two narrow arms, A and B as shown in Fig. 2.76 (A), are the hot arms with a width of 120  $\mu\text{m}$ . The hot arms are covered using titanium/platinum with about 100 nm of film thickness, which acts as a heater. Arm C is the cold arm; its width in the base is 100  $\mu\text{m}$  and it becomes about 1 mm in the middle of the microgripper. The microgripper thickness is 100  $\mu\text{m}$ . The initial end-effector opening is 30  $\mu\text{m}$ , which increases by about 100  $\mu\text{m}$  based on the results of simulation [101].

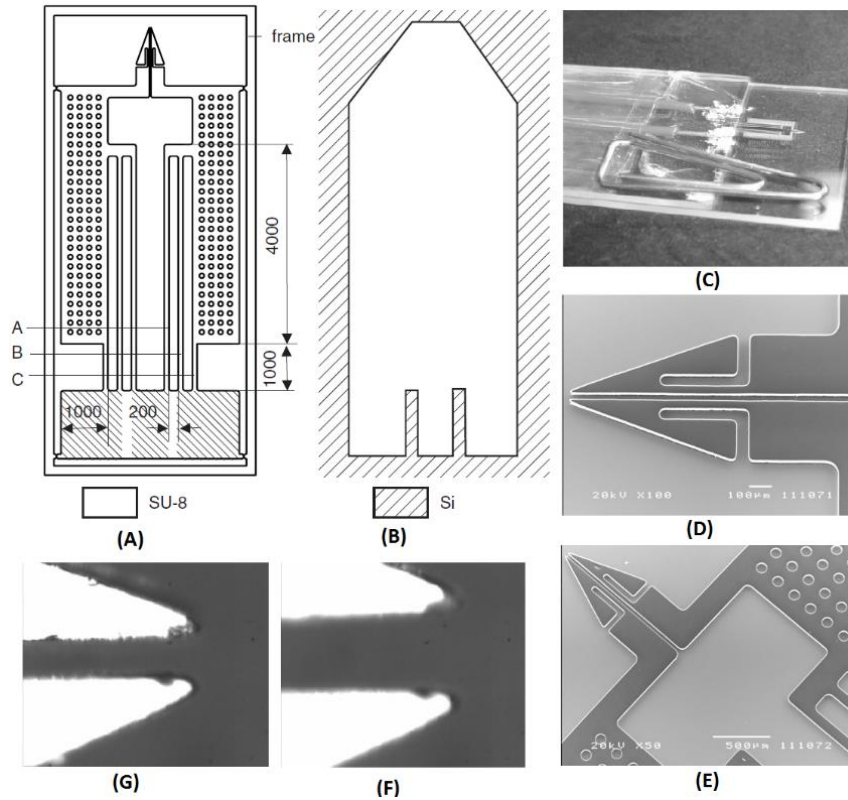


Fig. 2.63 Hot/cold arms microgripper [100]

However, the images in Fig. 2.63 (G) and (F) do not show a big displacement, where the unactuated situation shows 62 pixels and the opening under actuation shows 110 pixels. In addition, the end-effectors are too thin to manipulate objects with a length less than 100  $\mu\text{m}$ . Another disadvantage of this design is that the heater conductor is placed on the top of the surface of the microgripper. This leads to a temperature difference between the top and the bottom surfaces. As a result, the actuator deforms and loses some of the expanding displacement as an out of plan displacement.

A two DOF (opening and closing) three-beam microgripper is shown in Fig. 2.64. This design was developed at the Technical University of Denmark in 2007. The dimensions are 200  $\mu\text{m}$ , 40  $\mu\text{m}$ , and 5  $\mu\text{m}$  for overall length, width, and thickness. One arm contains two separate heaters one the edge beams while the middle beam acts as a cold arm. When a voltage is applied to one of the hot arms it pushes the end-effector and a displacement towards the corresponding direction happen. This is illustrated in Fig. 2.65. The actuation generates a maximum opening change of 8  $\mu\text{m}$  which means each end-effector moves  $\pm 2 \mu\text{m}$  [102].

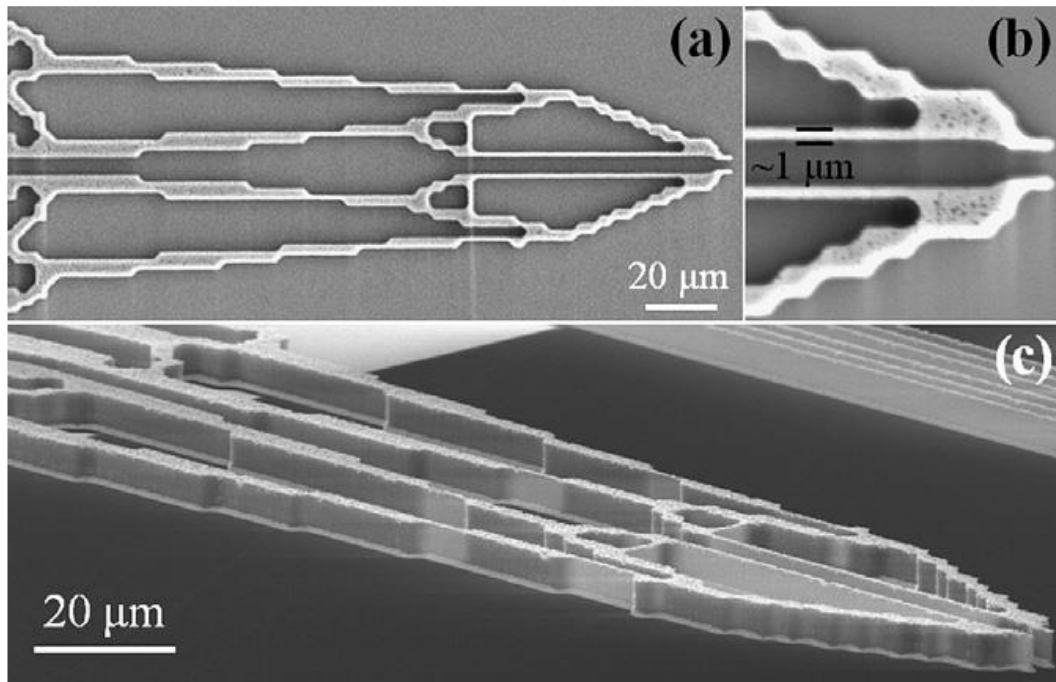


Fig. 2.64 Three heating beam microgripper [102]

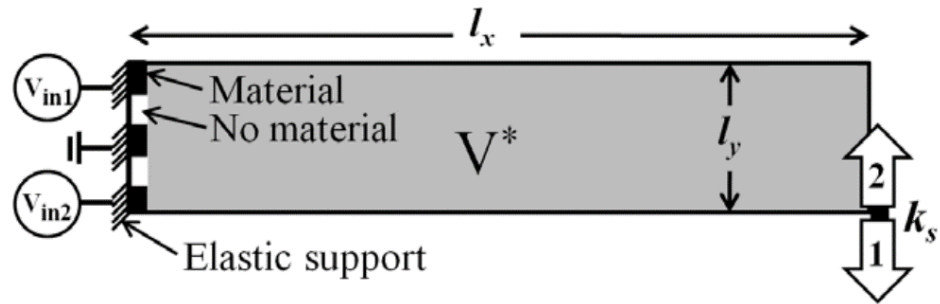


Fig. 2.65 Three beam working principle [102]

A microgripper with three actuator beams which is closed when a voltage is applied, has been designed and manufactured. This design is made using a combination of silicon/SU-8 and aluminum. Through the fabrication process of the silicon part, piezoresistors are made as sensors. The hot arm is based on silicon and an aluminum heater on the top surface with a layer of SU-8 polymer. The dimensions of the whole microgripper are 490  $\mu\text{m}$ , 350  $\mu\text{m}$ , 30  $\mu\text{m}$ , and 40  $\mu\text{m}$  for length, width, thickness, and in initial opening. The length of the cantilevers is 390  $\mu\text{m}$  and it contains the piezoresistors with a length of 68  $\mu\text{m}$  and width of 1  $\mu\text{m}$ .

The piezoresistors bend when the jaws are actuated so their resistance changes. This has been used to estimate the displacement by calibrating the resistance value change with the displacement change. Then, the force also can be estimated from the material's stiffness, the amount of power applied, and the measured displacement. After applying about 4.5 V on the heater part, a displacement of 30  $\mu\text{m}$  and a temperature of about 180° C are measured [103].

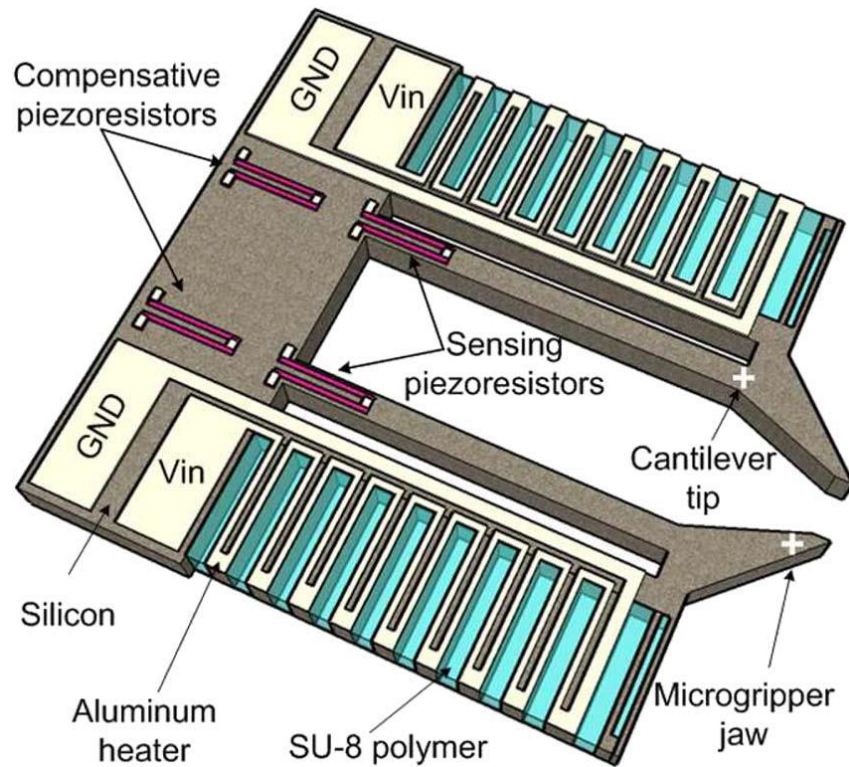


Fig. 2.66 Hybrid designed microgripper using silicon and SU-8 as structural materials [103]

Other designs were developed at the University of Durham and are shown in Fig. 2.67. These designs are also based on the hot/cold arm configuration, where the conductors on the cold arms are wider than on the hot arms to generate a difference in the resistance values, so that the narrow conductor (heater) generates a higher temperature than the wider one. The hot and the cold arms are designed in such a way that the end-effectors get closer when the voltage is applied. It is claimed that the first design showed  $120\text{ }\mu\text{m}$  of deflection when a current of  $32\text{ mA}$  was passed through the heater [104]. There is no information about the heater temperature at this deflection or the temperature at the end-effectors.

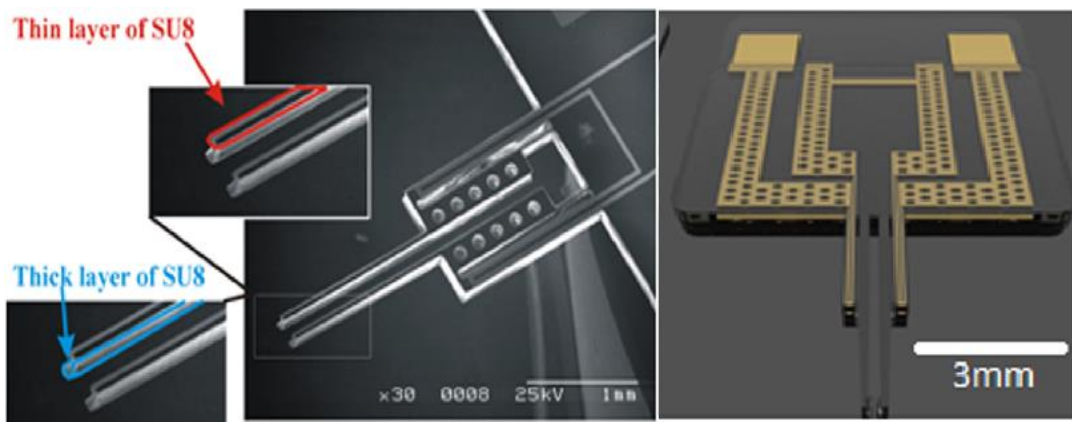


Fig. 2.67 Hot/cold arms microgripper [104, 105]



The second design was manufactured with an initial opening of  $100\ \mu\text{m}$  and the microgripper base length is  $7\ \text{mm}$ , the base width is  $7.5\ \text{mm}$ , and the arm length is  $3.5\ \text{mm}$ . This microgripper has been tested for different thicknesses and the results show different responses, as shown in Fig. 2.68 [105].

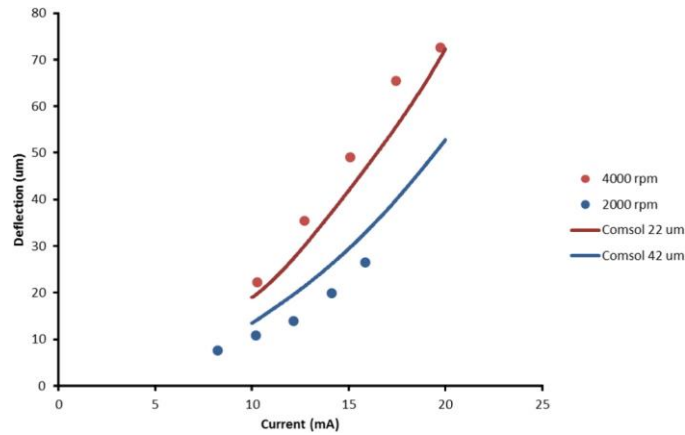


Fig. 2.68 Deflection with current for different microgripper thickness [105]

## 2.8 Multi-Finger Micro-Cages gripper

This microgripper was developed for microbiological applications. It has many fingers, and the structure is like a cage opened and closed by applying electrical power. The fingers are made of three layers. The first layer (top layer) is made of a thick SU-8 film, the middle layer is a heater made of a thin layer of a metal such as aluminium, and the last thin layer is diamond-like carbon (DLC). The stress property of DLC layer after releasing bends the finger structure upwards making a closed cage. Applying power on the heater generates an expansion which is much larger in the SU-8 compared to the DLC. The difference in the expansion ratio bends the fingers to open the cage as shown in Fig. 2.69 [106].

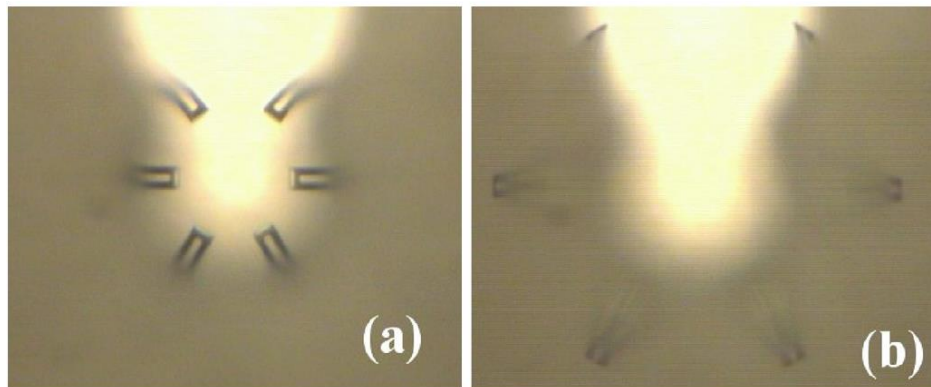


Fig. 2.69 Optical photograph of the microcage (a) no power applied (b) less than  $9\ \text{W}$  applied; the angle is about  $80^\circ$  [106]

As shown in Fig. 2.70, the fingers are deformed after the fabrication and depends on the length of the fingers, i.e., the angle of the fingers is proportionally related to the length of the fingers [106].

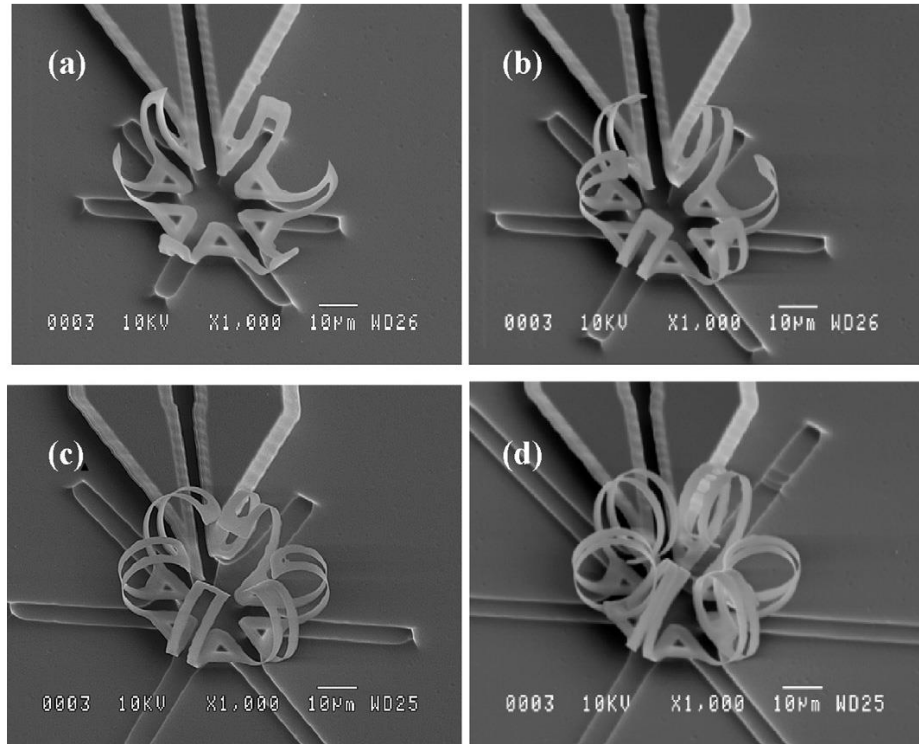


Fig. 2.70 SU8/DLC micro-cages with L of (a) 20  $\mu\text{m}$ , (b) 30  $\mu\text{m}$ , (c) 40  $\mu\text{m}$ , and (d) 50  $\mu\text{m}$  [106]

Although this gripping methodology can be used for some applications, it cannot be used for live cell manipulation. This is because the opening and closing processes heat the end-effectors. In addition, the mechanism for grasping objects is not carried out by the fingers. It clinches an object, so it leads to inaccurate placing and positioning tasks in assembly and manipulation.

## 2.9 Actuation Principles - Externally Actuated Microgripper

This section reviews the existing methods of externally actuated microgrippers, i.e. the mechanical force is externally generated to actuate the end-effectors.

### 2.9.1 Pneumatically Actuated Microgripper

Micro-pneumatic power is a possible source that can be employed to design microactuators. It has many advantages such as large displacement, well-known mechanical behavior, and high force etc. Compressed air and sometimes fluid are used to generate the required force to control the microactuators. Pistons are used to translate the compressed air into movement.

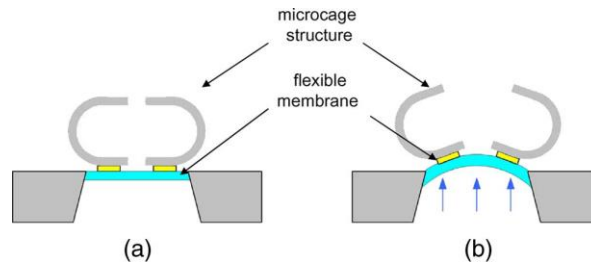


Fig. 2.71 Simplest microcage based on pneumatic actuation. When a pressure is applied on the membrane, it pushes the two arms [107]

A very simple microgripper has been designed using a flexible membrane and microcage structure, as shown in Fig. 2.71. The design principle is that the microcage shape changes when pressure is applied on the bottom of the membrane. As a result, the two (C) finger shapes are pushed away from each other [107].

Another design is shown in Fig. 2.72 and Fig. 2.73 using a small membrane fixed on the end of a tube. Pressure is produced by injecting air into the tube. This pressure causes membrane deformation. Then, this deformation generates a displacement in the base of the microgripper and increases the opening. The microgripper structure is fabricated using 1 mm thick PMMA material and cut by a TROTEC Speedy 300TM CO<sub>2</sub> laser cutter. In addition, a syringe is used to generate the airflow and pressure which is successfully used to grasp different objects of sizes from 0.2 mm to 2 mm [108].

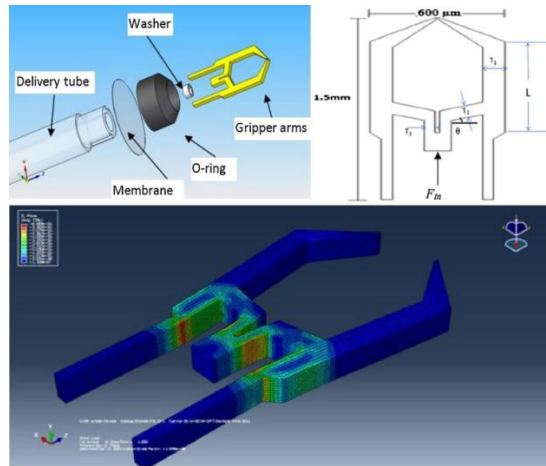


Fig. 2.72 PMMA microgripper design and dimensions [108]

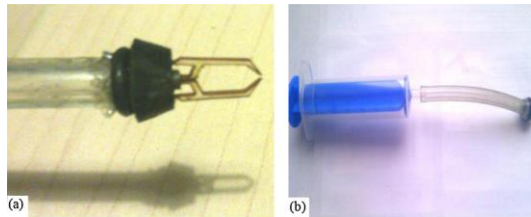


Fig. 2.73 Syringe based microgripper. The microgripper is actuated by the force that is generated because of the pressure due to the syringe movements [108]



Fig. 2.74 shows an SU-8 microgripper design based on the external actuation method. This microgripper was actuated using the pressure of compressed air. Air pressure is produced and transported to the microgripper using two capillary tubes with a diameter of  $300\text{ }\mu\text{m}$ . The pressure force is transformed by the two pistons to push and pull a microspring from one side and they are connected to gears to drive two end-effectors from the other side. When the air flows, the piston is pushed and transforms the air force to a displacement on the end-effectors. A displacement of  $600\text{ }\mu\text{m}$  is generated at the end-effectors when a pressure of 120 mbar is applied to the piston. This generates a force of about 10 mN on the spring [109, 110, 111].

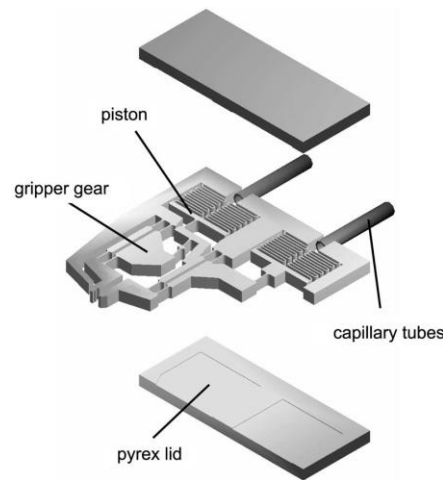


Fig. 2.74 Microgripper designed using SU-8 and driven pneumatically [109]

### 2.9.2 Voice Coil Actuated Microgripper

Magnetism can produce a bipolar force so it could be employed to generate a displacement by changing the polarity. It could be produced from a permanent magnet or by applying an electric current. A combination of the two sources of magnetics using two coils to generate electromagnetism, or one of the magnetic materials and coil, has been used to transfer the magnetic force into movement and actuation. This could be used to actuate anything from very simple valves to a very complicated device. Using the magnetic field offers design flexibility so multi-axis actuators could be achieved [112, 113].

A microgripper structure was fabricated using nickel titanium (NiTi) alloy. The NiTi alloy has a super-elastic property, which leads to a high displacement without causing permanent deformations or cracks in the structure. This microgripper is actuated externally using the principle of Lorentz force, and a voice coil motor (VCM) is employed for this purpose, as shown in Fig. 2.75. A shaft is attached to the center of the VCM. This shaft

transforms the coil displacement to the microgripper. The direction of actuation depends on the applied voltage polarity. The displacement is linearly related to the current because the relationship between the force and the current in the VCM is linear. The driving force ( $F_v$ ) is calculated by the law of Lorentz force, as expressed in equation (2.6).

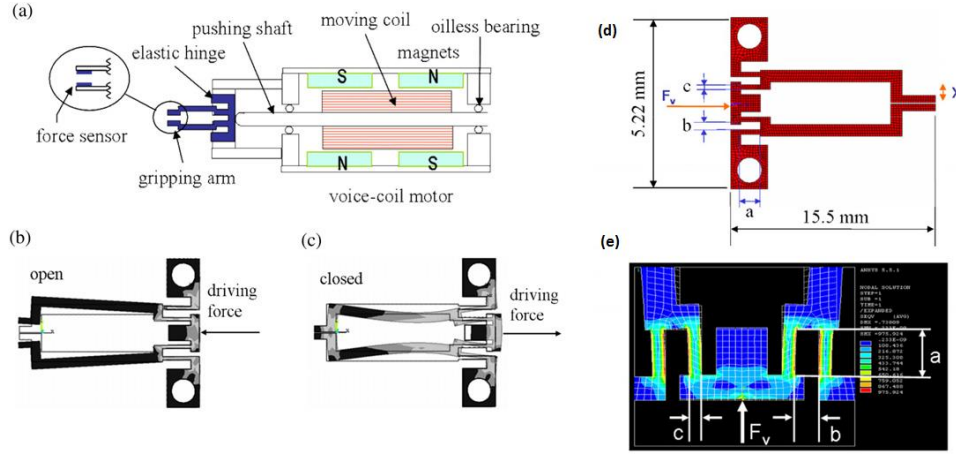


Fig. 2.75 Electromagnetic actuated microgripper. The figure shows the dimension, components, and the actuation method [114]

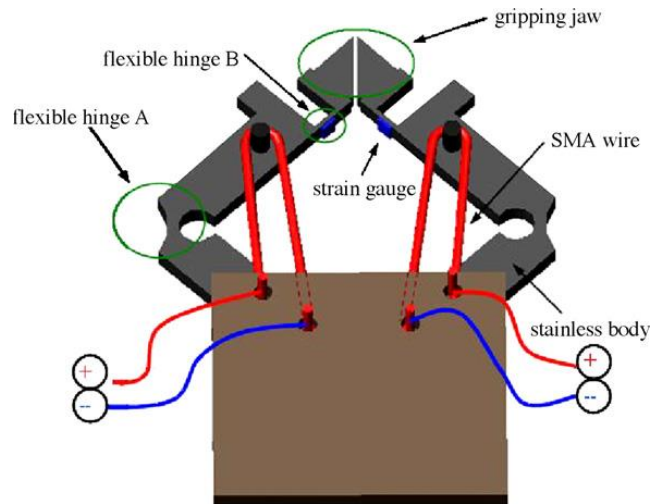
$$F_v = q (E + v \times B) \quad 2.11$$

Where  $q$  is the charge,  $v$  is the velocity,  $E$  is the electric field, and  $B$  is the magnetic field. Also, both  $E$  and  $B$  are vectors. This design offers about 0 – 150  $\mu\text{m}$  of displacement with a force up to 30 mN [114].

### 2.9.3 SMA Actuated Microgripper

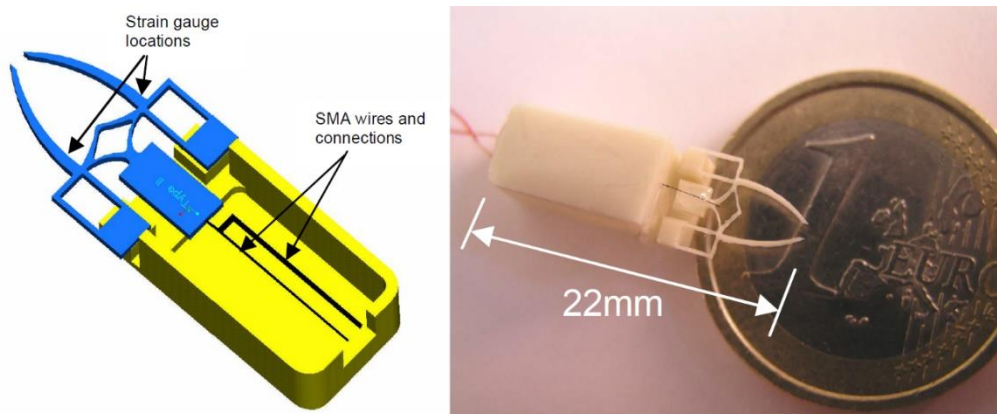
Shape Memory Alloys (SMAs) materials (such as copper based, nickel titanium based, and iron based) can recover their shape after the cause of deformation is removed. The properties of these materials are beneficial to the design of an actuator to drive different mechanic structures [115].

An (SMA) microgripper is shown in Fig. 2.45. This is driven by a 100  $\mu\text{m}$  NiTi based wire. The principle is that when a voltage is applied to the SMA wire, it generates heat which causes a shrinkage in the wire length. This pulls the gripper's arm and rotates it around the flexible hinge A. The microgripper thickness is 1 mm and the width in the hinge parts is 15 mm. The experimental result shows a maximum displacement of 120  $\mu\text{m}$  [116].



*Fig. 2.76 An SMA microgripper with a strain gauges to measure the force on the flexible hinge [116]*

Another (SMA) design is shown in Fig. 2.46. The gripper structure is made by moulding polyurethane in silicon moulds by the technique of shape deposition manufacturing (SDM) [117]. The initial displacement of this design is about  $180\ \mu\text{m}$  and the full power opening is about  $20\ \mu\text{m}$  by applying a current of  $70\ \text{mA}$  [117].



*Fig. 2.77 An SMA microgripper with integrated strain gauges to sense the force [117]*

A microgripper with a thickness of  $145\ \mu\text{m}$  is fabricated using a thick SU-8 photoresist and one mask. A  $10\ \mu\text{m}$  thickness thin film of a TiNi shape memory alloy (SMA) is fabricated as an actuator. This microgripper is shown in Fig. 2.78. A monolithic process is used to microfabricate the SMA part and several masks are used for this purpose. The assembly with the SU-8 microgripper is maintained in a closed state position. The SMA material has strong specifications such as large deformation up to 10% of its length, and high force etc. The SU-8 microgripper dimensions are  $1.7\ \text{cm}$ ,  $0.6\ \text{cm}$ , and  $145\ \mu\text{m}$  for length, width, and thickness respectively. The displacement of this microgripper was about  $250\ \mu\text{m}$  when a maximum current of about  $0.1\ \text{A}$  is passed through the SMA part [118].

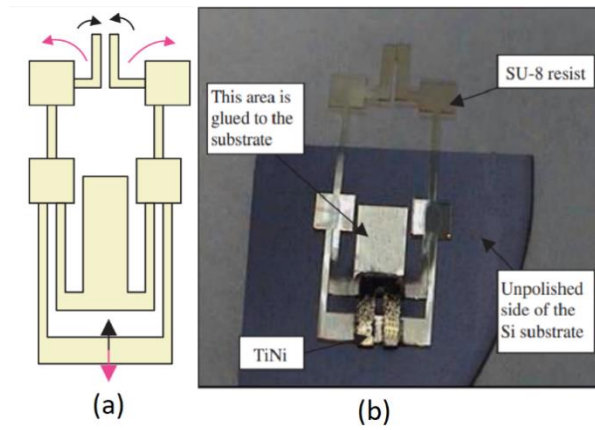


Fig. 2.78 SU-8 microgripper actuated using SMA (a) the actuation method (b) the assembled microgripper [118]

#### 2.9.4 Piezoelectric Actuator

A piezoelectric actuator is also used to drive microgrippers. Fig. 2.79 shows an example of using piezo material to drive a microgripper. The structure is fabricated from a single piece of spring steel using a micro-wire electrical discharge machine (EDM) [119]. Then it is mounted on a holder and it is driven by a rod connected to a piezo actuator.

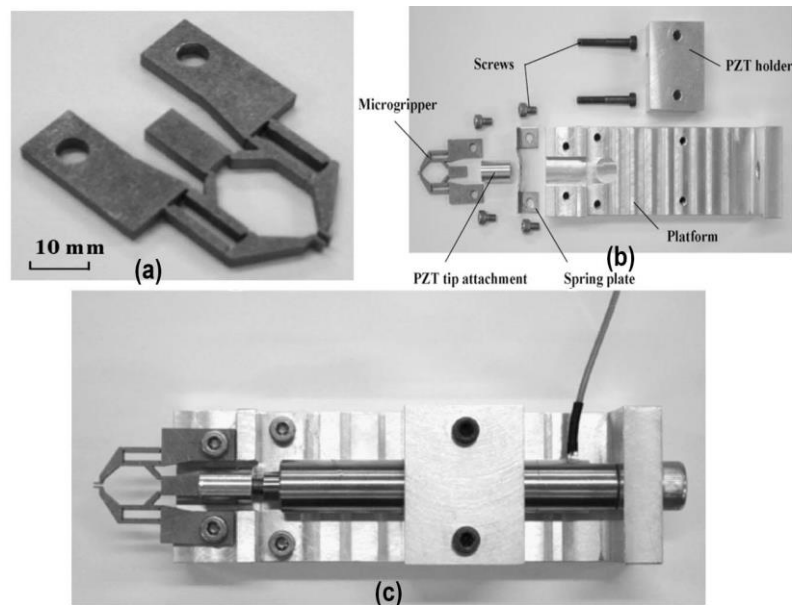
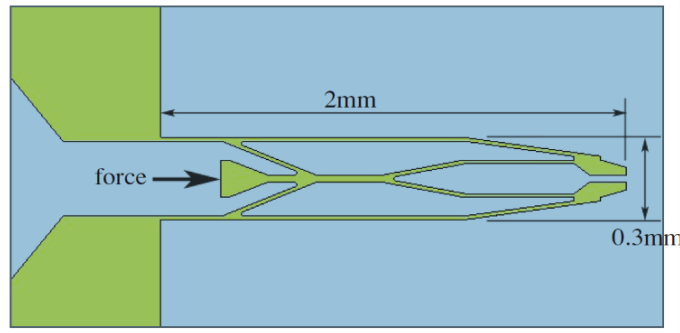


Fig. 2.79 Externally actuated microgripper using piezoelectric (a) the microgripper structure (b) the microgripper parts (c) the assembled microgripper [119]

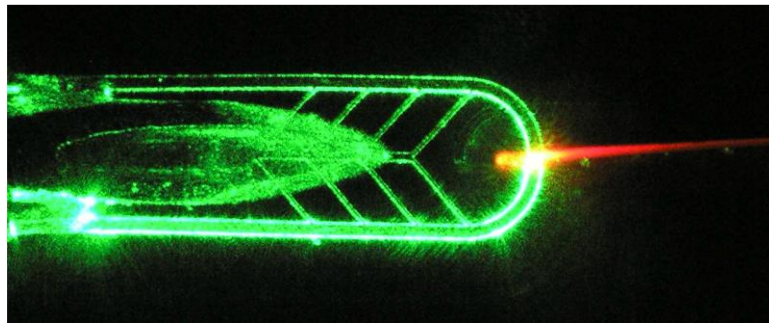
Fig. 2.80 shows an SU-8 microgripper with an external piezoelectric actuator. The operating mode depends on the applied force so if the actuator applies a pulling force, the end-effectors are displaced towards each other. However, if the applied force is pushing, the end-effectors are displaced away from each other. The microgripper is fabricated using photolithography processes. One mask is used for patterning and KOH (30%) is

used for the releasing process. The overall microgripper dimensions are 2 mm, 0.3 mm, and 0.1 mm for length, width, and thickness respectively. Then, the microgripper is glued onto an adapter and actuated using a translation piezo actuator of type (PI, P840.10). The maximum displacement of the actuator is 15  $\mu\text{m}$  at 100 V of voltage. However, the actuator was limited to 10  $\mu\text{m}$  of displacement to avoid over-pushing and damaging the microgripper. This microgripper design has a range of opening displacements between 30  $\mu\text{m}$  to 170  $\mu\text{m}$  [120].



*Fig. 2.80 Piezo actuated SU-8 microgripper [120]*

Another microgripper has been designed based on SU-8 and actuated externally using a piezoelectric actuator. The standard contact photolithography method is used to fabricate this design. The arms are used as a wave guide which is connected to an optical fiber with a source of a green laser at 532 nm. The light is guided through the gripper's arm and comes out from the end-effectors. This helps to accurately align micro-objects with the end-effectors, as shown in Fig. 2.81 [121, 122].



*Fig. 2.81 An optical guide microgripper [121]*

#### *2.9.5 Microgripper with Micrometer Screw*

Another polymer microgripper based on external actuation is shown in Fig. 2.82. The SU-8 25 is used to fabricate this microgripper with thickness of 30  $\mu\text{m}$ , and 1250  $\mu\text{m}$  and 500  $\mu\text{m}$  for the length and width. This microgripper is driven using a micrometer accuracy actuator with its end glued onto the microgripper. The testing result shows that a maximum of 80  $\mu\text{m}$  displacement could be achieved [123].

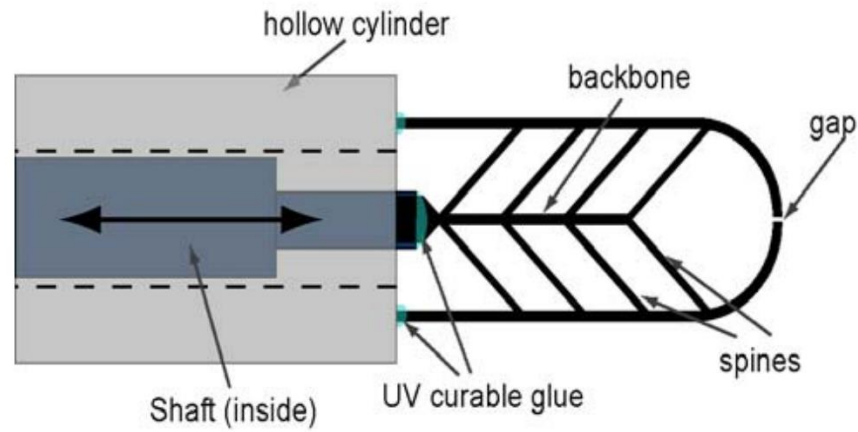


Fig. 2.82 Microgripper diagram showing the components [123]

### 2.9.6 Disadvantages of Externally Actuated Microgrippers

The externally actuated microgripper needs a microgripper to assemble the components precisely. This is because the actuator position is very sensitive and needs to be installed accurately. The dimensions of these microgrippers are large and this limits the possible applications and increases the required working area. However, the design of the piezo grippers has a wide opening and it cannot be used for micro-objects with a dimension of less than 100  $\mu\text{m}$ . The SMA and the pneumatic microgrippers can be used to manipulate micro-objects in several hundreds of microammeters to millimetre scale. The proper assembly of the component increases the production cost and needs complicated microassembly processing equipment. Therefore, the externally actuated microgrippers cannot be fabricated in single manufacturing process. Also, the requirement of accurate assembly will increase the production coast significantly. Table 2-3 provides a summery comparison between different actuation method used to design externally actuated microgrippers.

Table 2-3 Summery of the externally actuated microgrippers

Actuation method	Initial opening	Displacement	End-effectors Material	Disadvantages
Pneumatical microcage	-	-	polysilicon	Work as cage to grasp an object. It cannot be used for precise assembly.
Pneumatical microgripper	2 mm	1.8 mm	PMMA	Main drawback is this microgripper required an assembly itself. Also, the gripping arm thickness is 0.5 mm which limit the object size to 0.25 mm. Required a precisely controlled air pressure.

Pneumatical SU-8 microgripper	0.8 mm	0.6 mm	SU-8	Main drawback is this microgripper required an accurate assembly of the covering without destroy the hinges and springs. Required a precisely controlled air pressure.
Voice Coil	0	150 $\mu$ m	nickel titanium	Required an accurate assembly of the coil core to the actuated part. Required a force sensor feedback because of the high force generated.
SMA	140 $\mu$ m	120 $\mu$ m	polyurethane	Required an accurate assembly of the SMA wire. Microgripper thickness is 1 mm which limit the manipulated objects to 0.5 mm.
SMA	100 $\mu$ m	200 $\mu$ m	SU-8	Required an accurate assembly of the SMA wire. The SMA required high current and working in high temperature.
Piezoelectric	500 $\mu$ m	170 $\mu$ m	-	Required an accurate assembly of the piezoelectric material and the Aluminum base with the microgripper. The displacement is small comparing with the size of the microgripper about 6 cm.
Screw	150 $\mu$ m	170 $\mu$ m	SU-8	Required an accurate assembly of the screw to the base of the microgripper.

## 2.10 Summary

### 2.10.1 Micromanipulation Methods

In order to miniaturise complex equipment, microassembly methods were developed. Each microassembly method is based on micromanipulation approaches. This chapter highlights some of the important methods of microassembly then focuses on some of the popular robotic microassembly methods. However, the micromanipulation methods are studied and presented in more detail. In general, the micromanipulation methods are divided into two main groups based on the interaction between the manipulator and the micro-object. Table 2-4 summarises the contactless manipulation methods presented in this chapter with some key features. The positioning using contactless method suffer from accuracy, therefore it is not suitable for microassembly. The manipulation using end-effectors is more suitable for manipulating a micro-object accurately.

*Table 2-4 Contactless micromanipulation methods*

Method	Advantages	Disadvantages
Photophoresis	Good at sorting micro-objects	Poor multi-axis control and flexibility of manipulation. Therefore, not suitable for microassembly
Hydrogel Microgripper	Completely contactless and works through some barriers efficiently	Requires a liquid medium to work efficiently
Acoustic Manipulations	Good at sorting micro-objects	Poor multi-axis control and flexibility of manipulation. Therefore, not suitable for microassembly
Air Flow Manipulation	High force. Good at positioning	Poor multi-axis control and flexibility of manipulation. Therefore, not suitable for microassembly
Electrostatic Force Positioning	Good at positioning	Low resolution and poor multi-axis control

*Table 2-5 Single end-effector microgrippers*

Method	Advantages	Disadvantages
Capillary Gripping	Easy to fabricate and control	Low force and requires a drop of liquid to function. Poor at reorientations
Vacuum Gripper	Easy to control and high force	Not suitable for fragile micro-objects. Poor at reorientations
Van der Waals Forces	Simple and easy to control, suitable for fragile micro-objects	Low force. Not easy to release objects. Poor at reorientations
Cryogenic Grippers	Independent to manipulated micro-object size	Complex and requires liquid to operate. Works under freezing temperatures therefore not suitable for temperature sensitive application
Electrostatic End-effector	Easy to fabricate and use	Requires high voltages. Not easy to reorientation the manipulated micro-objects

Table 2-5 summaries the grippers based on one end-effectors. Except the vacuum microgripper, all required a mechanism to release the picked objects. In addition, they require a complicated assembly process, and they are not cheap to fabricate. The vacuum based microgrippers are not suitable to manipulate fragile objects which is the case in microassembly. Therefore, a microgripper based on two end-effectors should not suffer at releasing stages. Also, the applied force on manipulated objects should be controlled by controlling the opening.

Microgrippers based on two end effectors can be divided into two groups, externally actuated microgrippers and embedded actuator based microgrippers. The first group was summarised in Table 2-3 and the second group is summarised in Table 2-6. Each of them is suitable for specific application, input, and limitation. Also, the used actuator defines the



working conditions and the range of the suitable materials for microgripper fabrication. Microgrippers designed with embedded actuator are easier to fabricate because they do not need an assembly process and they could be fabricated in one manufacturing sequence. As a result, microgrippers with jaws (two end effectors) based on embedded actuators are the most suitable manipulator for microassembly field.

*Table 2-6 Microgrippers with Jaws with Integrated Actuators*

Method	Advantages	Disadvantages
Electrostatic Actuated Microgripper	High force	Nonlinear. Complex control is required. High voltage operation
Electromagnetic Actuated Microgripper	High force. Large displacement	Nonlinear. Complex control is required. Large microgrippers
IPMC Actuated Microgripper	Large displacements up to 3 mm	Requires a close loop control
Electrothermally Actuated Microgrippers	Wide range of material is suitable. Easy to control	Some material requires high temperature

### *2.10.2 Materials Used in Microgripper Design*

There are different materials used in development of microgrippers. Material selection is limited by the requirements of the application and it limits the selected actuation method. For years these materials in Table 2-7 were used to fabricate microgrippers depending on the required specification and application limitations.

*Table 2-7 Materials used for microgrippers design.*

Piezoelectric	Generally, it requires high voltage. Complex control system. Expensive. Used to design microgrippers arms with high deflection
Silicon	Low CTE when used with electrothermally actuated microgrippers so it operates at a high temperature. Good for electrostatic actuated microgrippers
PMMA	Used mostly with an external actuator
Nickel titanium and Metglas	Used with magnetically operated microgrippers
SMA	Has negative CTE and used as external actuators
IPMCs	Used to fabricate the microgripper arms and sensor is required
SU8	Polymer based material used to fabricate the microgripper structure. Has a high CTE therefore large displacement at low temperature

Many researchers used these materials to fabricate microgrippers, however the SU-8 was the easiest and cheapest among them not only to fabricate different MEMS devices. SU-8 is an epoxy-based negative polymer photoresist material sensitive to the UV spectrum. The part that is non-exposed to UV can be removed during the development processes. The SU-8 patterning method is commonly based on the photolithography

approach. There are different formulations of SU-8 depending on its density such as the SU-8 2000 series which includes SU-8 2025, SU-8 2035, SU-8 2050 and SU-8 2075. These formulations can be used to fabricate layers of 0.5  $\mu\text{m}$  to 100  $\mu\text{m}$  of thickness. Another example is SU-8 3000 which is used for film thickness between 2  $\mu\text{m}$  and 75  $\mu\text{m}$ . The physical properties can be seen in Table 2-8 [124, 125]. In addition, it is a biocompatible material, has a chemical resistance, and can be used in air, vacuum, and liquid. Therefore, it gets an attraction to be used for microassembly and single cell manipulation [126]. The high CTE value of the SU-8 material in comparison to the other materials make it the ideal material to fabricate microgrippers with embedded electrothermal actuators.

*Table 2-8 The physical properties of SU-8 2000 and SU-8 3000 series photoresist materials [124, 125]*

<i>SU-8 Series</i>			<i>2000</i>	<i>3000</i>
<i>Adhesion Strength</i>	<i>mPa</i>	<i>Silicon</i>	<i>38</i>	<i>69</i>
		<i>Glass</i>	<i>35</i>	<i>35</i>
		<i>Glass &amp; HMDS</i>	<i>35</i>	<i>59</i>
<i>Glass Transition</i>	<i>T<sub>g</sub> °C</i>		<i>210</i>	<i>200</i>
<i>Thermal Stability</i>	<i>°C @ 5% wt. loss</i>		<i>315</i>	<i>300</i>
<i>Thermal Conductivity</i>	<i>W/mK</i>		<i>0.3</i>	<i>0.2</i>
<i>Coeff. of Thermal Expansion</i>	<i>CTE ppm</i>		<i>52</i>	<i>52</i>
<i>Tensile Strength</i>	<i>Mpa</i>		<i>60</i>	<i>73</i>
<i>Elongation at break</i>	<i><math>\epsilon_b</math> %</i>		<i>6.5</i>	<i>4.8</i>
<i>Young's Modulus</i>	<i>Gpa</i>		<i>2.0</i>	<i>2.0</i>
<i>Dielectric Constant</i>	<i>@ 10MHz</i>		<i>3.2</i>	
	<i>@ 1GHz</i>			<i>3.28</i>
<i>Bulk Resistivity</i>	<i><math>\Omega \cdot \text{cm}</math></i>			<i><math>7.8 \times 10^{14}</math></i>
<i>Water Absorption</i>	<i>% 85°C/85 RH</i>		<i>0.65</i>	<i>0.55</i>
<i>Transmittance</i>	<i>About 70% for 360 nm wavelength</i>			

### *2.10.3 Fabrication Method for SU-8 Polymer*

The SU-8 solutions have been employed to manufacture the micro-electro-mechanical systems (MEMS). The photolithography fabrication processes can be summarised by the following steps. First, the masks for each layer required are designed and fabricated. Then the SU-8 should be uniformly deposited on a wafer such as silicon

or glass. The spin coating speed depends on the required thickness and SU-8 formulation. The SU-8 needs to be baked for some time depending on the application and desired specifications to harden the film. Then, it is exposed to a UV source to cross-link the SU-8 film through a photomask to create the desired pattern. Then the SU-8 is developed with a solvent to remove the un-exposed SU-8. In addition, a new process was developed recently to use an electron beam within nanometer resolution directly on the SU-8 film instead of using a mask [127, 128, 129].

Because of the low cost, well known manufacturing procedures, and biocompatibility etc., SU-8 materials are widely used to design and fabricate microgrippers, especially for bio-manipulation. These SU-8 microgrippers are driven using different actuation methods and materials such as piezo material. The SU-8 microgripper can be classified into two groups according to the actuation mechanism: externally actuated and integrated actuators.

## Chapter 3 Design, Simulation and Fabrication

### 3.1 Introduction

This chapter presents the work on design and simulation of the microgrippers. These microgrippers were based on the electrothermal actuation mechanism and SU-8 materials. This actuation method with the high CTE value of the SU-8 make it ideal for design and fabrication of large displacement microgrippers. Also, the biocompatibility of SU-8, its chemical resistance and very good elastic specification make it ideal for many applications [100]. Embedding heater with SU-8 to create an actuator can be done in one fabrication process without the requirements of microassembly. COMSOL Multiphysics was used to study and improve the performance of these designs to obtain the most effective devices.

### 3.2 Actuation Design Principles

#### 3.2.1 Displacement Force and Reaction Force

The principle of electrothermal actuation method is based on Joule heating. When a current is passed through a resistor, the dissipated power is transformed to heat. This heat causes thermal expansion in the actuator which it translated to a pushing force on the end-effectors arms at the point of connection as described Fig. 3.1. Therefore, this force is employed to deflect the arms in the microgrippers.

The actuator in microgrippers is supported from a side and the generated expansion is translated to a force at the connection point on the beam. If it is supposed the microgripper is a 2D plane in (XY), the expansion is in the X direction at the point (a). The weight of the beam is distributed load vertical on the XY plane (Z axis) which is ignored because it is not in the interested plane and it is not enough to effect on the beam. When the heated region expands and actuates the beam, this beam will react to the actuator and causes compression stress. This force is equal to the force required to deflect the beam by the same amount. This can be expressed by equation 3-1 and is shown in Fig. 3.1. Because the designed microgrippers do not have a uniform arm, this figure only explain the principle of the microgripper design, and the actual calculation done using a simulation module with COMSOL Multiphysics.

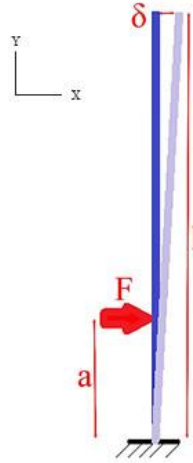


Fig. 3.1 Beam deflection when a force ( $F$ ) is applied at the distance  $a$  from the base to generate the deflection ( $\delta$ ) at the edge of the beam

$$F = \frac{6 \delta E I}{a^2 (3l - a)} \quad 3-1$$

Where  $F$  is the reaction force,  $\delta$  is the deflection of the far end of the beam,  $E$  is the Young's modulus of the SU8 material,  $I$  is the area moment of inertia,  $a$  is the distance between the supporting point and the force point, and  $l$  is the beam length, as shown in Fig. 3.1.

In addition, the heated beam can bear a critical compression force before it deforms or buckles, as shown in Fig. 3.2. The deformation shape depends on the edge support type. If the reaction force exceeds the critical force in equation (3-2), it causes a failure in the heated region of the beam and it can buckle. The value of the critical force  $F_c$  is inversely proportional to the square of the effective actuator length. The effective length is equal to half to double of the actual actuator length depending on the supporting structure shape of the edge. In addition, the critical force is directly proportional to the Young's modulus ( $E$ ) and the area moment of inertia ( $I$ ), while this is directly proportional to the width ( $W$ ) and to the cubic power of the thickness ( $h$ ), as expressed in equation (3-3).

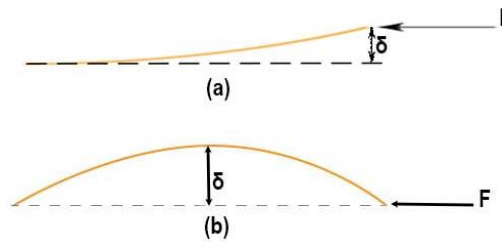


Fig. 3.2 Effect of the compression force exceeding the critical force on a beam shape when the tangent edge is (a) free point (b) fixed point

$$F_c = \frac{\pi^2 EI}{L_{eff}^2} \quad 3-2$$

$$I = \frac{Wh^3}{12} \quad 3-3$$

$$\delta_{max} = \frac{Fa^2}{6EI} (3l - a) \quad 3-4$$

Where  $L_{eff}$  is the effective length which depends on the support method of the beam end and  $\delta_{max}$  is the maximum deflection at the end of the beam.

Equation (3-4) shows the deflection on the end (end-effector) of the beam which results from the thermal expansion. The force required to be applied on the arms to produce this displacement should be less than the critical force in equation (3-2). The deflection force increases when any of the values of Young's modules, width and thickness of the beam is increased.

The design of these microgrippers is based on SU-8 material, which is an epoxy polymer which is sensitive to UV light with a large CTE of 52 ppm/°C [21] and a high cross-linked temperature over 200 °C [39]. However, the Young's modulus decreases when the temperature increases [40 – 41]. Therefore, the buckling critical force also decreases when the temperature increases. The maximum displacement decreases if the critical force is not calculated carefully. In addition, the force applied on the micro-particles for manipulation decreases. The width of the heated are can be increased to increase the critical force; therefore, displacement and the applied force increase too.

### 3.2.2 Displacement Amplification Ratio

The ratio of the displacement at the end-effectors and the actuator expansion is known as displacement amplification ratio. By calculating this, the required actuator expansion at an operating temperature can be calculated. The displacement ( $\delta$ ) in Fig. 3.1 is related to the expansion at point a ( $\delta_a$ ) can be expressed in equation (3-5) while the temperature can be calculating using equation (3-6).

$$\delta = \frac{l}{a} \delta_a \quad 3-5$$

$$T = \frac{\delta_a}{\alpha L} - T_o \quad 3-6$$

Where the  $\delta$  is the target displacement at the end-effector,  $l$  is the end-effector length,  $a$  is the distance between the fixed end of the end-effector and the actuation point, the displacement at the point  $a$ ,  $T$  is the operating temperature,  $T_o$  is room temperature and it is 20° C,  $\alpha$  is the CTE of the SU-8 and it is 52 PPM/°C, and  $L$  is the active length of the actuator. Proposed L-Shape Actuator

### 3.2.3 Design History

One of the most used methods in designing electrothermally actuated actuators is the U-shape (hot & cold arms) technique. This method is based on dividing the microgrippers into two parts: one is called a hot arm and it contains a narrower conductor, while the other is called a cold arm and it contains a wider conductor as discussed in Chapter 2 and shown in Fig. 3.3. In the conventional U-shaped actuators, there is a current passing through both hot and cold arms. Therefore, there is still a temperature generated in the cold arms and this affects the displacements because in this method it depends on the temperature difference between the hot and cold arms [100]. Although the conductor is wider in the cold arms than the hot arm, there is still resistance in the cold arms, therefore some power is dissipated, and this reduces the temperature difference between the two arms.

In addition, the conventional U-shaped actuators are narrow and cannot be wider because of their design, therefore its stiffness is small. Also the stiffness depends on the Young's modulus which is temperature dependent [130]. Therefore, actuators operating at higher temperatures will deform as will be shown in Chapter 6. Having a conductor passing through a hinge limits the ability to design narrower hinges. This results in a higher reaction force which leads to deformation of an actuator as described at the beginning of this chapter. Also, the existence of a heat source in the arm could lead to an increment of the arm temperature which could subsequently increase the temperature of the endeffectors.

A new and novel actuator structure was designed and proposed in this chapter. This design has all connectors in the actuator parts, and they have sufficient separation from the cold arms to decrease the effect of the raised temperature in the gripper arms and the undesired expansion. In addition, this method has the advantage of an ability to design narrower hinges therefore less reaction force on the actuators. Also, a novel structure with thicker actuators than the cold arms is proposed. This results in a stiffer actuator and eliminates the effect of the drop of the Young's modulus at high temperatures.

### 3.2.4 L-Shaped Actuator Principle

To overcome the described disadvantages, a modification is proposed in the following designs to replace the U-shape actuator with the L-shape actuator. Fig. 3.4 shows the proposed actuator principle and showing the hot and cold arms combined in one structure.

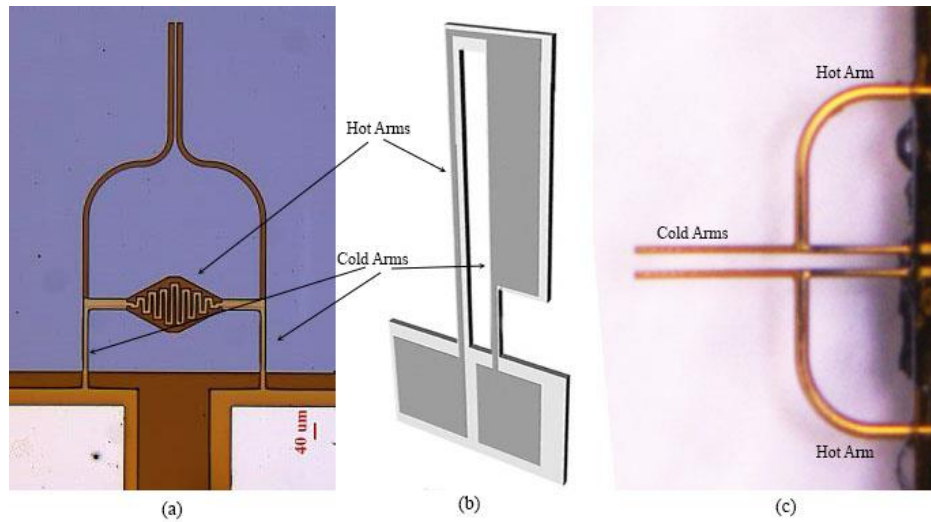


Fig. 3.3 Three selected of different design based on the U-shape actuator

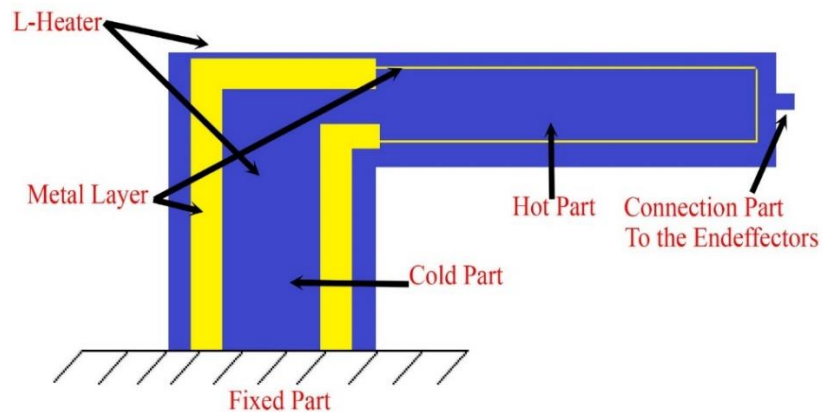


Fig. 3.4 Proposed L-Shape actuator structure and showing the details of the parts

The advantages of the new design method can be summarised as follows:

- i. The support part is wide enough in the L-Shape actuator, therefore most of the expansion effects are along the desired direction. Comparing this with the example in Fig. 3.3 (c), it is clear some of the action is lost due to bending in the hot arms.
- ii. The arms or the end-effectors are isolated from the conductor/heater section and there is no electric current to pass through the hinges, therefore the designers have freedom to choose narrow hinges. Also, there is no rise of temperature in the arms as shown later in the microgrippers designed based on this concept.



- iii. The connections between the actuators and the arms are very narrow and the SU-8 material is an insulator. Consequently, the heat passed from the actuators by conduction is very limited compared with the heat loss because of the heat flow to the ambient environment by convection. By comparing Fig. 3.3 and Fig. 3.4 the arms (cold arms) are part of the structure and directly connected to the heaters.

### 3.3 One Mode Microgrippers

#### 3.3.1 Design 1: Indirectly Actuated Microgripper

The target of this design was to have an initial opening of  $120\text{ }\mu\text{m}$  and it should be fully closed at  $100^\circ\text{C}$ . A mechanical interface between the actuator and the end-effector arm was added for two reasons. Firstly it is to increase the insulation between the end-effector arms and the actuators. Secondly it is to increase the displacement amplification by a factor of 2.5. The final amplification is 14.4. The hinges were designed to be  $100\text{ }\mu\text{m}$  in length and  $20\text{ }\mu\text{m}$  in width in order to decrease the stiffness in the actuation direction, i.e. to decrease the reaction force while the remaining structure was designed to be wider to increase the deflection at the hinge structures.

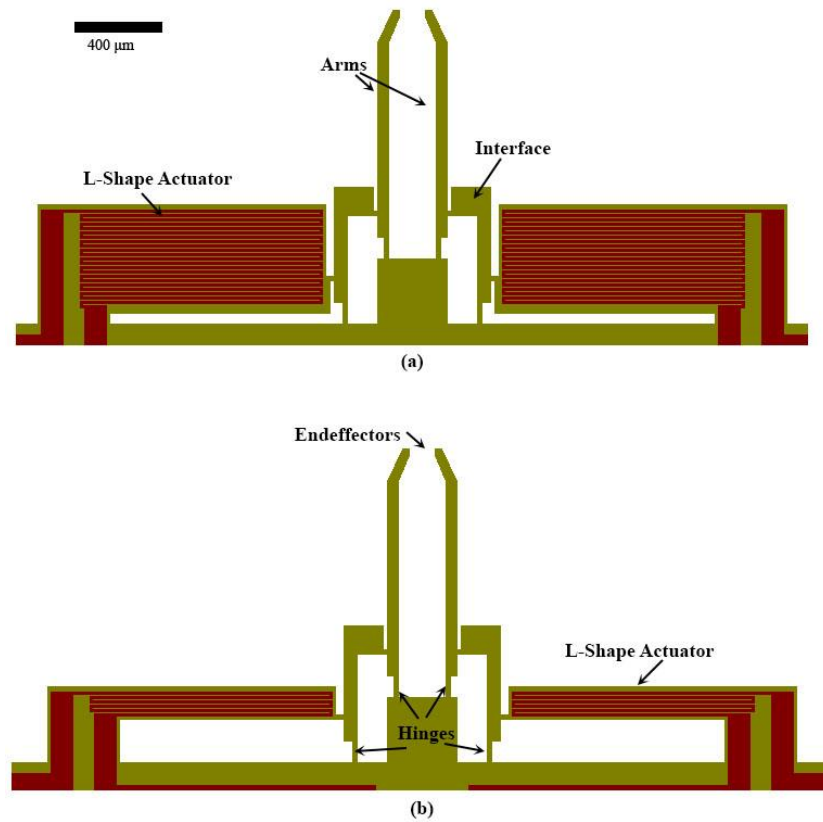


Fig. 3.5 A proposed design for a microgripper based on the L-shaped actuation method and isolated actuator with interface stages. The L-Shape actuator part is detailed in Fig. 3.7 and the end-effectors arm is detailed in Fig. 3.6

As shown in Fig. 3.5, the L-shaped actuator was employed to design microgrippers with an interface between the actuators and the arms. The thickness of all microgrippers was designed to be 20  $\mu\text{m}$ . The actuators were designed in two different widths (150  $\mu\text{m}$  and 500  $\mu\text{m}$ ) to study their effect on the microgripper's behavior. The length of the actuator was calculated using equation (3-5) and equation (3-6) and it is 1 mm. It is connected to the interface with a hinge which is 20  $\mu\text{m}$  in width and 40  $\mu\text{m}$  in length. The width of the heater conductor is 10  $\mu\text{m}$  and it is connected to the pads with a conductor line of 100  $\mu\text{m}$  in width. All conductor designs were 300 nm thick gold film sandwiched between two adhesive chromium layers of 10 nm of thickness. The actuator support part was 330  $\mu\text{m}$  in width to eliminate any expansion to the opposite direction.

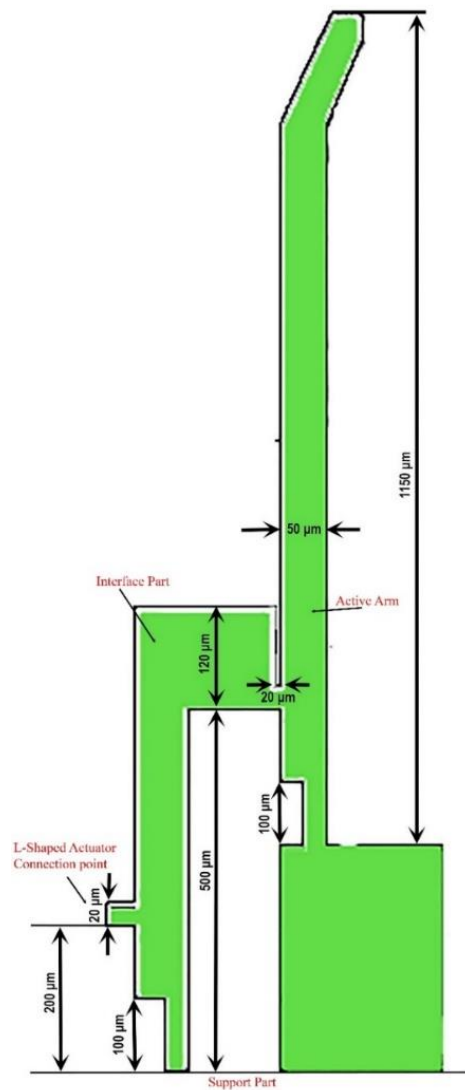


Fig. 3.6 Details of one microgripper arm design showing the interface part and the end effector

The dimensions of the interface, hinges and the arm are shown in Fig. 3.6. The interface is connected to the L-shaped actuator from one side and the active arm from the

other side. The actuator structure is shown in Fig. 3.7. The initial gripper end opening of this design is 120  $\mu\text{m}$  and it is closed when it is actuated.



Fig. 3.7 L-Shape actuator used to design the interfaced microgrippers.

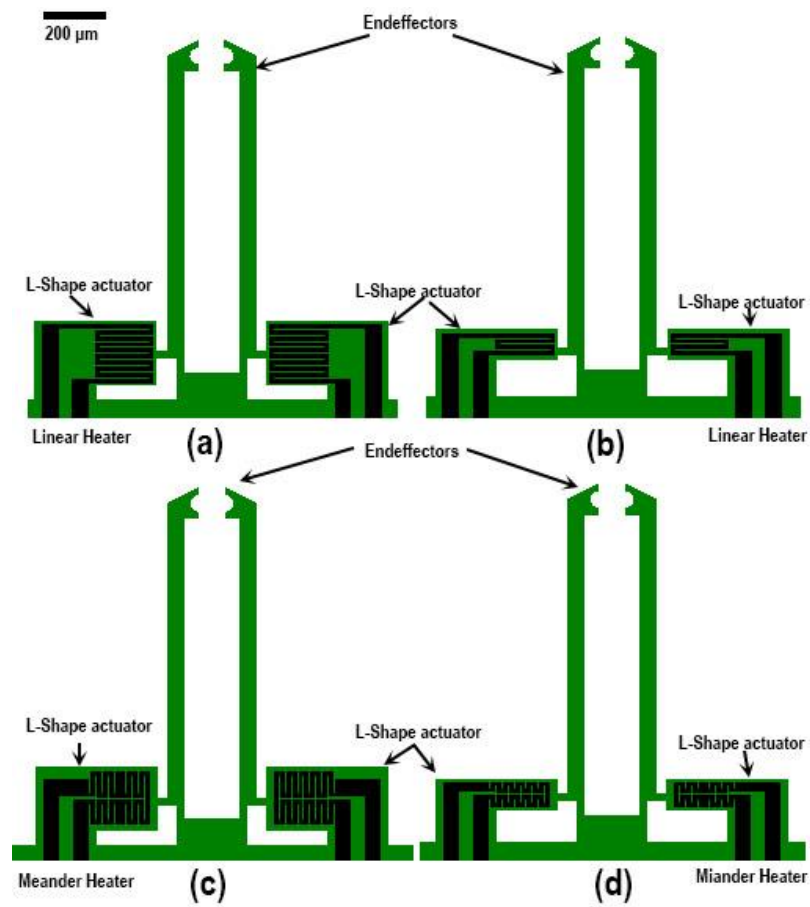


Fig. 3.8 Directly actuated microgripper based on the L-shape actuator. The heaters' conductors were designed in different shapes linear (a & b) and meander (c & d). Also, the actuator is in different width (a & c) 210  $\mu\text{m}$  and (b & d) 100  $\mu\text{m}$ .

### 3.3.2 Design 2: Directly Actuated Microgripper

The consideration of this design is to have an initial opening of 100  $\mu\text{m}$  and it should be fully closed at 200° C. This was designed with an amplification ratio of about 20. The hinges were designed to be 50  $\mu\text{m}$  of length and 20  $\mu\text{m}$  of width. The L-shaped actuator was used in this design to actuate the microgripper, as shown in

Fig. 3.8. The length of the actuator in this design is 200  $\mu\text{m}$  with two different widths of 100  $\mu\text{m}$  and 210  $\mu\text{m}$ , and thickness of 20  $\mu\text{m}$ . A conductive layer of chromium/gold/chromium (7/200/7 nm) configuration was used. Similar to the previous design, the heater conductor is 10  $\mu\text{m}$  wide and it is connected to the pads by 100  $\mu\text{m}$  wide conductors. The shape of the actuator is designed with two different layouts to find the most efficient shape.

The arm is connected to the base and the actuator by hinges and their lengths are 50  $\mu\text{m}$  and 40  $\mu\text{m}$  respectively, and the width is 20  $\mu\text{m}$ . The arm is about 1.1 mm in length and 50  $\mu\text{m}$  in width. Two thicknesses (10  $\mu\text{m}$  and 20  $\mu\text{m}$ ) are used for the arms and hinges in this design to study the stiffness effect on the microgripper's behavior. This was also for study of the effect of the actuator thickness on the gripper performance. Table 3-1 shows the dimensions of eight different designs.

*Table 3-1 List of direct actuated (one mode) microgrippers*

Design	Actuator Thickness ( $\mu\text{m}$ )	Actuator Length ( $\mu\text{m}$ )	End-effectors Thickness ( $\mu\text{m}$ )	Heater Shape
L100D	20	200	20	Linear
L210D	20	200	20	Linear
L100S	20	200	10	Linear
L210S	20	200	10	Linear
M100D	20	200	20	Meander
M210D	20	200	20	Meander
M100S	20	200	10	Meander
M210S	20	200	10	Meander

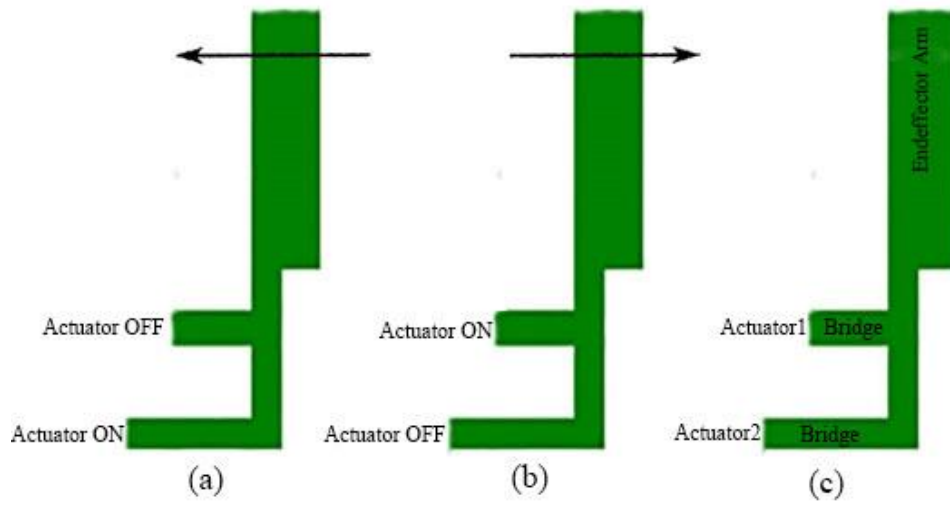
### 3.4 Dual Mode Microgripper

To have a more flexible microgripper with large displacement and small actuator size, a dual mode microgripper was designed. The main advantage is in using two short actuators to drive the microgrippers in two directions instead of using one long actuator to drive the microgripper in only one direction. Because the longer the actuator is the less stiffness is. Therefore, the actuator can withstand a higher reaction force, i.e. it can apply a higher force to deflect the end-effector.

#### 3.4.1 Design Concept

This new concept of using two L-Shape actuators to drive the end-effectors is shown in Fig. 3.9. The end-effector arm has two hinges which each of them is connected to an

actuator to drive the arm mechanically. Each of the actuators can drive the arm in one direction. In each operating mode, one of the hinges is fixed and the other is operated by the actuator. This results in a beam deflection in the desired direction. For example, in Fig. 3.9 (a), if actuator 2 is powered and actuator 1 is off then the end-effector is deflected to the left and vice versa as shown in Fig. 3.9 (b). The lowest part of the arm is designed to be narrower than the upper part in order to decrease the deflection stress and consequently, increasing the lifetime of the actuator. The width of the connection bridge is 20  $\mu\text{m}$  while the length is 60  $\mu\text{m}$  for actuator 1 and 100  $\mu\text{m}$  for actuator 2.



*Fig. 3.9 Bi-directional actuator principal (a) actuated to deflect the endeffector to left, (b) deflection to right, (c) labelled actuator structure Design 3: Dual Mode Microgripper*

Two bi-directional actuators based on the proposed concept in section 3.5.1 were combined to design microgrippers. The conductor of the heater parts is designed in two different shapes: straight line and meander line, as shown in Fig. 3.10. The dimensions of the two microgrippers are the same except for the initial opening which is 60  $\mu\text{m}$  or 250  $\mu\text{m}$  for the design with line shape heater, and 90  $\mu\text{m}$  for the design with meander shape heater. The shape of the end-effectors is different in both designs in order to use them for different applications. The conductive film is 10  $\mu\text{m}$  wide in the actuator area (the heater parts) and 50  $\mu\text{m}$  wide in the other parts to concentrate the dissipated power in the heater area. The thickness of the conductive film is 100 nm. The length of the arms is about 1.1 mm and the width is 50  $\mu\text{m}$  except the hinges which are 20  $\mu\text{m}$  wide. Each actuator is 300  $\mu\text{m}$  wide and the length is 400  $\mu\text{m}$  for H1 (actuator 1) and 360  $\mu\text{m}$  for H2 (actuator 2). The SU-8 layer thickness is 20  $\mu\text{m}$ . These two different designs were used to study which heater shape performs better.

Both actuators in each side are fixed to a rectangle shape anchor and this has an advantage of isolating the actuator from the base anchor. Consequently, the temperature is more evenly distributed in the actuators and the difference between the maximum and the minimum temperature is reduced. The ratio of the arm length to the actuated part is about 11 to 1, i.e. the amplification ratio is about 11. The expansion is about  $3.3\text{ }\mu\text{m}$  and  $3.7\text{ }\mu\text{m}$  in actuator 1 and actuator 2 respectively at  $200\text{ }^{\circ}\text{C}$ . If the deflection in the hinges is assumed not to affect the displacement at the end-effectors, the displacement will be about  $36\text{ }\mu\text{m}$  and  $40\text{ }\mu\text{m}$  for each arm in each direction.

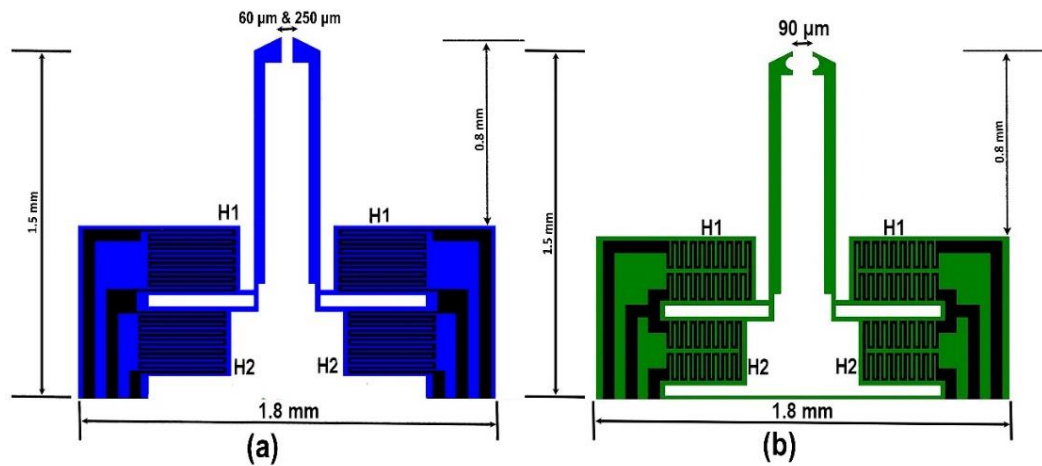


Fig. 3.10 Two different designs of dual-mode microgripper based on bi-directional actuator (a) design 1 with line shaped micro-actuator (b) design 2 with meander shaped micro-actuator

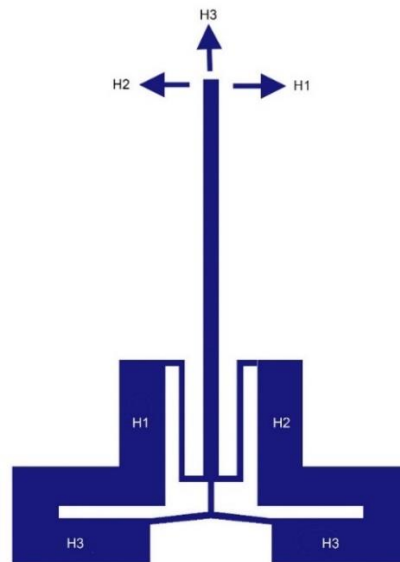


Fig. 3.11 Tri-directional actuator design, the arrows show the effect of each actuator on the movement of the arm.

### 3.5 Tri-Directional Actuator Design

#### 3.5.1 Design Principle

Fig. 3.11 presents a novel tri-directional actuator design. It consists of four actuators to achieve three directions of displacement by operating them in proper combinations. This actuator can be used in many applications requiring multi-directional displacements such as a multi-direction microswitch. The displacement direction of the end-effector depends on which heater is powered, for example when heater h1 or h2 is operated, the arm deflects horizontally, while when the heater h3 is ON, the arm deflects vertically. The effects of these heaters on actuation are indicated by the arrows. The total length of this actuator is 1.6 mm. The actuator length and the arm length are directly proportional to the horizontal displacement as shown in equation (3-5), however the length of the arm does not affect the vertical displacement.

An optimisation to improve the design is to use only heater h3 and remove both heaters h1 and h2. In this method, each heater is driven individually. If the right heater is powered, the arm is deflected to the right, while the left actuator drives the arm to the left. If both actuators are powered with same current, the arm is expanded vertically.

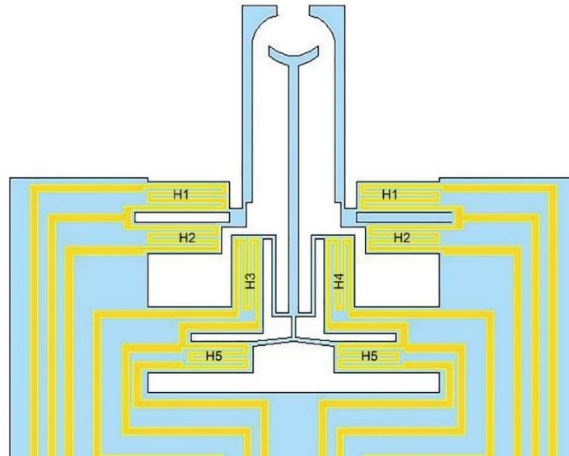
#### 3.5.2 Design 4: Three-Armed Electrothermal Microgripper

By combining a bi-directional actuator and a tri-directional actuator, a novel 3 arm microgripper with multiple degrees of control is proposed, as shown in Fig. 3.12. The dimensions of this microgripper are given in Table 3-2. This microgripper can be used to manipulate a wide variety of micro-objects. A larger object can be manipulated using the space between the three arms such as a sphere larger than 150  $\mu\text{m}$ . The operating characteristics and control of the gripping tips can be determined by the analysis of the operating modes of the individual arms. Powering heater h1 drives the end-effectors in closing mode while heater h2 drives the two outer arms to increase the opening. The third (middle) arm has three directions of deflection, as explained in the previous section. Fig. 3.13 shows this design of the optimised tri-directional actuator which is based on two heaters instead of four.

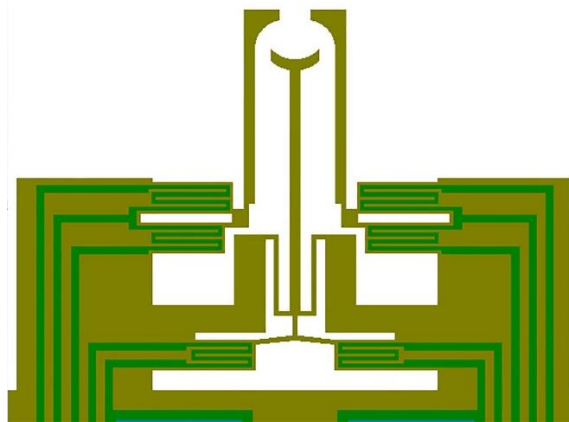
Table 3-2 Tri-Arm Microgripper

Part	Length ( $\mu\text{m}$ )	Width ( $\mu\text{m}$ )
Side arms	1080	50
Midle arm	1250	50

Heater (H1)	400	150
Heater (H2)	350	150
Heaters (H3, and H4)	350	150
Heater (H5)	300	150



*Fig. 3.12 Schematic layout of the three-armed microgripper showing the heaters and conductor lines (yellow) and the SU8 based structure (blue).*



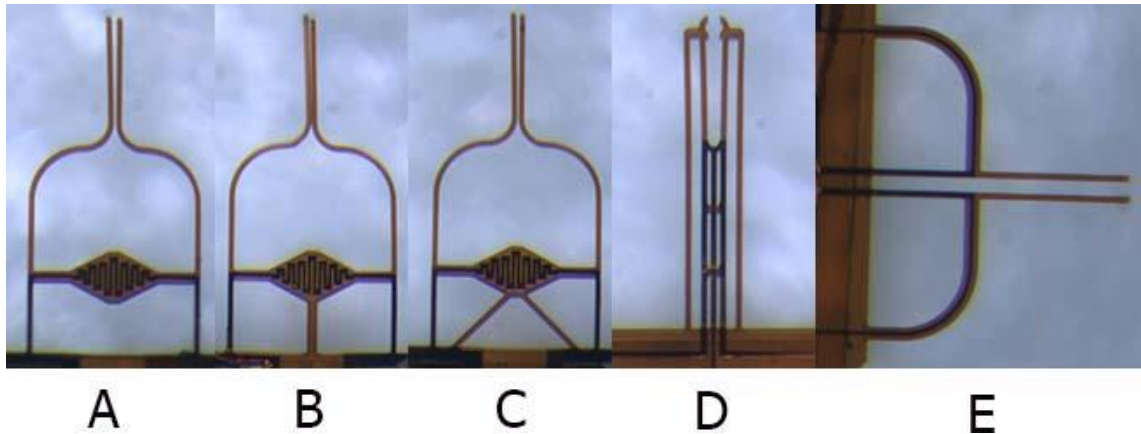
*Fig. 3.13 Layout of the optimised three-armed microgripper showing the absence of the heaters h3 and h4.*

### 3.6 IMT Designs

Other designs were also used to study microgrippers in the thesis. Fig. 3.14 shows different electrothermally actuated microgrippers based on the U-Shape actuator principle (hot/cold arms). These microgrippers were designed by IMT, except D which was designed by Politecnico di Torino in Italy, and all manufactured at IMT. These microgrippers were all fabricated using the SU-8 polymer with embedded chromium/gold/chromium heaters. Designs A-D were in two different sizes. The first

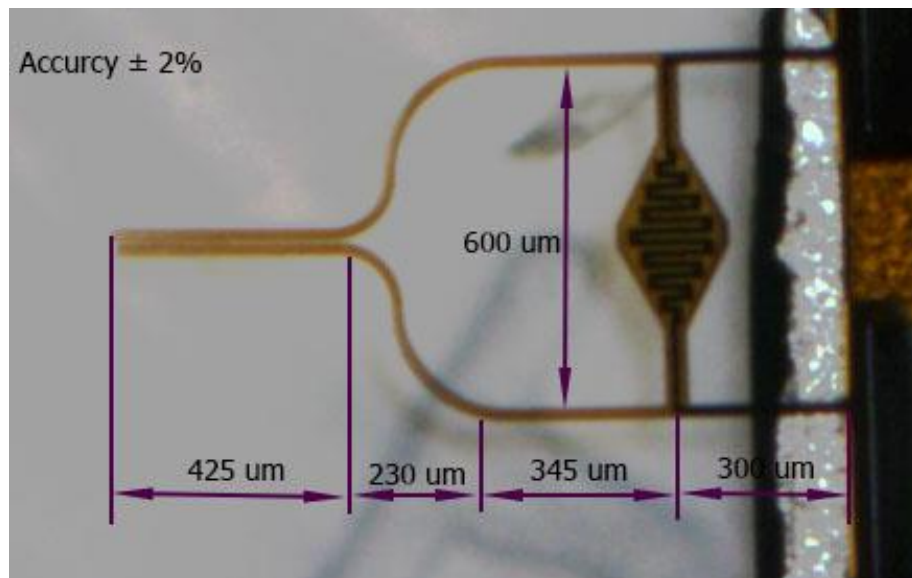


three designs (A–C) and E were based on normally closed type while design D is for normally open operation so the microgripper closes when power is applied.

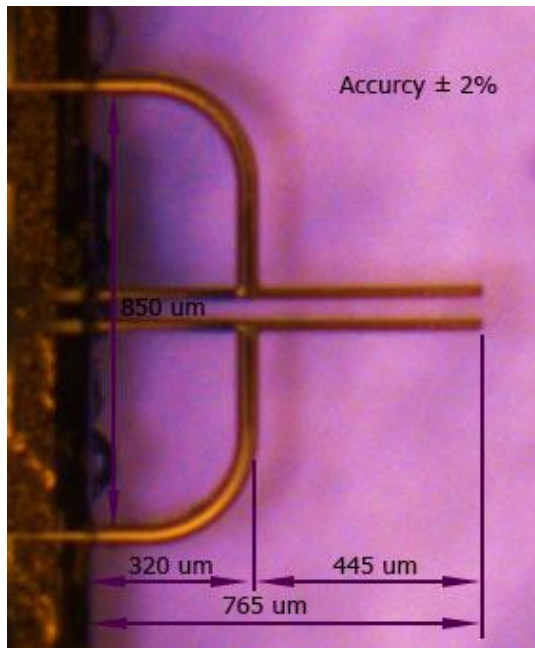


*Fig. 3.14 Microgrippers by IMT design group 1. All these microgrippers were designed and fabricated by IMT except Design E which was designed in Italy and fabricated by IMT. The images are not to scale and the microgripper designs are in different sizes. Designs A and D were designed in two different sizes.*

Fig. 3.15 shows the dimensions of the designs (A – C) in the larger group. The actuator dimensions are about 200  $\mu\text{m}$  in width and 325  $\mu\text{m}$  in length. The dimensions of the whole device are about 1300  $\mu\text{m}$  in length, 640  $\mu\text{m}$  in width, and 20  $\mu\text{m}$  in thickness. All these measurements were taken on a Zygo white light interferometer system. The initial opening was approximately 17  $\mu\text{m}$ . The ratio of the arm length to the actuator length at the effect point (the displacement amplification) is 4.3.

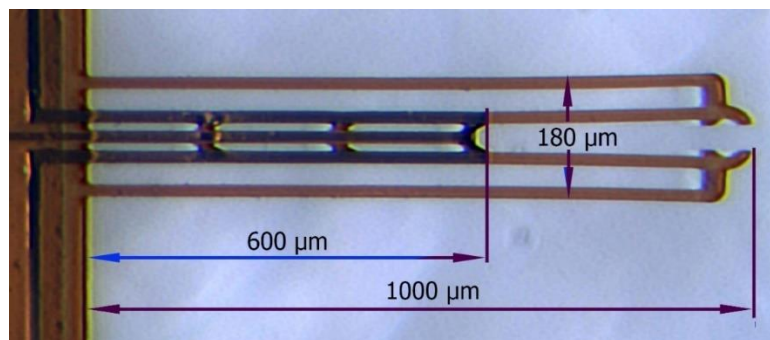


*Fig. 3.15 Optical microscope image showing the dimensions of design (A - C) the large groups which was measured using the Zygo metrology system*



*Fig. 3.16 Optical microscope image showing the dimensions of design (D) the large groups which was measured using a Zygo metrology system.*

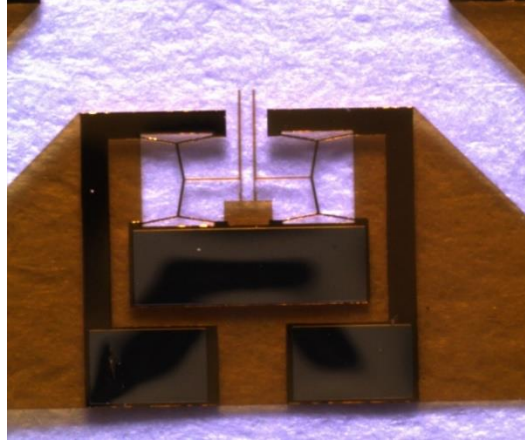
Fig. 3.16 shows the dimension of the larger design (D). It is 765 μm for the total length, 850 μm for the total width, 20 μm in thickness, around 40 μm of initial gap, 320 μm for the cold arm length, 445 μm for the extended end-effectors, about 44 μm for the hot arm width, and about 14 μm for the cold arm width. The dimensions of the small design are 380 μm for the total length, 460 μm for the total width, 20 μm in thickness, around 20 μm for the initial gap, 160 μm for the cold arm length, and 220 μm for the extended end-effectors. All these dimensions were taken on a Zygo system.



*Fig. 3.17 Optical microscope image showing the dimensions of design (E) and the measurement was taken using Zygo metrology system*

The microgripper design (E) was proposed to be used for cell manipulation. The biocompatibility property of the SU-8 was very important in terms of its use as a structure material. It is actuated using the concept of hot/cold arms, and a Cr/Au/Cr layer was used for the heaters for the hot arms to generate the required displacement. As it was proposed, the temperature did not rise on the end-effectors to a level which could damage the cells. This design and its dimensions are shown in Fig. 3.17. The length of the whole

microgripper is 1 mm and its width is 180  $\mu\text{m}$ . All the arms are 20  $\mu\text{m}$  in width and the device thickness is about 20  $\mu\text{m}$ . The distance between the cold arm and the hot arm is 30  $\mu\text{m}$  and the actuator part is 600  $\mu\text{m}$ . The V-shaped microgripper is shown in Fig. 3.18. It was designed using 100 nm thick gold film as the conductor layer sandwiched between two 10  $\mu\text{m}$  thick SU-8 layers.



*Fig. 3.18 Microgripper based on V-shaped actuator*

### **3.7 Fabrication**

The fabrication process of all microgrippers required a 3 mask based approach. The lift-off method was used for heater fabrication and an Omnicoat layer was used as the sacrificial layer to release the microgripper structure from the substrate. First a thin layer of Omnicoat was deposited on a silicon wafer by spin coating at 3000 rpm and then baked at 200° C on a hotplate for 1 minute. Then, the SU-8 polymer was deposited on the wafer at 4000 rpm in order to obtain a thickness of about 10  $\mu\text{m}$ . The wafer was soft-baked for 1 minute at 65°C and 2 minutes at 95°C. Then the SU8 layer was exposed to UV light using the first mask. After that, the wafer was post-baked at 65°C for 1 min and 95°C for 3 mins. Then it was processed using a developer and thermally treated by hard-baking at 185°C for 15 minutes in order to complete cross-linking of the SU-8 polymer.

A thick AZ positive photoresist was spun to coat the wafer at 3000 rpm. Then, a thermal treatment at 90° C was applied. The wafer was exposed to UV light using the second mask to pattern the photoresist layer. After development of the photoresist, a metal layer of Cr/Au/Cr films of 10/300/10 nm , 7/200/7 nm or Au film of 100 nm, was deposited by e-beam evaporation, depending on the design configuration for the heater and connection lines. The lift-off process was applied by removing the AZ photoresist pattern in acetone and hence the metal layer on the surface of the photoresist leaving behind the heater structure on the SU8 structure.

The second SU-8 layer was fabricated using the same steps as for the first layer. The final thermal process of the polymer in this step was hard-baking at 195°C for 30 minutes to cross-link the SU-8 polymer. To release the microgripper structures, the Omnicoat layer was etched using a piranha solution and deionized water for rinsing. Fig. 3.19 shows a schematic cross-section of the design shown in Fig. 4.6(a) which illustrates the microgripper's layers on the wafer before the releasing processes while Fig. 3.20 shows the fabrication process flow. Fig. 3.19 shows some of the fabricated microgrippers.

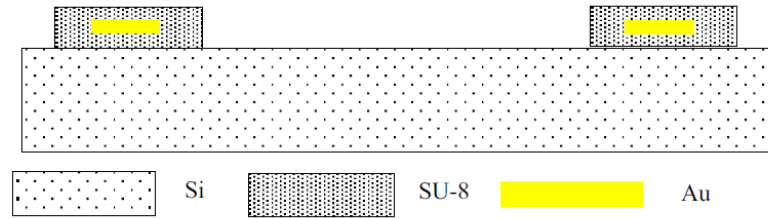


Fig. 3.19 Schematic of the cross-section of the microgripper's arms showing the SU-8 and the metallic layers (not to scale)

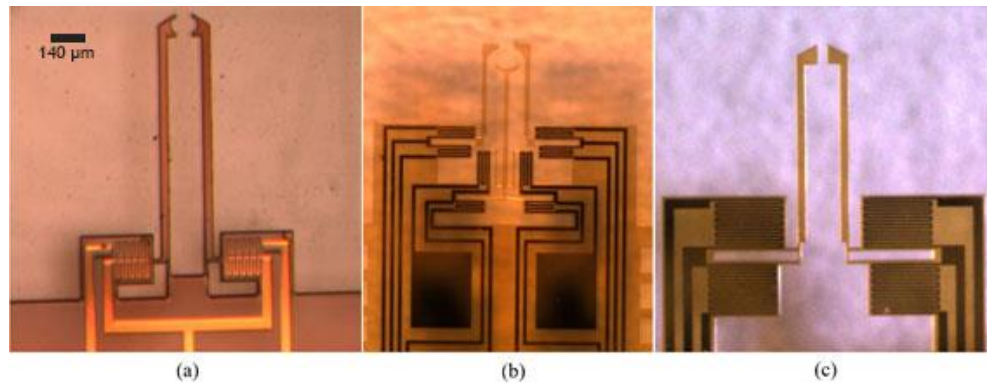


Fig. 3.20 Fabricated Heriot-Watt designs (a) Directly actuated microgripper with heart configuration of 7nm / 200 nm / 7nm (Cr/Au/Cr) (b) Multi-degree of freedom microgripper with same heater configurations (c) Bi-directional microgripper with heart configuration of 100 nm of gold.

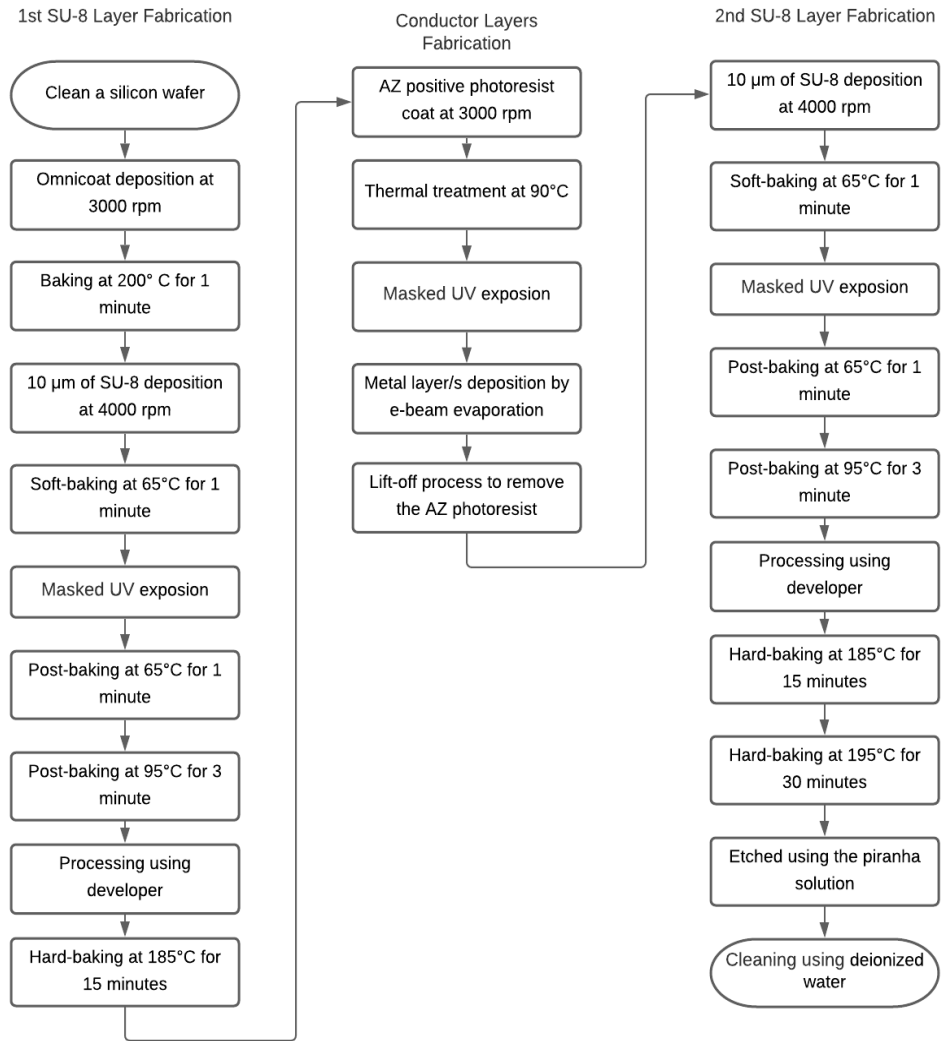


Fig. 3.21 Fabrication processes chart

### 3.8 Modeling and Simulation

The COMSOL Multiphysics software tool was used to evaluate and optimise the actuators and the microgripper designs. Since the microgrippers are symmetrical, only one side was modeled to minimise the simulation time. The surrounding environment was considered in the module as a block of air to increase the accuracy of the results. The built-in geometry was used to build the modules (designs). The structure was divided into two layers and the heater was situated in between them. The SU-8 structure was created using 3D blocks while the heater was implemented using 2D plan geometry.

#### 3.8.1 Simulation Method

The modules in the COMSOL Multiphysics software tool used were Solid Mechanics, Heat Transfer in Solids, Electric Currents (Shell), and Membrane. The

Electric Currents software module simulates the resistance of the heater and the effect on the current. The dissipated power in the actuator is converted into heat energy based on the Joule heating effect. This energy was transferred to the Heat Transfer in Solids module using the Multiphysics model (Boundary Electromagnetic Heat Source). Then, the distributed temperature was transferred to the Solid Mechanics module and Electric Currents module using the Temperature Coupling module. This is because the heat generates an expansion and affects the resistivity of the heater. Finally, a Multiphysics module (Thermal Expansion) was used to interface the heating and the expansion.

The simulation did not ignore the effect of the heater layer on the expansion. It was modeled using Membrane Physics and the expansion was added to it. The electric current simulation was applied to this part only and it was configured as a source of the heat in the microgripper. The conductivity of the gold thin film layer ( $\sigma$ ) was set to be temperature ( $T$ ) dependent using equation (3-7). The chosen values of the temperature coefficient of resistance ( $\alpha$ ) and the reference resistivity ( $\rho_0$ ) were based on experimental results for the same gold and chromium / gold / chromium film thicknesses and the fabrication processes. These values were calculated to the reference temperature ( $T_{ref}$ ) of 20°C. Chapter 4 will provide more information on this.

$$\sigma(T) = \frac{1}{\rho_0(1 + \alpha(T - T_{ref}))} \quad 3-7$$

The solid mechanics study was only applied to the SU-8 structures because the air has a negligible effect on the beam deflection produced, while the electric current simulation is limited to the metal heaters. A Fixed Constraint was applied to the fixed parts of the actuators and microgrippers. The Heat Transfer in Solids function was applied on all domains. The air block surfaces were assumed to lose heat, hence a Heat Flux was applied on the outer surfaces by choosing convective heat flux with heat transfer coefficient of 10 W/(m<sup>2</sup>.K). The glass was assumed to be fixed from the bottom surface and its temperature was fixed to 20 °C. However, the effect of the glass was not considered since the function parts of the grippers are suspended in air for operation, so it was removed from the other simulations. The design model was mashed using the COMSOL's physics-controlled configuration with normal element sizes for the actuator structures while the air was set as coarser size. A stationary study was selected with parametric sweep for the applied current. Variable steps and ranges were applied depending on the actuator design under study.

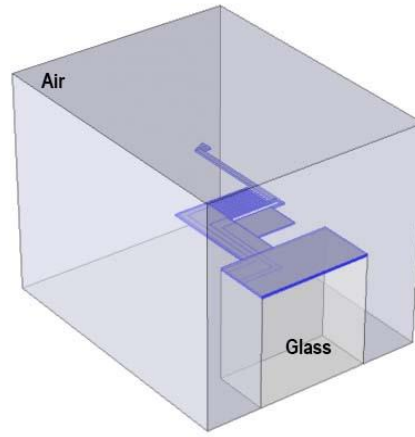


Fig. 3.22 Models of the COMSOL Multiphysics simulation to study the dual-mode microgripper design.

Table 3-3 Properties of the SU-8 layer

Parameters	Value	Unit
Thermal conductivity	0.3	W/(m·K)
Coefficient of thermal expansion	$52 \times 10^{-6}$	$1/^{\circ}\text{C}$
Density	1.2	$\text{g}/\text{cm}^3$
Heat capacity at constant pressure	$1.2 \times 10^3$	$\text{J}/(\text{kg} \cdot \text{K})$
Young's modulus	Variable see Fig. 3.14	
Poisson's ratio		

Table 3-4 Properties of the metal layer

Parameter	Value	Unit
Gold Thermal conductivity	318	W/(m·K)
Density	19.3	$\text{g}/\text{cm}^3$
Heat capacity at constant pressure	129	$\text{J}/(\text{kg} \cdot \text{K})$
TCR	0.00145	$1/^{\circ}\text{C}$
Resistivity	68	$\text{n}\Omega \cdot \text{m}$

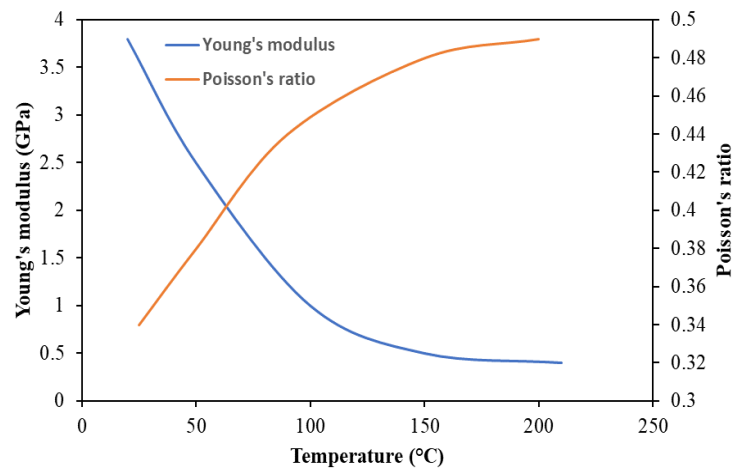


Fig. 3.23 Young's modulus and Poisson's ratio for SU-8 as a function of temperature change, generated by COMSOL using the interpolation function and five data points. The properties of the SU-8 and gold are shown in Table 3-3 and Table 3-4 respectively. The Young's modulus and Poisson's ratio of the SU-8 were assumed to be temperature dependent, as shown in Fig. 3.23, using data from the literature [130], [131] and [132]. The graphs were produced in the COMSOL model using the built-in interpolation function and 5 data points for each curve. Results and Discussion



### 3.8.2 Design 1- Indirectly Actuated Microgripper

In order to understand how this microgripper design behaves, the electro-thermo-mechanical simulation is based on the modeling method described in section 3.7. Fig. 3.24 shows the deflection and the temperature distribution on the design shown in Fig. 3.4 when a 12 mA of current was applied. At this low current, a displacement of about 90  $\mu\text{m}$  was achieved on each arm. The average temperature in the actuator was about 210  $^{\circ}\text{C}$ .

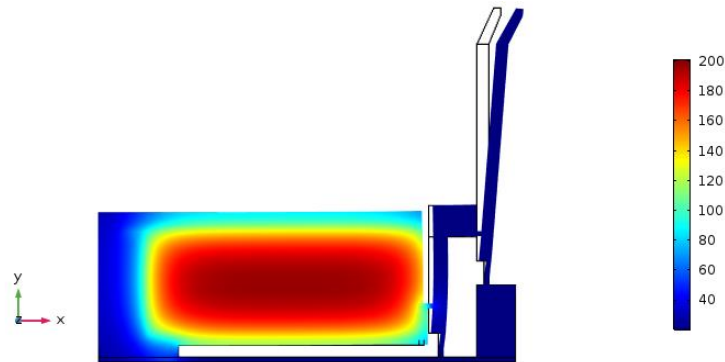


Fig. 3.24 Temperature distribution and arm deflection of the interfaced microgripper using COMSOL multiphysics simulation model

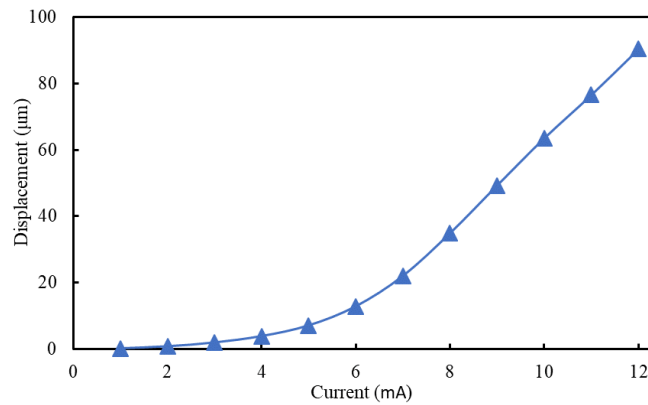


Fig. 3.25 Displacement as a function of current result from the COMSOL modulation of the interfaced microgripper

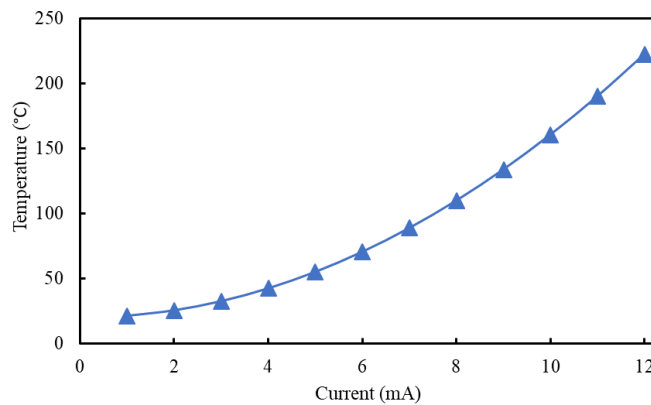
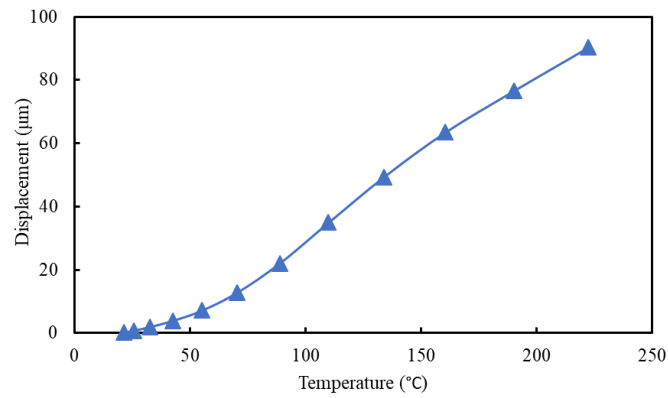


Fig. 3.26 Temperature as a function of current result from the COMSOL modulation of the interfaced microgripper





*Fig. 3.27 Displacement as a function of Temperature result from the COMSOL modulation of the interfaced microgripper*

Fig. 3.25 to Fig. 3.27 show the simulation results of the indirectly actuated microgripper. The current and the average temperature is clearly a second order relationship because the temperature produced from Joule heating is proportional to the square of the applied current. The relationship between the displacement and the applied current and the average actuator temperature is more complicated. The deflection is affected by the mechanical properties in addition to the expansion produced because of their temperature dependence. These properties are themselves affected by the temperature too. The microgripper was designed to have 60  $\mu\text{m}$  of displacement on each arm at the average temperature of 100° C.

Fig. 3.28 and Fig. 3.29 show the effect of the Young's Modulus on the displacement as a function of the heater average temperature and the applied current respectively. The results show the comparison between fixed values of Young Modulus and the temperature dependent material property. These results can be compared to the experiments displacements test to find out what is the right Young's modulus. This is because it reported different values such as 4.95 GPa [133], 4.02 GPa [128] 3.48 GPa for hard backed and 2.92 GPa for non-hard backed [134].

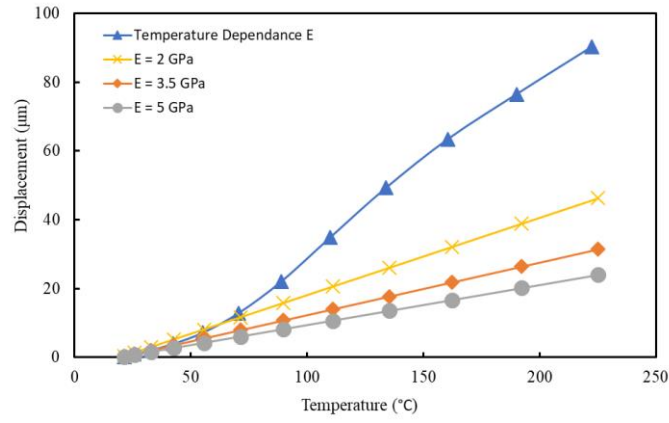


Fig. 3.28 Displacement as a function of temperature compression between different fixed values of Young modules with the variable one which this study was based on

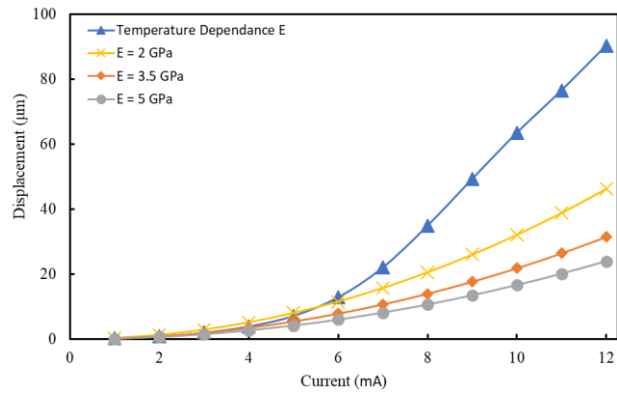


Fig. 3.29 Displacement as a function of current compression between different fixed values of Young modules with the variable one which this study was based on

### 3.8.3 Design 2- Direct Actuated Microgripper

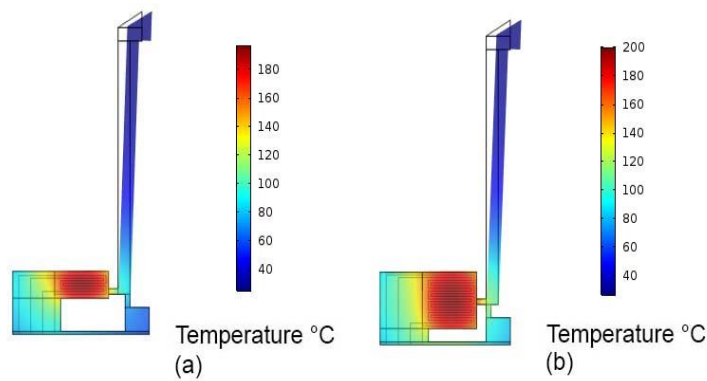
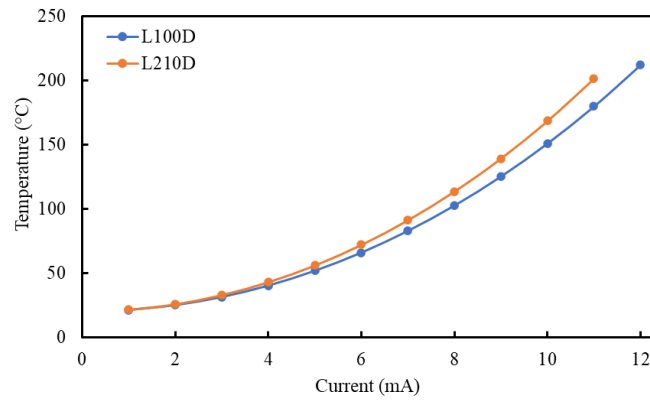


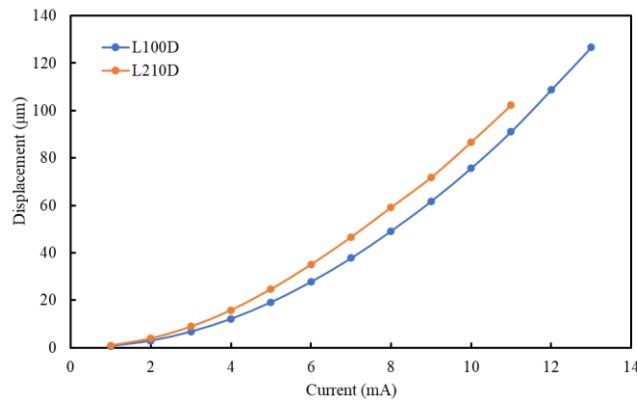
Fig. 3.30 Modelling result showing the temperature distribution and deflection of the direct actuated microgripper (a) with actuator width of 90 μm and current of 11 mA (b) with actuator width of 200 μm and current of 10 mA

The previous method was used to study the direct actuated microgripper. Fig. 3.30 shows the deflection of one end-effector and the temperature distribution of both designs. As expected, the temperature was concentrated in the actuator part exactly similar to design 1. However, some heat was passed into the arm by convection. This effect was limited, and the end-effectors temperature was raised by 5 °C only.

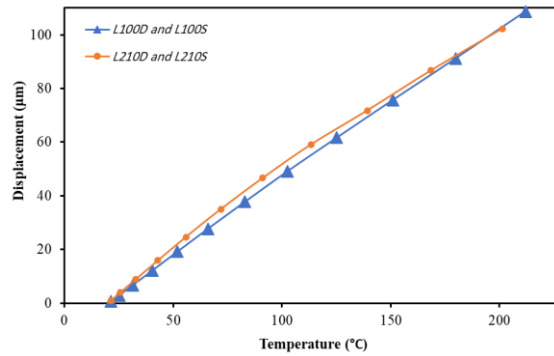


*Fig. 3.31 Temperature as a function of current result from the COMSOL modulation of the direct actuated microgripper with two different actuator widths*

Both Fig. 3.31 and Fig. 3.32 show the temperature and the displacement of both end-effectors as a function of the supplied current to each actuator, i.e. the heaters are connected in series. There was not a noticeable difference in the simulation results between the two designs, L210D and L100D. In addition, the simulation was carried out for a 10  $\mu\text{m}$  arm thickness design, L210S and L100S, but there was not any difference in the results as compared to design L210D and L100D respectively as shown in Fig. 3.33.



*Fig. 3.32 Displacement as a function of current results from the COMSOL modulation of the direct actuated microgripper with two different actuator widths*



*Fig. 3.33 Displacement as a function of the average heater temperature from the COMSOL modulation of the direct actuated microgripper with two different actuator widths*

### 3.8.4 Design 3 - Dual-Mode Microgripper

The same simulation method was used to study this design. The gold layer thickness was set to be 100 nm and the TCR value was set to be  $0.003/^{\circ}\text{C}$ . The study was implemented on the actuator with the linear heater shape. Fig. 3.34 shows the distribution of the temperature in the actuator area when a current of 10 mA was applied to each heater. The temperature rise causes an expansion which is translated into displacement of the end-effectors. When heater 1 is powered, the arm is deflected to the right side (working in closing mode), and when heater 2 is powered the arm is deflected toward the left side (working in opening mode), as shown in Fig. 3.34 (a) and (b) respectively. The temperature distribution is mostly smooth in the actuators and it is concentrated in the actuator part in both modes. Also, the temperature on the end-effectors is low - the same as the ambient temperature. When a 10 mA of current was applied in the closing mode, the maximum temperature in heater 1 was  $191^{\circ}\text{C}$  while the minimum was  $92^{\circ}\text{C}$ . In the opening mode, the maximum temperature was  $185^{\circ}\text{C}$  and the minimum was  $83^{\circ}\text{C}$  at the same applied current.

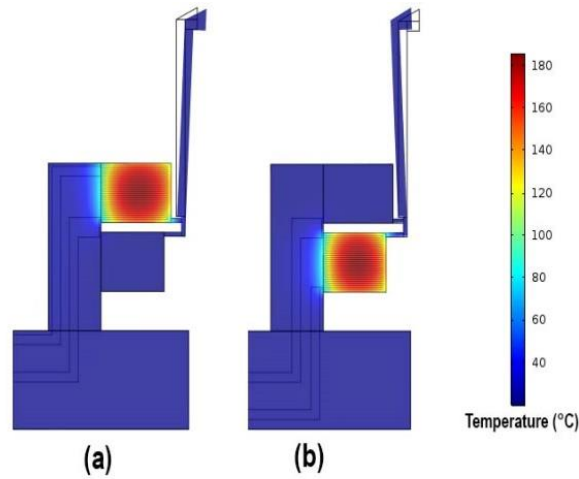


Fig. 3.34 Temperature distribution and arm deflection caused by applying a current of 10 mA on (a) heater 1 (b) heater 2

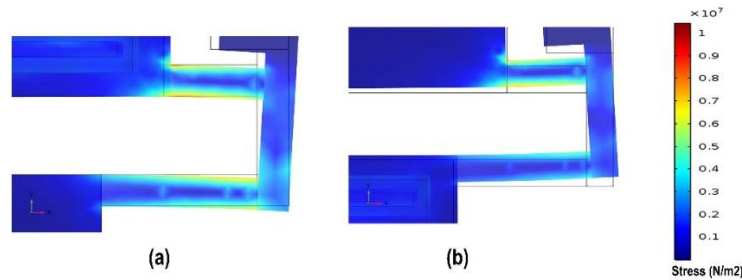


Fig. 3.35 Stress in the hinges when 10 mA current was applied on (a) heater 1 (b) heater 2

Fig. 3.35 shows the stress distribution in the hinges in both modes and how they react to the actuator expansion. The maximum stress from COMSOL simulation was  $10 \text{ kN/m}^2$  and it is much lower than the maximum stress of SU-8 which is  $34 \text{ kN/m}^2$  [133]. Therefore, the hinges work properly and there is no risk of breaking.

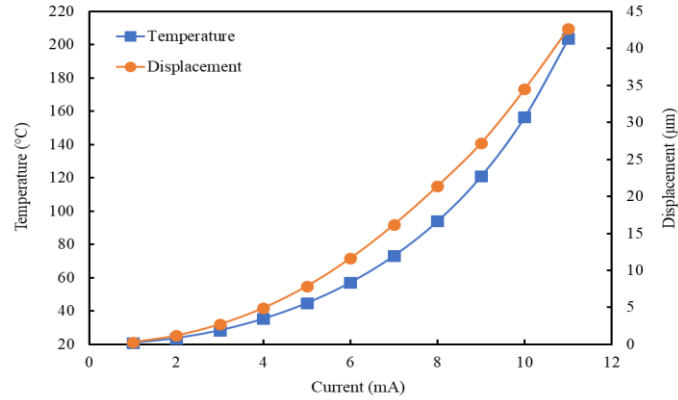


Fig. 3.36 Simulation results of one arm showing the displacement and temperture as a function to the applied current for heater 1 and in closing mode

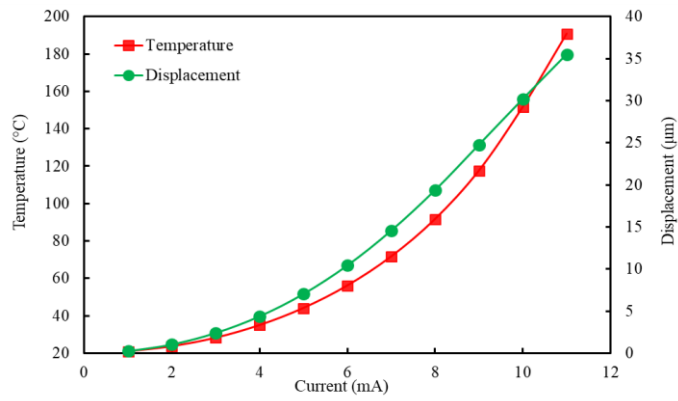


Fig. 3.37 Simulation results of one arm showing the displacement and temperture as a function of the applied current for heater 2 and in opening mode

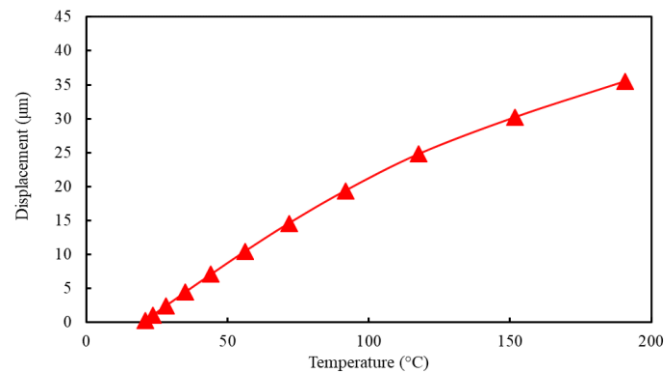


Fig. 3.38 Displacement of the end effector in opening mode as a function of heater 1 average temperature

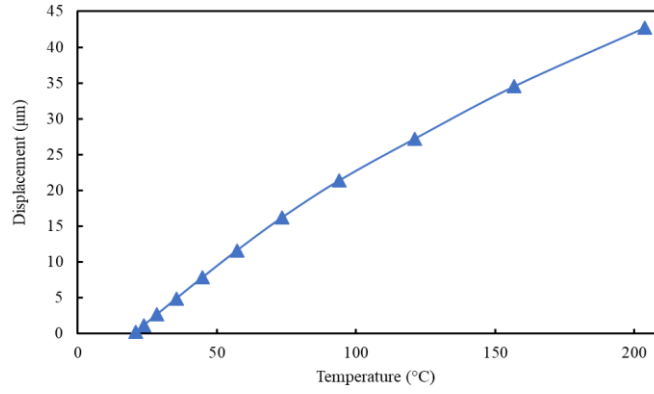


Fig. 3.39 Displacement of the end effector in closing mode as a function of heater 2 average temperature

The simulation result of the displacement of one arm of the microgripper was about 40  $\mu\text{m}$  in the closing mode when the average temperature of heater 1 was about 200°C. It was about 36  $\mu\text{m}$  in the opening mode at the same temperature in heater 2. The temperature and the displacement as a function of the current are shown in Fig. 3.36 for the closing mode operation and Fig. 3.37 for the opening mode. Fig. 3.38 and Fig. 3.39 show the displacement as a function of temperature for the opening mode and the closing mode respectively.

The displacement as a function of the actuator's average temperature in each mode shows that the displacement increases faster when the actuator's average temperature below 125°C. The slope decreases a little bit because of the drop in the Young's modules value. In other words, the material pliability increases, and the reaction force become more than the critical force. This causes a smaller deflection in the actuator at higher temperature. This effect is shown in Fig. 3.40. The results of displacement as a function of average temperature show that the desired performance can be achieved.

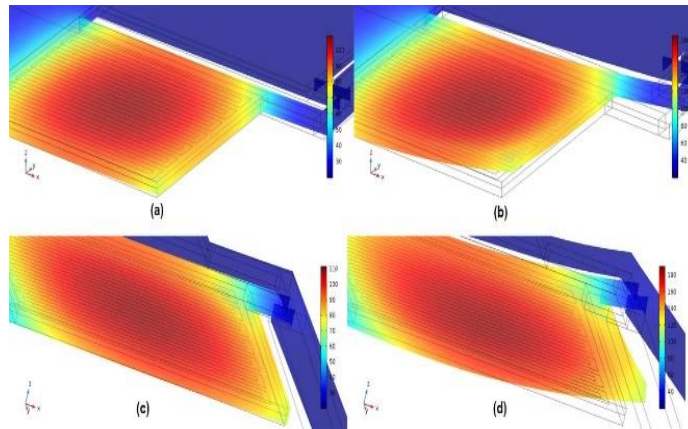


Fig. 3.40 Effect of an increase in the actuator temperature on the actuator's pliability causing deformation. The opening mode and heater (2)'s average temperature is about (a) 110 °C (b) 190 °C and the closing mode when heater (1)'s average temperature is about (c) 100 °C (d) 180 °C. The deflection was scaled 1:7 to make it easy for observation.

### 3.8.5 Tri-Directional Actuator

Fig. 3.41 shows the simulation results for the tri-directional actuator. In Fig. 3.31 (a) and (b), applying a voltage of 1.2 V on heater h2 increased the temperature to about 200°C. This caused a deflection on the arm tip of about 12  $\mu\text{m}$  to the left side. It is the same as shown in Fig. 3.31 (c) and (d) by applying the same voltage to heater h1 but with 12  $\mu\text{m}$  of displacement to the opposite (right) side. Heaters h3 and h4 are designed to work simultaneously. Applying 1 V of voltage to each of them, the average temperature in these actuators is raised to about 200 °C, and a deflection of about 12  $\mu\text{m}$  of the beam is obtained in the vertical direction, as shown in Fig. 3.31 (e) and (f). Fig. 3.42 and Fig. 3.43 show the average temperature in each actuator and the displacement as a function of the applied voltage respectively.

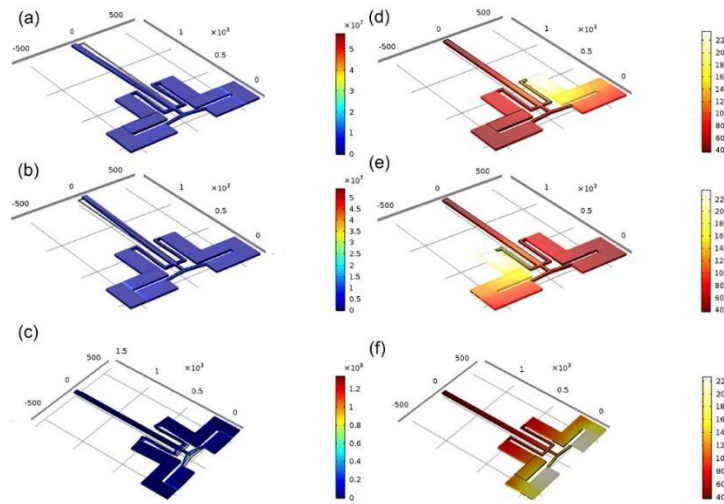


Fig. 3.41 Simulation results of the tri-directional actuator. (a) and (d) deformation and temperature distribution when heater h4 is operated, (b) and (e) deformation and temperature distribution when heater h3 is operated, (c) and (f) deformation and temperature distribution when heaters h5 and h6 are used.

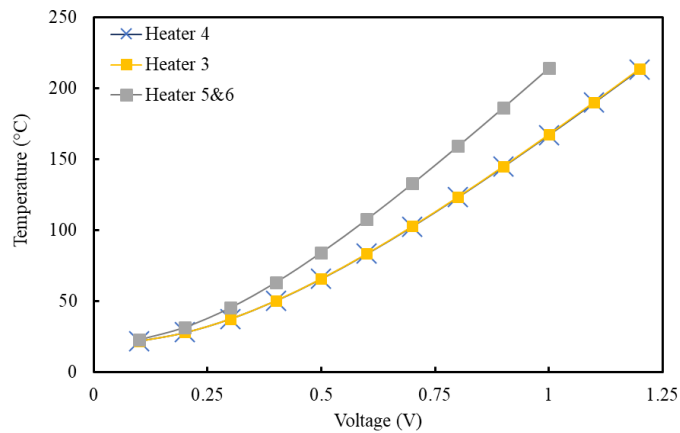


Fig. 3.42 Simulation results of the tri-directional actuator showing the average temperature in each actuator when they are in operation as a function of applied voltage

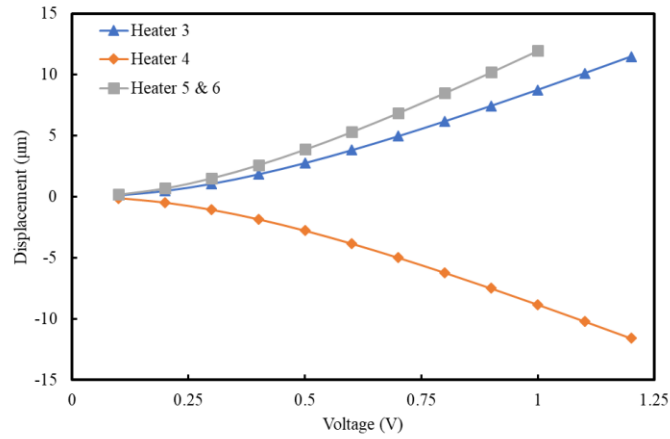


Fig. 3.43 Simulation results of the tri-directional actuator showing the displacement of the beam tip when each heater is operated as a function of applied voltage

### 3.9 Summary

Actuators used to drive microgripper operation produce a source of mechanical force to drive the end-effectors. As discussed at the beginning of this chapter there are two forces which should be taken into account when a microgripper is designed. The force that would cause actuator deformation should be much higher than the deflection force for operation, otherwise the actuator will suffer from deformation and the microgripper will fail. The conventional U-shaped microgripper design use both arms to carry current to drive the heaters. Therefore, there is temperature rise in both arms. Consequently, the displacement depends on the temperature difference between the two arms. So, the U-shape actuator requires to be operated at a higher temperature to increase the temperature difference in order to produce a useful displacement. Also, this will raise the end-effector temperature. Therefore, it will not be suitable for applications where the objects are sensitive to high temperature such as live cells.

The novel L-Shape actuator has no metal layer in the cold arms (end-effectors). Therefore, there is no heat source in the end-effectors, and the displacement depends on the temperature in the actuator only not on the temperature difference between the hot arms and cold arms as it is the case in the U-Shape actuator. Therefore, this actuator is able to produce the same displacements but at a lower operating temperature. In addition, the absence of heat source in the end-effectors allows microgrippers to be designed using these actuators temperature sensitive applications such as live cell and tissue manipulation.

This actuator was used to design four different microgrippers. Each of them has its own specifications. In Design 1 the arms were indirectly driven by the actuator. There



is a mechanical interface between each actuator and arm. This design was aimed to produce 120  $\mu\text{m}$  of displacement at 100° C but the simulation result showed less displacement. This is because the actuator was long and some of the expansion for actuation is lost due to the buckling effect. This results from the increase of the reaction force of the interface. These limitations were overcome in Design 2 in which each arm is directly driven by the actuator. Also, the actuators were designed to be shorter to increase the stiffness. The simulation results meet the design aim and the targeted performance.

To increase the displacements without increasing the actuator's length a novel dual-mode actuator based on the L-Shape actuator structure was designed. Two actuators were integrated to design a bi-directional actuator. Then, this actuator was used to design bi-directional (two-mode) microgrippers. The simulation results show that a displacement of more than 150  $\mu\text{m}$  can be achieved.

In addition, a novel tri-directional actuator was proposed in this chapter. This actuator was integrated with a bidirectional actuator to design the novel multi-directional three-arm microgripper.

This method was compared with the conventional method by using a function to model the temperature dependence of each relevant material property. The conventional method suffers from uncertainty about which coefficient values to use, therefore results are unreliable. In addition, this new method used to simulate these microgrippers by adding a block of air surrounding the designs. This addition shows a very closed results to the experiments results without changing any of the heat transfer coefficients.

The simulation results of displacement of one arm of Design 1 show about 90  $\mu\text{m}$  at an applied current of 12 mA and the corresponding temperature was about 220°C. In Design 2, the directly actuated microgripper shows about 120  $\mu\text{m}$  of displacement at the same current for both designs (the actuators with 90  $\mu\text{m}$  and 200  $\mu\text{m}$  of width). There was just a small difference between the two designs. The bi-directional microgripper showed about 40  $\mu\text{m}$  of displacement in both modes when a current of about 11 mA is applied on Heater 1 or 2. The displacement in these designs as a function of temperature is approximately linear at the low temperatures and then sublinear at higher temperatures.

## Chapter 4 TCR Measurements

The temperature dependence of resistance of the conductors is given in equation (4-1). Most conductors have a linear and positive temperature coefficient of resistance (TCR). This property was employed to measure the accurate temperature of heaters in all microgrippers. The value of TCR is essential for characterisation and operation of electrothermally actuated microgrippers.

$$R = R_o (1 + \alpha \Delta T) \quad 4-1$$

Where  $R$  is the resistance at any temperature,  $R_o$  is the resistance at 20° C,  $\alpha$  is the TCR, and  $\Delta T$  is the temperature difference from the 20° C.

This chapter presents the methods and results of TCR measurements for two groups of microgripper devices. The first group was designed and fabricated by IMT in Romania, and the other group was designed and presented in this thesis as discussed in Chapter 3. Also, different measurement methods of TCR of different configurations of metal layers were carried out in order to obtain accurate results of the TCR values. The materials used to fabricate the conductor layer were gold and chromium. The TCR values of the bulk materials are 0.0033 °C<sup>-1</sup> for the gold (Au) and 0.0000059 °C<sup>-1</sup> for chromium (Cr).

### 4.1 Temperature Coefficient of Resistance (TCR) Measurement

The most important factors to know about any microgrippers are the relationships between the applied power, displacement, and the temperature in the heaters. More results will be presented in the proceeding chapters. There are several methods to measure the temperature such as thermal couple, temperature sensors and IR thermal cameras. The first two methods are not applicable because of the area size of the heaters. There was no IR camera fitted with a microscope in the research facility. As a result, the only remaining method is to measure the temperature indirectly by measuring its effect on the resistance of the heaters. The temperature coefficient of resistance (TCR) is the factor that determines the relationship between the resistance (or resistivity) value and its temperature, as shown in equation (4-1).

#### 4.1.1 TCR Measurement Methods

It is important to measure the actual value of TCR instead of using the known value of the bulk material. This is because the thin film resistivity and TCR can be significantly

different to the bulk materials. Four different methods were used to measure the TCR of the conductive layer of the heaters.

Three of these methods were based on the measurements during the rise of the microgripper's heater temperature and the last one is based on the cooling effect. The relationship between the conductive layer resistivity and the temperature is linear, so the resultant data can be saved in a data file for subsequent analysis. The data is used to determine the regression line then to calculate this line equation. The format of the line equation is shown in equation (4.2) to drive the TCR.

$$R = AT + B \quad 4-2$$

$A$  and  $B$  are the linear equation coefficients and can be calculated using equation (4-3) and equation (4-4). From equation (4-1) the resistance as a function of temperature can be rewritten as equation (4-6). So, the line equation coefficient can be represented as equation (4-7). There are two unknowns ( $R_o$  and  $\alpha$ ) and two equations. By solving the first equation to  $R_o$  and subtracting it in the second equation,  $\alpha$  can be calculated in equation (4-8). The square root error,  $r$ , can be calculated using equation (4-5) then  $r^2$  can be calculated. The range of the square root error is from 0 to 1. The closer to 1 the  $r$  is the better the fit is to the linear equation.

$$A = \frac{\sum_n T_n R_n - \frac{\sum_n T_n \sum_n R_n}{n}}{\sum_n T_n^2 - \frac{(\sum_n T_n)^2}{n}} \quad 4-3$$

$$B = \frac{\sum_n R_n}{n} - A \frac{\sum_n T_n}{n} \quad 4-4$$

$$r = \frac{\sum_n (T_n R_n) - \frac{\sum_n T_n \sum_n R_n}{n}}{\sqrt{\left[ \sum_n T_n^2 - \frac{(\sum_n T_n)^2}{n} \right] \left[ \sum_n R_n^2 - \frac{(\sum_n R_n)^2}{n} \right]}} \quad 4-5$$

$$R = R_o \propto T - R_o(1 + \alpha T_o) \quad 4-6$$

$$A = R_o \propto , B = -R_o(1 + \alpha T_o) \quad 4-7$$

$$\alpha = \frac{A}{A T_o + B} \quad 4-8$$

#### 4.1.2 Closed Chamber Test Method

In this method, the TCR measurements were carried out by mounting the gripper for characterisation in a small chamber which was placed on a hotplate. Two small

thermocouple temperature sensors were placed above and below the microgrippers and an average temperature was obtained. The resistance of the microheater was measured using a multimeter and the average temperature of the chamber was recorded using the thermocouple. The heater resistance was measured over a range of values of temperature. The glass slide, which was used to hold the microgripper, was isolated from the holder to reduce the temperature conduction through the glass slide to the microgripper. This setup is shown in Fig. 4.1.

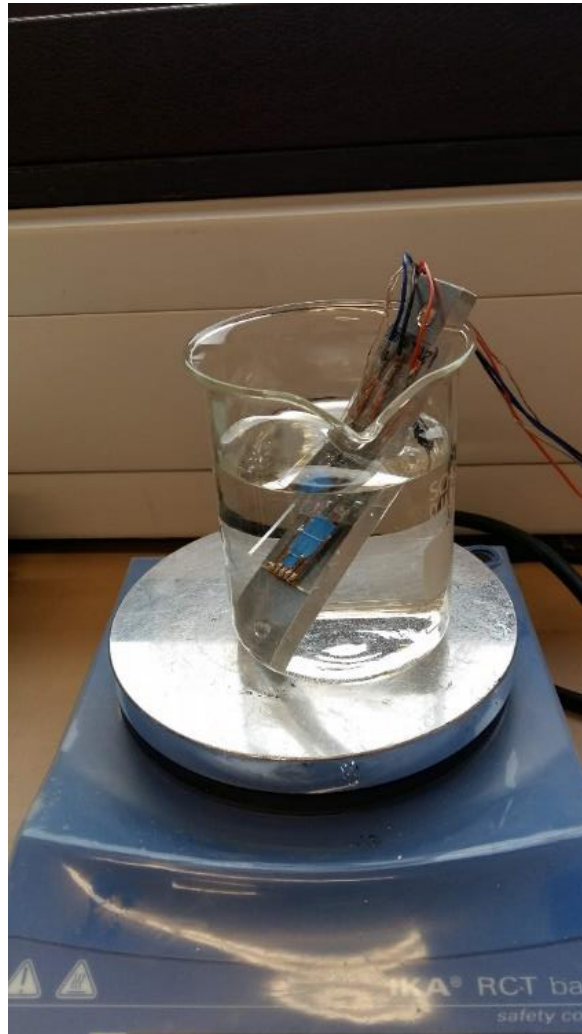


*Fig. 4.1 Equipment setup used to carry out the TCR measurements for the first method using a chamber.*

#### *4.1.3 Water Bath based Test Method*

In this method, a microgripper was glued at the edge of a microscope slide. Then, copper tape was used to interface the electrical connection between the microgripper and wires, as described in section 4.2 . Then, the microgripper was covered using epoxy glue as insulator and to protect the microgripper from damage because of the water. A glass beaker was filled with distilled water and the prepared microgripper was immersed in the water. In addition, a thermocouple sensor was used to measure the water temperature

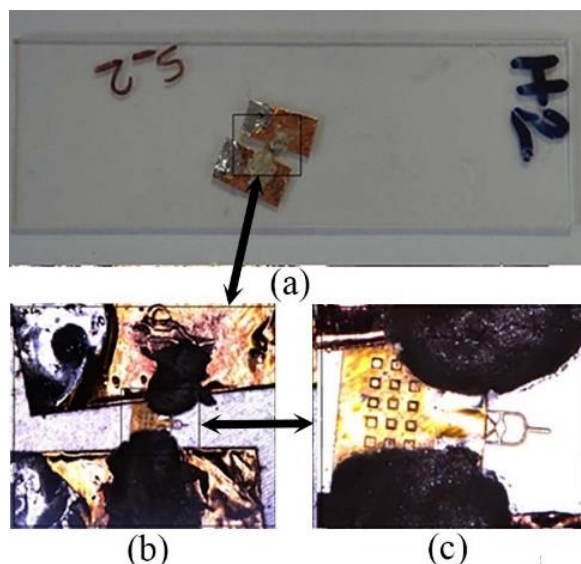
surrounding the microgripper, as shown in Fig. 4.2. The water was heated up gradually using a hotplate. The resistance and the temperature were recorded for the analysis of the results of TCR measurements.



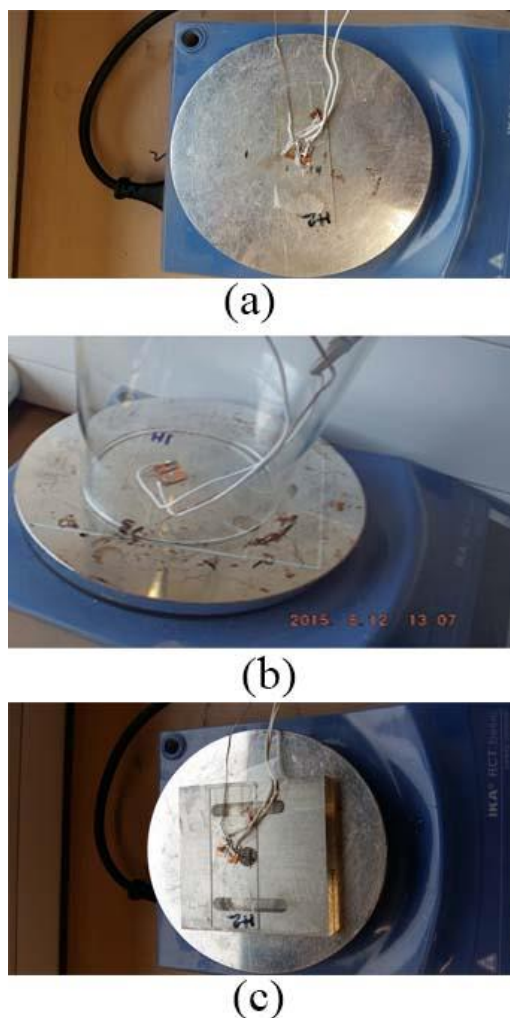
*Fig. 4.2 Using distilled water to raise the temperature of the microgripper*

#### *4.1.4 Third TCR Measurement Method*

In this method, a different approach of mounting the microgripper on a glass slide was used. The microgripper was completely glued onto the center of the glass slide, as shown in Fig. 4.3. The temperature of the glass slide and the microgripper was assumed to be the same because there was no gap between them and the thermal mass of the microgripper is negligible compared with the mass of the glass slide. A thermocouple sensor was glued onto the glass slide close to the microgripper. Three different methods were used to raise the temperature of the glass slide, as shown in Fig. 4.4. Both heating up and cooling down processes were monitored to record the temperature and the microheater resistance.



*Fig. 4.3 The microgripper was glued onto glass sheets and connected using copper tape and conductive adhesive (a) A camera photograph of this method showing all the component (b) the microgripper focused under the microscope (c) extra zoom of the microgripper*



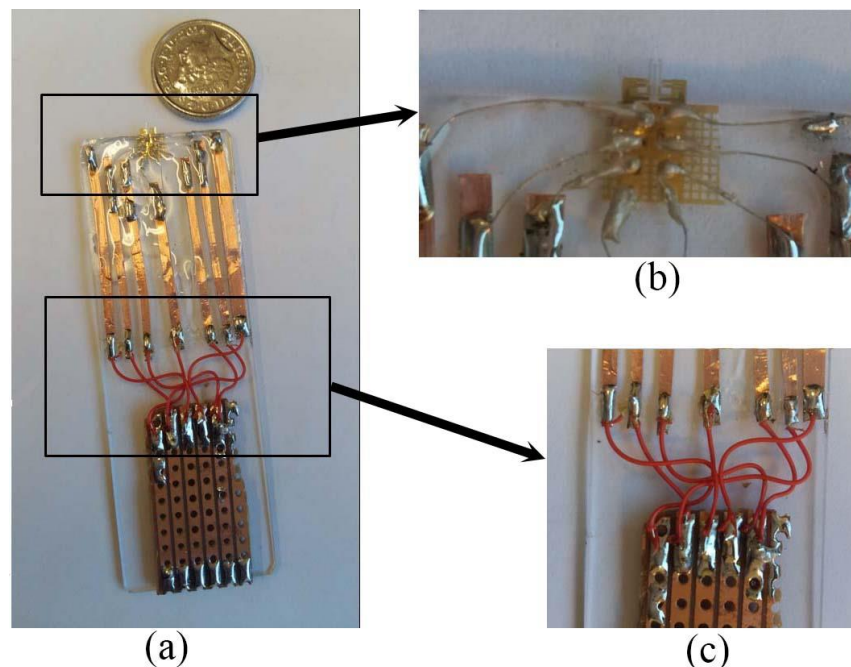
*Fig. 4.4 Three methods were used to heat up the microgrippers. Thermocouple was used to measure the temperature. (a and b) the glass was placed on the hot plate without any interface while in (c) a block of Aluminium was used to stabilise the temperature by adding more mass to the glass sheet.*

## 4.2 Gripper Mounting and Connection

The microgripper was mounted on a microscope glass slide using an epoxy glue. There were several methods used to connect the electrical pads of these microgrippers in order to carry out the testing. The first method was done by using thin wires (about 0.05 mm in diameter) and silver-loaded epoxy conductive adhesive. One end of a wire was soldered to a PCB or copper stripe tape as shown in Fig. 4.5. Then, the other end of the wire was connected to the contact pad on the microgripper using the conductive adhesive. Then, the adhesive was cured using a hot plate at 90°C for 15 minutes.

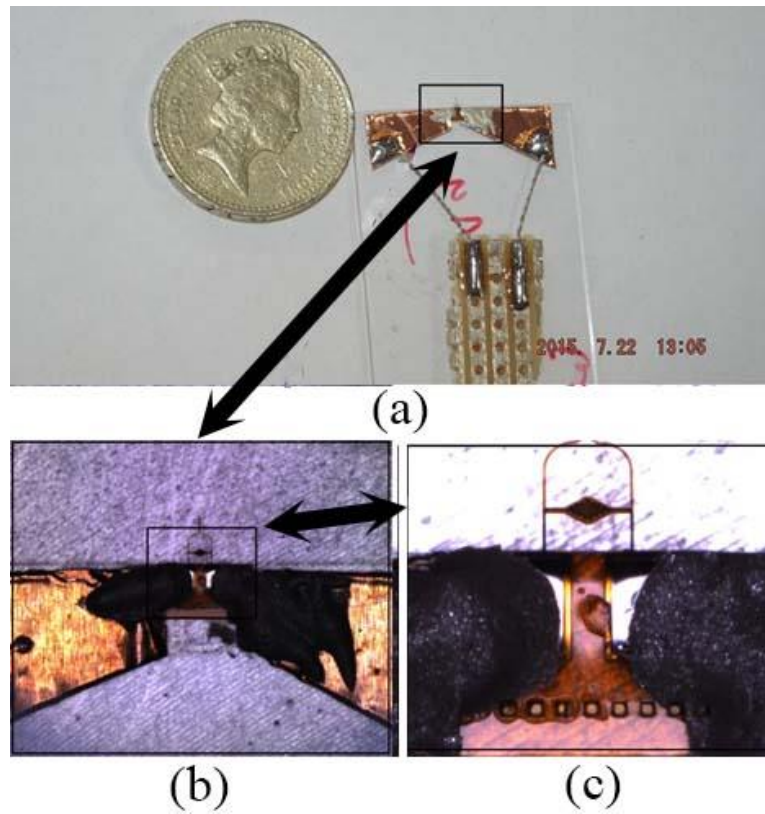
Another useful method was to extend the microgripper pads using narrow strips of copper tape with triangular tip. These were positioned on the glass slide with the triangle end close to the pad. Then, the conductor was connected to the pads using silver adhesive, as shown in Fig. 4.6 and Fig. 4.7. Then, the conductive copper strips were connected to a small piece of PCB using thin wires.

Finally, another method was developed to mount and connect the microgrippers. A PCB was designed with the conductive traces to match the pad layout of the microgripper to connect each line trace to the corresponding pad. The connections were made using the silver loaded epoxy adhesive and cured on hotplate for 30 minutes at the temperature of 50°C. The connected microgripper is shown in Fig. 4.8.

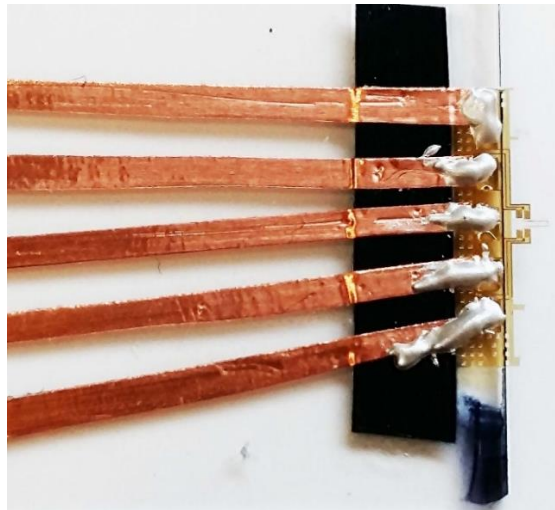


*Fig. 4.5 The first electrical connection method which was used to connect the three arms of the microgripper (a) Whole system showing the microgripper, copper tape strips, and PCB (b) The microwires glued on the microgripper pads and soldered on the copper strips on the other side (c) tiny wires used to connect the copper strips to the PCB*



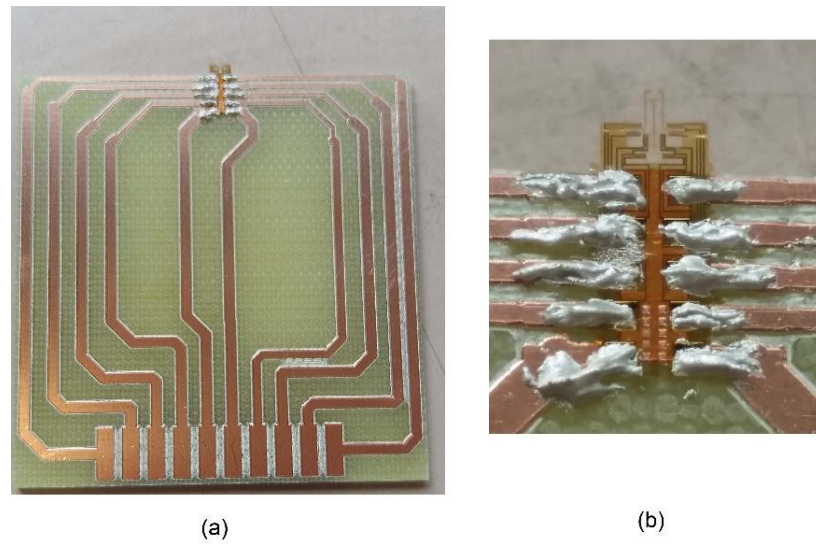


*Fig. 4.6 Second connection method used to connect the microgripper pads to carry out the required tests. (a) Image was taken using a photographic camera showing all the components. Images b& c were taken using an optical microscope showing the connection between the copper strip and the pads under focus.*



*Fig. 4.7 The second method of electrical connection used to set up the 2 DOF microgripper*





*Fig. 4.8* The third method used to connect the multi-degree of freedom microgripper. (a) Whole PCB shows the microgripper and the electrical pads. (b) Zooming in the microgripper to show the conductive paste connecting the microgripper pads to the PCB traces.

### 4.3 Results

The resistance was measured for the different microgripper designs and different samples using different measurement environments. The TCR value was slightly different from one method to another and from one design to another. In addition, the TCR value varied depending on the thickness of the chromium layers.

#### 4.3.1 TCRs of Cr/Au/Cr Film with Thickness 10 / 300 / 10 nm

##### i. Design A:

Two samples of design A were investigated using the first measurement method. The first sample was tested twice and the other was tested once. The results of these tests are shown in Fig. 4.9. The error (R-squared value) of each trend line generated by Microsoft Office Excel was more than 99%. The linear equations of these tests are shown in equation (4-9), equation (4-10), and equation (4-11). Equation (4-8) was used to calculate the TCR values from the trend line equations. The TCR for the first sample was 0.00148 and 0.00147 for the first and second tests respectively, while it was 0.00146 for the second sample.

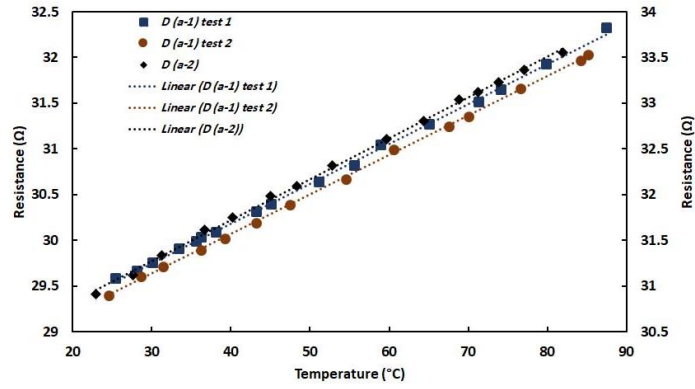


Fig. 4.9 Result of the resistance as a function of temperature for design A sample 1 two tests and one test for the second sample. The left vertical access is the resistance of sample (1) while the right is for sample (2).

$$R = 0.0437 T + 28.434 \quad 4-9$$

$$R = 0.0432 T + 28.341 \quad 4-10$$

$$R = 0.0447 T + 29.932 \quad 4-11$$

ii. Design B:

Two samples of design B were tested to measure the TCR in two different ways. The first sample TCR measurement was done using the first method only while the second was done using both the first and second methods. The results of these tests are shown in Fig. 4.10. The trend line is shown in equation (4-12), equation (4-13) and equation (4-14). The TCR values were 0.0014, 0.00134 and 0.00159 for the first sample test using the chamber-based method and second sample using the camber-based method and the water bath-based method, respectively.

$$R = 0.0416T + 28.612 \quad 4-12$$

$$R = 0.042T + 30.401 \quad 4-13$$

$$R = 0.0499T + 30.122 \quad 4-14$$

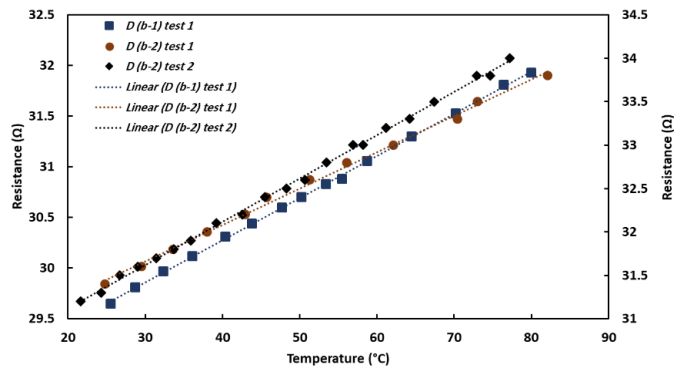


Fig. 4.10 Microgripper design B TCR measurements on two different samples and methods. The left vertical axis is for sample (1) and the right is for sample (2).

iii. Design C:

Two different samples of design C were tested using the first method in a heated chamber. The results of the resistance as a function of temperature are shown in Fig. 4.11. The linear equations of the generated trend lines are shown in equation (4-15) and equation (4-16) for the first and second samples. The measured TCR values were 0.00154 for the first sample and 0.00143 for the second sample.

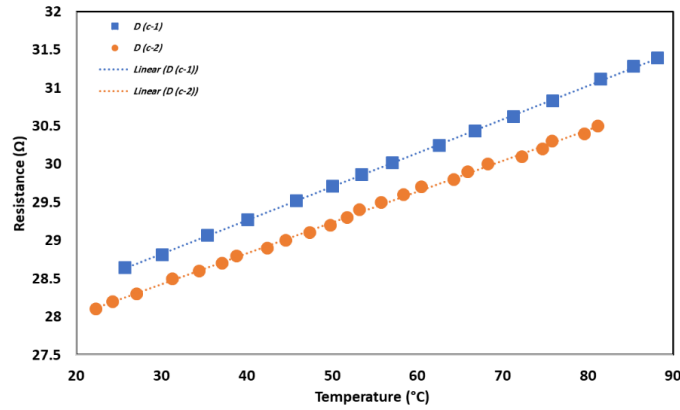


Fig. 4.11 Experiment results of TCR measurement using microgripper design C

$$R = 0.0441T + 27.498 \quad 4-15$$

$$R = 0.0405T + 27.211 \quad 4-16$$

iv. Design B & C

The designs B and C were studied using the third method of TCR measurement and labelled as H1 and H2 respectively. The H1 was tested in four different ways, three of which are shown in Fig. 4.4. The last test was done by cooling the sample on an aluminum block by putting it in a freezer. The sample H2 was tested with the method shown in Fig. 4.4 (a) only. Fig. 4.12 shows the results using the third method shown in Fig. 4.15 (a) to test both H1 and H2. Fig. 4.13 shows the results using method 3 shown in Fig. 4.15 (b) and (c). The linear equations generated using Microsoft Excel are shown in equations (4-17) to (4-20). The square root errors were above 99% for all of these results and the calculated TCR were 0.00155 and 0.00136 for H1 and H2 using method 3 in Fig. 4.15 (a) respectively and 0.00154, 0.00149 using method 3 in Fig. 4.15 (b) and (c) on H1 respectively.

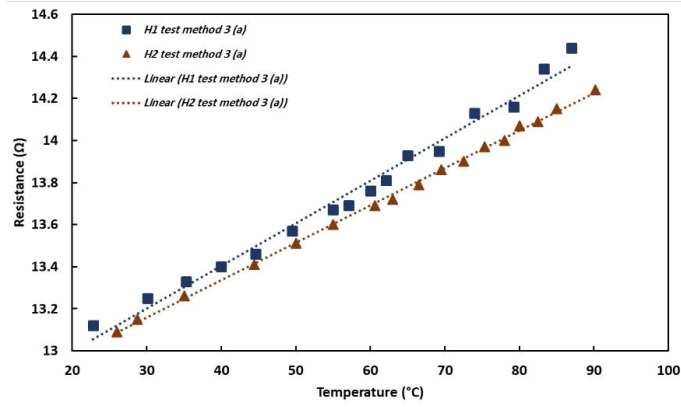


Fig. 4.12 Result of testing H1 and H2 using the third method (a)

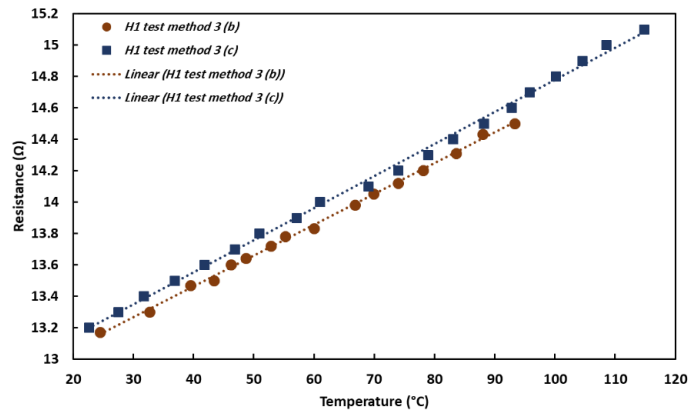


Fig. 4.13 Result of testing H1 using the third method (a & b)

$$R = 0.0203T + 12.593 \quad 4-17$$

$$R = 0.0178T + 12.626 \quad 4-18$$

$$R = 0.0204T + 12.736 \quad 4-19$$

$$R = 0.0196T + 12.68 \quad 4-20$$

The results obtained using cooling instead of heating are shown in Fig. 4.14 and the linear fit is shown in equation (4-21). The calculated TCR using this method was 0.00156.

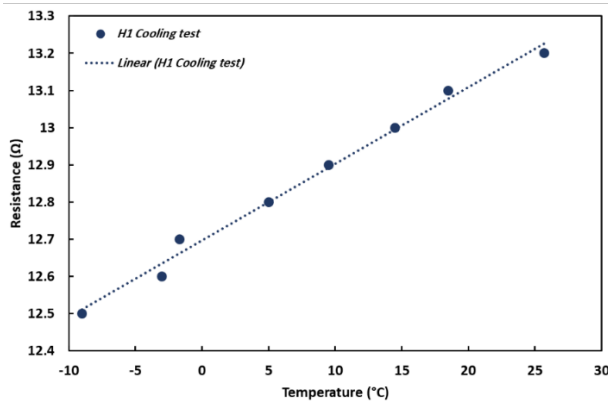


Fig. 4.14 Results of testing sample H1 using the cooling method

$$R = 0.0206T + 12.697$$

4-21

v. Design D & E:

Designs D & E have two separate heaters so the TCR values were measured for each heater separately and together by connecting them in parallel. The three tests on design D are shown in Fig. 4.15 and their linear equations are shown in equation (4-22) to (4-24) for the right heater, the left heater, and the heaters connected in parallel respectively. The TCR values calculated out of these three tests were 0.00144, 0.00142 and 0.00148.

The results for Design E are shown in Fig. 4.16 and their linear equations in equation (4-25) to (4-27) for the right, left and the parallel connection respectively. The TCR values were 0.00136 for the right heater, 0.00133 for the left heater, and 0.00135 for the parallel connection.

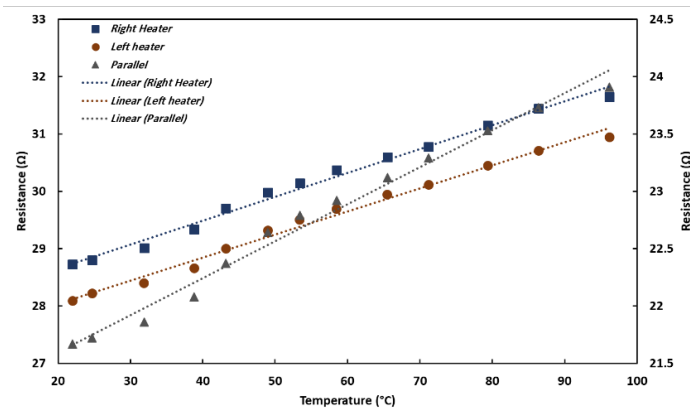


Fig. 4.15 Testing design D using each heater separately and in parallel connection. The left axis shows the single heater resistance while the right is for the parallel.

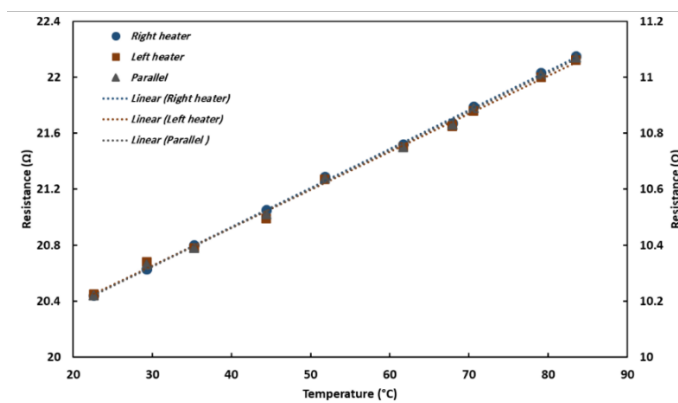


Fig. 4.16 Results of testing design E which has two heaters. The left vertical axis shows the resistance of the single heater test while the right axis shows the resistance of the parallel connection.

$$R = 0.0416T + 27.827$$

4-22

$$R = 0.0402T + 27.236$$

4-23

$$R = 0.0322T + 20.954 \quad 4-24$$

$$R = 0.0279T + 19.813 \quad 4-25$$

$$R = 0.0272T + 19.837 \quad 4-26$$

$$R = 0.0138T + 9.9089 \quad 4-27$$

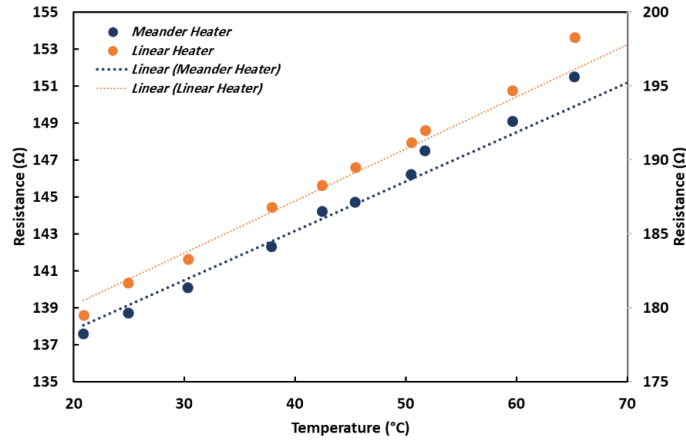


Fig. 4.17 Resistance as a function of temperature for the directly actuated microgrippers with two different heater shapes. The left vertical axis is for the meander heater while the right axis is for the linear heater resistance value.

$$R = 0.2671T + 132.49 \quad 4-28$$

$$R = 0.352T + 173.15 \quad 4-29$$

#### 4.3.2 TCRs of Cr/Au/Cr Film with Thickness 7/200/7 nm

Two samples of designs (directly actuated microgrippers) as shown in Fig. 3.20 were used to measure the TCR for a metal layer with 7nm / 200 nm / 7nm configuration for Chromium / Gold / Chromium, respectively. Each sample has a different heater shape, as shown in Fig. 4.17 A & C. The first method was used to measure the change in the resistance to the temperature. Fig. 4.18 shows the result of both designs and the generated linear equations are shown in equation (4 28) and (4 29) for the meander and linear heater shape. The calculated TCR values were 0.00193 and 0.00195 for the meander and the linear heater shapes.

Other tests were done on two samples of the same design with a smaller heater width and meander heater shape. The results of these tests are shown in Fig. 4.18 and the linear equation is shown in equation (4-30) and (4-31). The calculated TCR values using this method was 0.00203 and 0.00195 for the first and second sample respectively.

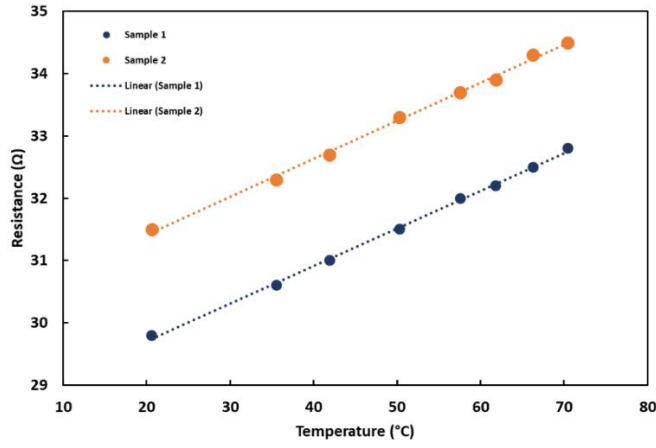


Fig. 4.18 Resistance as a function to temperature for the directly actuated microgrippers with meander heater

$$R = 0.0604T + 28.498 \quad 4-30$$

$$R = 0.0611T + 30.184 \quad 4-31$$

The last test was done using the heater H1 in a multi-degree of freedom microgripper, as shown in Fig. 3.20. The first TCR measurement method was used to carry out the measurement. The resistance change as a function of temperature is shown in Fig. 4.19 and the linear fit is shown in equation (4-32). The calculated TCR was 0.00199.

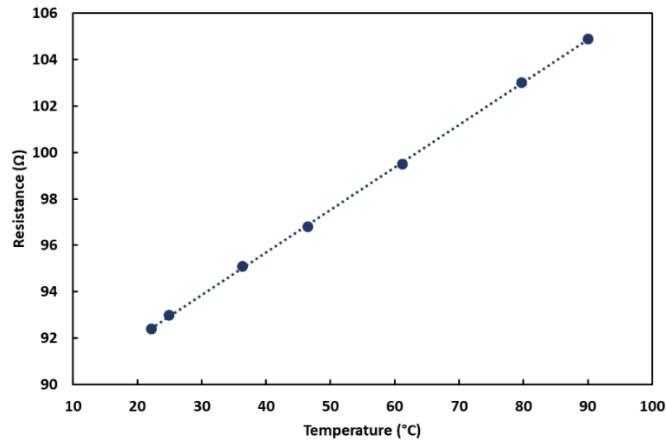


Fig. 4.19 TCR measurement of the multi-degree of freedom microgripper

$$R = 0.1831T + 88.375 \quad 4-32$$

#### 4.3.3 TCRs of Gold with a thickness of 100 nm

The bi-directional microgripper design shown in Fig. 3.20 (b) was used to determine the TCR for a heater with gold only and 100 nm of thickness. The first method was used to carry out the change in the resistance as a function of temperature. The results for both heaters are shown in Fig. 4.20. The linear equations of these results are shown in equation (4-33) and (4-34). The calculated TCR values were 0.0031 and 0.003 for heater 1 and heater 2 respectively.

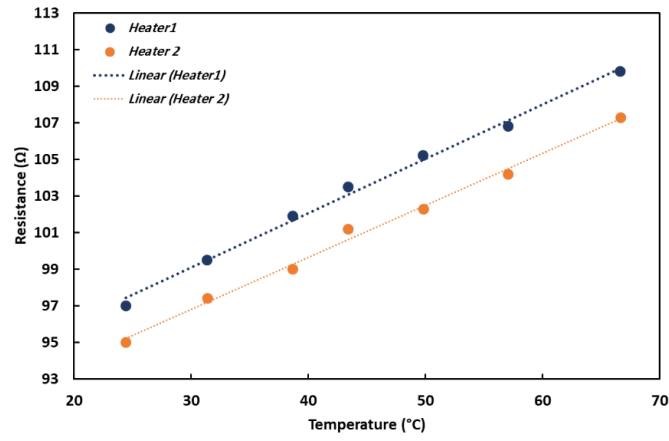


Fig. 4.20 Results of heater resistance as a function of temperature of the bi-directional microgripper

$$R = 0.296T + 90.18 \quad 4-33$$

$$R = 0.284T + 88.28 \quad 4-34$$

The V-shaped microgripper shown in Fig. 3.18 was used to measure the TCR for a heater with gold only and a thickness of 100 nm. Fig. 4.21 shows the results of the measurement based on the first TCR testing method. The linear fit is shown in equation (44-35). The calculated TCR was 0.0033.

$$R = 0.013T + 3.78 \quad 44-35$$

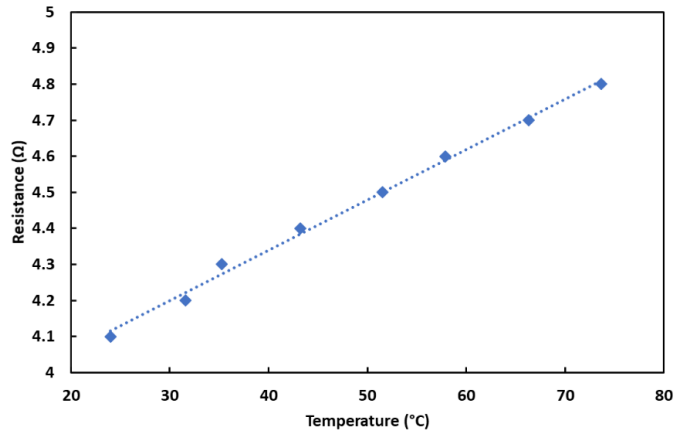


Fig. 4.21 TCR measurement result of the V-shaped based small size

Two more tests on two samples of the same microgripper but in a larger size are shown in Fig. 4.22. The TCR values were 0.0031 for both samples.



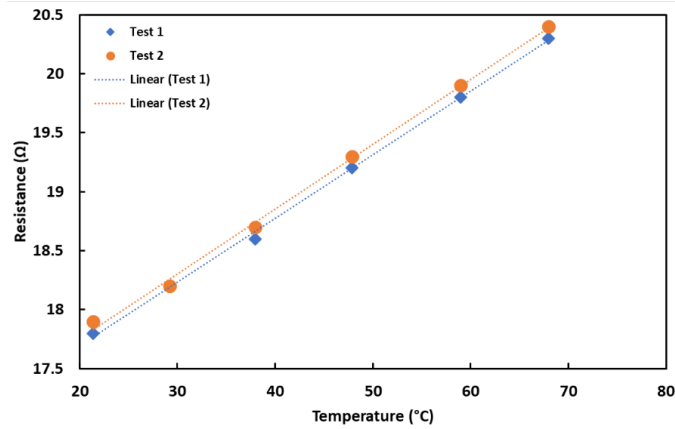


Fig. 4.22 TCR measurement result of the V-shaped based large size

#### 4.4 Summery

Both IMT and Heriot-Watt designs were used to study the Temperature Coefficient of Resistance (TCR) of different heater configurations. These configurations used different metal layers as listed below:

- 1- 10 /300 / 10 nm of Chromium / Gold / Chromium respectively summarised in Table 4-1.
- 2- 7 /200 / 7 nm of Chromium / Gold / Chromium respectively summarised in Table 4-2.
- 3- 100 nm of Gold only summarised in Table 4-3.

Table 4-1 Summery of designs with heater configuration of 10 /300 / 10 nm of Chromium / Gold / Chromium respectively

Device	TCR from test method 1 (1/°C)	TCR from test method 2 (1/°C)	TCR from test method 3 (1/°C)
Design A 1 <sup>st</sup> -sample test 1	0.00148		
Design A 1 <sup>st</sup> -sample test 2	0.00147		
Design A 2 <sup>nd</sup> -sample	0.00146		
Design B 1 <sup>st</sup> -sample	0.00159		
Design B 2 <sup>nd</sup> -sample	0.0014	0.00134	
Design C 1 <sup>st</sup> -sample	0.00154		
Design C 2 <sup>nd</sup> -sample	0.00143		
H1			0.00155 & 0.00154
H2			0.00146 & 0.00149
Design D Right heater	0.00144		
Design D Left heater	0.00142		
Design D heaters connected in parallel	0.00148		
Design E Right heater	0.00133		
Design E Left heater	0.00136		
Design E heaters connected in parallel	0.00135		

*Table 4-2 Summery of designs with heater configuration of 7 / 200 / 7 nm of Chromium / Gold / Chromium respectively*

Device	TCR from test method 1 (1/°C)	TCR from test method 2 (1/°C)	TCR from test method 3 (1/°C)
HW Design2 Heater width 210 µm Meander	0.00193		
HW Design2 Heater width 210 µm Linear	0.00195		
HW Design2 Heater width 100 µm Meander sample1	0.00203		
HW Design2 Heater width 100 µm Meander sample2	0.00195		
H1 in Three Arms Microgripper	0.00199		

*Table 4-3 Summery of designs with heater configuration of gold only with thickness of 100 nm*

Device	TCR from test method 1 (1/°C)	TCR from test method 2 (1/°C)	TCR from test method 3 (1/°C)
HW Design2 H1	0.0031		
HW Design2 H2	0.003		
V-shaped microgripper small	0.0033		
V-shaped microgripper large sample1	0.0031		
V-shaped microgripper large sample2	0.0031		

These microgrippers were tested using three different methods to increase the reliability of the results. A closed and insulated environment was used in the first method. In this method, the air was heated up using an electric hot plate. The air temperature was measured using two thermocouple sensors positioned close to the microgrippers. In the second method, distilled water was used as environment surrounding the microgrippers. The temperature of the water was assumed to be same as that of the heaters. In the third method, different microgrippers were glued onto a glass sheet then the temperature of the glass was raised on a hotplate. The temperature of the glass and the microgripper was assumed to be the same.

These microgrippers were mounted on microscope glass slides and electrically connected to pieces of PCBs using different methods. Then, they were tested using the respective methods. The results were analysed using Microsoft Excel to find the linear equations for each test. Then, the TCR values were calculated.

Nineteen tests of different microgripper designs of heater with 10/300/10 nm Cr/Au/Cr configurations were tested. All the results were over 95% matching the linear equations generated by Microsoft Excel. The average of all results was 0.00137. Five other tests of different microgrippers with 7/200/7 nm Cr/Au/Cr configuration were carried out. The accuracy of the generated linear equations was similar to the previous tests. The average of the five results was 0.00197. For the 100 nm Au heater configuration, only four microgrippers were tested. The average of the results was 0.00313 with same accuracy as the previous tests.

There is a small difference (about 5%) between different devices and different designs for the same configuration which can be attributed to the imperfections of the conductor lines due to the fabrication limitation. In addition, the lowest  $r^2$  was about 0.99, i.e. the linear regression equation is very accurate and reliable. This small difference may be due to the sampling error and accuracy. However, it is clear the extra layers of chromium have a significant effect on the TCR of the metal layer. The TCR of bulk gold is about 0.0033 while it is 0.0000059 bulk chromium. It is shown that chromium layers of thickness of only 7nm in the Cr/Au/Cr configuration reduce the TCR to be about half of the value of the 100 nm thick gold film. In the literature, similar behavior has been described for gold alloy materials. Adding a small percentage of chromium significantly affects the TCR and resistivity value of the alloy material. Although the metal layer of Cr/Au/Au is not a bulk alloy material, but it has a similar behavior. The most important conclusion of the work is that it is necessary to make independent measurement of TCR of the heaters in a microgripper in order to determine the temperature of a microgripper under operation. In the previous work in literature, the bulk value of gold was used to calculate the heater temperature which would indicate wrong values for the temperature [95], [96], [100], and [99].

## Chapter 5 Characterisation and Measurement Methods

### 5.1 Introduction

This chapter describes the methods developed to obtain the steady state and dynamic responses of microgrippers. The measured TCR values were used to determine the operating temperature by using the resistance change as temperature. An image processing program based on OpenCV integrated with the software of the robotic system (Chronogrip) manufactured by Percipio Robotics in France. The displacements of the endeffectors were measured by optical tracking of their positions. Then the results were used to analyse the behaviors of the microgrippers listed in Table 5-1 and Table 5-2. The first group was designed by IMT while the second group was designed in the thesis work. All designs were fabricated by IMT.

*Table 5-1 Group one of IMT design microgrippers*

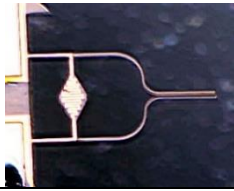
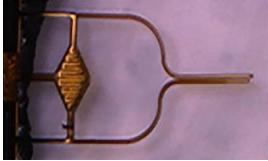
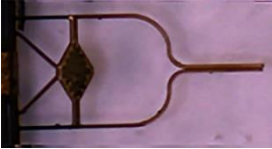
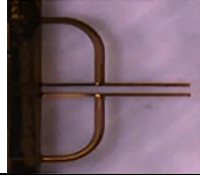

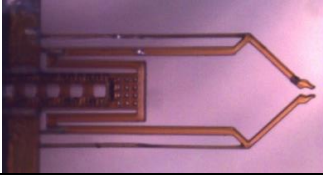
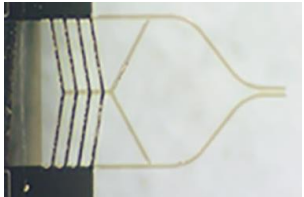
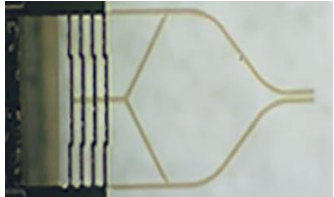

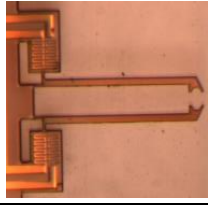
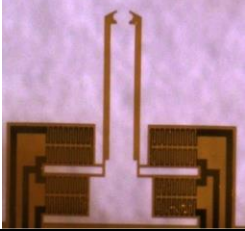
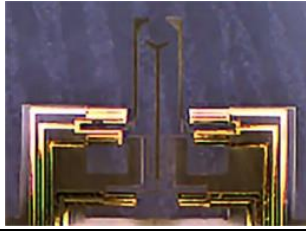
Design IMT-A		Design IMT-B	
Design IMT-C		Design IMT-D	
Design IMT-E		Design IMT-F	
Design IMT-G		Design IMT-H	

Table 5-2 Microgrippers Designed at Heriot-Watt University

Design HWU-A (Interfaced Microgripper)		Design HWU-B (Direct Actuated Microgripper)	
Design HWU-C (Bi-Directional Microgripper)		Design HWU-D (Multi-degree of Freedom Microgripper)	

## 5.2 Temperature Calculation Method

Because the relationship between temperature and the resistance of the heater is known and the TCR values were determined in Chapter 4, the temperature can be determined using the measured resistance. Fig. 5.1 shows the circuit diagram of a microgripper connected to a power supply. This was used to supply an electrical current to the microgripper. Two multimeters were used to measure the voltage and the current of the microgripper. Hence the resistance could be calculated using the measured voltage and current. The exact heater resistance of the microgripper is calculated using equation (5-1) and the temperature was calculated using equation (5-2), which was based on equation (4-1).

$$R_g = \frac{V}{A} - R_w \quad 5-1$$

$$T_g = \frac{R_g - R_o}{R_o \alpha} + T_o \quad 5-2$$

Where  $R_g$  is the microgripper's heater resistance,  $V$  and  $A$  are the voltage and the current measured using the multimeters,  $R_w$  is the connection wire resistance,  $T_g$  is the average heater temperature,  $R_o$  is the heater resistance at 20° C,  $R_g$  is the heater resistance during operation,  $\alpha$  is the measured TCR from Chapter 4, and  $T_o$  is 20°C.

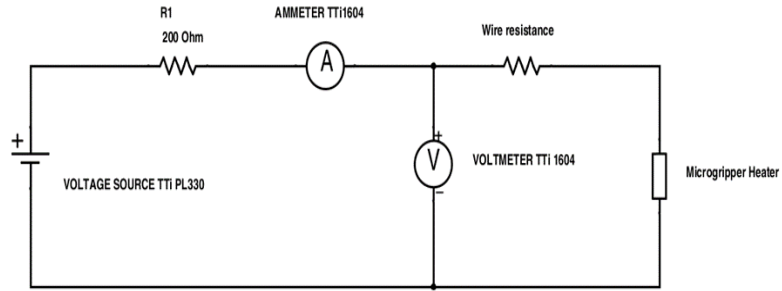
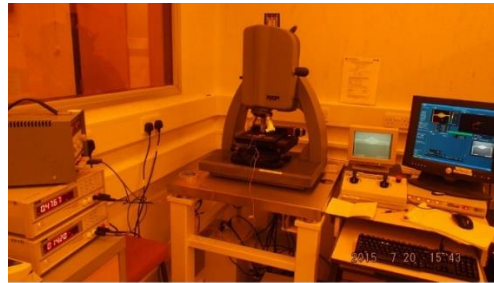
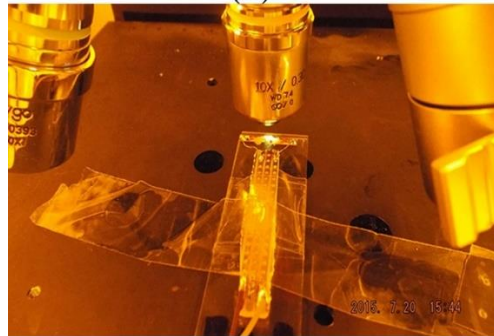


Fig. 5.1 Circuit diagram for the connection of the microgripper to measure the voltage and current then to use them to calculate the resistance.



(a)



(b)



(c)

Fig. 5.2 Setup of the zygo metrology system. (a) shows the whole system and the test setup whereby on the left is the power supply and two multimeters to measure the voltage and the current, in the middle is the optic part, and on the left is the control and monitor part. (b) shows the microscope glass sheet carrying the microgripper and it fixed on the system stage using a tape. (c) shows the monitor and the user interface running and showing a result of one of the measurements.

## 5.3 Displacement Measurements

### 5.3.1 Displacement Measurement on Zygo Metrology System

The Zygo system is an optical metrology instrument designed to measure microobjects accurately with nanometer resolution. This was used to measure the opening (gap) between the end-effectors to calculate the displacement. Fig. 5.2 shows the Zygo system used in the measurements. The microgripper mounted on a glass slide was fixed on the stage of the system using a tape to avoid any vibration during the test which could be caused by the instability of the samples. Then, the power supply and the multimeters were set up and connected, as illustrated in the schematic shown in Fig. 5.1.

The Zygo system has a powerful measurement software called (MetroPro) with an easy access user interface. The microgrippers were powered and the voltage was increased gradually. During this, the gap (separation) between the end-effectors of the microgripper was measured. The voltage and the current were recorded simultaneously. Fig. 5.3 shows an example of the measurements using the Zygo system. This figure illustrates how it is used to measure the displacement. The display window (A) shows the image of the gripper under investigation and it shows the arrow line to define the line for measurement. The important data for the characterisation is the (xDst) in window B which shows the distance between the two cursor lines in window C.

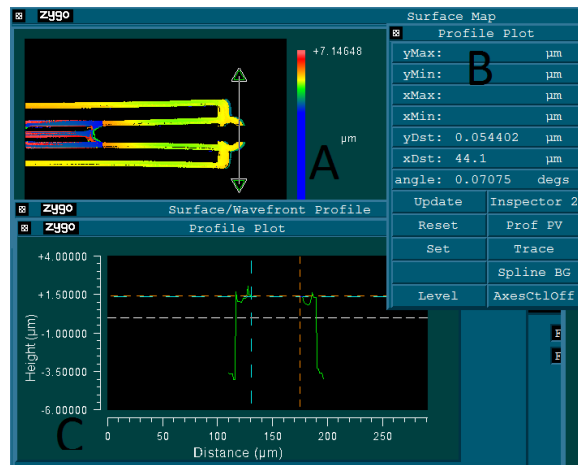


Fig. 5.3 Screenshot from the Zygo user interface software showing one of the parts under test. (a) shows the microgripper part under observation, the line is the slicing tool and shows the result on (c). (b) shows the inspector's result.

### *5.3.2 Displacement Measurement Using Percipio Chronogrip Robotic System*

The Chronogrip system is a light robotic platform which was developed by Percipio Robotics for robotic microassembly. This system has built-in facilities which were used to characterise the microgrippers. One of these is a high magnification optical microscope connected to a high resolution camera. Also, the system has a hexapod platform with six motion axes which were used to position the microgripper under the microscope. The microgripper holder (glass slide) was fixed on the stage of the hexapod using tape, as shown in Fig. 5.4. The microgripper was connected as described previously in Chapter 4. In addition, the voltage was raised in a small increment step each time. The resolution of the attached camera is  $1.67 \mu\text{m}/\text{pixel}$ . Two microscopic objectives with X5 and X20 magnification were used for the displacement measurements. There were two methods of measuring the displacement. The first was by using the built-in scale after calibrating the software scale, as shown in Fig. 5.5. The other method was by automating the system to track the end-effectors. In this method the system software feeds a program with the tracked area coordinates. This method is more accurate than the previous method because there is no need to choose points to measure the distance between them. This method was based on a small Java script to track the movement the end-effectors and display the positions of the tracked areas on a computer screen. This information was used to extract the displacement values.



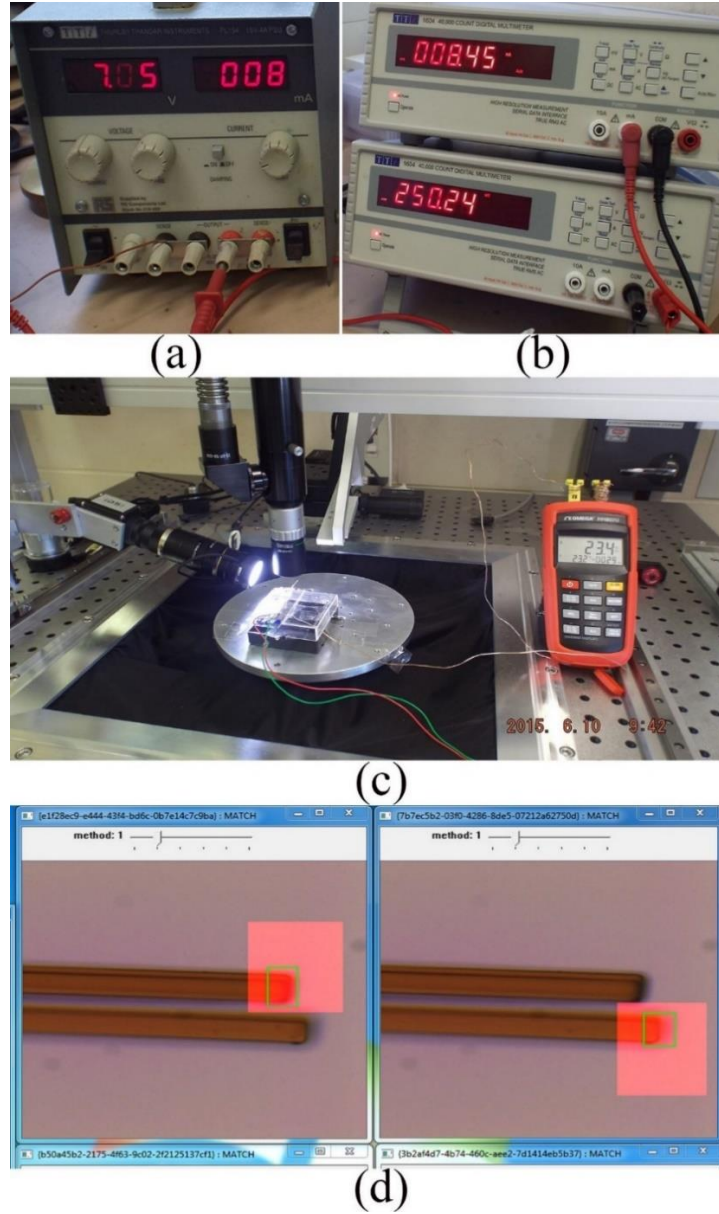


Fig. 5.4 Chronogrip robotic system setup to measure the displacements showing (a) the used power supply and (b) the used multimeters to measure the current and voltage (c) microgripper on the system's hexapod stage and the used microscope objective which is connected to a camera, a thermometer was also used to measure the test environment temperature (d) the tracking software user interface, the red area is the searching area while the green rectangle is the area of interest.

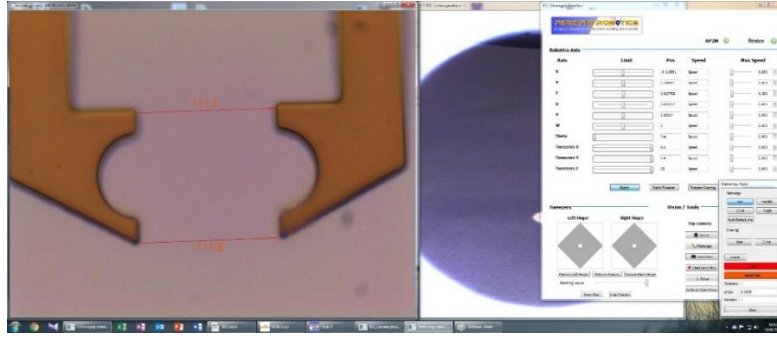


Fig. 5.5 Screen shot from the control computer of the Chronogrip robotic system showing the direct measurement technique. The left of the screen shows the image of the end-effectors taken from the microscope and overlapped with rulers to carry out the measurements. On the right of the screen is the user interface to control the robot and calibrate the ruler.

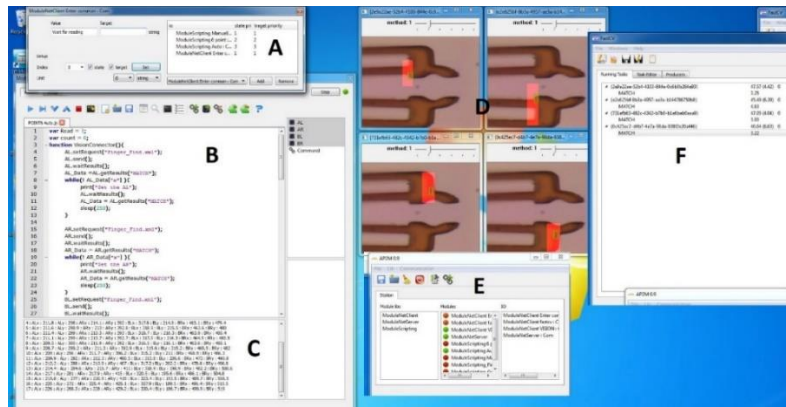


Fig. 5.6 User interface software in the Chronogrip Robotic System which was developed in order to carry out the characterisation of the microgrippers

The vision software libraries were based on FastCV. This is an open source software for image processing. It was integrated with the system in order to carry out the real time image analysis tasks. The software interface provides up to four different measurements at a time to be used for any particular application such as taking a measurement of object movement. As shown in Fig. 5.6 (D and F), the tracking software was called four times using a small piece of Java software which was written for this purpose, as shown in (B). Each picture in (D) represents one connection of the software request.

The Java software was designed to request ten readings of each connection. This was designed to be instructed from the user interface using the window that is shown in (A). Then, the average of the requested data is calculated and printed in (C) as a coordinate pair, i.e. for each tracking area, the center coordinates were printed. The reason for using ten readings each time is to filter the results from any noise that may affect them.

After that, these coordinates were converted mathematically into a displacement for each tracked point and each pair represents the x- and y-axis. Then, the two displacements were added with the starting opening which is measured separately. Finally, the relationship between the applied voltage (current) and the displacement can be calculated.

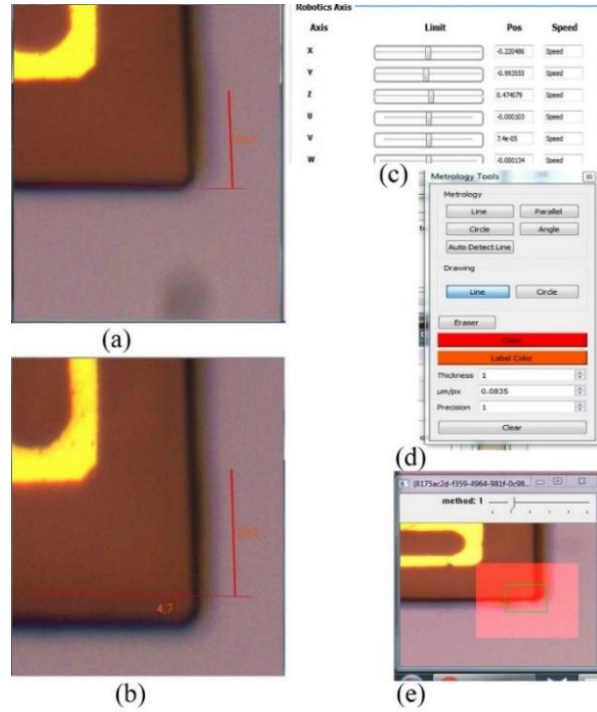


Fig. 5.7 Testing and verifying the pixel size by moving an edge of the actuator several micrometers and measuring the displacement in pixels. (a & b) is the measurement in pixels multiplied by the factor in (d) while (c) shows the movement control of the hexapod and (e) the displacement measurement using the tracking software.

### 5.3.3 Measurement accuracy

To verify the pixel size as mentioned in the camera's datasheet is equal to  $1.67 \mu\text{m}$  per pixel, two tests were done. The first one was to compare the robot software ruler and the other was to test the tracker software output. The verification was implemented by marking the edge of an actuator then moving it several micrometers. The displacement was feedback by the motor sensors and the robot software. Then, a comparison between all these data verified that the pixel size is exactly equal to the displacement that occurred by the motors, as shown in Fig. 5.7.

The vision system provides more reliable results than the Zygo system. This is not due to an inaccuracy in Zygo itself but due to the way of using it for distance measurements.

The Zygo system was designed to be used for depth measurement. Fig. 5.8, shows the result using Zygo system for the same device at the same time but different readings resulted in a  $1.5 \mu\text{m}$  of difference in displacement due to the very small difference in the arrow position which could not be noticed. In the robotic system, the measurement does not depend on a specific point but on an area selected by the user and traced by the software in the system.

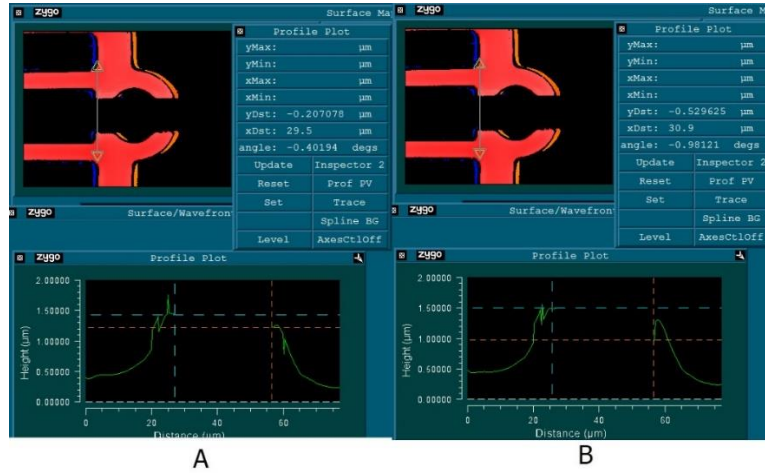


Fig. 5.8 Two different readings for same device and same conditions

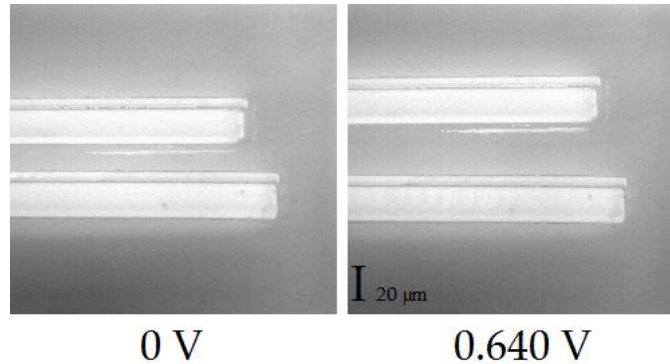


Fig. 5.9 Design (a) testing pictures were taken by Zygo system to measure the displacement

#### 5.4 Measurement of Dynamic Response Methods

The steady state displacement results showed there is a change in the opening every operation. In addition, it is useful to understand the effect of the Young's modulus value change when temperature is raised under the steady static displacement. Therefore, it was essential to develop a method to determine the dynamic responses of the endeffectors.

#### *5.4.1 Introduction*

The endeffectors of a microgripper move quickly to the steady state when an actuation voltage is applied to the heaters, therefore the dynamic response cannot be studied directly using the methods described previously in the steady state study and it requires an interface to save the data before they can be analysed. In the previous work [105] a limited amount of study was done using video recording of the displacement but there are some disadvantages in this method. Firstly, it is asynchronous, and the recording starts before the actuation voltage is applied. Secondly, it is time-consuming if all the video frames are to be analysed. Therefore, only selected frames are studied which can miss some important information in between the selected frames causing inaccurate measurement results. These disadvantages were overcome by developing an interface that can be used to synchronise the triggering the drive voltage and the start of the video recording process. In addition, image processing software was developed to analyse each frame to have better information for understanding of the microgripper behavior.

There are three main parts in this method: the microgripper driver hardware, interfacing the UART and the vision software, and the GUI software. This method of measurement was mainly based on the area tracking software which was part of the image processing software of the robotic system. This software was driven by the GUI through a JAVA script code. Also, the microgripper driver was controlled by the GUI through another JAVA script. The main software (GUI) was designed using C++ and visual studio 2019 IDE.

In the new measurement method, the user is able to set the gripper driving voltage and the ON/OFF time. When the test is started, the microgripper driver supplies the required voltage and continuously record the current and the voltage supplied to the tested microgripper for one second. It also simultaneously and continuously logging the position of the end-effectors during the measurement process. Then, the microgripper driver was instructed by the GUI to turn the power off while the position logging of the end-effectors continues to start the relaxation of the gripper response. By calculating the resistance from the recorded values of voltage and current, the heater temperature can be calculated.

### 5.4.2 Interface Unit

This section presents the interface unit design which was used to study the dynamic behavior and the reliability of the microgrippers. This was designed to automate the testing process and save the measurement results. In addition, the interface unit supplied power to the microgripper driver unit so the microgrippers can be studied on different applied voltages, as shown in Fig. 5.10.

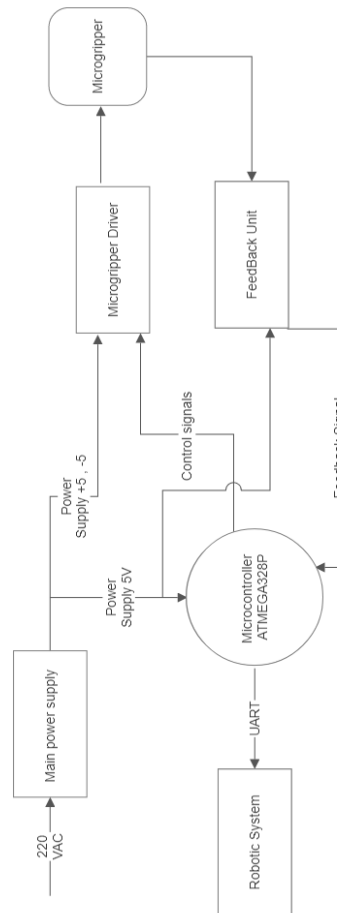


Fig. 5.10 Block diagram of the interface Unit



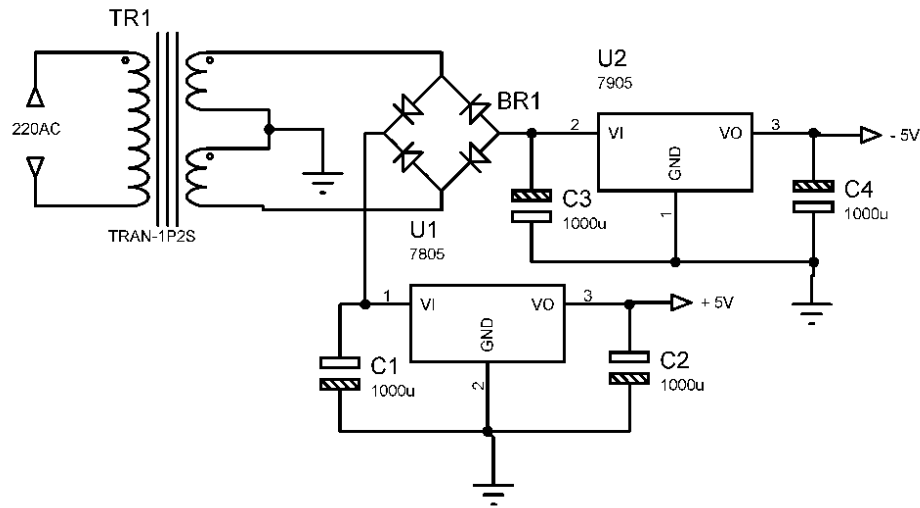


Fig. 5.13 Main power supply based on an AC transformer with dual 6V output and 240V input. Large capacitors were used to smooth the rectified AC voltage by the bridge diodes then regulators were used to regulate the output voltages.

#### 5.4.2 Interface Unit Schematic

Fig. 5.12 shows the schematic of the interface unit. It can be divided into three main sections: power supply, ADC section and DAC section. The power supply has mains power (240V AC) input, as shown in Fig. 5.13 and +5 V, -5 V and 0 V output. A transformer with dual 6 V output and 240 V input was used. Then, the AC voltage was rectified and regulated using a smoothing circuit and regulators to get a stable output voltage. In addition, there is a voltage reference circuit based on the first operational amplifier (OP Amp) to supply the DAC with the required reference. The OP Amp was configured as a voltage follower which is current independent with one resistor and a Zener diode.

The DAC was used as a reference voltage to another OP Amp which was configured as a voltage follower to supply the microgrippers with the required power. The DAC was controlled using an I2C bus. To measure the current, a 5.1  $\Omega$  resistor (R4) was placed as a shunt resistor. The voltages across the shunt resistor and the microgripper were measured using two ADCs. The ADCs were connected to the Arduino using the I2C. Then, the current was calculated from the voltage drop on the shunt resistor, R4. The temperature was calculated from the measured resistance and the TCR values obtained in Chapter 4.



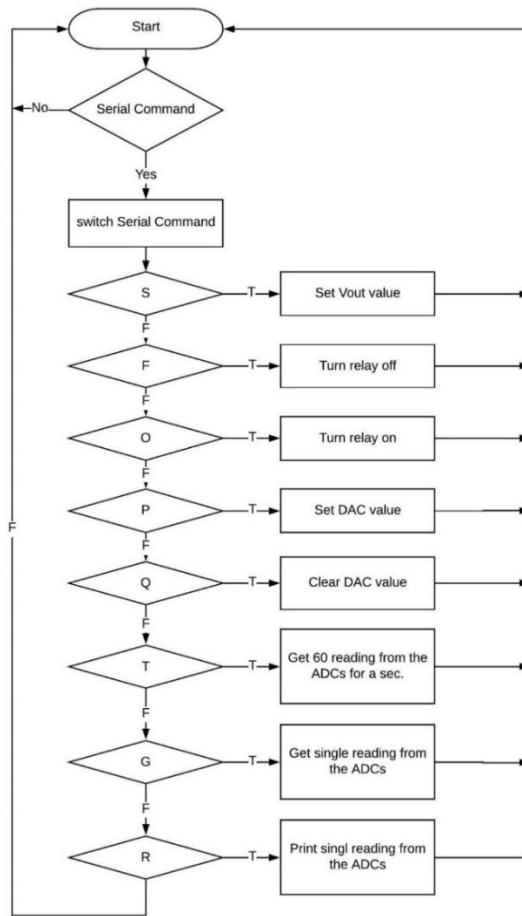


Fig. 5.14 Flow chart showing the process in the Arduino microcontroller dev. Board

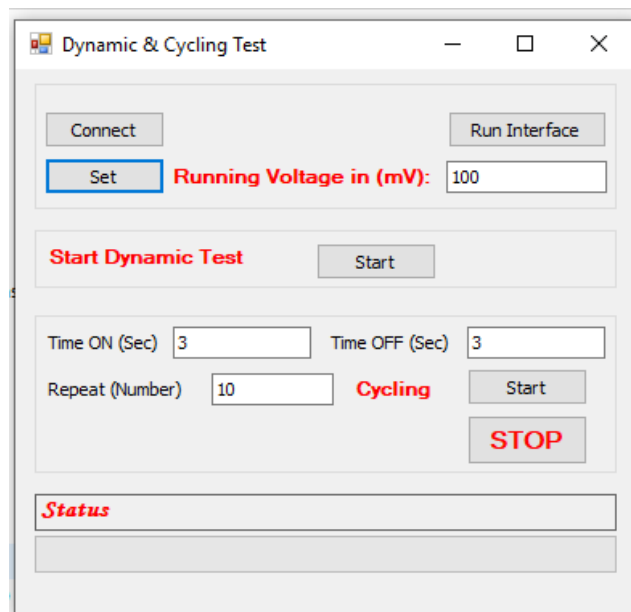


Fig. 5.15 UI used to control and configure the system measurements.

### *5.4.3 Interface Unit Software*

The Arduino has firmware written using C and Arduino IDE. The software sets up the ADCs and the DAC at the power-on time. Then, it enters a waiting loop for a command to be received through the serial communication (USART) with the computer of the robotic system. This communication was implemented by the USB to RS232 bridge built on the Arduino dev. Board. The serial receive event interrupt was programmed to wait for 8 ASCII characters, as shown in Fig. 5.14 and ignore anything else. Each character was used to call different functions to implement the required tasks.

Receiving (S) should be followed by a value between 0 and 2500 to set the approximate gripper voltage. This setting will not become active until two other command are received, so this value will be saved in a register. The “O” command runs a function to turn the relay on and connect the gripper to the system. To apply the voltage to the gripper, the previous function should be followed by sending the “P” command. The reason for this will be explained in the characterisation section of the interface unit. The “Q” command was used to clear the DAC value, but the gripper was still connected to the system. To disconnect the gripper, the “F” command was used to call the required function. Lastly the “T” command was used to trigger the Arduino to instruct the ADCs to sample and decode in the rate of 60 readings per second. The saved raw values were sent through the serial port to the robotic system by a function triggered by “R” command. Lastly, the “G” command was added to read a single sample from each ADC.

### *5.4.4 GUI Software*

This interface unit was integrated with the robotic manipulation system, as mentioned previously. The control computer has three different sections to be integrated with this interface unite. First of all, it is the UI program. This program was written using visual C++ using visual studio 2015, as shown in Fig. 5.15.

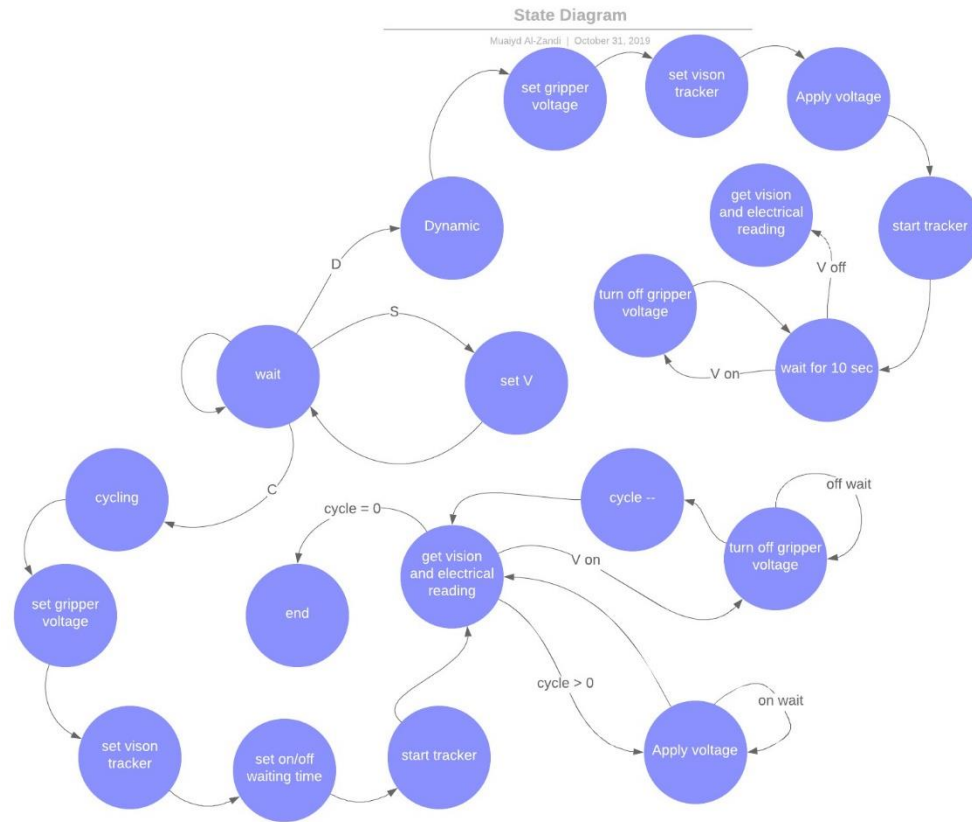


Fig. 5.16 UI state machine showing the flow of the states in this program

The software UI can be divided into three parts. The upper part is the common settings and configuration. The user should first run the interface, which is a program which was part of the robotic system, and it communicates directly with the Arduino Interface unit using RS232 and with the vision processing programs and cameras using Gigabit Ethernet. This software will be discussed later. Then, the user should initiate the communication with the interface by pressing the connect button. The value of voltage can be entered in the text box and sent to the Arduino through the interface by pressing the set button.

This software can be used either to get the dynamic response of the microgripper or to study its behavior in cycling tests in reliability studies. To start the dynamic study, no more setting is required, just press the start button and the status bar will show the progress of the measurement process. This software will run the test for 10 seconds in the gripper “ON” state and the length of same time for “OFF” state to measure the gripper tip deflection as a function of time for a given applied voltage. To start a cycling study, three more

settings are required. The period of ON state and OFF state is set for three seconds or more because the minimum acceptable value is 3 seconds for each. Then, the last setting is the number of cycles before terminating the test. The status bar will show the progress during the test.

Fig. 5.16 shows the state machine of the UI program. The program is idle in a waiting state until it is connected to the interface software. This communication is based on the internal TCP/IP protocol. The software can set two directions depending on which testing is going to be implemented. Then, in each path there are several functions which are called in a sequence depending on the user entered settings. In this software ASCII characters were also used as commands to trigger the functions of the robotic system.

#### *5.4.5 Robotic System Integration*

There were two pieces of Java software written for the robotic controller system. First, a software program was designed to request the tracking area position from the video processing part. The second program was to communicate with the Arduino and synchronise the commands, so all run simultaneously. Each software program communicates with the UI through internal TCP/IP. The vision software communicates with the video processing program through some defined modules in the robotic system, while the Arduino uses the hardware serial port.

As soon as the interface software was called by the pressing running interface in the UI software, the video processing software and the UI were called, as shown in Fig. 5.17 (f). The screen shows a link to set up the tracking area of the microgripper. On clicking this link a video screen from the microscope will appear, then the user can select the tracking area and area of interest, as shown in Fig. 6.8(a). As soon as the first link is set, a new link appears for the second setting. By clicking “Connect”, the Serial Java sets up communication with Arduino board. When the test starts, each Java software will automatically set the commands and acquire data from the camera connected to the microscope and the ADCs.

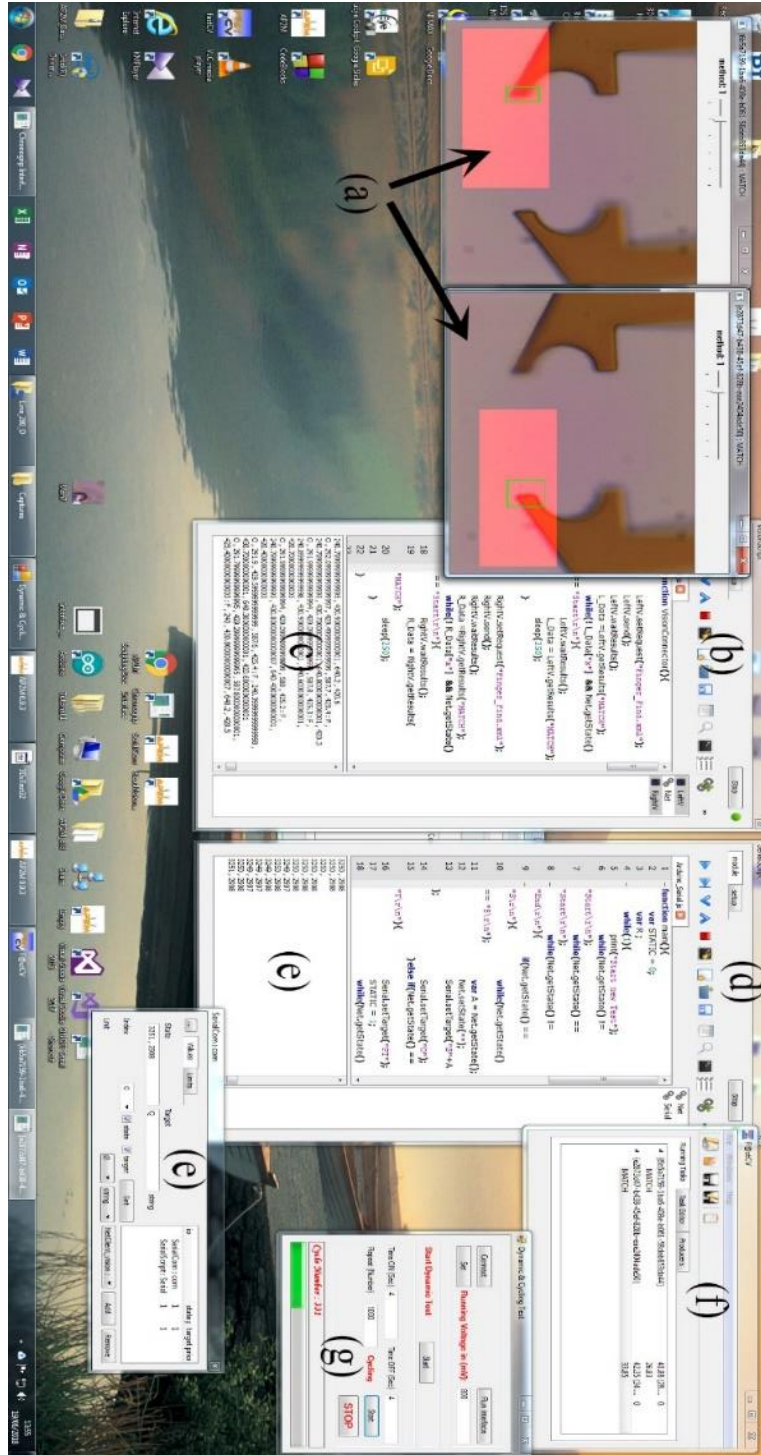


Fig. 5.17 Example of running the cycling test on one of the microgrippers (a) shows the video processing track function interface (b & c) the video processing Java software and the result respectively (d & e) the Arduino Java control and the raw data from the ADCs respectively (f) the video processing UI run the FastCV lib (g) C# UI (e) serial communication control module

The UI sends one command at a time then each of the two pieces of the Java software interprets it into commands to be sent to the microscope video processing software and the

Arduino interface unit, as shown in Fig. 5.18 and Fig. 5.19. The ASCII characters sent by the UI through the TCP/IP protocol are received by the robotic software in a buffer. This buffer is readable by both Java software programs and translated into different execution functions.

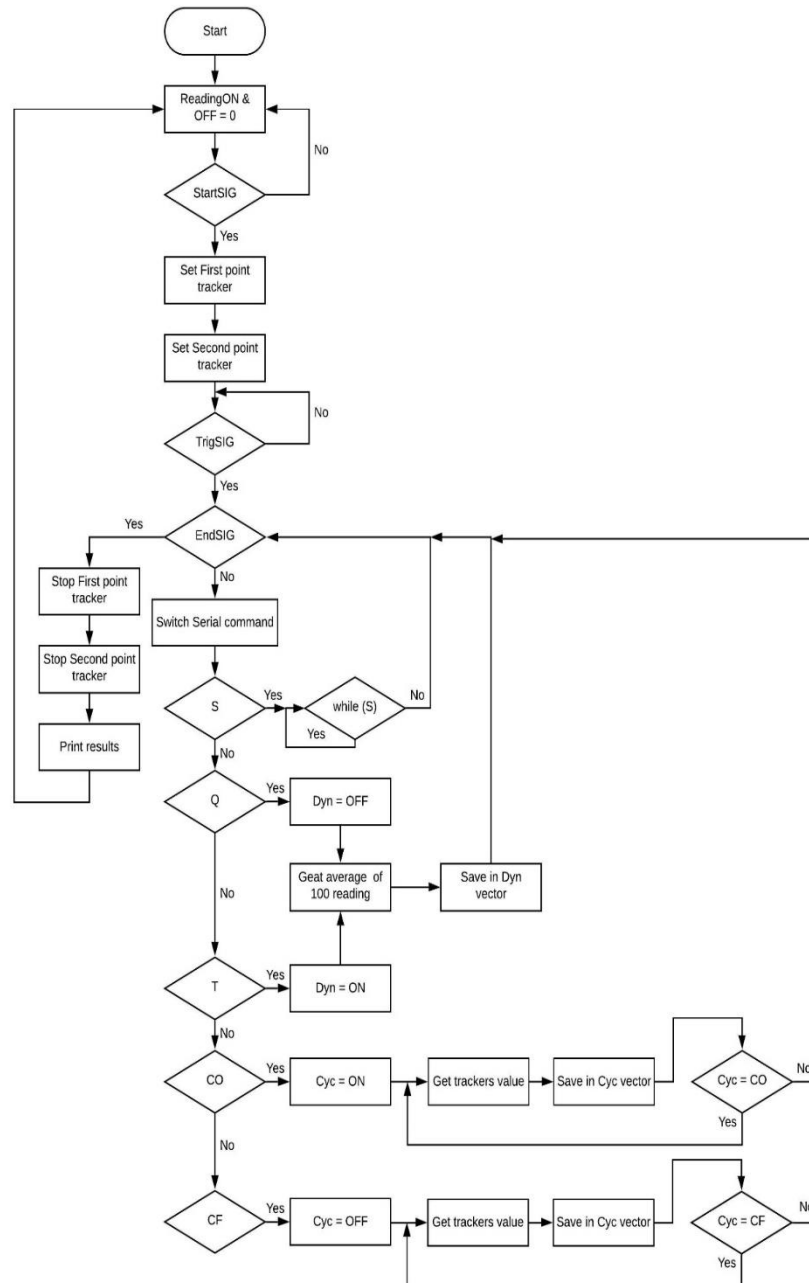


Fig. 5.18 Flow chart shows the Java software structure of communication with the microscope through the video processing lib to send commands and fetch results

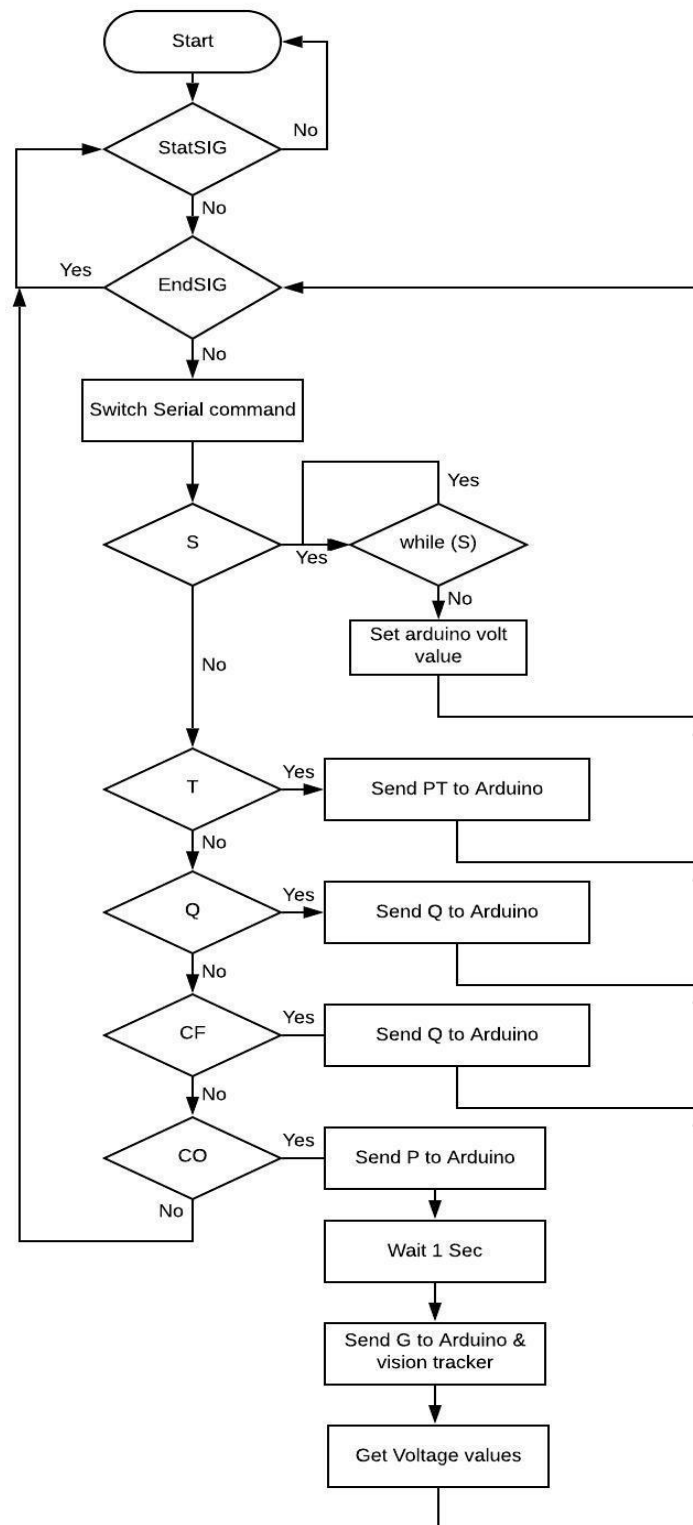


Fig. 5.19 Flow chart shows the Java software structure of communication with the Arduino to send commands and acquire results

#### 5.4.6 Interface Unit Characterisation

The first design was based on a relay to provide power to the microgripper, but after testing the timing it was discovered that it took about 100 ms to switch on and there was fluctuation. However, using a DAC to supply voltage and hence power to the microgripper gave a much faster and stable output. Fig. 5.20 and Fig. 5.21 show the testing of the output voltage using an oscilloscope. There was a delay of 100  $\mu$ s between the end of the serial command and the DAC output response. This delay is processing time of the Arduino board. The output voltage had a slew rate of about 5  $\mu$ s.

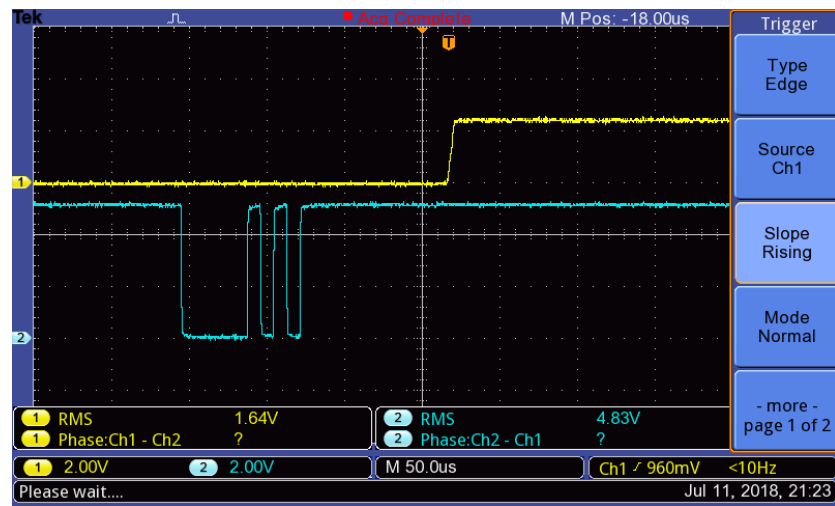


Fig. 5.20 Arduino output delay after receiving the serial commands where the blue signal represents the UART and the yellow signal represents the microgripper voltage

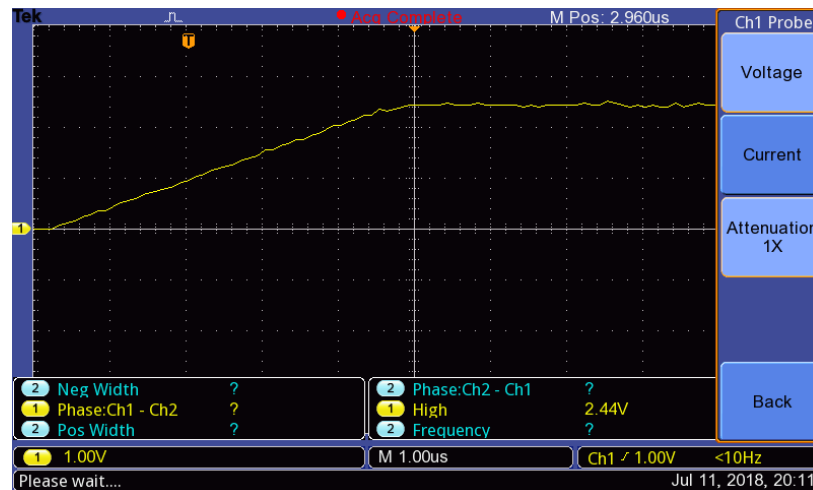


Fig. 5.21 Microgripper voltage rising when the DAC was powered



#### *5.4.7 Measurement Method*

This section presents the method for dynamic study of selected microgrippers. In addition, there is a case study of one design with different configurations to study the effect of actuator stiffness on the microgripper behavior and response to get sufficient understanding.

The interface unit described in the previous sections in this chapter was used to implement the study. An X5 microscope objective was used with the optical system of the vision system producing a pixel resolution  $0.334\text{ }\mu\text{m}$  without software magnification. Each selected microgripper for this study was mounted on a microscope slide using same method described previously. The interface unit was configured to drive the supply voltage just enough to raise the heater temperature of the microgripper to  $\sim 170^{\circ}\text{C}$ . The selected ON/OFF time was set to be 5 seconds. Then, the image tracking data was analysed using Microsoft Excel. The sampling interval was about every 15 ms which was limited by the tracking software and the computer of robotic system. However, sixty six samples per second are not very fast, but it is enough to record the mechanical behavior over the 10 seconds of interest. Then a 5 sample moving average filtering method was selected to smooth the dynamic responses to reduce the effect of overshooting in the results. However, the first five samples were used as obtained and the averaging started after sample number 5.

### **5.5 Method for Reliability Study**

This section presents the method that was developed to study the reliability and lifetime of the microgrippers. It was based on testing of the number of on/off cycles before failure under given operating conditions and analysis of failure modes. The Arduino based interface unit described previously was used to conduct controlled experiments. Each selected microgripper was cycled in ON/OFF operation for 10 seconds in each status. The selected applied voltage was just enough to raise the average heater temperature to  $150^{\circ}\text{C}$ . The system was programed to wait for one second after each power ON and OFF cycle to allow calculation of the average of 100 readings of the position of the end-effector.

## **5.6 Summery**

The displacement measurements of all of the previous work in literature on microgrippers were based on pixel calculation using image editors or any other software that provides pixel information, i.e. which was a time consuming process. In this research, an image tracking software was employed to measure the displacement in addition to the Zygo system. Although the image tracking method was based on pixel calculation, the process was done instantaneously, and there was no additional step required to do the analysis. As a result, many microgrippers could be studied in a short time.

## Chapter 6 Results, Analysis and Demonstration

A new automated method was developed to measure the dynamic behavior and the reliability of the different microgrippers. For this purpose, an electronic interface was designed, assembled, and integrated into the robotic system. Then, four pieces of software were written in Visual C++, Embedded C, and Java script to manage the control and communication and to save the results. Results, Analysis and Demonstration

This chapter presents the characterization results of the study of different microgrippers designed by IMT as listed in Table 5-1 and those designed in the thesis work listed in Table 5-2. First of all, the results of the steady state displacement and actuator temperature are presented. Then, the dynamic responses and the results of lifetime measurements are described and discussed. The results of demonstration of the microgrippers for microassembly application are presented.

### 6.1 Temperature and Displacement Measurements of IMT Designs

#### 6.1.1 Design IMT-A

This design was tested to measure the displacement in both methods - Zygo and the robotic system. Fig. 5.9 and Fig. 6.1 show images taken using these systems. These show the displacements at no power and maximum power at maximum applied voltage of about 650 mV.

The measurement results using both systems show a maximum displacement of about 10  $\mu\text{m}$  when a voltage of about 650 mV was applied, and the average heater temperature was about 190 °C. The results are presented in Fig. 6.2 - Fig. 6.5. The horizontal error on the robot measurement was based on the difference of the TCR measurements and the resistance tolerance of the series resistor, while the vertical error was based on  $\pm$  one pixel.

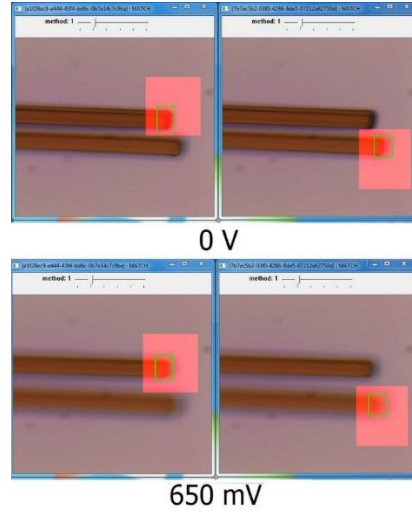


Fig. 6.1 Pictures taken by the Chronogrip robotic system to carry out the displacement measurement using the integrated vision processing software. The two pictures were taken on different applied voltages and show the traced area in the green square.

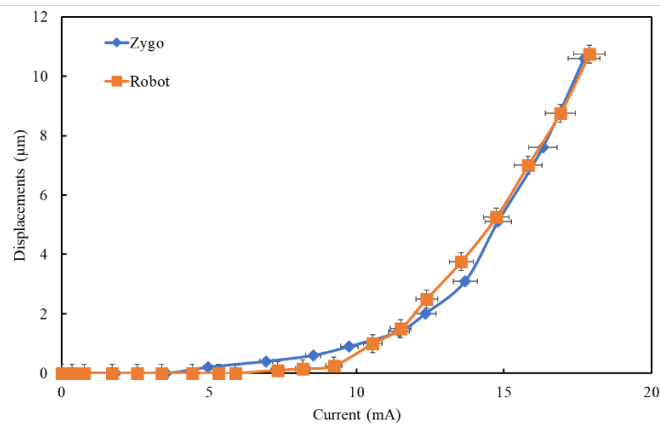


Fig. 6.2 Comparison of displacement results as a function of the applied current from the two measurement systems on design (A)

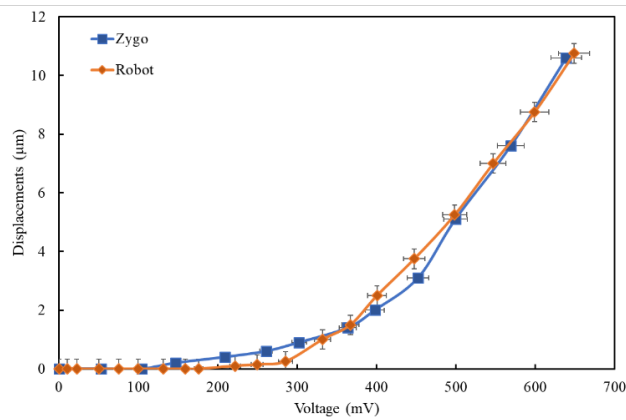
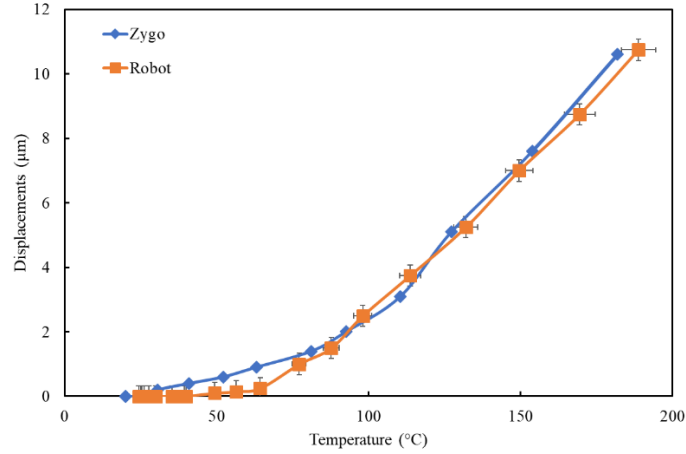
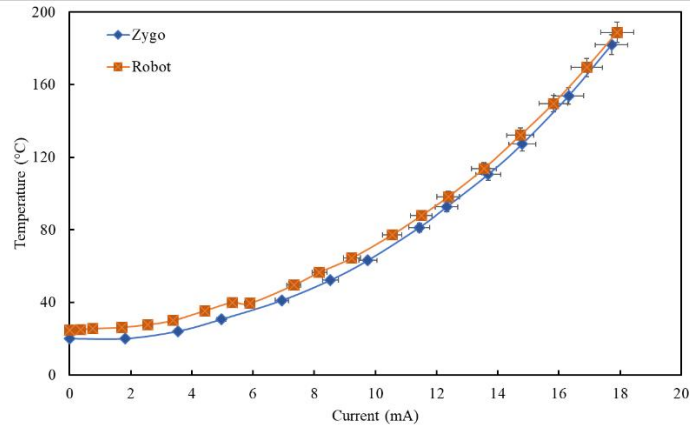


Fig. 6.3 Comparison of displacement results as a function of the applied voltage from the two measurement systems on design (A)



*Fig. 6.4 Comparison of displacement results as a function of the applied current from the two measurement systems on design (A)*



*Fig. 6.5 Design (a) average heater temperature as a function of the applied current*

An important advantage of the tracking method to measure the displacement is that the output of the software is in coordinates, i.e. the displacement of each end-effector can be measured individually in both directions – in-plane deflection and along the gripper arm. Fig. 6.6 shows the displacement of the end-effectors along each gripper arm as a function of the applied current. The results show that there is displacement along the direction of each gripper arm although it is small. There is also displacement in the cold arms.

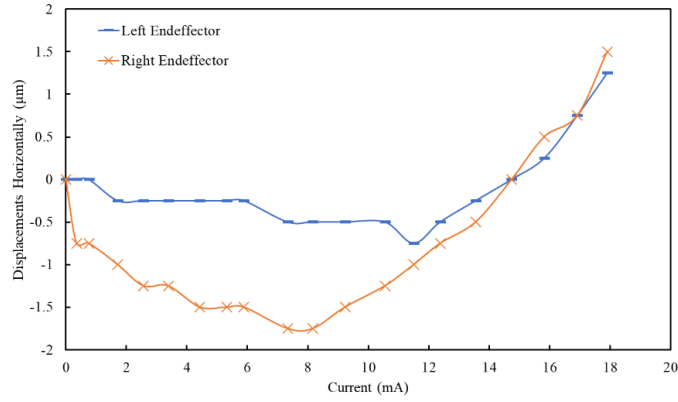


Fig. 6.6 Horizontal displacement of each end-effectors

### 6.1.2 Design IMT-B & IMT-C

Fig. 6.7 - Fig. 6.9 show images of both designs tested using the Zygo and robotic systems. Fig. 6.10 shows the displacement and the average temperature as a function of the applied voltage. The temperature increase in both designs was similar because the heater and the actuator shape and dimensions are similar. The initial opening was 18  $\mu\text{m}$  and 17  $\mu\text{m}$  for design B and design C respectively. It decreased to 9  $\mu\text{m}$  and 15  $\mu\text{m}$  while the voltage increased to about 650 mV for design B and about 450 mV for design C respectively. After that, the opening increased sharply when the hot arm expansion exceeds the cold arm expansion.

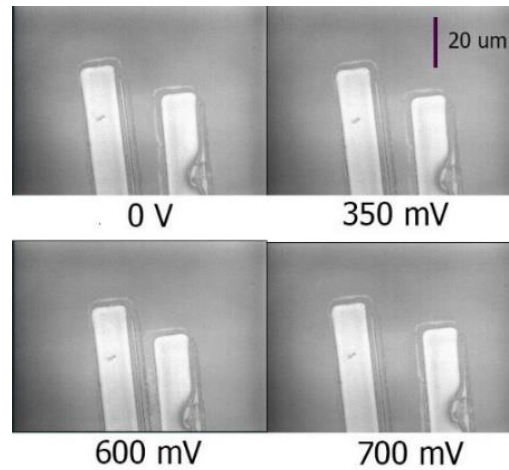


Fig. 6.7 Images taken using the Zygo system for design (B) and showing the end-effectors in different situations.

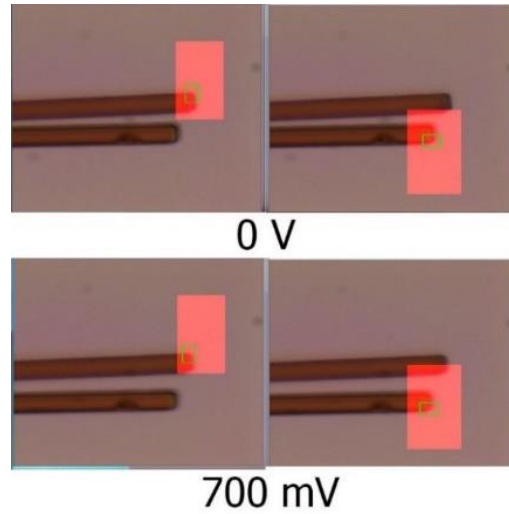


Fig. 6.8 Robotic measurement of design (B). The two pairs of images show the end effectors with and without an applied voltage. The green area is the tracking part to measure the change in the position. The red area is the search area of the tracked part

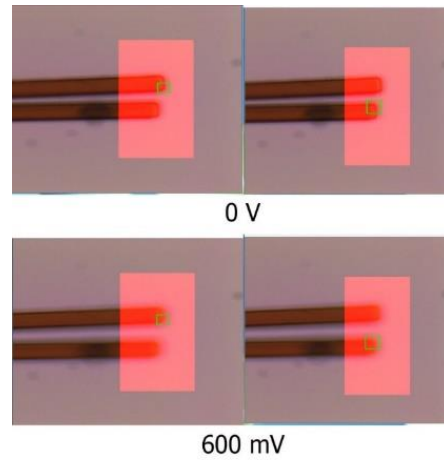


Fig. 6.9 Design (C) when it was tested using the robotic systems

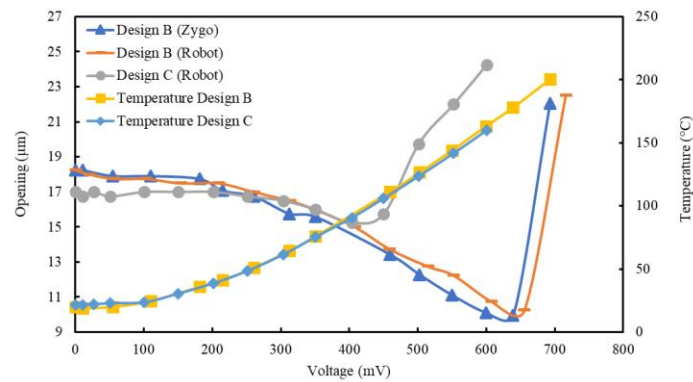
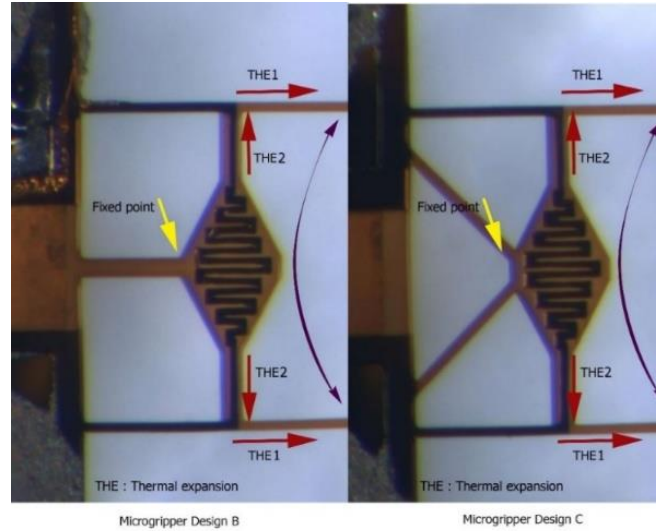


Fig. 6.10 Displacement and heater average temperature measurements of design (B and C) as a function of the applied voltage measured using Zygo and robotic system



*Fig. 6.11 Two different expansion effects in these microgrippers on the end-effector displacements. The first expansion comes from the cold arm (THE1) while the other comes from the actuator (THE2). The first expansion has the effect of closing operation while the second has the effect of opening operation on these microgrippers. As a result, the final displacement is the difference between the two effects*

These two designs were proof that the cold arms are not really cold. There was enough temperature to generate expansion to change the expected behavior. The end-effector displacements of both designs show that the gripper arms shrink or contract at low applied currents. Fig. 6.11 shows the reason for this behavior. There are two different expansions and each one affects the end-effectors in a different direction. Because of the fixed point is in the middle of the actuator, the first thermal expansion THE1 was amplified and affected the inverse direction of the thermal expansion THE2.

### 6.1.3 Design IMT-D

This design differs to the other by its mode of operation. This is normally open design, and it closes when a power is applied. This design was characterised using both measurement methods. Fig. 6.12 shows the image taken using the Zygo system on three occasions. These were at no voltage applied, 300 mV and 600 mV. Fig. 6.13 shows images taken during the testing using the robotic systems on two occasions: no applied voltage and 600 mV.



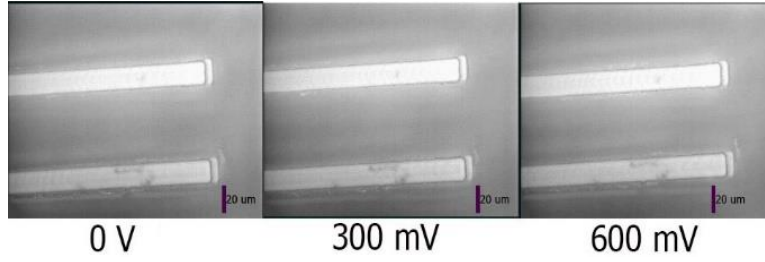


Fig. 6.12 Displacement measurements of design D using the Zygo system in different applied voltages

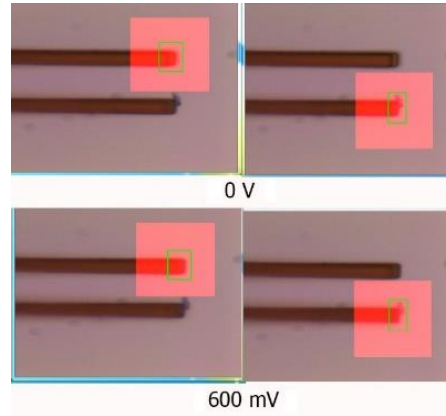


Fig. 6.13 Displacement measurements of design (D) using the image processing on the robotic system

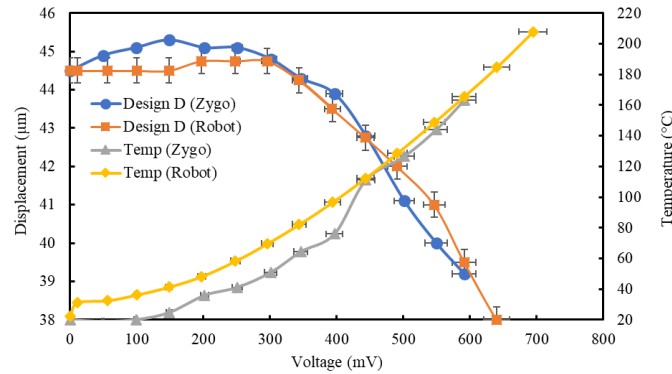


Fig. 6.14 Displacement and temperature as a function of the applied voltage for design D measured using the two testing methods

Fig. 6.14 shows the results of displacement measurements and the calculated temperature as a function of the applied voltage. The initial opening was about  $44\text{ }\mu\text{m}$  at room temperature and it decreased by about  $8\text{ }\mu\text{m}$  when a voltage of about  $600\text{ mV}$  was applied. The temperature at this voltage was about  $210\text{ }^{\circ}\text{C}$ . In addition to the displacement measurements, the expansion in the cold arms was also measured, as shown in Fig. 6.16 as a function of the applied voltage.

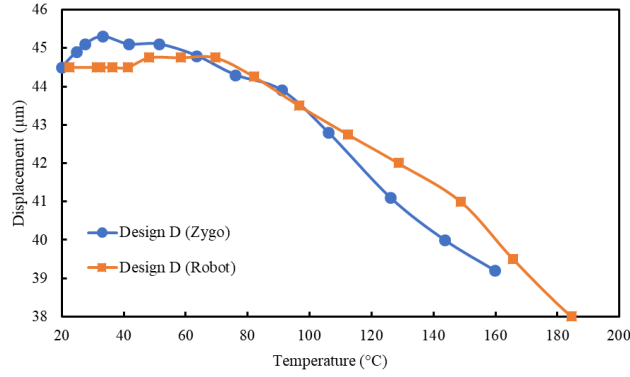


Fig. 6.15 Displacement and temperature as a function of the average heater temperature for design D

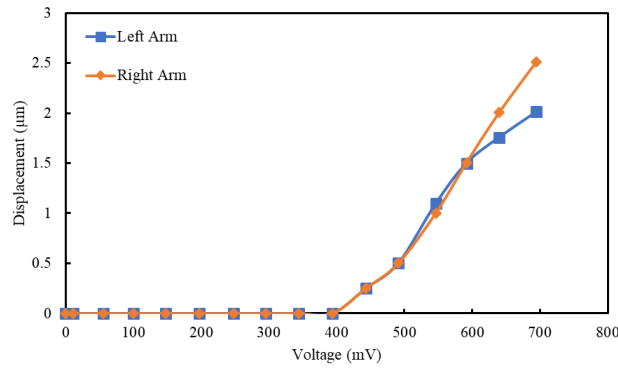


Fig. 6.16 End-effectors horizontal displacement measured using the robotic system

#### 6.1.4 Design IMT-E

This design was tested using both systems (Zygo and robotic system), as shown in Fig. 6.17 and Fig. 6.18. The microgripper openings at room temperature measured using the Zygo system and the robotic system for this design were 30.5  $\mu\text{m}$ , 30.1  $\mu\text{m}$ , and 49.2  $\mu\text{m}$  labeled A, B, and C respectively. When power was applied on the microgripper, the opening was increased. At an applied voltage of about 650 mV, the displacement increased to 50.75  $\mu\text{m}$ , 46.75  $\mu\text{m}$ , and 67  $\mu\text{m}$  for point A, B, and C respectively. The measured temperature was about 200  $^{\circ}\text{C}$ . These results are shown in Fig. 6.19 and Fig. 6.20.

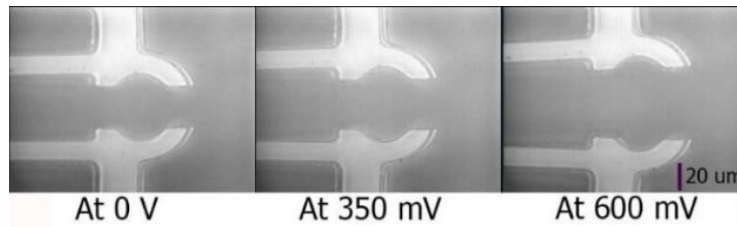


Fig. 6.17 Zygo measurement of design E

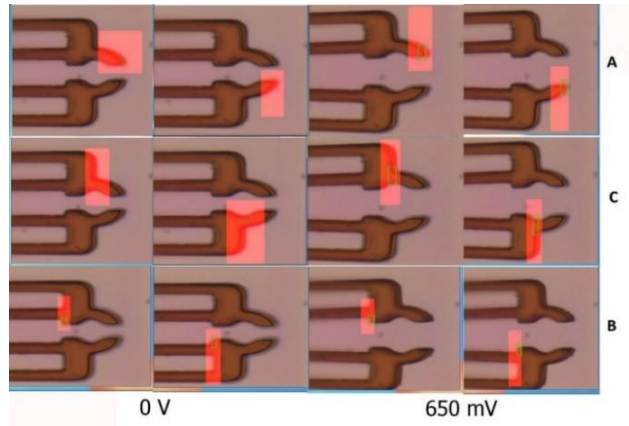


Fig. 6.18 Robotic measurement of three points simultaneously on two conditions - when the microgripper was off and while a 650 mV was applied

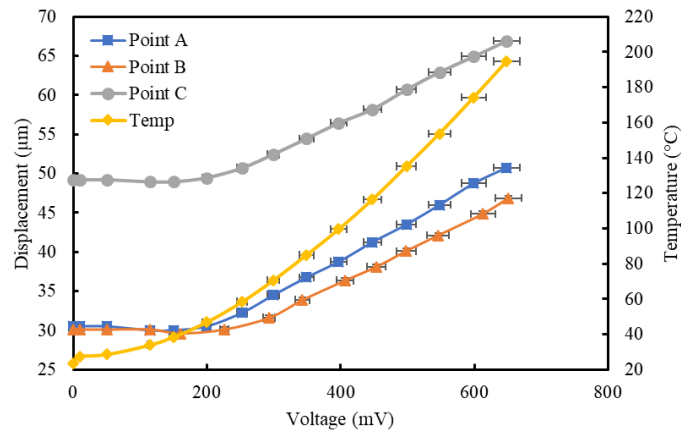


Fig. 6.19 Robotic test of design (E) displacement result at three points as a function of the applied voltage

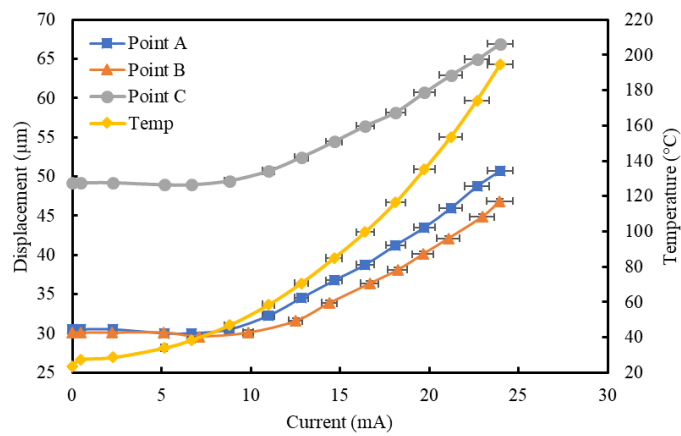


Fig. 6.20 Zygo test of design (E) displacement result at three points as a function of the applied current

### 6.1.5 Design IMT-F (with Vertical Actuator)

Fig. 6.21 shows another IMT design. This design was based on a new actuation method similar to Design-E but with one large vertically situated actuator in the middle. The robotic system was used to characterise this design and measure the displacement. Fig. 6.22 and Fig. 6.23 show the displacement and temperature results as a function of the applied voltage and current respectively. The initial opening of this design was about 25  $\mu\text{m}$  and it works as a normally closed design and the gripper arms open when a voltage is applied. The opening was increased by about 30  $\mu\text{m}$  when a voltage of about 550 mV was applied, and the average temperature was about 160  $^{\circ}\text{C}$ .

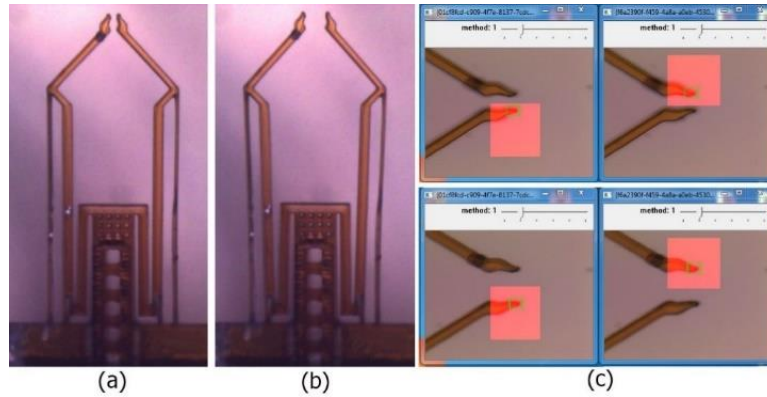


Fig. 6.21 IMT design with vertical microheater (a) is with off power (b) with applied voltage of 550 mV (c) picture from the robotic system showing the microgripper in the two previous conditions

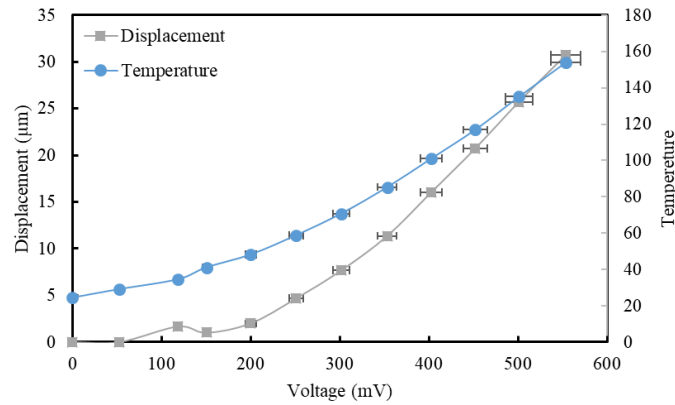


Fig. 6.22 Displacement and temperature as a function of the applied voltage for design F using the robotic system

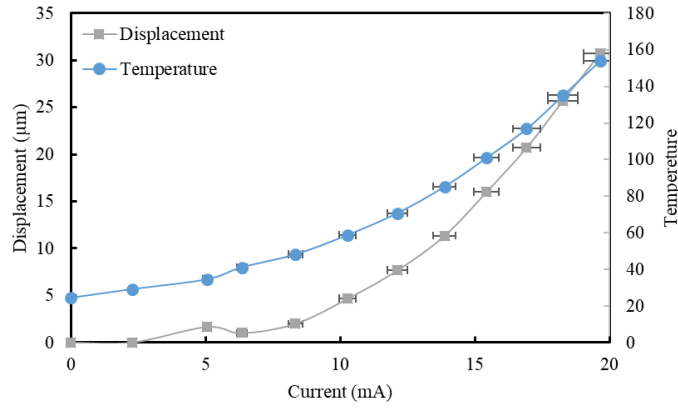


Fig. 6.23 Displacement and temperature as a function of the current passed for design F using the robotic system

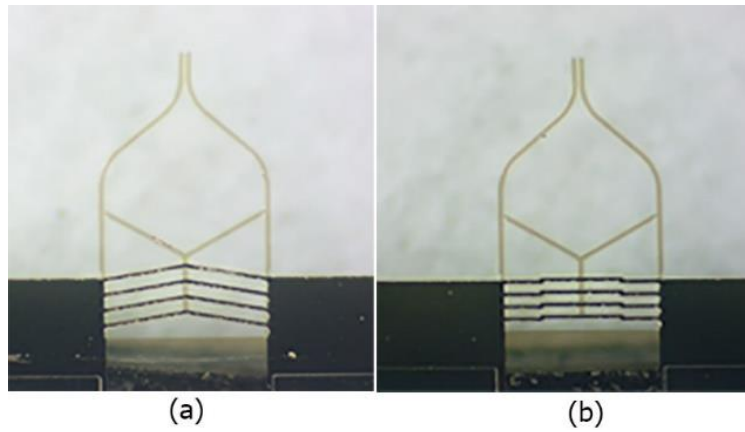


Fig. 6.24 Optical images of the fabricated IMT developed design A actuated using (a) V-shaped actuator (b) Z-shaped actuator

#### 6.1.6 Design IMT-G and Design IMT-H

Fig. 6.24 shows two microgrippers of these designs. Both were a development of design A using a new actuation mechanism based on the V- and Z- shaped types. Both designs were characterised using the robotic system. The initial opening for both designs was about 3  $\mu\text{m}$  and both designs were based on the normally open mode of operation. By applying a voltage of about 370 mV, the opening was increased to about 45  $\mu\text{m}$  and 40  $\mu\text{m}$  for the V-shaped and the Z-shaped microgrippers respectively. The average temperature in both designs at the applied voltage was about 160  $^{\circ}\text{C}$ . Fig. 6.25 and Fig. 6.26 show the displacement and temperature results as a function of the applied voltage and current respectively.

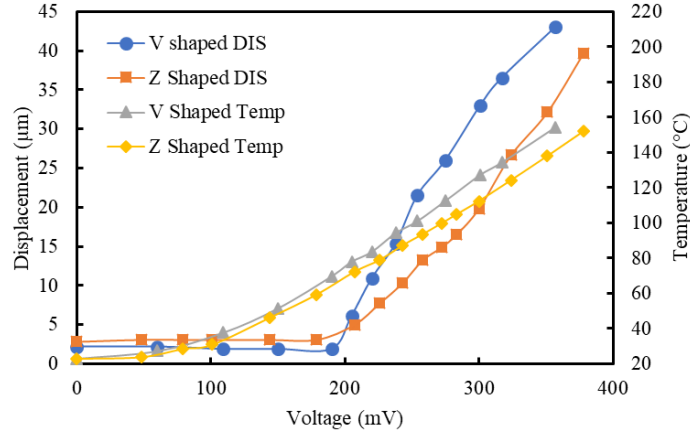


Fig. 6.25 Design V and Z microgripper test results of displacement and temperature as a function of the applied voltage

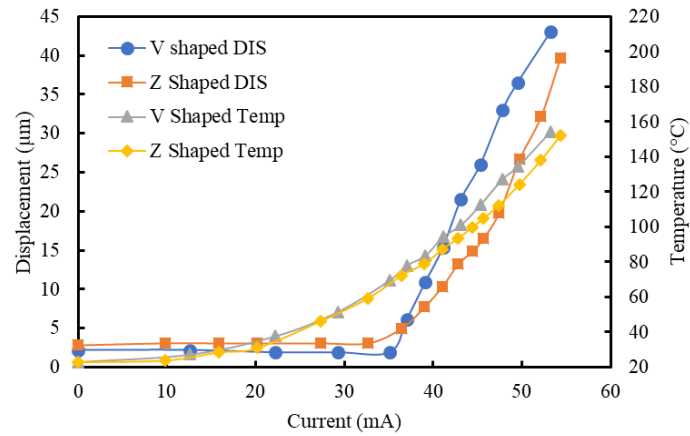
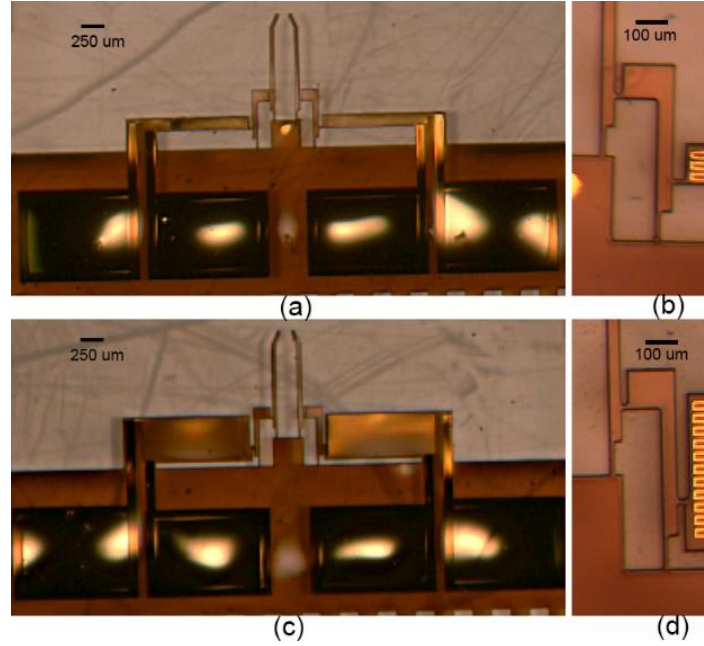


Fig. 6.26 Design V and Z microgripper test results of displacement and temperature as a function of the applied current

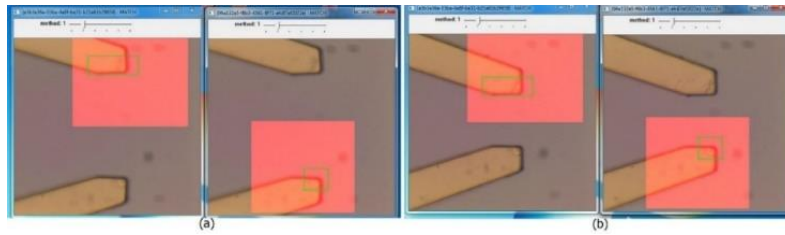
## 6.2 Temperature and Displacement Measurements of Heriot-Watt Designs

### 6.2.1 HWU-A: Indirect Actuator Based Microgripper Design

Fig. 6.27 shows two microgrippers based on different actuator designs. These designs were based on the new actuation method which was proposed in Chapter 3. The interface connects the actuator with the arm and translates the expansion into end-effectors displacement. In addition, it reduces the heat transfer from the actuators into the arms. However, the main insulation in this method was to remove any conductor section from the cold arms.

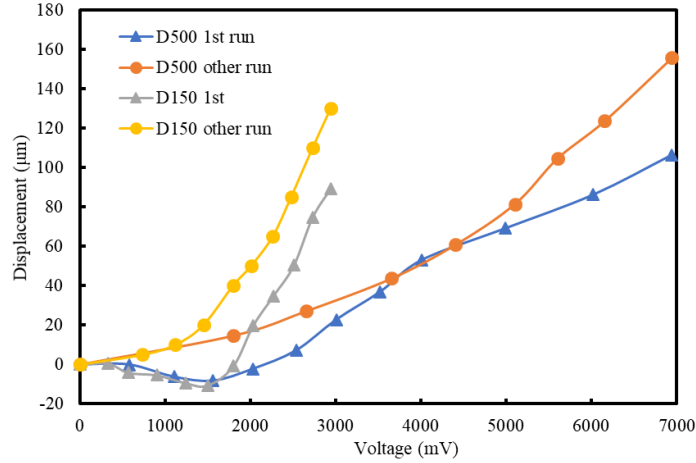


*Fig. 6.27 (a & c) Interfaced actuator microgripper with two actuator width (b & d) are the interface part between the actuator and the arms*



*Fig. 6.28 Interfaced actuator microgripper displacement measurement using the robotic method (a) 0 V is applied (b) 1.2 V is applied*

These designs were tested using the robotic system, as shown in Fig. 6.28. The opening after each first run increased for several cycles, however it restores some of this after a long rest time (one day or longer). The opening of the first design with an actuator width of 150  $\mu\text{m}$  was increased each time it operated for several cycles. After the first run, the opening increased by about 80  $\mu\text{m}$  and after a long rest, it was restored to about 70% of this increment. After several operations, the initial opening increased from 120  $\mu\text{m}$  to about 200  $\mu\text{m}$ , and then after long period it restored to 120  $\mu\text{m}$ . Then the opening increased each operation after this test by about 60  $\mu\text{m}$  when powered for first time after a long rest. This increment was able to be restored after a long rest time. The other design with an actuator width of 500  $\mu\text{m}$  behaved in the same way. However, the opening increased to about 200  $\mu\text{m}$  for first several cycles. Then it was increased by about 40  $\mu\text{m}$  each time powered.



*Fig. 6.29 Displacement as a function of the applied voltage obtained using the robotic system. D150 and D500 refers to the actuator width 150  $\mu\text{m}$  and 500  $\mu\text{m}$  respectively. This chart shows the displacement result of the first cycle and the cycles after that.*

Fig. 6.29 and Fig. 6.30 show the displacement results of both designs (D150 for the microgripper with a actuator width of 150  $\mu\text{m}$  and D500 for the microgripper with a actuator width of 500  $\mu\text{m}$ ) as a function of the applied voltage and the corresponding current respectively. Fig. 6.31 shows the displacement related to the measured average heater temperature. The first cycle in both designs shows a negative displacement at the low applied current, then the opening decreased sharply. After the first cycle, the negative displacement disappeared in both designs, and the displacement increased linearly as a function of the heater temperature. This behavior was repeatable after leaving the microgripper for a long time before the next measurement was made.

Fig. 6.32 shows the measured temperature as a function of the applied current. The results show a quadratic behavior between the temperature and the applied current. Fig. 6.33 shows only negative displacement on the longitude direction of the arms. This is due to the horizontal displacement and proves there is no expansion in the cold arms because there is no current heater section in the cold arms.



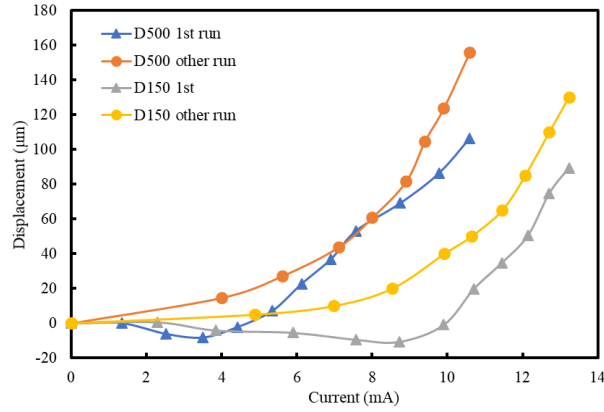


Fig. 6.30 Displacement as a function of the applied current obtained using the robotic system. D150 and D500 refers to the actuator width 150  $\mu\text{m}$  and 500  $\mu\text{m}$  respectively. This chart shows the displacement result of first cycle and the cycles after that.

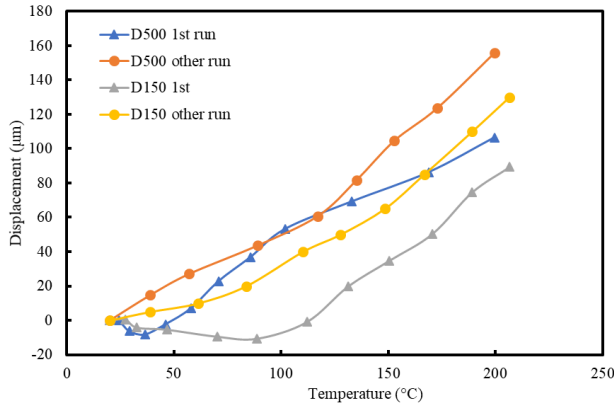


Fig. 6.31 Displacement as a function of the average heater temperature measured using the heater TCR and the resistance obtained using the robotic system. D150 and D500 refers to the actuator width 150  $\mu\text{m}$  and 500  $\mu\text{m}$  respectively. This chart shows the displacement result of first cycle and the cycles after that.

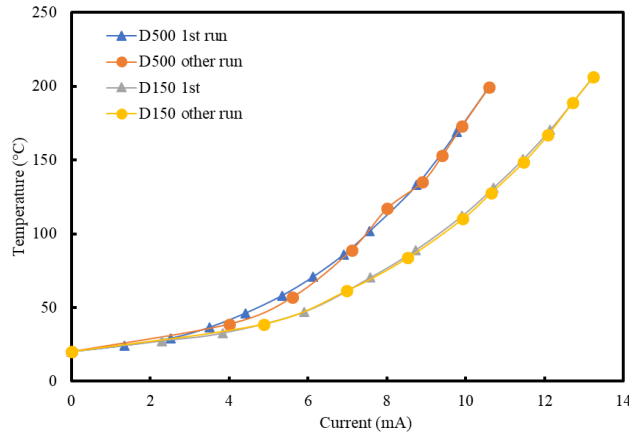


Fig. 6.32 Heater average temperature as a function of the applied current obtained using the robotic system. D150 and D500 refers to the actuator width 150  $\mu\text{m}$  and 500  $\mu\text{m}$  respectively. This chart shows the heater temperature result of first cycle and the cycles after that.

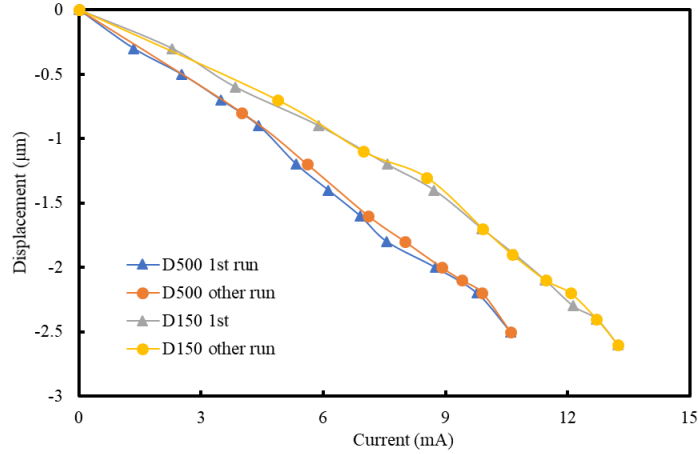


Fig. 6.33 Cold arm expansion as a function of the applied current obtained using the robotic system. D150 and D500 refers to the actuator width 150  $\mu\text{m}$  and 500  $\mu\text{m}$  respectively. This chart shows the expansion result of the first cycle and the cycles after that.

### 6.2.2 HWU-B: One Mode Microgripper

This microgripper was designed in eight different variants with two main groups depending on the heater conductor shape, as shown in Fig. 3.5 and listed in Table 3-1. However, the fabricated microgrippers have different conductor layer thicknesses of 7/200/7 nm of chromium/gold/chromium while the simulation was 10/300/10 nm. Fig. 6.34 shows optical images of two variants of the meander heater design, one with a actuator width of 100  $\mu\text{m}$  and the other with 210  $\mu\text{m}$  of actuator width. These two designs have two variants each where the actuator width in one variant is twice of that of the other variant. The thicknesses of the actuator in all the four variants are the same as 20  $\mu\text{m}$ . These microgripper designs were named M100D, M100S, M210D, and M210S, where M is the folded meander heater design, D denotes double structure thickness (20  $\mu\text{m}$ ) as compared with the other variant with the S (single) (10  $\mu\text{m}$  thickness of the structure except the actuator which is 20  $\mu\text{m}$ ). The other group were named L100D, L100S, L210D, and L210S, where L means single meander hear design, D and S have the same meanings as before.

Fig. 6.36 and Fig. 6.37 show the displacement measurements using both robotic methods to study these designs. Fig. 5.45 shows the results obtained using of the image tracking method while Fig. 5.46 shows the results using the ruler based method.

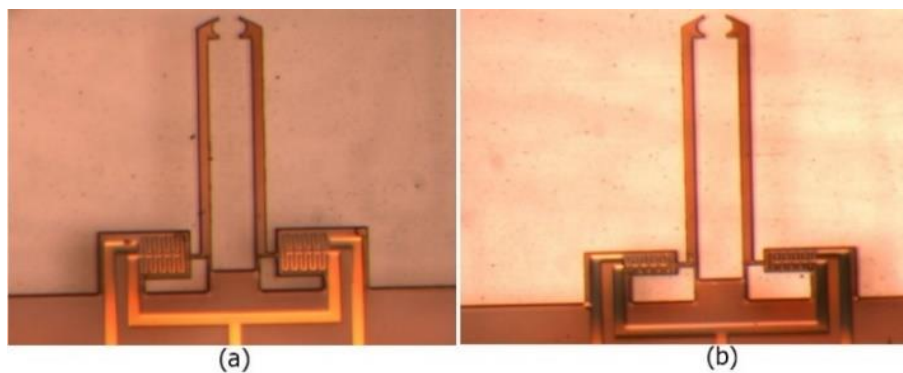


Fig. 6.34 1 DOF direct actuated microgripper optical images for two different actuator widths of meander heater (M) design (a) actuator width is  $210\ \mu\text{m}$  and (b) is  $100\ \mu\text{m}$ .

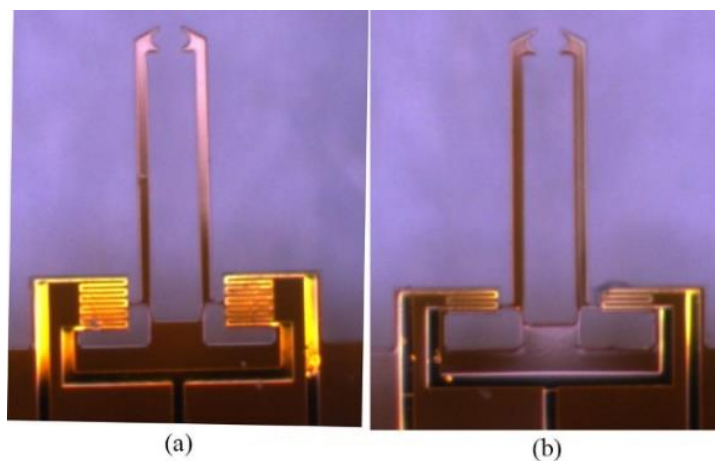


Fig. 6.35 Directly actuated microgripper optical images for two different actuator widths of linear heater (L) design (a) heater width is  $210\ \mu\text{m}$  and (b) is  $100\ \mu\text{m}$ .

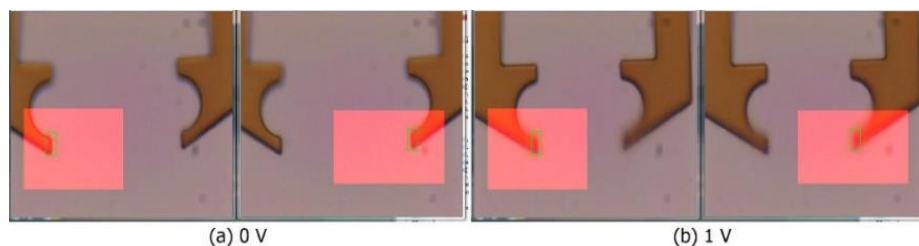


Fig. 6.36 1 DOF direct actuated microgripper using the robotic method showing two test conditions

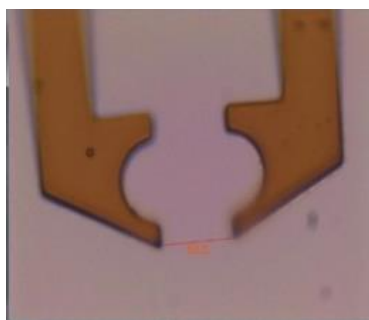


Fig. 6.37 Measuring the opening of 1 DOF direct actuated microgripper using the robotic system

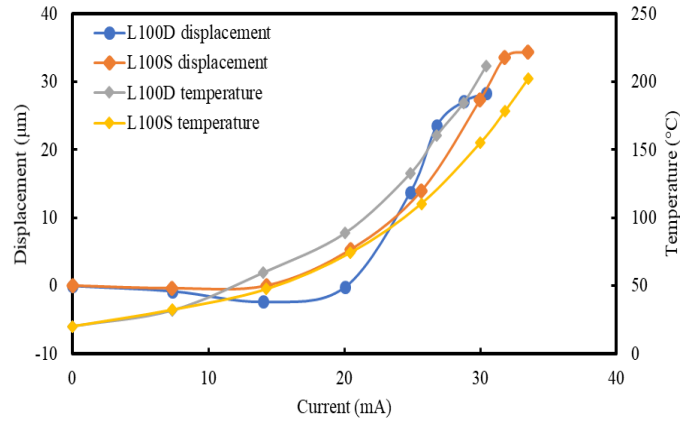


Fig. 6.38 Displacement and temperature as a function of the applied current for a linear shaped heater with a width of 100  $\mu\text{m}$  for both designs of arm with single layer and double layers

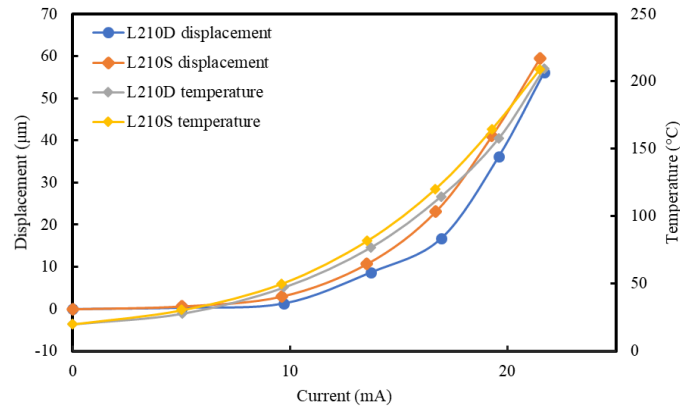


Fig. 6.39 Displacement and temperature as a function of the applied current for a linear shaped heater with actuator width of 210  $\mu\text{m}$  for both designs of arm with single layer and double layers

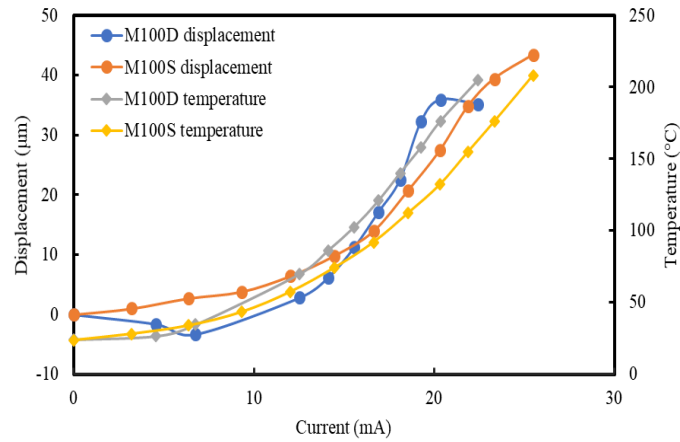


Fig. 6.40 Displacement and temperature as a function of the applied current for meander shaped heater with actuator width of 100  $\mu\text{m}$  for both designs of arm with single layer and double layers

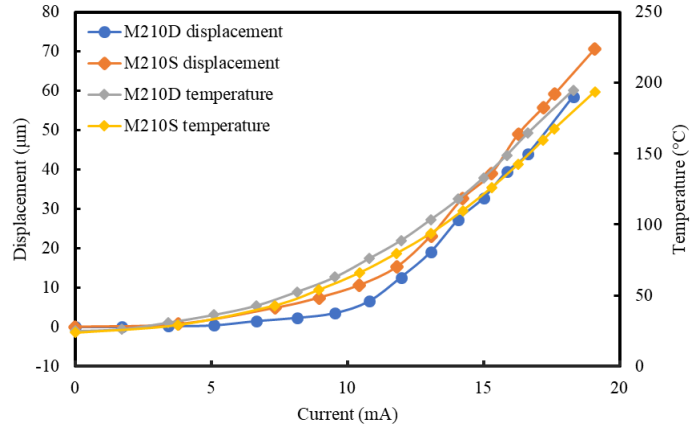


Fig. 6.41 Displacement and temperature as a function of the applied current for a meander shaped heater with actuator width of 210  $\mu\text{m}$  for both designs of arm with single layer and double layers

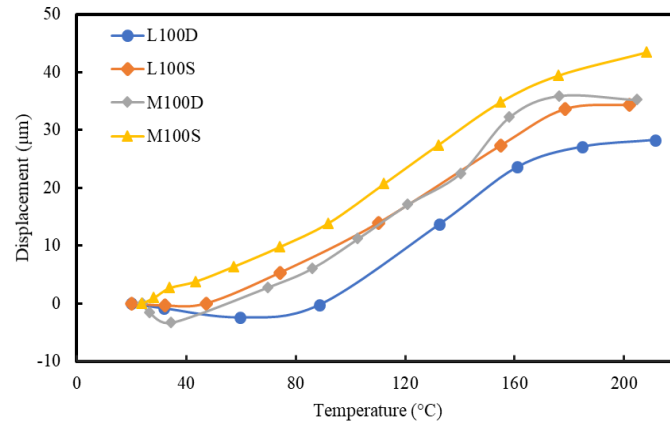


Fig. 6.42 Displacement result of the four microgripper variants with actuator width of 100  $\mu\text{m}$  as a function of the average heater temperature for the microgrippers

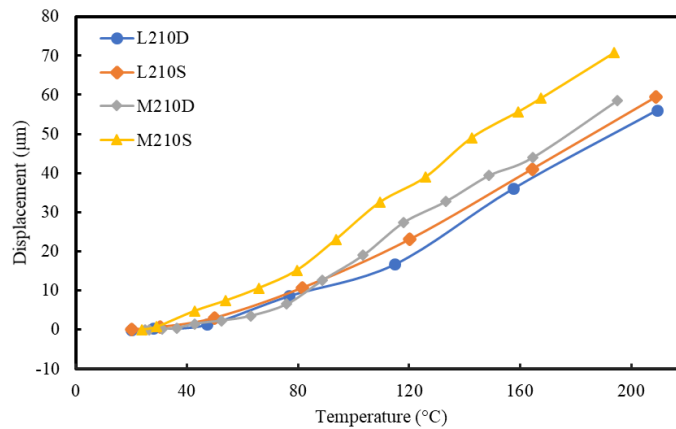


Fig. 6.43 Displacement result of the four microgripper variants with actuator width of 210  $\mu\text{m}$  as a function of the average heater temperature for the microgrippers

The results of displacement as a function of the applied current for all of the eight different designs are shown in Fig. 6.38 to Fig. 6.41. Fig. 6.42 and Fig. 6.43 show the displacement as a function of the average heater temperature showing the behavior with the actuator width. All the average temperatures of the microgripper showed nonlinear increase as the applied current.

All of the microgrippers with 100  $\mu\text{m}$  of actuator width behaved in the same way. The displacement trend can be divided into three parts when the current was increased. At the low current region (less than 5 mA for design M210, less than 10 mA for design L210 and M100, and less than 20 mA for design L100), all of the microgrippers show a negative displacement except design M100S. This design had a gradual increase in displacement at the low applied current. Then, at medium applied current (between 5 and 15 mA for design M210, between 10 and 20 mA for design L210 and M100, and between 20 and 30 mA for design L100), all the designs with 100  $\mu\text{m}$  actuator width had a faster increase of the displacement. At the higher applied current, the displacement showed a gradual increase.

The other microgrippers with wider actuators showed no negative displacement and the trends in all of these designs was a second order polynomial function with the applied current. However, by comparing the results as a function of the average heater temperature as shown in Fig. 6.43, there are some differences. The 100  $\mu\text{m}$  designs showed similar responses as a function of the current, except design M100S. This design showed linear behavior until the average heater temperature was about 170°C and then less increase of displacement.

The trend for all 210  $\mu\text{m}$  actuator width microgrippers is close to linear behavior with a slow increase below 80°C and becoming faster above this temperature. The characteristics are closer except M210S. This design showed larger displacement at the same temperature. The best performance in the L design group is L210S and the best in the M group is M210S. Fig. 6.44 and Fig. 6.45 show the comparison between these two designs as a function of the temperature and the applied current respectively. Clearly, design M210S has the best performance among all of the eight different designs. The results show the expected improvement as discussed in Chapter 3 using a double thickness of actuators as compared to thickness of the gripper arms. The double thickness is eight

times stiffer because the stiffness has a cubic dependence on the thickness as shown in equation 3-3. While the stiffness is increased twice only when the width is doubled. In addition, the meander heater shape performed better than the linear shape. This is because the linear heater design has the conductor along the main expansion direction.

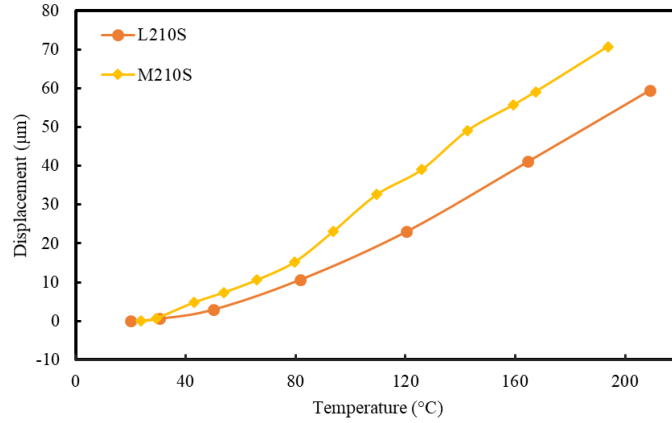


Fig. 6.44 Displacement compression of the result of the best two microgripper designs as a function of the average heater temperature

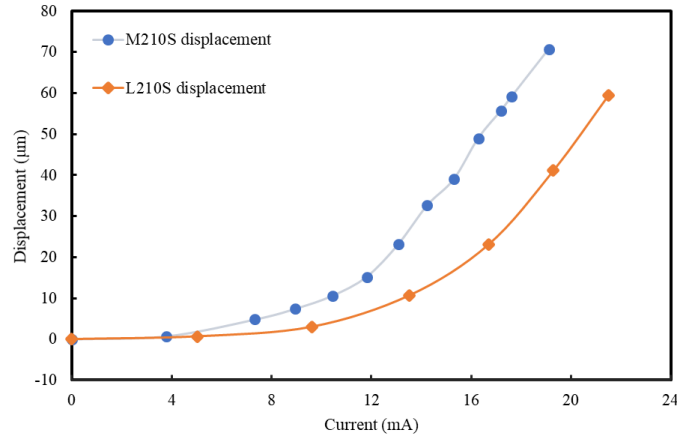


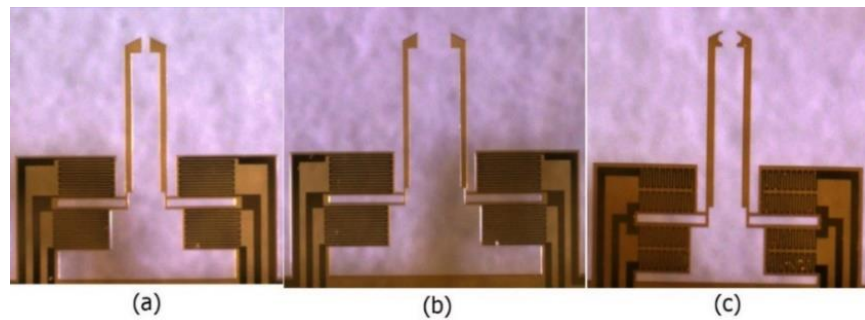
Fig. 6.45 Displacement result of the best two microgripper designs as a function of the applied current

### 6.2.3 Design HWU-C: Dual-Mode L-Shaped Microgripper

Fig. 6.46 shows the different designs of the dual-mode microgrippers. There are two main designs depending on the heater conductor shape and they are classified as design 1 and design 2. These microgrippers were fabricated with the same design dimensions of the SU structures and also the same conductor thicknesses and configurations. The robotic system and the image tracking measurement method were used to characterise these

microgrippers, as shown in Fig. 6.47. It shows the microgripper under three conditions: closing under actuation, no actuation, and opening under actuation. Fig. 6.48 shows three photographs of the end effectors under the same testing conditions.

The displacement results of the closing mode of design 1 show about  $90\text{ }\mu\text{m}$  of displacement at the heater average temperature of about  $200^{\circ}\text{C}$ . The applied current was  $23\text{ mA}$  passing through the heaters. While in the same mode, the displacement of design 2 was about  $80\text{ }\mu\text{m}$  when the average heater temperature was about  $200^{\circ}\text{C}$ . This was at an applied current of about  $15\text{ mA}$  through the heaters. These results are shown in Fig. 6.49. The results of the opening mode operation of design 1 has a maximum displacement of about  $80\text{ }\mu\text{m}$  when the average heater temperature was about  $200^{\circ}\text{C}$  and the applied current was  $24\text{ mA}$  on the heaters for this operation. In the same mode, design 2 reached a maximum displacement of about  $70\text{ }\mu\text{m}$  when the average heater temperature was about  $200^{\circ}\text{C}$ . This was at an applied current of  $15\text{ mA}$ , as shown in Fig. 6.50. Fig. 6.51 shows the displacement as a function of the heater temperatures. It is clear from these results that there is no significant difference between the two designs. However, the displacement trend as a function of the applied current and the average temperature of design 2 are closer.



*Fig. 6.46 Optical microscope images for the microgrippers (a) design 1 with opening  $60\text{ }\mu\text{m}$  (b) design 1 with opening  $250\text{ }\mu\text{m}$  (c) design 2 with opening  $90\text{ }\mu\text{m}$*



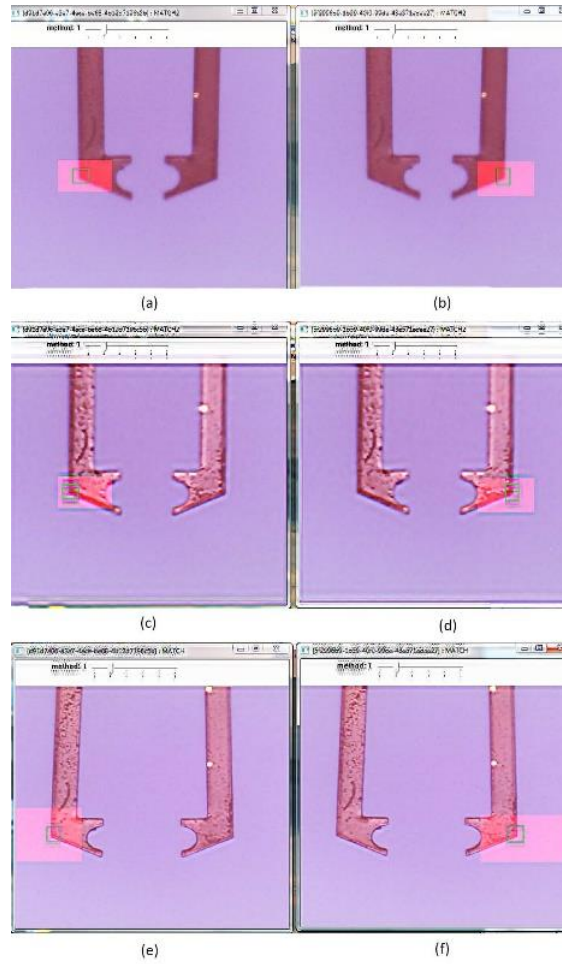


Fig. 6.47 Screen shots of displacement measurement based on vision tracking method. The microgripper design 2 is under test and the images were taken on three occasions. (a) and (b) 13 mW applied on heaters and the microgripper is in closing mode, (c) and (d) both heaters are off, (e) and (f) 18 mW was applied on heaters and the microgripper is in opening mode

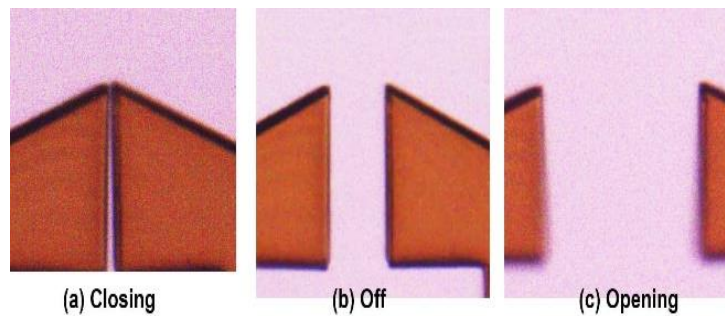


Fig. 6.48 Microscopic photo of design 1 with 60  $\mu\text{m}$  initial opening. (a) closing mode when power is applied on heaters, (b) no power applied (c) opening mode when power is applied on the heaters.)

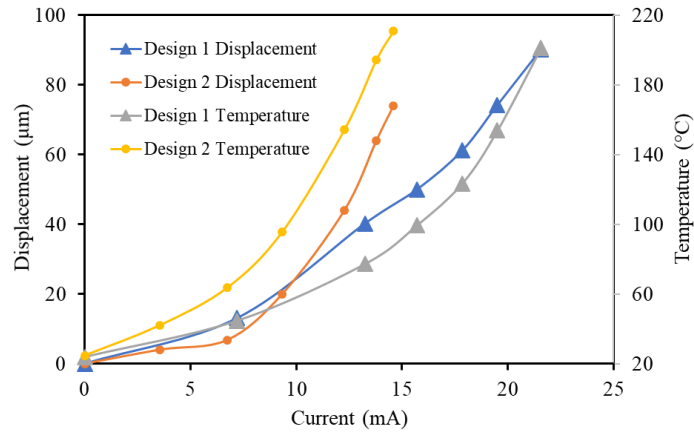


Fig. 6.49 Closing mode displacement and temperature measurements as a function of the current passed in both designs

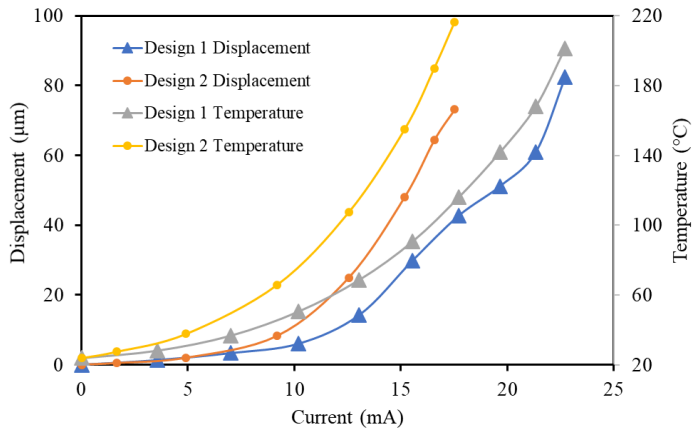


Fig. 6.50 Opening mode displacement and temperature measurements as a function of the current passed in both designs

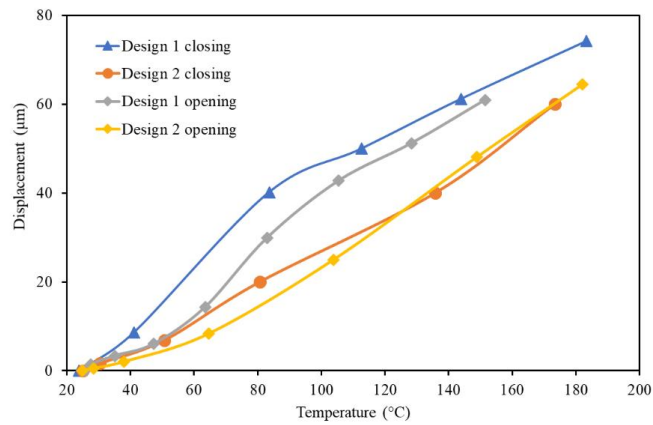
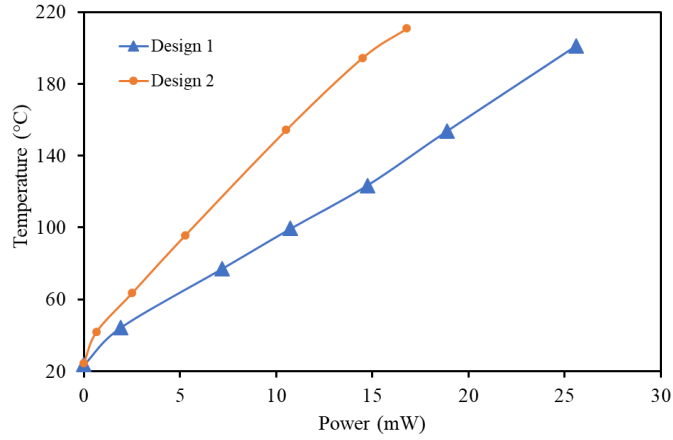
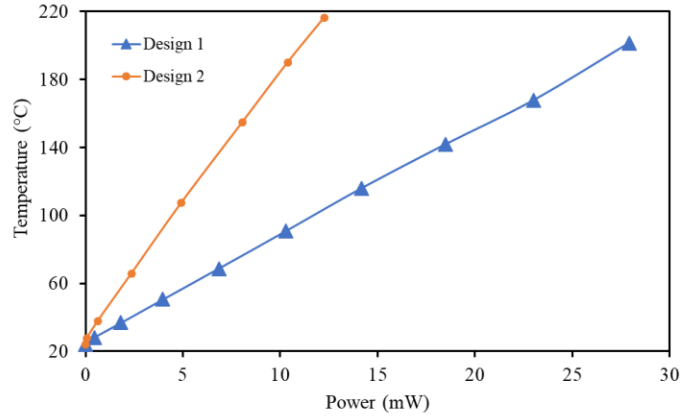


Fig. 6.51 Both opening and closing mode displacement measurements as a function of the average heater temperature



*Fig. 6.52 Closing mode heater (1) average temperature to the applied power*



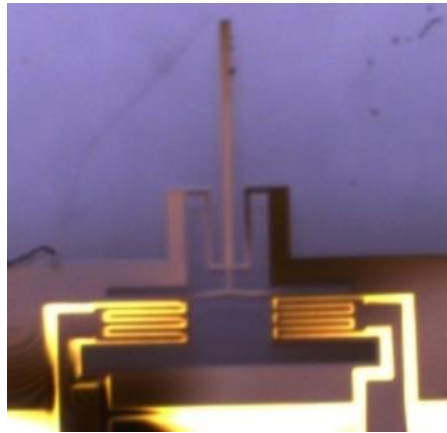
*Fig. 6.53 Opening mode heater (2) average temperature to the applied power*

The testing of both designs in both modes shows the temperature increased linearly with the applied power, as shown in Fig. 6.52 and Fig. 6.53. The average temperature of heater 1 in design 1 reached 200°C when a power of about 27 mW was applied, and the heater 1 of design 2 reached the same temperature when about 18 mW power was applied. The average temperature of heater 2 in design 1 rose to about 200°C at the power of about 29 mW. For the same temperature, heater 2 in design 2 consumed about 13 mW. Thus design 2 with the folded meander heater required less power to reach the same temperature as design 1 in both modes. This is because the heater in design 2 has a higher resistance value than in design 1.

#### 6.2.4 Tri-directional electrothermal Microactuators

Chapter 3 presented a tri-directional microgripper with four actuators as shown in Fig. 3.10 (design 1) and an optimised one with only the two bottom heaters (design 1). Fig. 6.54 shows the optimised microactuator with only two heaters which can be used to implement three directions of movement. Different combinations of the applied power on these heaters define different displacement directions. Applying power on a single heater deflects the arm to the opposite direction while applying the same amount of power drives the arm vertically.

The automated testing method using the robotic system and the image tracking software was used to measure the displacement of gripper arm. The test was done by observing two points at the same time to increase the reliability of the test and the displacement was obtained by averaging the two values. The advantage of the robotic system is that it tracks an area of centre axis deflection which does not need another point to measure the displacement, as shown in Fig. 6.55. This illustrates the method and shows the actuator under different operating conditions. This actuator was tested by tracking the end-effector using two points by requesting the tracking software twice to increase the result reliability by comparing the two results.



*Fig. 6.54 Tri-directional electrothermal microactuators optimised by using only two actuators instead of four*

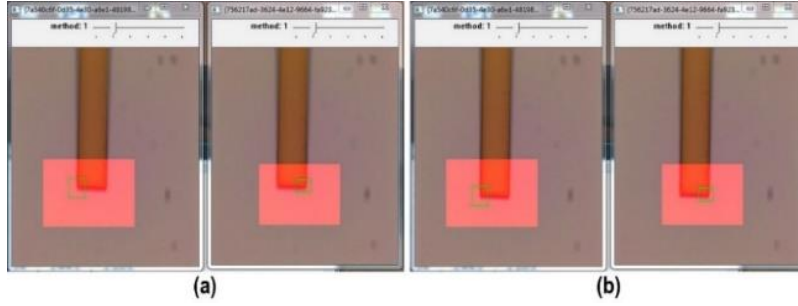


Fig. 6.55 Tri-directional actuator displacement measurement by running both heaters 3 (right and left) (a) is the first image before applying power, the two images are for two tracking requests so two results obtained to increase the accuracy (b) after applying about 41 mA and about 10  $\mu\text{m}$  of longitudinal displacement

The results of testing for design 1 are shown in Fig. 6.56. These results were obtained by applying power on each of the heater 1 and heater 2 at a time. Fig. 6.57 shows the results of applying power on the bottom heaters (H3), the right and the left ones in design 2 separately. However, design 2 draws more current to raise the heater temperature to about 200°C because the heaters have less resistance. The displacements of design 2 were larger than those of design 1, as shown in Fig. 6.58. Design 1 achieved a maximum displacement of about 15  $\mu\text{m}$  for both the right and left directions, while design 2 achieved about 3  $\mu\text{m}$  more at the same temperature. In other words, the optimised design has better performance and requires less electrical connections since it has only 2 heaters.

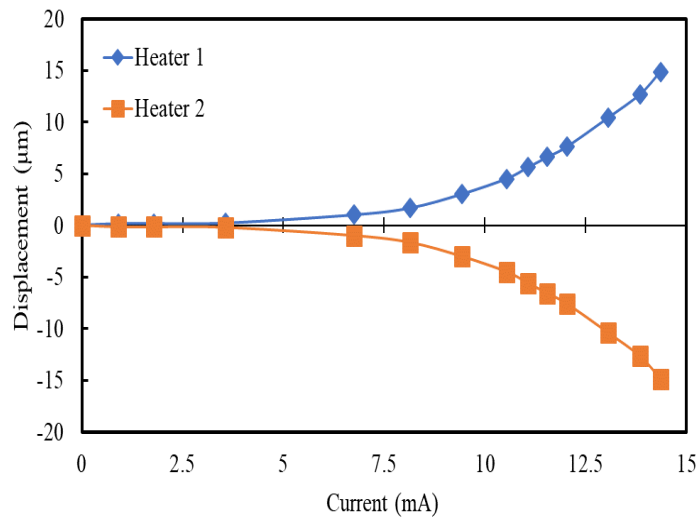


Fig. 6.56 Displacement result of applying power on heater (1 & 2) in the first design of the tri-directional actuator

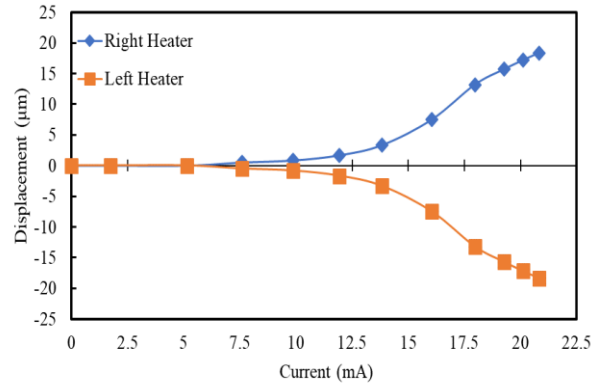


Fig. 6.57 Displacement result of applying power on each heater in the optimised design

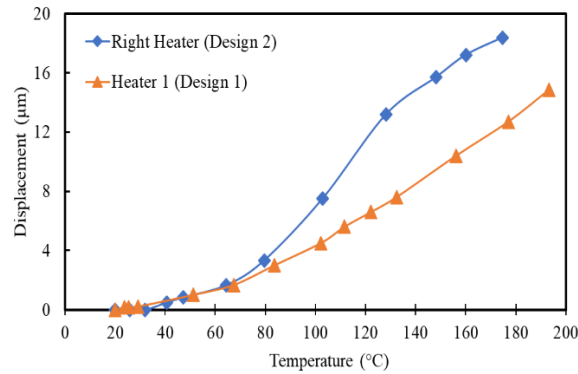


Fig. 6.58 Displacement as a function of the average heater temperature for both designs to actuate the arm to the side direction

Since both designs (see Fig. 6.60) have bottom actuators with the same dimensions, there were no difference in the longitudinal displacement measurements. Fig. 6.59 shows the displacement as a function of the applied current.

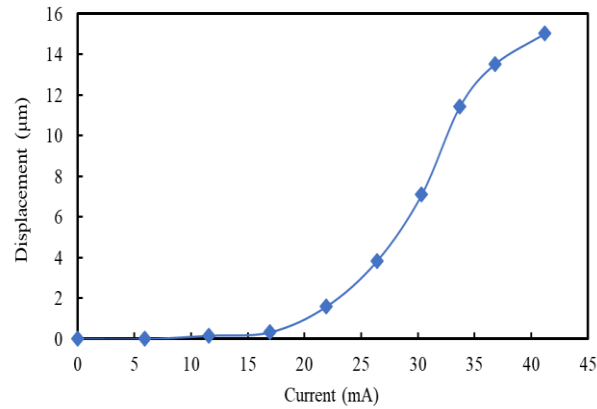
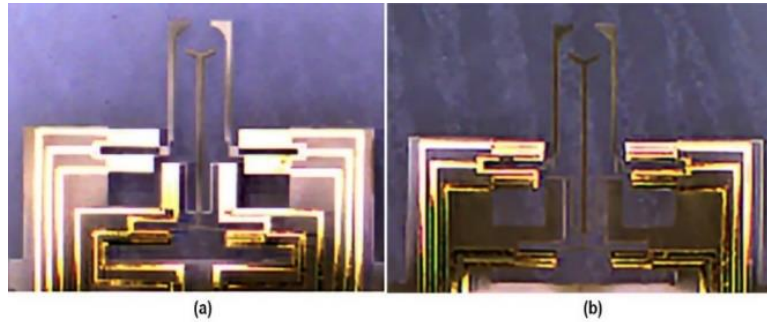


Fig. 6.59 Longitudinal displacement of design 1 when the two H3 are powered design 2 when both heaters are powered as a function of the applied current. The two designs are identical in their longitudinal displacement because they are based on the same dimension

### 6.2.5 Three-arm Electrothermal Microgripper

The dual-mode microgripper was integrated with the tri-directional microactuator to design a three-arm microgripper, as shown in Fig. 6.60. This microgripper offers more flexibility by adding a third arm. The principle of operation is that by applying power on a combination of heaters, a different displacement mode can be achieved. Fig. 6.61 illustrates the five different modes which can be achieved. The initial opening was  $160\text{ }\mu\text{m}$  and it decreased in the closing mode to about  $80\text{ }\mu\text{m}$  at a heater temperature of about  $180^{\circ}\text{C}$ . In the opening mode, the distance between the main end-effectors was increased to about  $240\text{ }\mu\text{m}$  at a heater temperature of about  $180^{\circ}\text{C}$ , as shown in Fig. 6.62.

The results of the displacement of the middle arm as a function of the corresponding average heater temperatures for both designs. When heater (H3) see Fig. 3.12 in design 1 was powered, the arm deflected to the right, and when heater (H4) was powered, the arm deflected to the opposite direction as shown in Fig. 6.63. For design 2 the deflection was obtained to the left by powering heater (H5-right) and to the right by powering (H5-left) i.e. by powering each side separately as shown in Fig. 6.64. The longitudinal displacement in both designs was achieved by powering both H5 heaters as shown in Fig. 6.65 and Fig. 6.66.



*Fig. 6.60 Tri-End-effector microgrippers (a) Design 1 with eight actuators (b) Optimised design (design 2) using six actuators only*

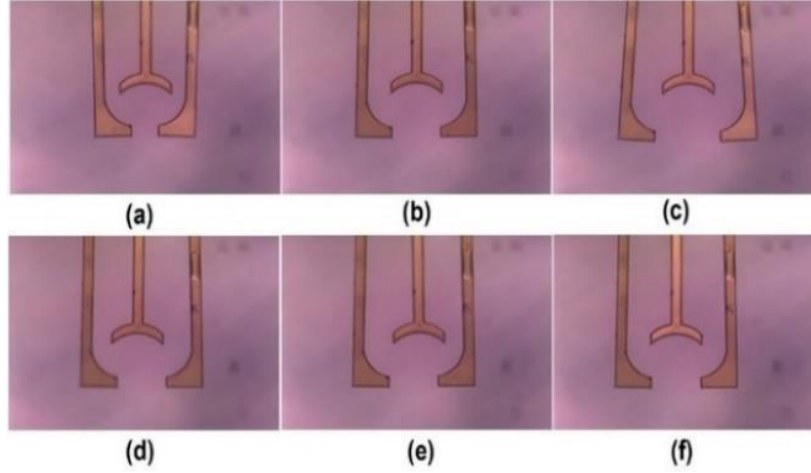


Fig. 6.61 Tri-arms microgripper in displacement measurement in six different situations where (a) closing mode (b) no power applied (c) opening mode. These results from the operation of the dual-mode actuator (d) tri-directional actuator (H3 in design 1 or the left heater in design 2) activated (e) tri-directional actuator (H4 in design 1 or the right heater in design 2) activated (f) tri-directional actuator (H5 & H6) activated

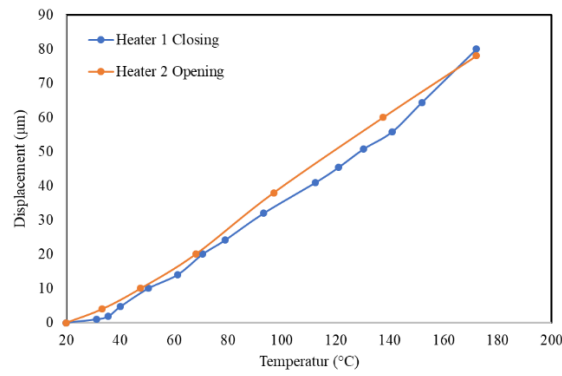


Fig. 6.62 Three-arm microgrippers displacement as a function of the average heater temperature for the main arms

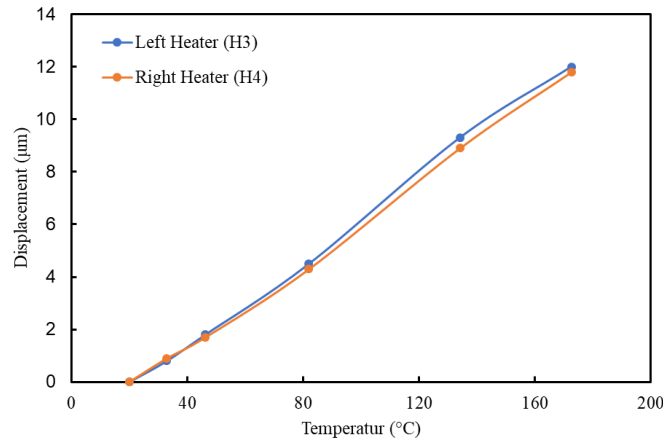


Fig. 6.63 Displacement as a function of temperature for the middle arm for design (1) by powering the heaters (H3) and (H4) for right and left displacements



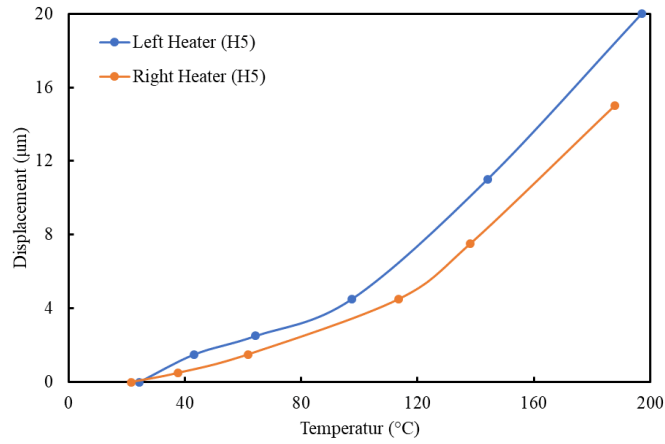


Fig. 6.64 Displacement as a function of temperature for the middle arm for design (2) by powering the left heater (H5) and the right heater (H5) for right and left displacements

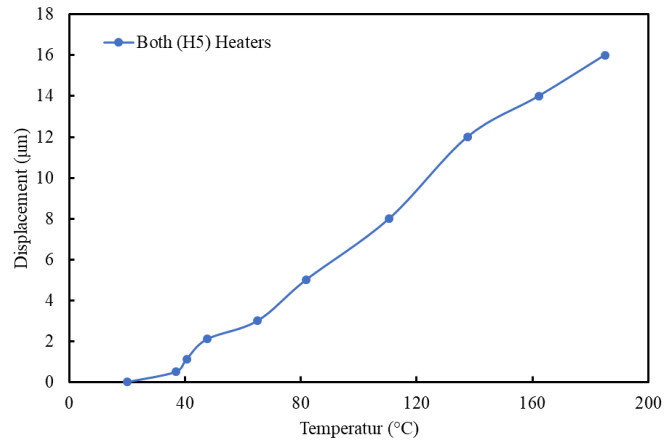


Fig. 6.65 Displacement as a function of temperature for the middle arm for design (1) by powering both heaters (H5) to achieve longitudinal displacement

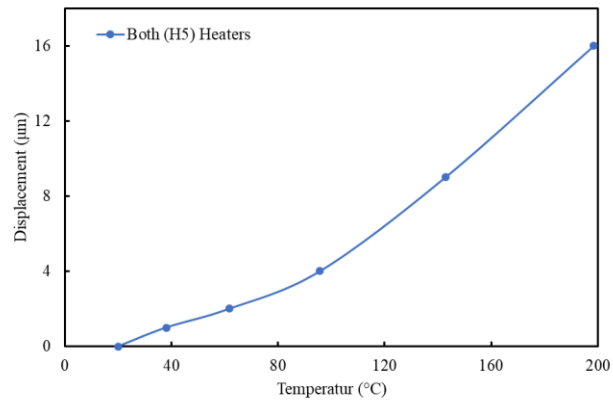


Fig. 6.66 Displacement as a function of temperature for the middle arm for design (2) by powering both heaters (H5) to achieve longitudinal displacement

### 6.3 Results of Dynamic Study

The main purpose of this study is to understand how different actuators respond to a step voltage/current at the onset of operation and recovery after the actuation voltage is terminated. Basically, when a heater is powered, the temperature increases and causes an expansion which drives an arm to its steady state displacement value. The temperature increase reduces the stiffness of the actuator, so if the reaction force is high enough the actuator will buckle. As a result, the displacement will start to decrease until the equilibrium state is reached.

This section presents the results of measurement of the dynamic response of selected microgrippers based on different actuators. This study was based on image tracking software which is a part of the robotic system image processing software. This is a new method and fully automated and it does not require a manual pixel calculation from the video frames. In addition, this behavior has not been reported in the literature.

#### 6.3.1 Design IMT-E

Fig. 6.67 shows the results of end-effectors displacement in the dynamic response when a voltage of 680 mV was applied to the heater of the microgripper for a duration of 10 seconds and also the response after the voltage was turned off. The average temperature was about 170° C at steady state as stated in Chapter 5. This microgripper showed a maximum displacement of about 25  $\mu\text{m}$  (55  $\mu\text{m}$  opening), then the opening decreased by about 3  $\mu\text{m}$  after about 3 seconds from onset of the applied voltage and stabilised at 23  $\mu\text{m}$  (52  $\mu\text{m}$  opening). After the drive voltage was terminated, the end-effectors showed a negative deflection of about 4  $\mu\text{m}$  from the original opening value of 30  $\mu\text{m}$ . opening). After a long relaxation period (about 24 hours), the gripper opening was measured to be 28  $\mu\text{m}$  showing a recovery of 2  $\mu\text{m}$  from the negative deflection but did not restore to the initial opening value of 30  $\mu\text{m}$  before the dynamic test.

Fig. 6.68 shows the heater temperature change as a function of time in comparison to the displacement. The temperature reached to the steady-state value in about 50 ms while the displacement took much longer, about 300 ms to reach the steady state value. The temperature was calculated based on the voltage and current reading from the ADCs in the

interface unit. However, since the sampling interval was 15 ms so there were only 3 sampling points in the 50 ms of sharp rise in the temperature response which caused uncertainty at the beginning of the temperature response. Fig. 6.69 shows the details of the dynamic responses of the gripper end-effectors based on the same data as for Fig. 6.67 but plotted within the one second of time duration.

The error in the measurement was  $\pm 1$  pixel ( $\pm 0.3 \mu\text{m}$ ) as indicated by the error bars.

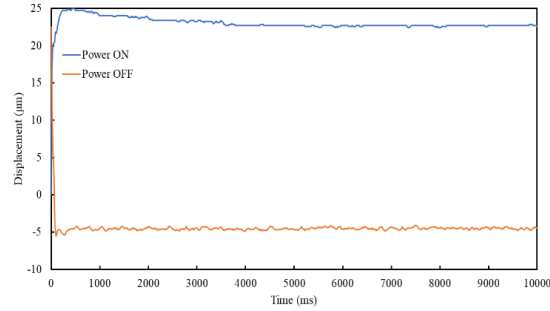


Fig. 6.67 Dynamic study of displacement as a function of time for both power ON and power OFF time of applied voltage of 670 mV on design 1-E

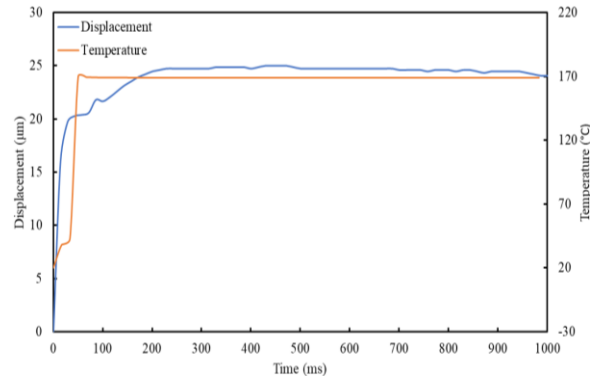


Fig. 6.68 Heater temperature and end-effectors displacement over 1 second sampled 60 times of applied voltage of 680 mV on design 1-E

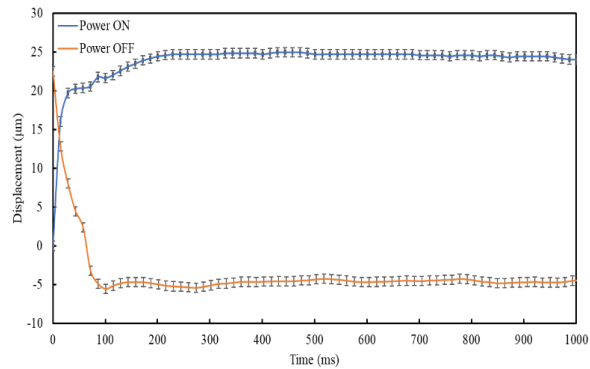
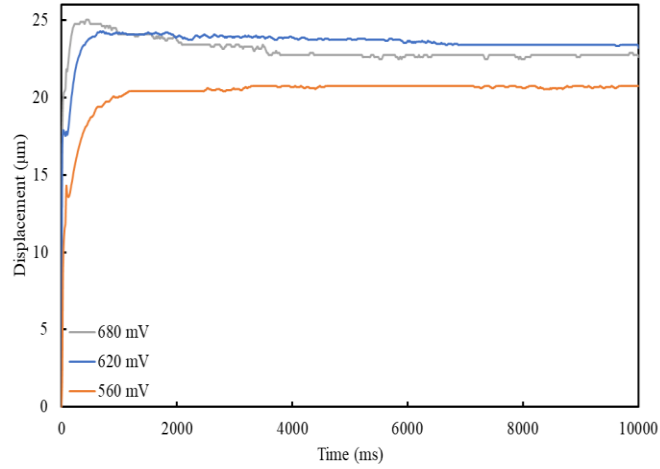
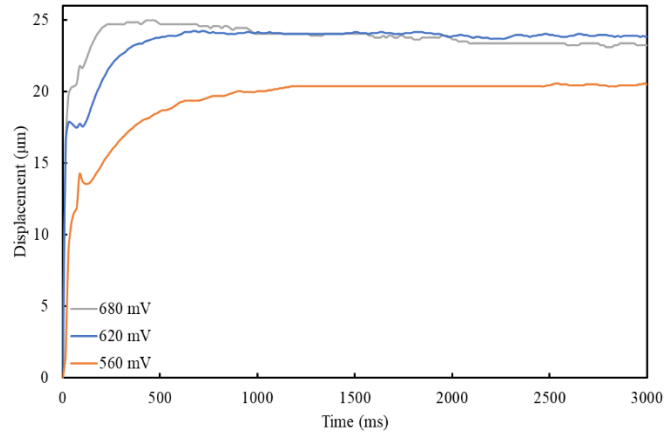


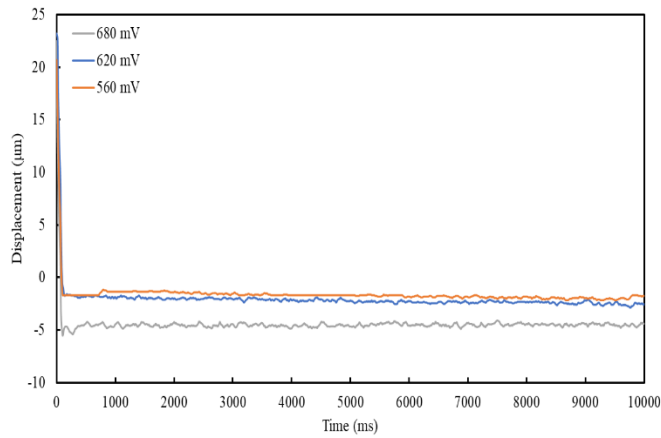
Fig. 6.69 Dynamic study result of displacement as a function of time for both power ON and power OFF time of applied voltage of 670 mV on design 1-E focused on the first second of transaction



*Fig. 6.70 Dynamic study of displacement as a function of time for power ON time of applied voltage of 560 mV, 620 mV, and 680 mV on design 1-E for 10 seconds*



*Fig. 6.71 Dynamic study of displacement as a function of time for power ON time of applied voltage of 560 mV, 620 mV, and 680 mV on design 1-E for 3 seconds*



*Fig. 6.72 Dynamic study of displacement as a function of time for power OFF time of applied voltage of 560 mV, 620 mV, and 680 mV on design 1-E for 10 seconds*

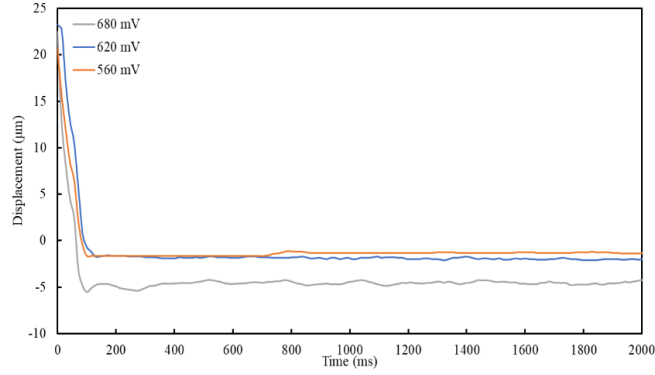


Fig. 6.73 Dynamic study of displacement as a function of time for power OFF time of applied voltage of 560 mV, 620 mV, and 680 mV on design 1-E for 2 seconds

Fig. 6.70 and Fig. 6.71 show the results of the dynamic responses of design 1-E for different actuation voltages over periods of 10 seconds and 3 seconds respectively. It can be seen that overshooting occurred only at the largest drive voltage of 680 mV. Fig. 6.72 and Fig. 6.73 show the results of relaxation of the gripper displacement after each applied voltage was removed over the time durations of the powering OFF time for the same applied voltages for the previous figures over 10 seconds and 2 seconds respectively. The average heater temperature was about 170°C, 160°C, and 150°C for the applied voltage of 680 mV, 620 mV, and 580 mV respectively. A large negative deflection was observed at the drive voltage of 680 mV. Considering the overshooting behavior shown in Fig. 6.70 and Fig. 6.71, it is better not to overdrive the microgripper for operation.

### 6.3.2 Design IMT-D

This design was selected because it has a simple structure. Fig. 6.74 shows a screen shot for testing using the selected areas for tracking in dynamic measurement of gripper displacement. Fig. 6.75 shows the results of the displacement as a function of time. The applied voltage was about 620 mV and the average heater temperature was about 170 °C. The error bars were set to  $\pm 1$  pixel, i.e. 0.3  $\mu\text{m}$ . Even considering the error bars, the displacement had an overshoot of about  $\mu\text{m}$ . However, there is no negative deflection over the original position of the end-effectors after the actuation voltage was removed.

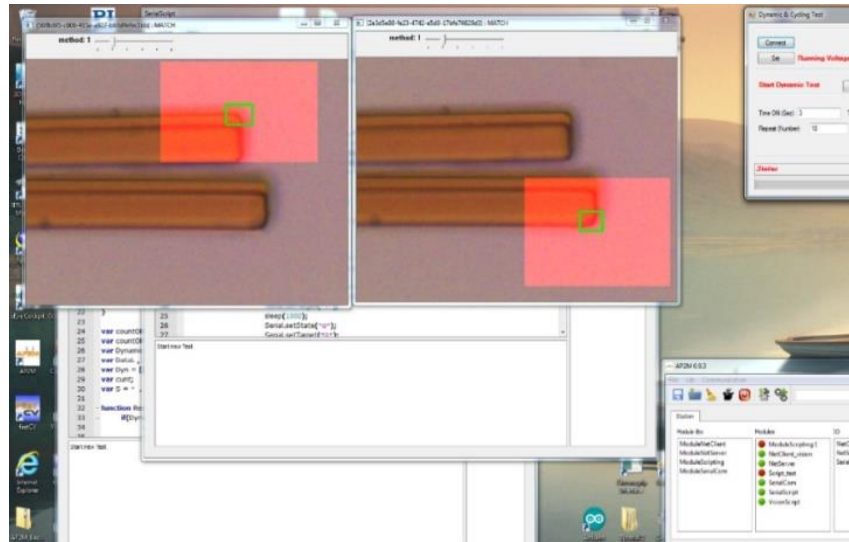
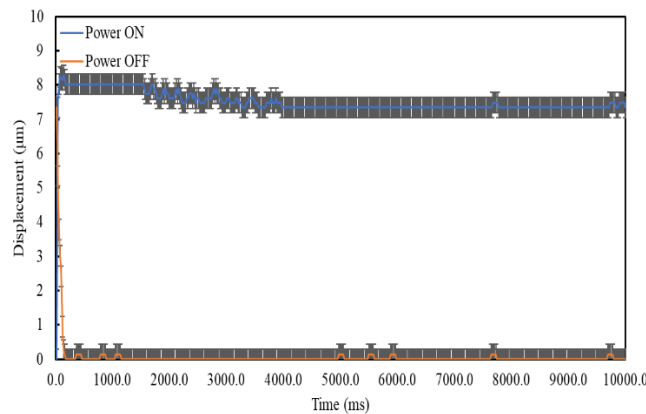


Fig. 6.74 Screen shoot of dynamic study of displacement of design 1-D



*Fig. 6.75 Dynamic study of displacement as a function of time for power ON/OFF time for applied voltage of about 620 mV on design 1-D for 10 seconds*

### 6.3.3 Design IMT-F

Fig. 6.76 shows a screen shot for the testing of this design. Fig. 6.77 shows the results of the displacement as a function of time. The applied voltage was about 580 mV and the average heater temperature was about 160°C. The displacement reached to a maximum value of 30  $\mu\text{m}$  within 1 second, then it decreased continuously and after 10 seconds it was about 25  $\mu\text{m}$ . In the relaxation behavior after the actuation voltage was removed, the gripper showed a negative displacement of 4  $\mu\text{m}$  after reaching steady state. After a long period (about a day), negative displacement reduced by 2  $\mu\text{m}$ . Fig. 6.78 shows the results in 1 s of duration after the actuation was applied or removed.

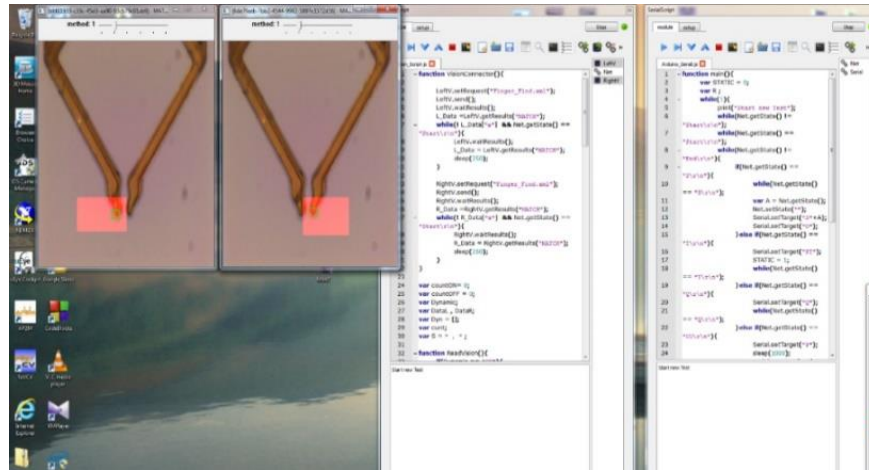


Fig. 6.76 Screen shot of dynamic study of displacement of design 1-F

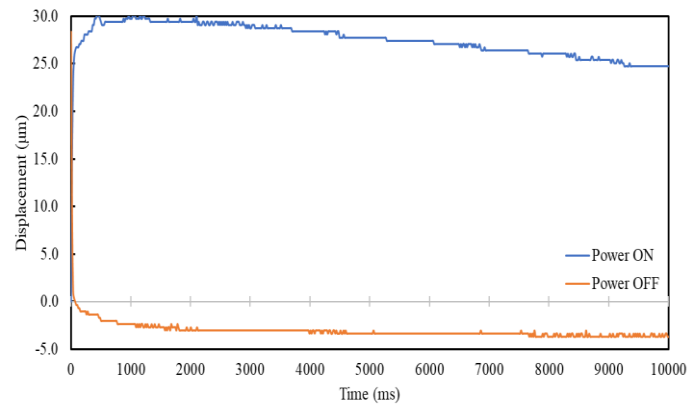


Fig. 6.77 Dynamic study result of displacement as a function of time over 10 seconds for both power ON and power OFF time of applied voltage of 580 mV on design 1-F

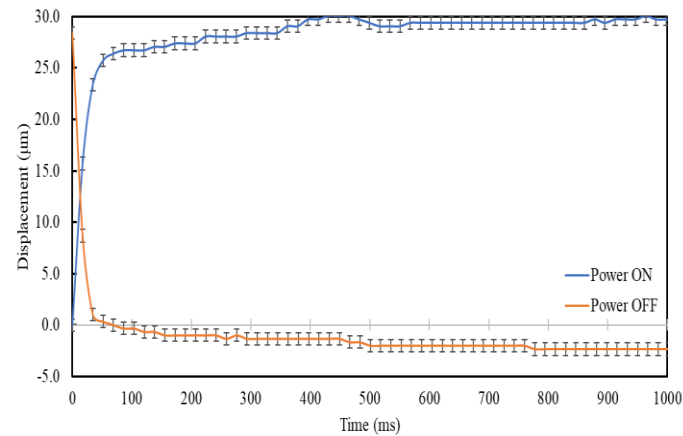


Fig. 6.78 Dynamic study result of the first seconds for both powering ON and powering OFF time of applied voltage of 580 mV on design 1-F

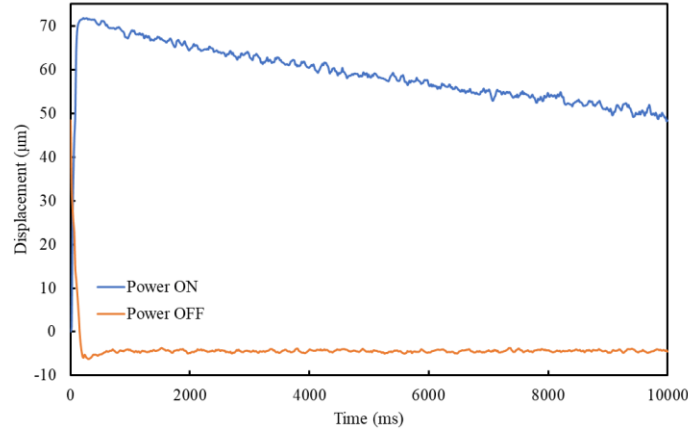


Fig. 6.79 Dynamic study result of the first 10 seconds for both powering ON and powering OFF time of applied voltage of 430 mV on design 1-G

#### 6.3.4 Design IMT-G

Fig. 6.79 show the results of the displacement as a function of time. The applied voltage was about 430 mV and the average heater temperature was about 170°C. There was a significant overshoot in the switch-on response with a maximum displacement of 70  $\mu\text{m}$ , then it decreased continuously by 20  $\mu\text{m}$  after 10 seconds. In addition, in the switch-off behavior, the negative displacement was about 5  $\mu\text{m}$ . After a long period (about a day), this value decreased by 2  $\mu\text{m}$  to 3  $\mu\text{m}$ .

#### 6.3.5 Design IMT-H

Fig. 6.80 shows the result of the displacement as a function of time. The applied voltage was about 400 mV and the average heater temperature was about 170°C. The maximum displacement was 46  $\mu\text{m}$  and then decreased continuously by 10  $\mu\text{m}$  about 35  $\mu\text{m}$  after 10 seconds. In the switch-off response, the gripper opening did not recover to the original value by about 2  $\mu\text{m}$  as shown in Fig. 6.80.



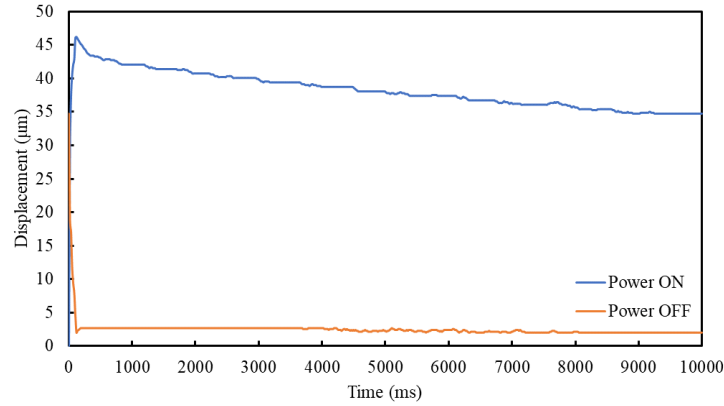


Fig. 6.80 Dynamic study result for both powering ON and powering OFF time of applied voltage of 400 mV on design 1-H

### 6.3.6 Dual-Mode L-Shaped Microgripper (Design HWU-C)

The dynamic behavior of displacement for both microgripper variants were studied in both modes (opening mode and closing mode), as shown in Fig. 6.81 and Fig. 6.82. The transient response of the displacement was acquired for both switch-on and switch-off operation. In the results of opening operation, the switch-on behavior was similar in both designs, there was no overshoot in the transient region. Design 1 reaches steady-state displacement in about 10 seconds while it was about 4 seconds for Design 2. In the switch-off behavior, Design 2 recovered almost to the original opening, but Design 2 showed a negative deflection of about 13  $\mu\text{m}$ .

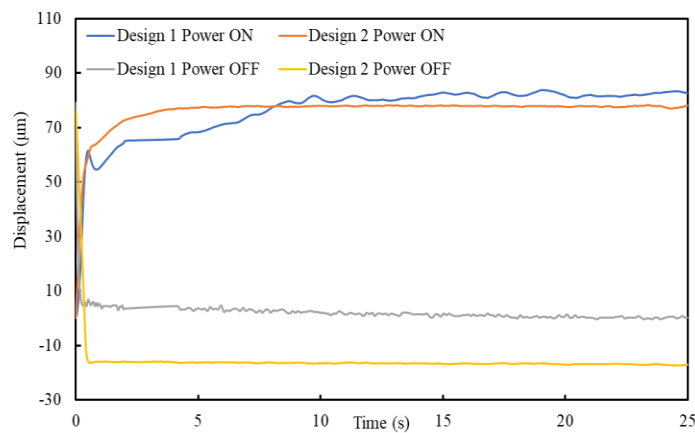
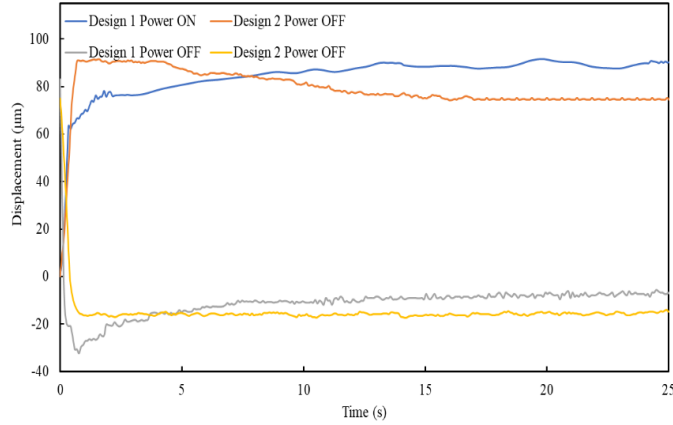


Fig. 6.81 Dynamic study result of the first 25 seconds for both powering ON and powering OFF time of applied voltage of 2V and 2.1V on opening mode for design 1 and design 2 respectively



*Fig. 6.82 Dynamic study result of the first 25 seconds for both powering ON and powering OFF time of applied voltage of 2V and 2.1V on closing mode for design 1 and design 2 respectively*

The transit at the switching off response for design 1 in the closing mode showed a springing behavior. However, it restored its original opening after about 25 seconds. However, it did not show this behavior in the opening mode. Instead, it dropped sharply by several hundreds of ms and the opening reduced by 4  $\mu\text{m}$ . Then, it restored the original opening in about 25 seconds. Design 2 shows an overshoot of about 20  $\mu\text{m}$  in both modes. This overshooting did not restore to the initial position even after a long time.

An interesting test result was noticed on both designs when it turned ON in one mode then OFF then ON in the other mode. For example, the design 1 initial opening was 90  $\mu\text{m}$ . When the power turned ON to raise the heater temperature to about 170  $^{\circ}\text{C}$  in open mode, the displacement was about 80  $\mu\text{m}$  and the opening was 170  $\mu\text{m}$ . When the power turned OFF, the opening was about 65  $\mu\text{m}$ , i.e. an increment of about 5  $\mu\text{m}$ . Then, it powered ON in closing mode to raise the heater temperature to 170  $^{\circ}\text{C}$ . The displacement was about 95  $\mu\text{m}$  and the opening was about 0  $\mu\text{m}$ . Then, when the power turned OFF, the opening was back to its original value (60  $\mu\text{m}$ ).

Another test was done on design 1 by running each mode twice. After first turning ON the opening mode, the opening was about 170  $\mu\text{m}$ . The first OFF time, the opening increased to about 65  $\mu\text{m}$ . After the second time the opening mode powered ON, the displacement was about 175  $\mu\text{m}$ , and 66  $\mu\text{m}$  on the second power OFF. At the first closing mode powered ON, the end-effectors were fully closed. At the first powered OFF the

opening was returned to its original value of 60  $\mu\text{m}$ . At the second closing mode powered ON, it was the same result while at the power OFF the opening decreased to 56  $\mu\text{m}$

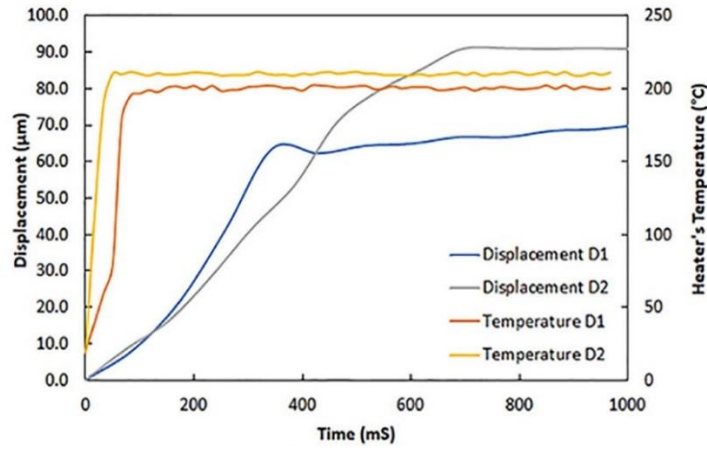


Fig. 6.83 Temperature and displacement measured as a function of time in closing mode for both designs over 1 second

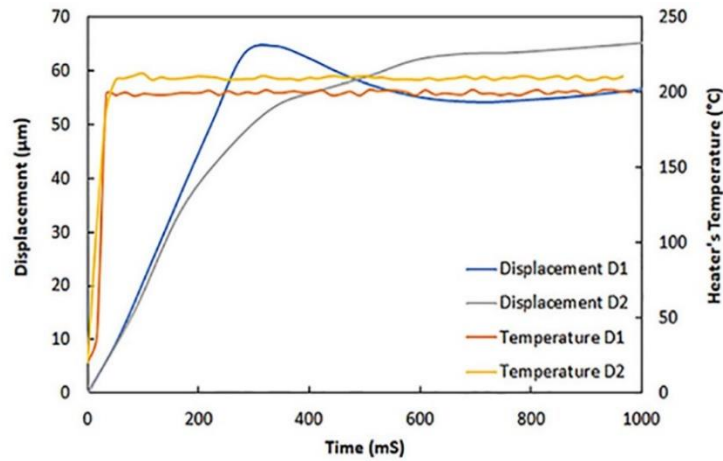


Fig. 6.84 Temperature and displacement measured as a function of time in opening mode for both designs over 1 second

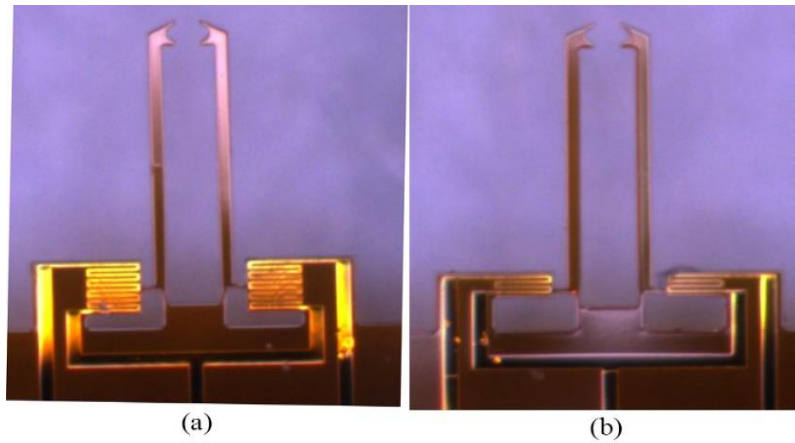
Fig. 6.83 and Fig. 6.84 show the responses of the displacement and average temperature in the heater for Design 1 and 2 after the actuation voltage was applied for the closing mode operation and the opening mode operation respectively. The temperature rise in the heaters is much faster than the SU-8 structure therefore the gripper displacement in both designs. The displacement reached the steady state in less than 70 ms. But it took about 700 ms for the displacement to reach steady state. This is due to the time for heat diffusion from the heater to the surrounding SU8 material to produce the thermal expansion of the material to actuate the microgripper's arms.

#### 6.4 Effect of Actuator Width and Thickness on Displacement

The microgripper designs shown in Fig. 6.86 with two different actuator widths were used to study the effect of the stiffness on the dynamic behavior of these microgrippers. Fig. 6.86 and Fig. 6.87 show the dynamic responses study for the four different designs. Fig. 6.88 shows the compression between the best design from each group. The microgrippers were labeled as shown in Table 6-1.

*Table 6-1 Microgrippers with different actuators and arm parameters*

	Actuator Width ( $\mu\text{m}$ )	Actuator Thickness ( $\mu\text{m}$ )	Arm Thickness ( $\mu\text{m}$ )
L100_S	100	20	10
L100_D	100	20	20
L210_S	210	20	10
L210_D	210	20	20



*Fig. 6.85 One DOF direct actuated microgripper optical photo for two different actuator widths of linear heater (L) design (a) actuator width is 210  $\mu\text{m}$  and (b) is 100  $\mu\text{m}$*

The L100\_S had a larger displacement than the L100\_D on the same average heater temperature. However, at the powering OFF, both design displacements decreased with time, as shown in Fig. 6.86. Both designs at powering OFF had an opening displacement larger than their original value. However, design L100\_S recovered most of this increment in a shorter time.

The same comparison on the designs with wider actuators showed similar behavior. Even though both designs had the same overshoot at powering ON, The L210\_S had a larger displacement than the L210\_D at the same average heater temperature. However, at powering OFF, both design displacements decreased with time, as shown in Fig. 6.87,

design L210\_S was more stable and recovered the original opening with a shorter time. Both designs at powering OFF had an opening displacement larger than their original values. However, design L100\_S recovered most of this increment in a shorter time.

Fig. 6.87 shows a comparison between the better behavior of the microgrippers in the two groups. It is clear that the wider and thicker actuator had better results. Design L210\_S had a stable and larger displacement. Also, it recovered the original opening faster than the other designs.

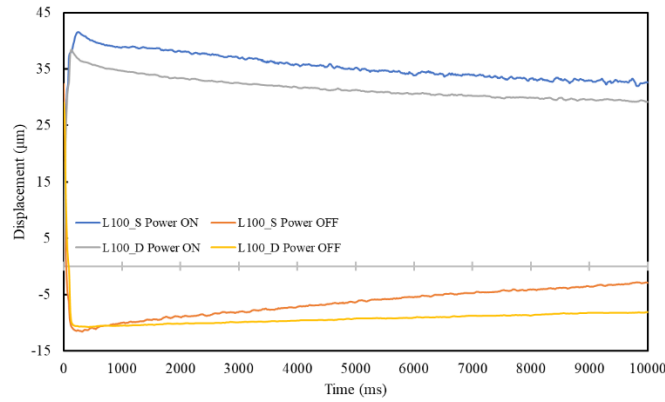


Fig. 6.86 Dynamic study result of the first 10 seconds for both powering ON and powering OFF time of applied voltage of about 700 mV on design L100. The heater average temperature was about 170 °C

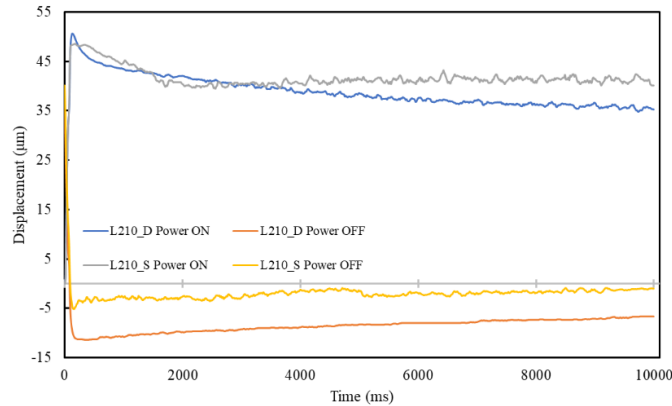


Fig. 6.87 Dynamic study result of the first 10 seconds for both powering ON and powering OFF time of applied voltage of about 810 mV on design L210. The heater average temperature was about 160 °C

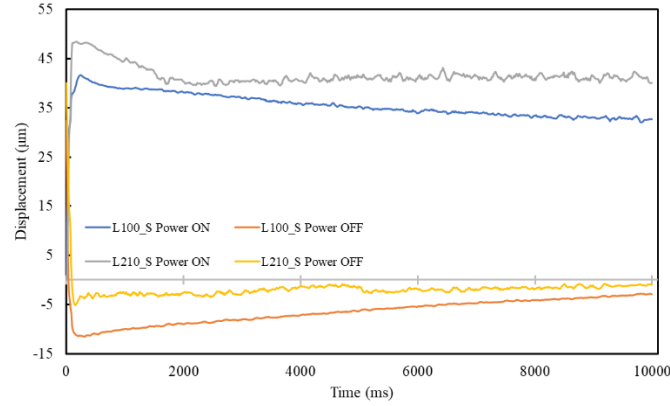


Fig. 6.88 Both dynamic responses of designs L210\_S and L100\_S with the heaters driven ON and OFF

## 6.5 Results of Reliability Study

This section presents the study of the repeatability and reliability of microgrippers.. The study was to investigate if the microgrippers can be opened repeatedly between ON and OFF for a large number of cycles. Faults of failure were also studied.

### 6.5.1 Design IMT-E ON/OFF Cycling Test

The interface unit was programmed to supply 560 mV of actuation voltage on this microgripper. The average temperature of the heaters was about 150°C. It was programmed to run 500 cycles, however it was stopped after 265 cycles. As shown in Fig. 6.89, the opening of the microgripper decreased after each cycle from its original value of 30  $\mu\text{m}$  to about 20  $\mu\text{m}$  after about 250 cycles. While the displacement was stable over the first 250 cycles which was about 20  $\mu\text{m}$ , the displacements value then dropped sharply since the microgripper failed to operate. Fig. 6.90 shows this microgripper before the cycling operation and after its failure. It shows that the opening was significantly changed from 30  $\mu\text{m}$  to about 20  $\mu\text{m}$  and this microgripper could not be operated again due to deformation of the gripper structure.

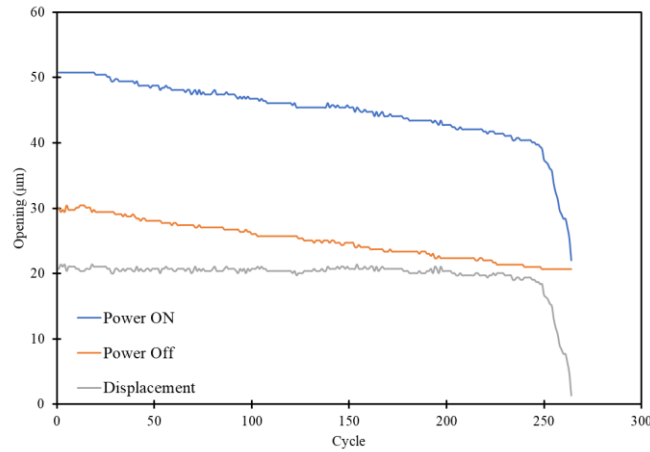


Fig. 6.89 Cycling test of the design 1-E. The microgripper was powered ON/OFF for 10 seconds each. The voltage used was about 560 mV and the average heater temperature was about 150°C

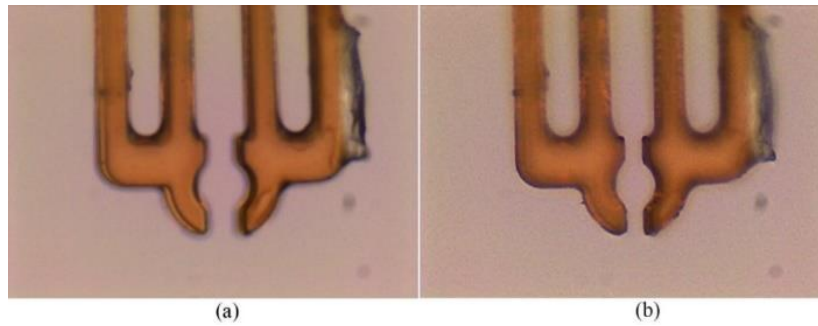


Fig. 6.90 Microgripper group 1 design E (a) before the reliability study (b) after 250 cycles of ON/Off by applying about 670 mV

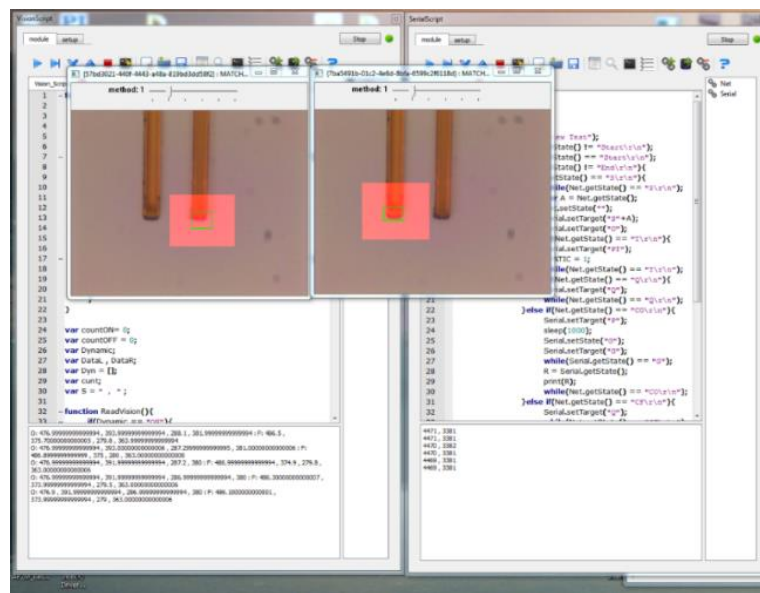


Fig. 6.91 Screen shot of cycling test of design 1-D

### 6.5.2 Design IMT-D ON/OFF Cycling Test

This microgripper was operated by also applying 560 mV of actuation voltage and the results are shown in Fig. 6.91. The average heater temperature was about 150°C. It was programmed to operate 200 cycles in the test. As shown in Fig. 6.92, the opening of this microgripper increased slightly after 200 cycles. The displacement was stable over all cycles with a value of about 5  $\mu\text{m}$ . This microgripper is stable and there is a negligible change in the opening. The displacement value of this microgripper is very small. The test was repeated for another 200 cycles and there was no noticeable difference to the results of the previous test.

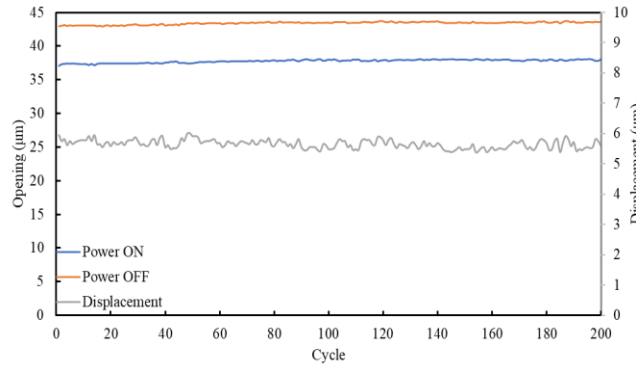


Fig. 6.92 Cycling test of design 1-D. The microgripper was powered ON/OFF for 10 seconds each. The voltage used was about 560 mV, the average heater temperature was about 150°C

### 6.5.3 Design IMT-F Cycling Test

This microgripper was tested by applying 500 mV of actuation voltage, as shown in Fig. 6.93. The average heater temperature was about 125°C. It was programmed to operate for 250 cycles. As shown in Fig. 6.94, the opening of this microgripper increased slightly after the 250th cycle. The displacement was stable over the testing period with a value of about 20  $\mu\text{m}$ .

This test was repeated for another 250 cycles but with a higher voltage of 580 mV to raise the average heater temperature to about 150°C, and the results are shown in Fig. 6.95. The opening increased slightly as compared with the previous test while the on-state displacement was generally stable and decreased by only several micrometers. However, the microgripper failed before the end of the test period (after about 230 cycles). The



photograph of the microgripper's actuator region shows evidence of buckling. In addition, the hinges were deformed and broken, as shown in Fig. 6.96.

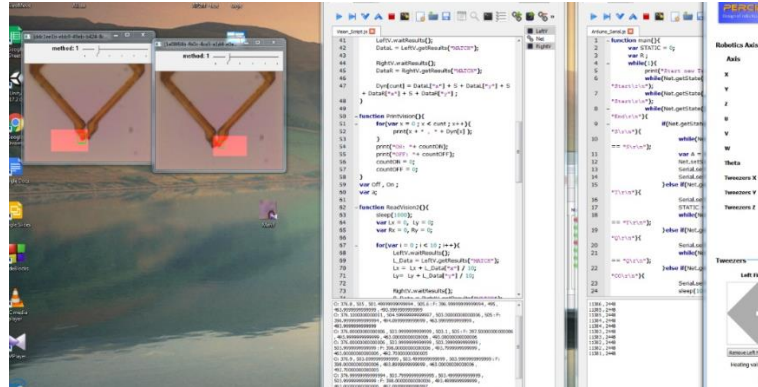


Fig. 6.93 Screen shot of cycling test of design 1-D

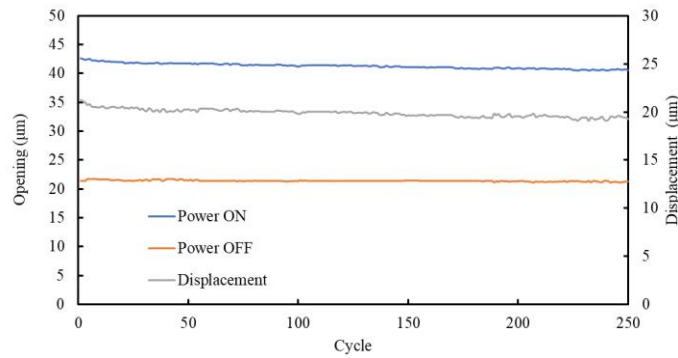


Fig. 6.94 Cycling test of design 1-F. The microgripper was powered ON/OFF for 10 seconds each. The voltage used was about 500 mV and the maximum heater temperature was about 125 °C

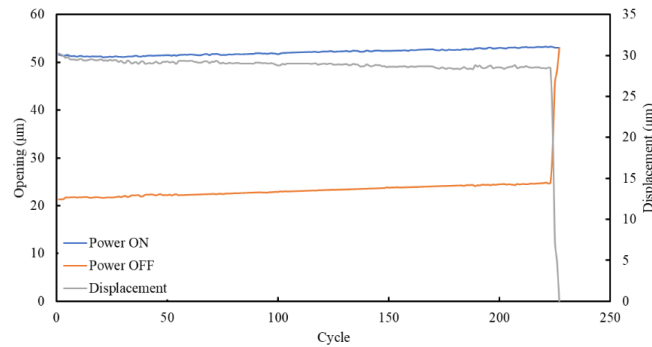


Fig. 6.95 Cycling test of design 1-F. The microgripper was powered ON/OFF for 10 seconds each. The voltage used was about 580 mV and the heater maximum temperature was about 150 °C

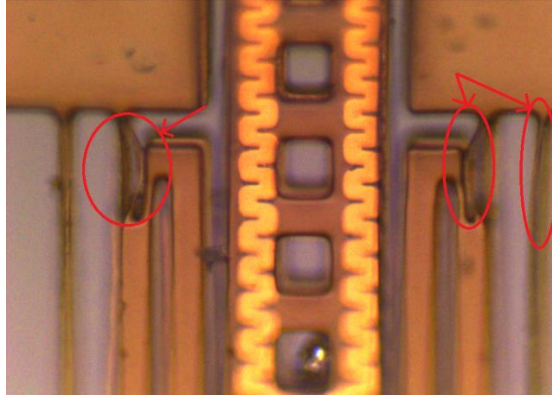


Fig. 6.96 Optical image of Design 1-F showing deformed hinges after the 250 cycles of test

#### 6.5.4 Design IMT-Z Cycling Test

This microgripper was operated by applying 300 mV of voltage and the results are shown in Fig. 6.97. The average heater temperature was about 130°C. It was programmed to operate 100 cycles. As shown in Fig. 6.98, the opening of this microgripper was stable but the displacement in on-state decreased sharply. This microgripper failed after only 46 cycles. As shown in Fig. 6.99 and Fig. 6.100, there is a clear evidence of overheating in one beam and deformation in the actuator region.

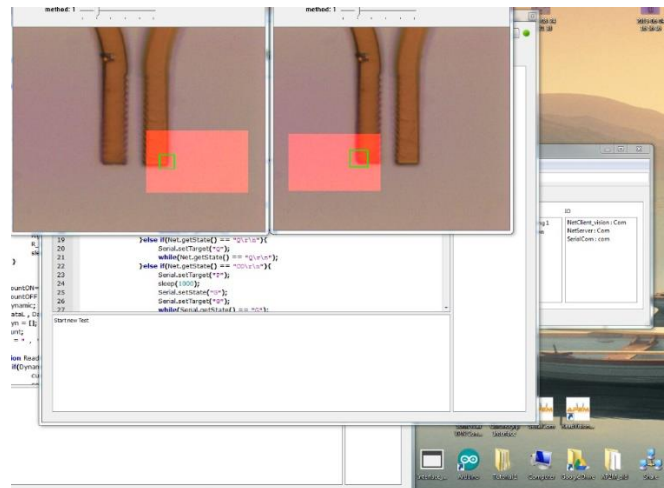


Fig. 6.97 Screen shot of cycling test of design 1-Z

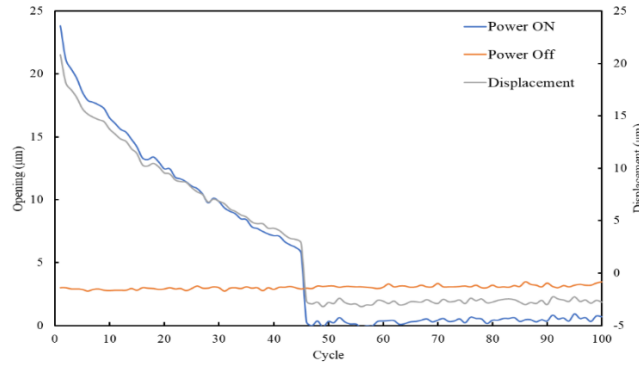


Fig. 6.98 Cycling test of design 1-Z. The microgripper was powered ON/OFF for 10 seconds each. The voltage applied was about 300 mV and the heater maximum temperature was about 130 °C

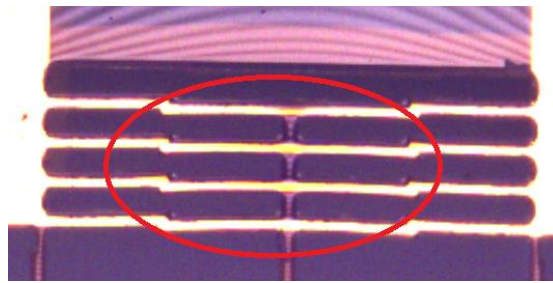


Fig. 6.99 Deformation in the actuator shape and over heating on one beam of design 1-Z microgripper

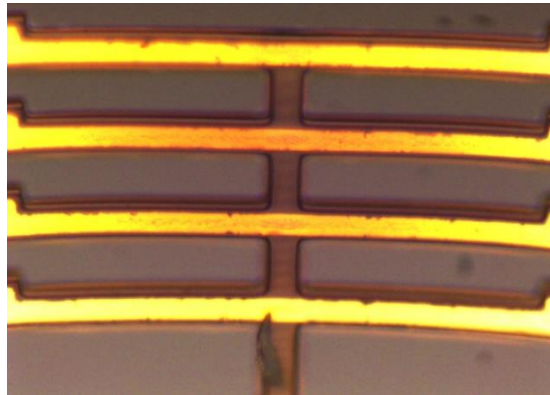


Fig. 6.100 Deformation in the actuator shape and over heating on one beam of design 1-Z microgripper

#### 6.5.5 Design IMT-V Cycling Test

This microgripper was operated by applying 340 mV. The average heater temperature was about 150°C. It was programmed to operate 200 cycles. As shown in Fig. 6.101, the opening of this microgripper was in both on-state and off-state decreased rapidly with but increasing displacement (net opening). This microgripper failed after about 120 cycles. As shown in Fig. 6.102, there is no evidence of overheating in the heater, but the gripper

structure was clearly deformed. In another test with same settings on a different microgripper of the same design, failure occurred after 100 cycles. This was caused by a broken hinge connection, as shown in Fig. 6.103.

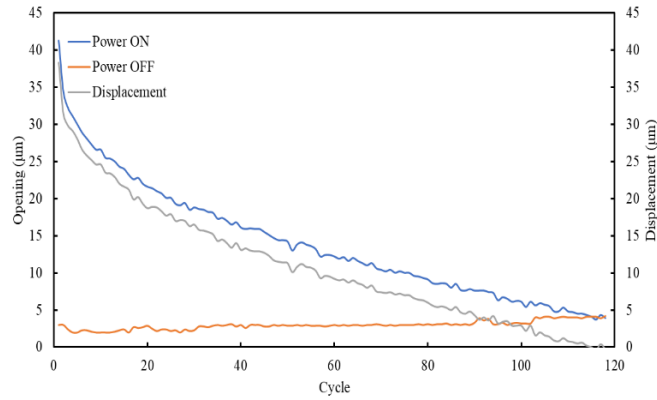


Fig. 6.101 Cycling test of design 1-V. The microgripper was powered ON/OFF for 10 seconds each. The voltage applied was about 340 mV and the maximum heater temperature was about 150 °C

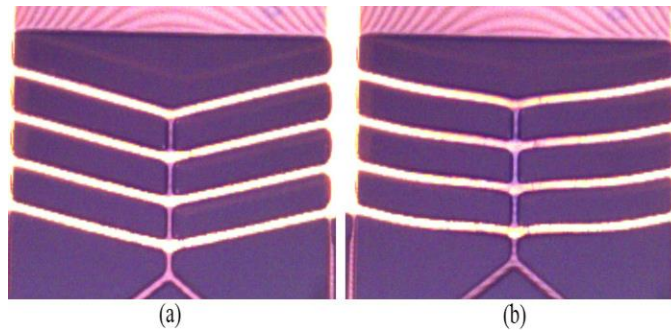


Fig. 6.102 (a) Not used microgripper's actuator (b) microgripper's actuator after 120 cycles showing structural changes in the actuator

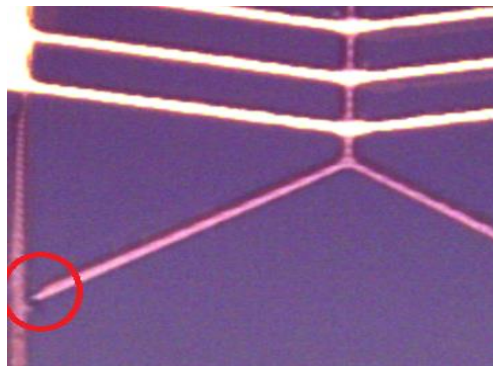


Fig. 6.103 Another failure in design 1-Z after the cycling test

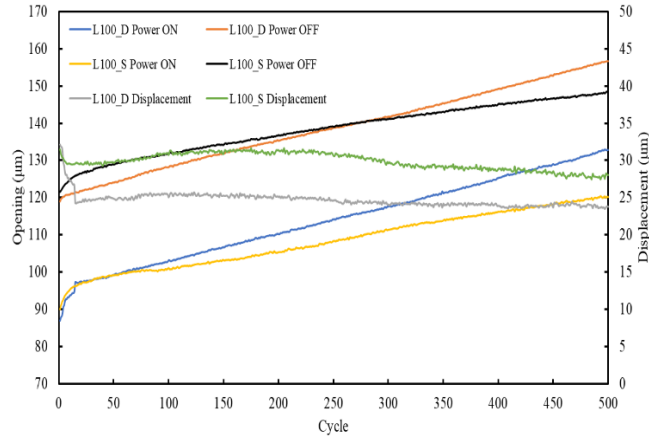


Fig. 6.104 Cycling test of design 1D-L100. The microgripper was powered ON/OFF for 10 seconds each. The voltage applied was about 700 mV and the maximum heater temperature was about 160°C

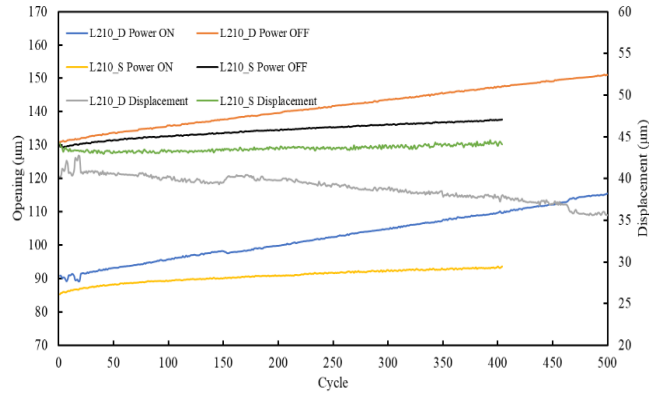


Fig. 6.105 Cycling test of design 1D-L210. The microgripper was powered ON/OFF for 10 seconds each. The voltage applied was about 830 mV and the maximum heater temperature was about 160°C

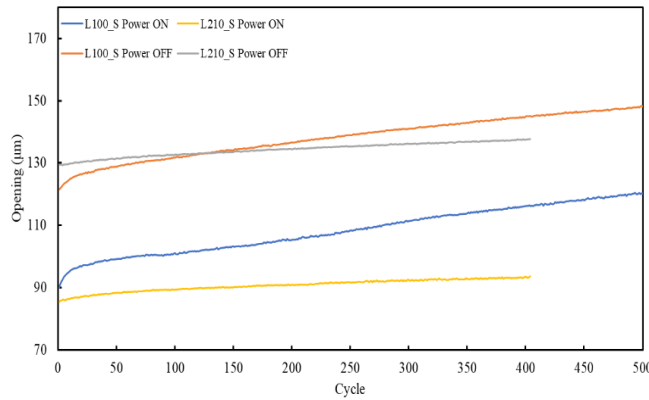


Fig. 6.106 Powering ON/OFF of designs L100\_S and L210\_S

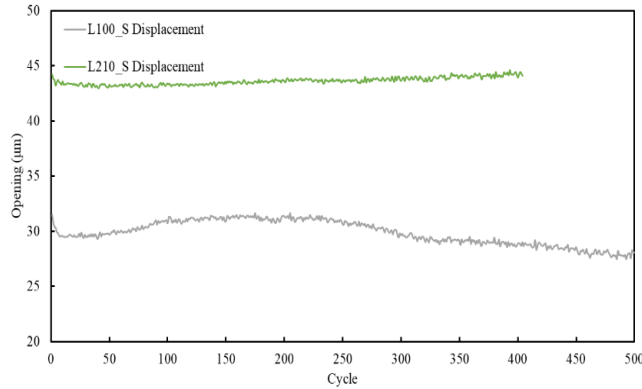


Fig. 6.107 Displacement of designs L100\_S and L210\_S

#### 6.5.6 Design HWU-B Cycling Test

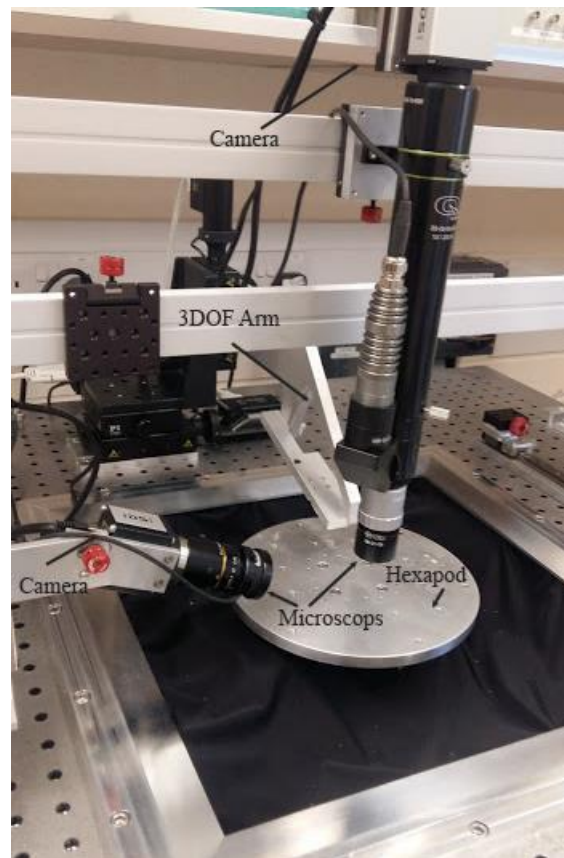
This microgripper was designed in four different configurations, as detailed in Chapter 3. Fig. 6.104 shows the results of opening at power-ON, power- OFF states, and the displacement for designs L100\_D and L100\_S. Both designs show a change in the opening at both power-ON and power-OFF states. However, design L100\_S has less change in its opening value than design L100\_D. The displacement in both designs s showed a small but sharp decrease in the first 15 cycles but then almost constant until the end of 500 cycles of testing. Design L100\_S had a larger displacement value and less change than Design L100\_D.

Fig. 6.105 shows the results of opening and the displacement in cycling testing of designs L210\_D and L210\_S. There was a linear change in the opening of both power-ON and power-OFF status in both designs. However, design L210\_S had significantly less change in its opening than design L210\_D. The displacement of design L210\_S was larger and more stable than design L210\_D over the 500 cycles of testing.

Fig. 6.106 compares the results of opening at power-ON and power-OFF states for the better performances in Fig. 7.16 and Fig. 7.17. The opening of Design L210\_S showed slow but consistent increase over the period of cycling test. Fig. 6.107 compares the displacement results of design L210\_S and design L100\_S. Design L210\_S had a large displacement, and it was very stable over the period of testing.

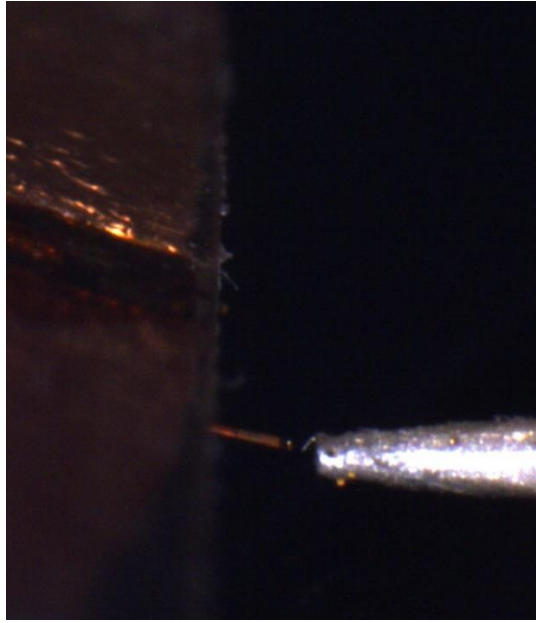
## 6.6 Demonstration of Manipulation of Micro-objects

This section presents the demonstration of manipulation of micro-objects using selected microgrippers described in the thesis. For this purpose, the microgrippers were mounted on the edge of glass microscope slides. Then, they were connected, as explained in the previous chapters. The slide was mounted on the robotic arm which has three DOF in the robotic system, as shown in Fig. 6.108. Two cameras were used to monitor the manipulation progress. The 6 DOF hexapod with an additional rotational stage was used as the platform for placement of the micro-objects or mounting of their carrier for micro-manipulation.

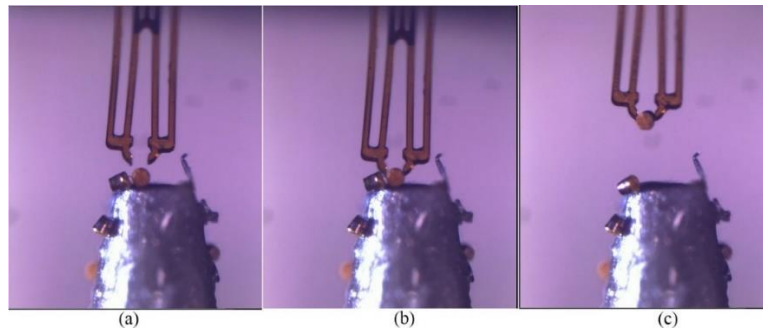


*Fig. 6.108 Robotic systems used for manipulation and testing*





*Fig. 6.109 Design 1-E mounted on the robotic arm to manipulate the gold micro-structure. These micro-objects were mounted on the head of a needle.*

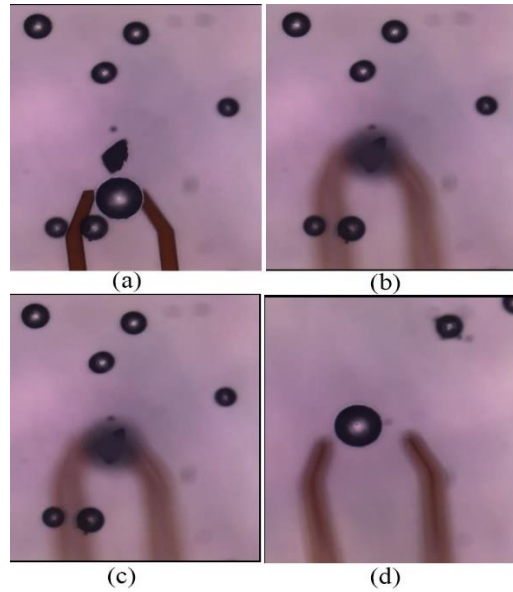


*Fig. 6.110 Design 1-E used to pick a micro-object*

#### *6.6.1 Manipulation Using Design IMT-E*

As shown in Fig. 6.109 and Fig. 6.110, a microgripper of this design was used to manipulate a micro-object on the tip of a needle. The microproject was a copper column (bump) of about 50  $\mu\text{m}$  of diameter and height fabricated by electroplating. The copper bumps were from the previous research work in the lab and had the ideal dimensions for the microgripper. Pick-and-place of a microbump has potential applications in flip chip assembly of microchip or MEMS for advanced interconnection between a chip or MEMS devices and the substrate. As shown in Fig. 7.22 the copper microbump was picked up successfully using the microgripper.

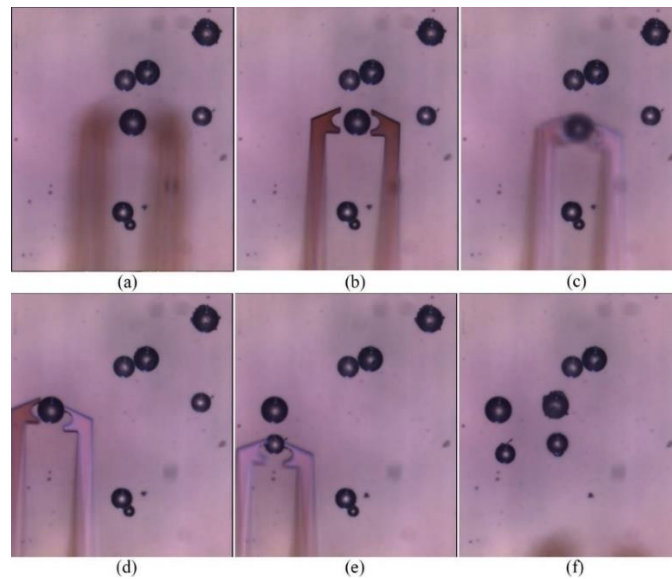




*Fig. 6.111 Manipulation of micro glass beads using design 2-A\_500 (the interfaced microgripper)*

#### *6.6.2 Manipulation Using Design HWU-A and Design HWU-B*

As shown in Fig. 6.111 and Fig. 6.112, spherical glass micro-beads were placed on a glass slide as the substrate on the platform of the robotic system for micro-manipulation. Design 2-A\_500 was used to manipulate glass beads of diameter of around  $100\text{ }\mu\text{m}$ . Design L210\_S was used to manipulate these beads as an array of 2x2. Different sizes of the micro-beads were grasped, repositioned and then released successfully.



*Fig. 6.112 Manipulation of micro glass beads using design 2-B (the L210\_S microgripper) to arrange four beads as an array.*

## 6.7 Microassembly Demonstration

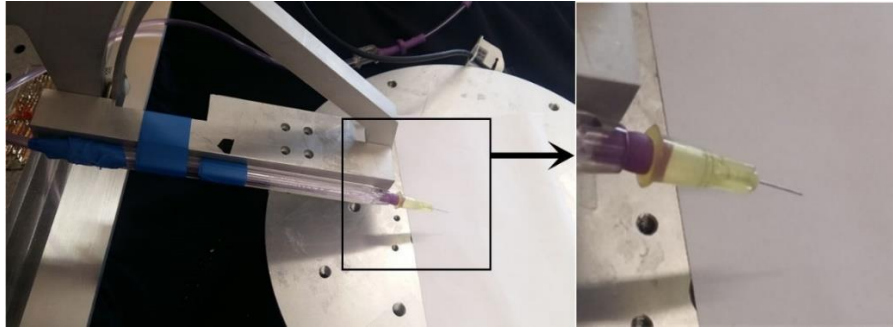
In this work 2D copper foil discs with diameter of 500  $\mu\text{m}$  and thicknesses of 25  $\mu\text{m}$  and 6  $\mu\text{m}$  were assembled on a carbon fiber rod with a diameter of 280  $\mu\text{m}$  at 90° angle. Because of the thickness of the disc, it was difficult to assemble it using manual operation. Techniques were developed to pick up the discs from the flat position to vertical orientation for gripping by a microgripper for manipulation and positioning for microassembly.

### 6.7.1 PMMA Holder

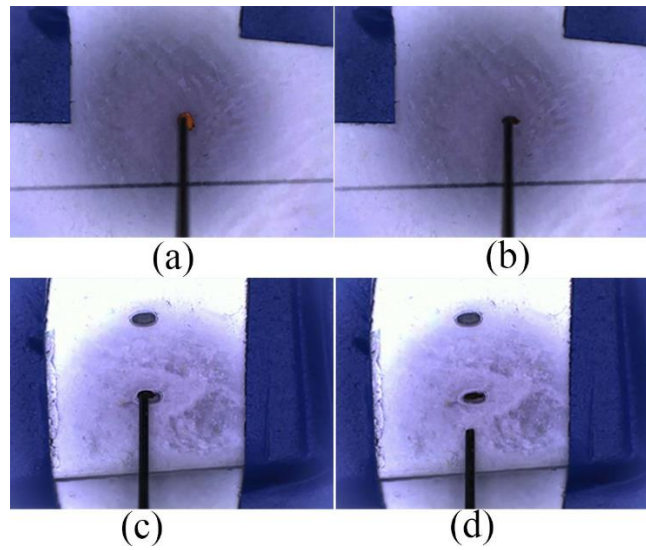
Slots with dimensions of 600  $\mu\text{m}$ , 200  $\mu\text{m}$ , 200  $\mu\text{m}$  in length, width, and depth respectively, were fabricated on PMMA (Poly(methyl methacrylate)) substrates using a laser cutter and a PMMA sheet of thickness of 600  $\mu\text{m}$ . The slots on the PMMA substrate was used to hold the discs in vertical position for grasping by the microgripper. To place a disc from its flat position into a slot on the PMMA substrate, a needle based tool was made to use vacuum based method to pick up the disc. Fig. 7.25 shows the needle mounted on the robotic arm. Fig. 6.114 and Fig. 6.115 show the successful pick-and-place of the micro-discs into the slots on a PMMA substrate, so the discs were roughly in vertical position for gripping by a microgripper. However, the needle based vacuum tool was not suitable for the microassembly work since it lacked the necessary ability to hold the disc securely for manipulation.

### 6.7.2 3D Printed Holder

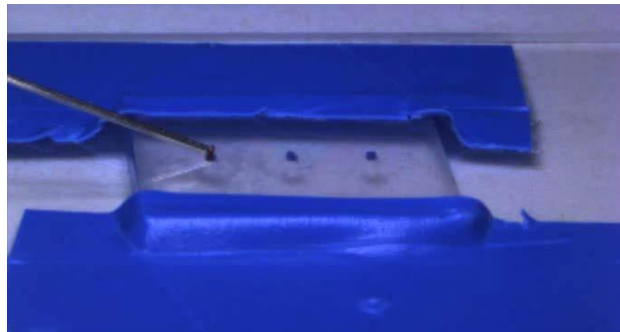
In order to perform the microassembly work, it is necessary to hold the carbon fiber rod in a suspended position. For this purpose, a holder (block) with trenches to support the rod at the two ends was fabricated by 3D printing. The fabricated blocks have rectangular trenches on the surface and v-grooves with semicircular cross-sections at each end were fabricated. The width and depth of the trench are 700 $\mu\text{m}$  and 1000  $\mu\text{m}$  respectively. The diameter of the semicircles for the grooves was about 280  $\mu\text{m}$ , matching the diameter of the carbon rods.



*Fig. 6.113 Micro-vacuum gripper designed using a needle to manipulate the discs*



*Fig. 6.114 Manipulation of the disc from a flat position into the slots (top view) using vacuum micromanipulation*



*Fig. 6.115 Manipulation of the disc from a flat position into the slots (side view) using vacuum micromanipulation*

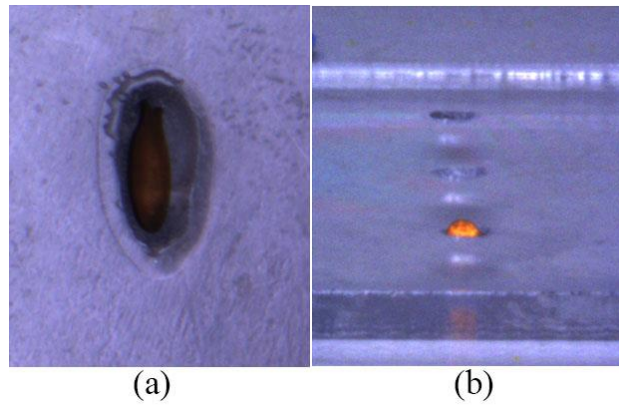


Fig. 6.116 Result from the needle (vacuum gripper) handling (a) top view (b) side view

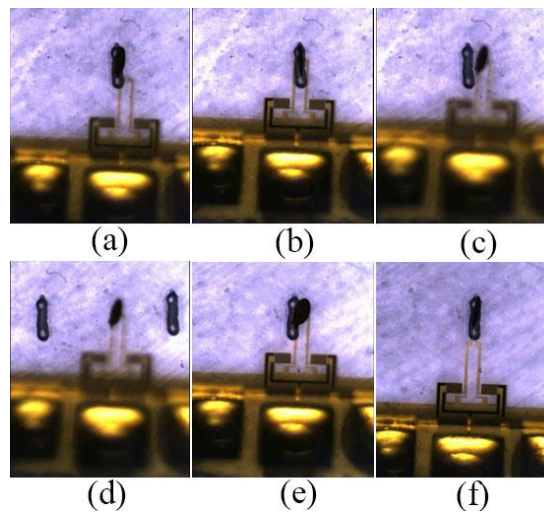


Fig. 6.117 Top view of manipulating a disc using design 2-C (2 DOF microgripper)

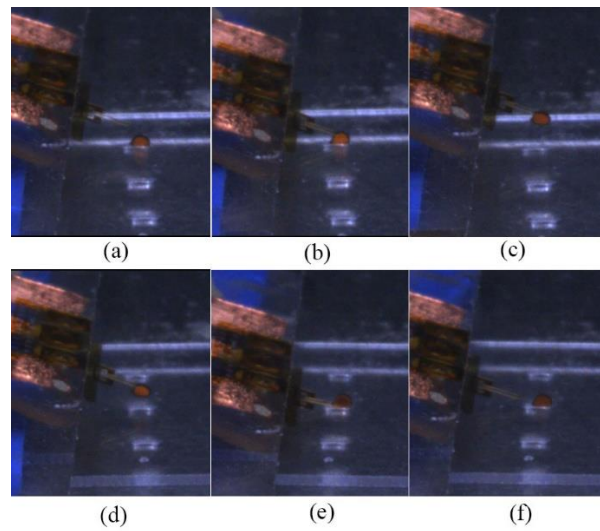
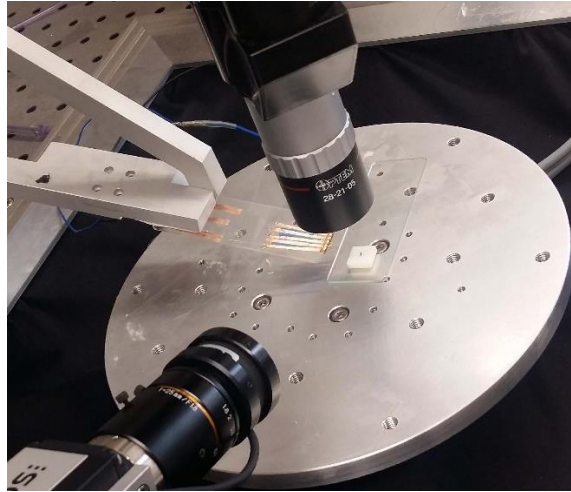


Fig. 6.118 Side view of manipulating a disc using design 2-C (2 DOF microgripper)



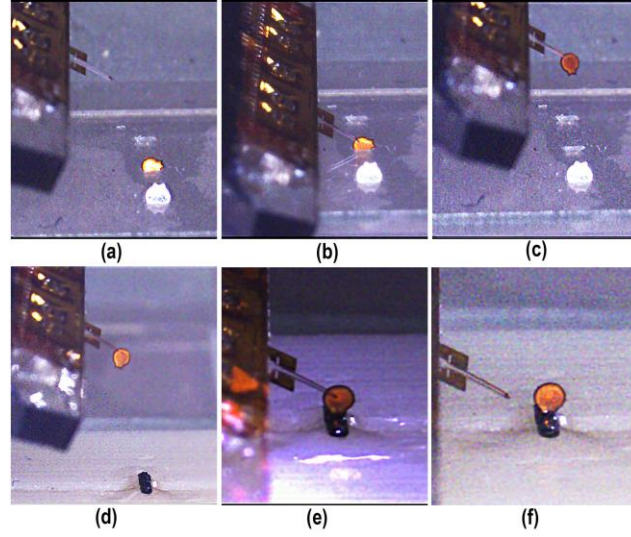
*Fig. 6.119 Robotic system used to implement the assembly process*

### *6.7.3 Microassembly Using Design HWU-C*

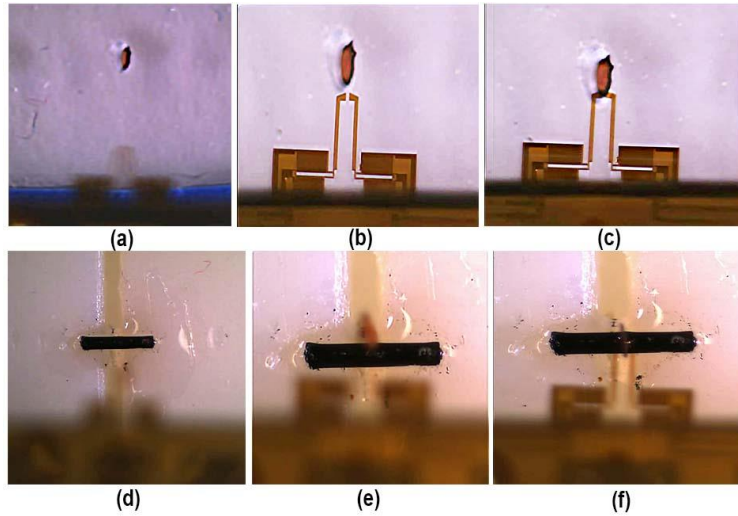
The microgripper design HWU-C was mounted on the 3 DOF robotic arm replacing the needle which was used for the vacuum pickup, as shown in Fig. 6.119. Two cameras were used to monitor the operation of the assembly processes. The Arduino based unit was used to drive the microgripper in both opening and closing operation modes to fully utilize the total amount of displacement. The two cameras were used to monitor the positioning and orientation of the disc for assembly. The holders of the fiber rods and the discs for assembly were placed on the hexapod platform providing 6 DOF for accurate positioning. The copper disc was picked by the microgripper, and its position was controlled by the X, Y, and Z stages of the robotic arm. This was done by gently catching the edge of the disc from a slot, lifting it up, then decreasing the applied voltage gradually to let gravity reorient the disc. Then, the voltage was increased to the previous value to hold the disc gently, as shown in Fig. 6.120 (a) to (c).

A small amount of UV glue was put on the carbon rod using a piece of hair which was used as a brush. Then, the copper disc was picked using the microgripper then it was aligned to the carbon fiber rod. It was positioned on the targeted position and aligned to be at right angle. After that, the glue was cured using a UV light source for about five minutes. The applied voltage was then turned off to release the disc and the microgripper was move away to complete the microassembly process, as shown in Fig. 6.120 and Fig. 6.121.





*Fig. 6.120 Side view of the assembly processes (a) disc is in the slot (b) picking the disc and change the disc orientation (c and d), Moving the disc to position, (e) aligning the disc on the carbon fibre and curing the UV glue using, (f) releasing the disc*



*Fig. 6.121 Top view of the assembly processes, (a) disc is in the slot, (b and c) picking the disc and manipulating the disc orientation (d) Moving the disc to position, (e) aligning the disc on the carbon fibre and curing the glue using UV, (f) releasing the disc*

## 6.8 Discussion

### 6.8.1 Temperature and Displacement Results

The first four IMT designs were based on the hot/cold arm configuration (U-shaped actuators). The conductor width in the cold arms was twice the conductor width of the hot arms, 20  $\mu\text{m}$  and 10  $\mu\text{m}$  respectively. The power dissipation in each part is proportional to the conductor (heater) resistance, as shown in equation (6-1). The resistance is inversely

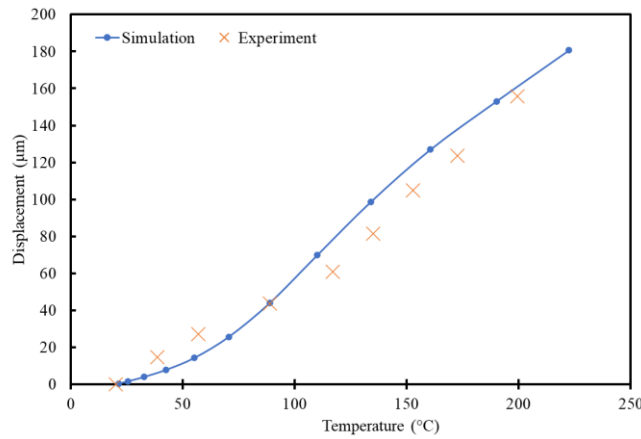
related to the conductor width, as shown in equation (6-2), i.e. the power dissipation in the cold arm is half that of the hot arm for same the conductor length.

$$P = I^2 R \quad 6-1$$

$$R = \frac{\rho L}{W T} \quad 6-2$$

Where  $P$  is the power,  $I$  is the current,  $R$  is resistance,  $\rho$  is the resistivity,  $L$  is the conductor length,  $W$  is the conductor width, and  $T$  is the thickness.

From this analysis, it is clear that power is also dissipated in the cold arm and it is not cold as it should be in the ideal case. The results in this chapter prove this and show the effect of this power dissipation on the microgripper behavior. The end-effector displacement in these microgrippers was the result of the difference in expansion between the two arms. The HWU microgrippers were based on the L-Shape actuator which was better in term of stability and displacement range. Also, the absence of conductor in the end-effectors has the advantage of significantly higher displacement.



*Fig. 6.122 Simulation and experiment results of displacement of both arms as a function to the heater average temperature of Design HWU-A*

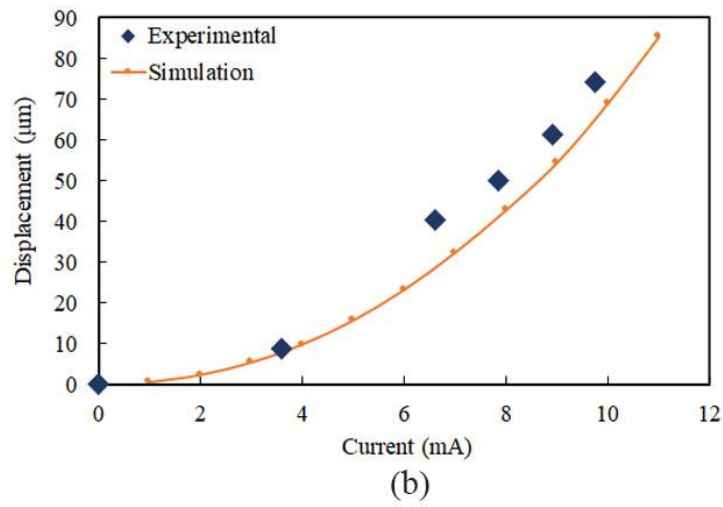
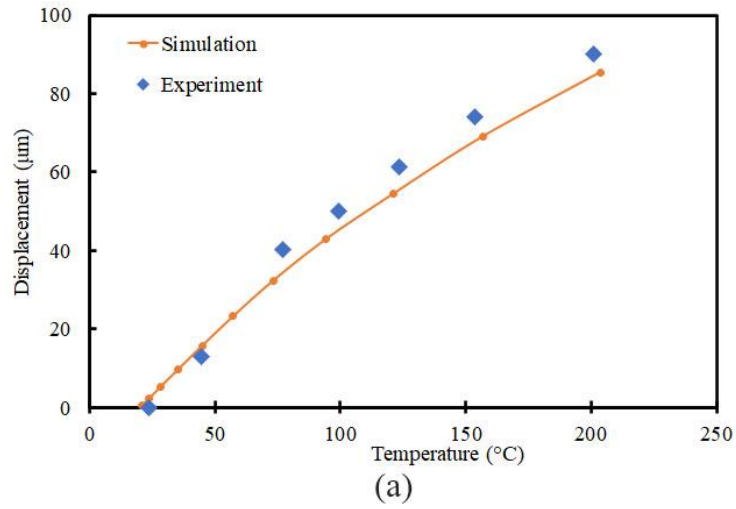


Fig. 6.123 Simulation and experimental results of displacement in closing mode operation as a function of (a) temperature and (b) current for the Design HWU-C



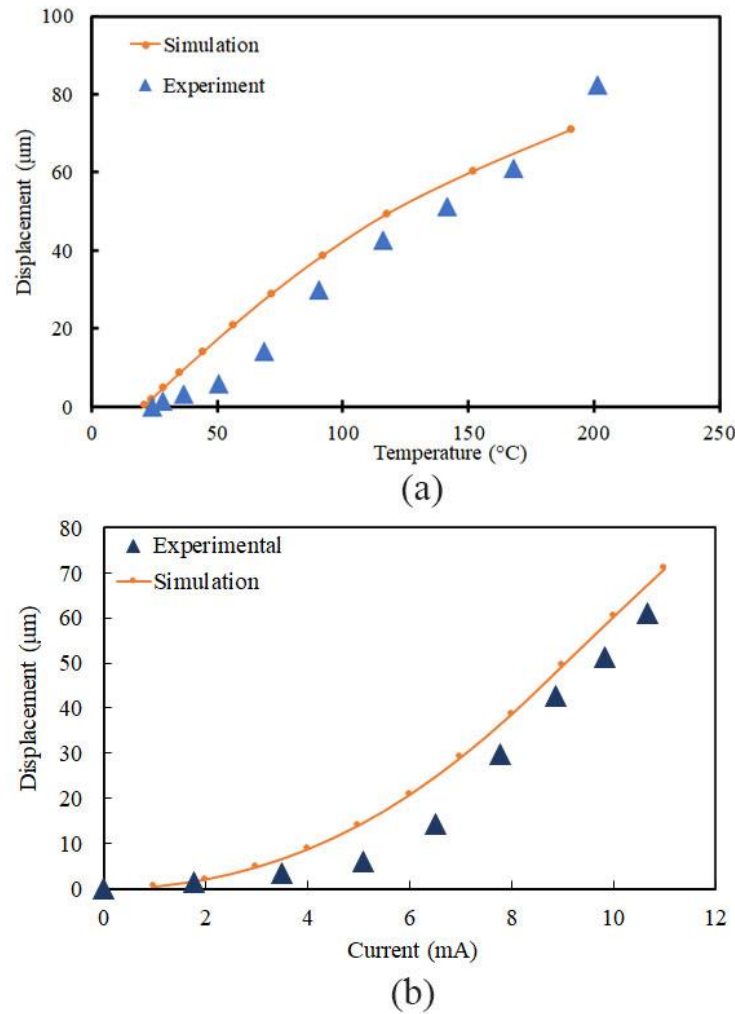


Fig. 6.124 Simulation and experiment results of displacement of both arms in opening mode operation as a function of (a) temperature (b) current of the Design HWU-C

The measured displacement results for first HWU design (Design HWU-A) as a function to the heater average temperature and the simulation results are shown in Fig. 6.122. It can be seen that the simulation results are in good agreement with the experiment results. However, for the results under 100°C, the simulated displacement was less than the experimental value while it was higher at a higher temperature. This difference could be due to the values of Young's modulus which were obtained from the literature. Therefore, it is necessary in future work to measure the Young's modulus of SU8 structures for different fabrication processes since the material properties depend on the process conditions.

Fig. 6.123 and Fig. 6.124 show the comparison between the simulation and the experimental results of the displacement as a function to the heater temperature and the applied current for closing and opening mode operation for design HWU-C respectively. There is a small difference between the results which may be due to the Young's modulus value, and fabrication limitation, etc.

### 6.8.2 *Dynamic Response Cycling Result*

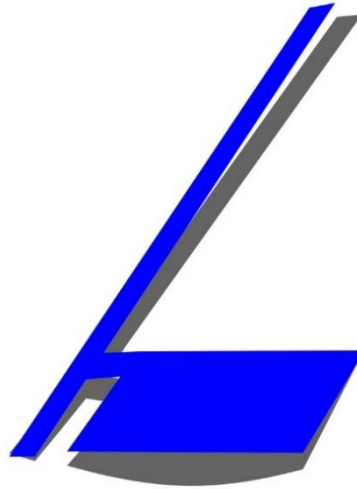
Using the heater resistance change as a feedback to determine the temperature is the most accurate, low cost and reliable method. This is because it is easy to implement and does not affect the microgripper operation. For example, using a thermocouple as a temperature sensor will reduce the actuator temperature and result in inaccurate reading. The same is true in using the image tracking method to calculate the end-effector position, the optical method does not affect the microgripper operation, but a position sensor will increase the reaction force. It would increase the bending of the actuator and result in wrong displacement measurements.

The characterisation of the interface circuit shows the voltage rising time was only 5  $\mu$ s and the ADC conversion time was about 16.6 ms. In other words, the interface delay has no effect on the study results. However, the conversion rate was less than required to show the full view of the temperature rise as time, which was less than 100 ms, i.e. there were only a few samples taken to characterise the rising curve. This effect of the sampling rate is reflected on the temperature curve.

The displacement was much slower, and the rise time was about 0.2 s to 1 s. The image processing rate was about 66 samples/s, i.e. there were about 12 – 60 samples to represent the rise time. Therefore, there was enough dynamic information in displacement compared to that of temperature.

The selection of the microgrippers was based on the displacement results from the displacement study. The microgrippers with a larger displacement were selected for the dynamic study because there was enough change to reflect the microgrippers' behavior. The results from design 1-E show the opening reached 25  $\mu$ m in 200 ms but it then decreased gradually after that. This behavior was caused by the change in the Young modulus due to the change in the heater temperature. For the first 200 ms, the heat was transferred from the heater conductor to the actuator structure. This caused a maximum displacement which represents the overshoot in the dynamic response. Then, because of the temperature increase, the Young modulus (the actuator structure stiffness) decreased which was reflected by the shrinking in the displacement. The actuator stiffness decreased and the deflection behavior shown in Fig. 6.125 was observed.

This behavior was noticed repeatedly over most of the studied microgrippers with different overshoot value comparing to the steady state value. From the results, the improvement in the actuator stiffness as compared to the arm stiffness decreased this overshoot value and it disappeared in design B, the (L210\_S) variant. Also, it was at the maximum in designs 1-Z and the 1-V. In addition, this behaviour is directly related to the applied voltage, i.e. the temperature within same microgripper design.



*Fig. 6.125 Actuator deformation after each on/off cycle and its effect on the end-effectors shape*

## 6.9 Summery

The first group of microgrippers designed by IMT was based on different electrothermal actuation methods. Designs IMT-A to IMT-C were based on hot/cold arms (U-shaped microactuators) for normally closed operation and Design IMT-D was based on the same actuation method, but it is in normally open mode for operation. The last design IMT-E in this group was different to the other designs in the shape of the heater. This design is normally closed, and it opens when power is applied.

Although both design B and C look similar to design A, they behave in a way which proves that the U-shaped actuator is not efficient because of the generated temperature in the cold arm. This generated undesirable expansion which noticeably affects the desired behaviour. In addition, the highest deflection of the actuated arms was small and in the best case design IMT-E only showed a displacement of about 20  $\mu\text{m}$ .

The other group from IMT contained three other designs: design IMT-F, V-shaped (design IMT-G) and Z-shaped (design IMT-H) electrothermal microactuators. However, they showed a larger displacement, up to 40  $\mu\text{m}$  in the V shaped microactuators. But they broke down and stopped working after running for several cycles. This is because of either the very narrow beam in the first design which broke easily after cycling it for some time or because of the very narrow actuator beam which buckled permanently after running for some time.

The L-shaped actuator design in the thesis work solved these problems. It has no cold arm, therefore there is no limitation to designing narrow hinges, and there is no heating source in the actuated arms. The wider actuators solved the buckling problem of the microgrippers cycling on/off many times more than the other designs. The flexibility and ease of designing this type of actuator results in different types of microgrippers with wide displacements up to 160  $\mu\text{m}$ .

There was a different design with different actuator to arm width ratio and different actuator width (of design HWU-B) as shown in Fig. 6.34 and Fig. 6.35 to study the relationship between the displacement and the actuator stiffness. The results of the displacement measurements proved that the actuator performed better when its stiffness was as high as possible. As the stiffness is related to the squared thickness and directly related to the width, it was more effective to increase the actuator thickness ratio compared with the actuated part.

The shape of the conductors in the heater part had an effect on the efficiency of the actuators. The results from this chapter proved the folded meander heater is more stable than the single meander design. This is because of the difference in the expansion ratio between the polymer and the metal layer. In the folded meander heater, there is no continuous conductor along the heater and the effect of the different CTE has less effect on the expansion ratio.

In all IMT's designs with U- shaped (design IMT-A to design IMT-E), V- shaped (design IMT-G) and Z-shaped actuator (design IMT-H), the displacement was not linear as a function of the average heater temperature because of the buckling effect. This was obviously the most important difference with the simple L-shaped actuators. All the L-

shaped microgrippers have a linear displacement as a function of the average heater temperature.

In addition, the L-shaped actuator was used to design a novel dual-direction actuator. This new method was employed to design a dual-mode microgripper (design HWU-C) with large displacement and stable operation. The results showed more than 80  $\mu\text{m}$  of deflection in each mode (opening and closing). A novel tri-directional actuator was tested and the optimised design using wider actuators instead of the traditional narrow beam chevron actuators has better performance. This new actuation method was more stable than the conventional approaches.

Most of the studied microgrippers showed an overshoot on powering ON for a short time, then the displacement reduced. This is due to the deformation in the heater shape and the change in the opening value on the powering OFF time proved that. The overshoot is directly related to the temperature because SU8 materials get softer at higher temperatures. This is due to the relationship between Young's modulus and temperature. The last four tests (L100\_D, L100\_S, L210\_D, and L210\_S) proved that when the actuator part stiffness is higher, the overshoot is less and the change in the heater shape has less effect than less actuator stiffness. Smaller time period sample does not show the real dynamic behavior of the microgrippers. The heater temperature rises much faster than the mechanical response. This behavior was not illustrated in the previously published dynamic study of microgrippers. This is because the previous study was based on a selected frame taken from a video recording. In addition, the previous study focused on the raising time more than what happened afterwards.

The wider actuators in designs IMT-E and IMT-F performed better than the other designs in the cycling test for reliability study. All the narrow actuators showed either a permanent deformation or overheating, even when the average temperature was low, as shown in design IMT-Z and IMT-V. Only design IMT-D was stable and had no deformation or overheating effect. The only difference between the IMT-Z, IMT-V, and IMT-D that IMT-D had a single heater. Both IMT-Z and IMT-V designs had multi-beams in the parallel actuators, the temperature in each beam depends on the beam resistance and

a small fabrication error causes a difference in the temperature, as observed in both design IMT-Z and IMT-V.

On the other hand, the smaller the displacement the less the reaction to the heater. In other words, there is less force to deform the actuator as it is clear from the test results of the IMT microgrippers. This was proved by the tests on the different configurations of the L-shaped microgrippers (L100\_D, L100\_S, L210\_D, and L210\_S). Increasing the actuator width or thickness resulted in better performance with less deformation and larger displacement.

The SU-8 electrothermal microgrippers were successfully used to manipulate different micro-objects. Design 1-A and design 1-B were used to pick and place glass micro-beads. Design 1-C was used to assemble micro-discs on carbon fiber rods in successful demonstration of the microgrippers for microassembly applications.

## Chapter 7 Conclusions

This chapter summarizes the outcomes of the research presented in this thesis. The most important contributions and discoveries are presented, and future work is proposed.

### 7.1 Summary

In the recent years many researchers and developers have become interested in miniaturised devices. Manufacturing of devices and systems at small scale requires advanced microassembly methods. In this thesis, some of the previous microassembly systems were presented in the literature review. Then, it focused on robotics based microassembly systems and some examples were presented.

#### 7.1.1 Micromanipulation Method Selection

There are many micromanipulation methods presented in the literature review. They are summarised in Tables 2.3 to 2.6 with key advantages and disadvantages. The microgrippers based on embedded electrothermal actuators were selected for these reasons:

- i. Easy to fabricate with the available facilities and it do not require extra assembly.
- ii. Easy to operate with open and close loop control system. Also, it does not require complex electronics because of the low operating voltages.
- iii. Can be designed in a small size of less than 1 mm, i.e. can be used to assemble micro-objects in small and narrow places where larger microgripper cannot be used.
- iv. Microgrippers with jaws (end-effectors) are more flexible than other design approaches because such microgrippers can be easily used for rotation, reorientation, picking and placing target micro-objects.
- v. Can be used regardless of the medium, i.e. in a dry environment or in liquid.

Electrothermal microgrippers are based on different materials. These materials were listed in Table 2.7. In this thesis, SU-8 was selected because of the following properties:

- i. It requires low operation force due to the low value of Young's modulus.
- ii. Reliable to design hinges because of its good elasticity specification.
- iii. Easy to fabricate using photolithography based microfabrication methods.
- iv. High softening and crosslinking temperature up to 210°C.
- v. High CTE over the other materials for electrothermal actuation.

### *7.1.2 Design and simulation*

In the literature review, it was pointed out that there are two approaches to designing electrothermally actuated microgrippers depending on the actuator shape. These are the U-shaped microgrippers (hot/cold arms method) and the Z-shaped and V-shaped microgrippers (the chevron method). Both methods have advantages and disadvantages, for example the hot/cold arm configuration can achieve high displacement with a strong force. However, the cold arm is not actually cold because of the current in the conductor path in the cold arm. In addition, the existence of a conductor passing through the hinges limit the width of the hinges and they cannot be as narrow as required. This is because the narrower the conductor is the higher temperature is. On the other hand, the chevron method has an isolated heater so it cannot achieve high forces because of the width of the actuators.

In this thesis, a new method of design (L-shaped approach) was proposed which combines the advantages of both previous methods. It can achieve high forces because the actuator width is not limited, and it has insulated hinges. Therefore, there is no heat source in the cold arms. In addition, a modification was proposed based on the chevron method to increase the beam stiffness. In this approach, there is one wide actuator beam instead of the multiple ones as in the previous method.

These new design approaches were utilised to design four different microgrippers and a three DOF actuator. The first design was indirectly actuated using the L-shaped SU-8 with embedded heater as an active part. Also, it has an interface between this part and the end-effectors arms. The second design was directly actuated using the new actuation method. The third design was a combination of two L-shaped actuators to achieve bi-directional microgrippers. Finally, a combination of the L-shaped actuators and a tri-directional actuator was used to propose a new microgripper design with three end-effectors.

A simulation method was proposed and used in this thesis to study these microgrippers. In this approach, a block of air was added to surround the gripper designs for simulation. This method solved the issue in the conventional method of changing the material properties to fit the practical results. The conventional method suffers from uncertainty over which coefficient values to use and therefore, the results are can be unreliable. This method shows that the simulation results are close to the practical results without changing any of the coefficient values.



The displacement results of the first design (the interfaced microgripper) were about 90  $\mu\text{m}$  when a current of 12 mA was applied while the heater temperature raised to about 200°C.

The second design (the directly actuated microgripper) shows different results of the eight variants. Some variants in this design showed a behavior with small total displacement started from 30  $\mu\text{m}$  in the linear shaped heaters conductor and 100  $\mu\text{m}$  width with arms thickness of 20  $\mu\text{m}$ . While they were reached about 70  $\mu\text{m}$  and 60  $\mu\text{m}$  of displacement for the meander shaped and the linear shaped heater conductor respectively, with width of 210  $\mu\text{m}$  width of the active SU-8 parts and 10  $\mu\text{m}$  thickness of the arms. These results were based on the average temperature of 200°C in all devices of this design. The narrower actuator width required more current to heat up the active parts to 200°C which was about 18 mA at the meander heater with width 210  $\mu\text{m}$  up to 35 mA at the linear heater with width of 100  $\mu\text{m}$ .

The third design (bi-directional microgripper) achieved about 40  $\mu\text{m}$  of displacement in each mode when an current of about 11 mA was applied on either heater 1 or 2. The displacement in these designs as a function of the temperature showed near linear behavior with slightly faster increase at the lowest temperature region than in the higher temperature region.

### *7.1.3 Temperature Coefficient of Resistance Measurements*

In order to measure heater temperature correctly and to eliminate the error in using TCR of the bulk material, the actual TCR of the heaters in each microgripper was measured. Both the IMT and Heriot-Watt devices were used to study the TCR of different heater layer configurations. The heater layer designs are as follows:

- i. 10/300/10 nm of Chromium, Gold, and Chromium respectively.
- ii. 7 /200/7 nm of Chromium, Gold, Chromium respectively.
- iii. 100 nm of Gold only.

Different methods were used to measure the TCR values to increase the reliability of the results. The first method was based on a closed chamber on a hot plate. The average air temperature was measured using two thermocouple sensors positioned close to the microgripper under test. Another method used distilled water based bath to heat up the microgripper and hence the heaters gradually since water bath can provide a stable temperature environment. In the third method, the microgripper for TCR measurement

was glued completely onto a glass slide which was then placed on the surface of the hot plate to ensure good thermal contact.

Nineteen tests of different microgripper designs with heater layer of 10/300/10 nm based Cr/Au/Cr configuration were carried out. All the results were over 95% matching the linear fits. The average of all results was about 0.00137. Five tests of different microgrippers of 7/200/7 nm based Cr/Au/Cr configuration were tested. The average of these results was 0.00197. In the 100 nm Au heater configuration, only four microgrippers were tested. The average of the results was 0.00313.

It is clear that the chromium films have a significant effect on the TCR of the heater metal layer. The TCR of bulk gold is about 0.0033 while it is 0.0000059 for chromium. Even 7 nm thick chromium films above and below the much thicker gold film have a significant effect on the TCR of heater layer. Although similar behavior was reported in the literature in bulk gold alloy material with a small percentage of chromium, it is the first time that it is observed in layered film structures of gold and chromium. The results show that it is important to measure the TCR of the heater in order to calculate the heater temperature correctly in microgripper characterisation and operation, the assumption of TCR as that of the bulk material as used in previous work would produce a wrong heater temperature for a given actuation voltage.

A new method was developed to measure the displacement using a robotic system and image processing software based on OpenCV library. This method has the advantage of tracking an area to automate the calculation of the displacement of any single point. The results of this method were compared to the measurements using the Zygo metrology system and a manual conversion of number pixels into length. In order to carry out the measurements of the dynamic responses of the microgrippers, an electronic interface was designed, constructed and integrated to the robotic system. Four pieces of software were written in Visual C++, Embedded C, and Java script to manage the control and communication, and to acquire the data for analysis.

Several microgrippers were studied using the method. The U-shaped microgrippers (hot/cold arm design) showed a small displacement value and permanent deformation after cycling test. Some of them stopped working after several cycles because of the permanent deformation of the actuator structure. The microgrippers based on the chevron heater structure with larger displacement showed similar behavior that there was deformation of the actuator structure after the on/off cycling test. These deformations

can be observed from the change in the opening after each cycling test. However, some of change in gripper opening did not recover over a day after the testing.

The microgrippers based on the new L-shaped actuator combined the large displacement of the chevron heater based microgripper showed better stability than the hot/cold arm microgrippers. These microgrippers have much less deformation after each on/off cycling test and were stable over thousands of cycles. In addition, the bi-directional microgripper showed better reliability. This is because the operation in each mode result in pulling the other actuator part and can alleviate the deformed shape. The dynamic studies showed that higher actuator stiffness compared to the arm stiffness results in more stable microgripper behavior.

#### *7.1.4 Demonstration*

The SU-8 electrothermal microgrippers based on the new actuator design (the L-shaped actuator) were successfully used to manipulate different micro-objects. The microgripper based on the interface design was successfully used to manipulate 100  $\mu\text{m}$  diameter glass beads. Based on the glass density of  $2.5 \text{ g/cm}^3$ , the mass of the glass beads is  $1.3 \mu\text{g}$ , therefore the microgripper can apply a sufficient gripping force to manipulate such objects. I The dual-mode microgripper was used to manipulate and assemble a copper disc on a carbon fiber rod successfully showing potential applications of the microgrippers for microassembly.

### **7.2 Contribution**

The key contributions of this thesis are:

- i. Discovered that the multilayer structure of gold and chromium thin films in heaters behaves similar to that of gold-chromium alloy. The TCR value of the metal layers decreased significantly to about 1/3 of the value of bulk gold even with very thin layers of chromium of 7 nm above and below a gold layer of 200 nm in a sandwich configuration.
- ii. Proposed a new simulation method that was not required to change the heat transfer coefficient values of the SU-8 material to fit the experimental results. The results of simulation showed a good agreement with the experimental results.
- iii. Developed a new method based on image tracking software to measure the dynamic responses of microgrippers. This study highlighted the effect of the design and dimensions of electrothermal actuators on the performance of the microgrippers.

- iv. Designed a new L-shape electrothermal actuator to eliminate the drawbacks of the previous methods. The results of the microgrippers based on this actuator design showed a stable, reliable and usable operation. In addition, in actuator design a thicker SU8 structure for actuators was used to increase the critical force of deformation to increase gripper displacement and performance. The SU8 thickness for the actuator structure is twice of that of the gripper arms.
- v. Designed a novel electrothermal tri-directional actuator based on two heaters. This new actuator can be used in many applications such as microswitches.
- vi. Designed a novel bi-directional microgripper with a large displacement and small microgripper dimensions.
- vii. Designed a novel three-arm microgripper.
- viii. Developed a new method to measure the displacement using a robotic system and image tracking software.
- ix. Developed an electronic interface unit and integrated it with the robotic system to measure the dynamic behavior and to conduct reliability studies of microgrippers.
- x. Demonstrated successful application of the microgrippers for microassembly of a thin foil disc onto a carbon fiber rod.

## **7.3 Future Work**

### *7.3.1 Tri-directional Actuator*

More research is required to improve the displacement range of this microgripper. At the moment, the displacement is about 10  $\mu\text{m}$  in each direction. There are two ways to do this. Firstly, by doubling the actuator width and keeping the arm thickness as it is, the out of plane displacement can be reduced and the arm displacement is increased. Secondly, the amplification ratio could be changed with some modifications to the hinges and lengths of the actuators.

### *7.3.2 Microgripper Structure Design*

In this thesis, doubling the actuator width to twice the arm's thickness increased the reliability and displacement of the microgripper. However, the thickness of SU8 microgripper structure was limited to 20  $\mu\text{m}$  in the standard fabrication processes at IMT. Therefore, it was only possible to design the actuator parts to be 20  $\mu\text{m}$  of thickness and the arm parts to be 10  $\mu\text{m}$ . Although this improved the behavior significantly, designing the actuator part of SU8 thickness to be 100  $\mu\text{m}$  and the arm thickness to be 20  $\mu\text{m}$  in

future study may eliminate any overshooting behavior and result in a more stable and reliable microgripper.

### *7.3.3 Dual-Mode Microgrippers*

This microgripper can be developed as a commercial product with further improvements. A microgripper with actuators of thickness of 100  $\mu\text{m}$  and the other parts with 20  $\mu\text{m}$  of thickness can be investigated. In addition, it is possible to design microgrippers with displacement as large as 1 mm by doubling the length of the actuators as compared with the the present design. Therefore, it will be suitable for a wide range of applications.

### *7.3.4 Limitations and proposed solutions*

The SU-8 material degrade after 210° C therefore the heater temperature should not exceed this value otherwise the microgrippers will be damaged and stop operating. The yield strength of the SU-8 is lower than many other materials therefore, this limits the stress applied on hinges and arms. If the yield strength is exceeded, it would cause permanent deformation of the gripper. In addition to this, the Young's modulus is temperature dependent therefore this also limits the maximum operating temperature. Some of these limitations have been studied in this thesis, such as the change in the Young's modulus and proposed a solution for better performance actuators. However, the temperature dependence of Young's modulus should be investigated for different fabrication processes of the SU-8. In addition, the heater temperature monitoring using the designed electronic interface provides a good solution to protect the microgripper from overheating, the software developed in the thesis work can be upgraded to include this function.

## References

- [1] N. Chaillet and S. Régnier, *Microrobotics for micromanipulation*, Hoboken: John Wiley & Sons, Inc., 2013.
- [2] P. Lambert, *Capillary forces in microassembly*, New York: Springer, 2011.
- [3] A. R. Kalaiarasi and S. H. Thilagar, "Design and modeling of electrostatically actuated microgripper," in *8th IEEE/ASME International Conference on Mechatronic and Embedded Systems and Applications*, Suzhou, 2012.
- [4] D. Janasek, J. Franzke and A. Manz, "Scaling and the design of miniaturized chemical-analysis systems," *Nature*, vol. 442, no. 7101, pp. 374-380, 2006.
- [5] G. Li, R. Ran, J. Zhao and Y. Xu, "Design, simulation, and optimization of a miniaturized device for size-fractioned DNA extraction," *ELECTROPHORESIS*, vol. 28, no. 24, pp. 4661-4667, 2007.
- [6] J. Agnus, N. Chaillet, C. Clévy, S. Dembélé, M. Gauthier, Y. Haddab, G. Laurent, P. Lutz, N. Piat, K. Rabenorosoa, M. Rakotondrabe and B. Tamadazte, "Robotic microassembly and micromanipulation at FEMTO-ST," *Journal of Micro-Bio Robotics*, vol. 8, no. 2, pp. 91-106, 2013.
- [7] F. Biganzoli and G. Fantoni, "A self-centering electrostatic microgripper," *Journal of Manufacturing Systems*, vol. 27, no. 3, pp. 136-144, 2008.
- [8] "SmarAct GmbH," SmartAct, [Online]. Available: <http://www.smaract.com/products/automated-microassembly-stations/>. [Accessed 22 12 2018].
- [9] "finetechusa.com," FineTechusa, [Online]. Available: <https://www.finetechusa.com/products/rd-bonders/fineplacer-pico-ma/>. [Accessed 22 12 2018].

- [10] "Femtotools.com," FemtoTools, [Online]. Available: <http://www.femtotools.com/products/ft-mta03/description/>. [Accessed 22 12 2018].
- [11] X. Herpe, Affordable Flexible Hybrid Manipulator for Miniaturised Product Assembly, Edinburgh: Heriot-Watt University, September 2017.
- [12] R. Lake and R. Coutu, "Using Cross-Linked SU-8 to Flip-Chip Bond, Assemble, and Package MEMS Devices," *IEEE Transactions on Components, Packaging and Manufacturing Technology*, vol. 5, no. 3, pp. 301-306, 2015.
- [13] A. Sieber, P. Valdastrì, K. Houston, A. Menciassi and P. Dario, "Flip chip microassembly of a silicon triaxial force sensor on flexible substrates," *Sensors and Actuators A: Physical*, vol. 142, no. 1, pp. 421-428, 2008.
- [14] N. Bassik, G. Stern and D. Gracias, "Microassembly based on hands free origami with bidirectional curvature," *Applied Physics Letters*, vol. 95, no. 9, p. 091901, 2009.
- [15] T. Leong, B. Benson, E. Call and D. Gracias, "Thin Film Stress Driven Self-Folding of Microstructured Containers," *Small*, vol. 4, no. 10, pp. 1605-1609, 2008.
- [16] T. Leong, P. Lester, T. Koh, E. Call and D. Gracias, "Surface Tension-Driven Self-Folding Polyhedra," *Langmuir*, vol. 25, no. 4, pp. 2550-2550, 2009.
- [17] X. Chen, Ed., Mechanical self-assembly, New York: Springer, 2013.
- [18] M. Probst, C. Hürzeler, R. Borer and B. Nelson, "A Microassembly System for the Flexible Assembly of Hybrid Robotic MemS Devices," *International Journal of Optomechatronics*, vol. 3, no. 2, pp. 69-90, 2009.
- [19] M. H. Y. a. L. P. Rakotondrabe, "Design, development and experiments of a high stroke-precision 2DoF (linear-angular) microsystem," in *IEEE International Conference on Robotics and Automation, 2006. ICRA 2006.*, Orlando, FL, USA, 2006.

- [20] Q. Chen, Y. Haddab and P. Lutz, "Microfabricated bistable module for digital microrobotics," *Journal of Micro-Nano Mechatronics*, vol. 6, no. 1-2, pp. 1-12, 2010.
- [21] A. Delettre, G. Laurent, Y. Haddab and N. Le Fort-Piat, "Robust control of a planar manipulator for flexible and contactless handling," *Mechatronics*, vol. 22, no. 6, pp. 852-861, 2012.
- [22] M. H. Y. a. L. P. Rakotondrabe, "Voltage/Frequency Proportional Control of Stick-Slip Micropositioning Systems," *Transactions on Control Systems Technology*, vol. 16, no. 6, pp. 1316-1322, 2008.
- [23] M. H. Y. a. L. P. Rakotondrabe, "Development, Modeling, and Control of a Micro-/Nanopositioning 2-DOF Stick-Slip Device," *IEEE/ASME Transactions on Mechatronics*, vol. 14, no. 6, pp. 733-745, 2009.
- [24] M. Rakotondrabe, Y. Haddab and P. Lutz, "Design, development and experiments of a high stroke-precision 2DoF (linear-angular) microsystem," in *2006 IEEE International Conference on Robotics and Automation*, Orlando, FL, 2006.
- [25] C. Clévy, A. Hubert and N. Chaillet, "Flexible micro-assembly system equipped with an automated tool changer," *Journal of Micro-Nano Mechatronics*, vol. 4, no. 1, pp. 59-72, 2008.
- [26] N. Dechev, R. Lu, W. Liu, L. Cleghorn and J. Mills, "Development of a 6 degree of freedom robotic micromanipulator for use in 3D MEMS microassembly," in *IEEE International Conference On Robotics & Automation*, Orlando, FL, USA, 2006.
- [27] N. Dechev, Cleghorn and J. Mills, "Microassembly of 3D MEMS structures utilizing a MEMS microgripper with a robotic manipulator," in *IEEE International Conference on Robotics and Automation*, Taipei, Taiwan, Taiwan, 2003.
- [28] N. Dechev, W. Cleghorn and J. Mills, "Microassembly of 3-D microstructures using a compliant, passive microgripper," *Journal of Microelectromechanical Systems*, vol. 13, no. 2, pp. 176 - 189, 2004.



- [29] percipio-robotics, "percipio-robotics," percipio-robotics, [Online]. Available: <http://percipio-robotics.com/solutions-de-micro-manipulation.html?lang=en>. [Accessed 30 12 2018].
- [30] S. KATZIR , "THE DISCOVERY OF THE PIEZOELECTRIC EFFECT," in *THE BEGINNINGS OF PIEZOELECTRICITY*, Dordrecht, Springer, 2006, pp. 15 - 16.
- [31] J. Tichý, J. Erhart, E. Kittinger and J. Prívratská, Fundamentals of Piezoelectric Sensorics, Berlin: : Springer , 2014.
- [32] C. Gao, D. Kuhlmann-Wilsdorf and D. Makel, "Fundamentals of stick-slip," *Wear*, Vols. 162-164, no. Part B, pp. 1139-1149, 1993.
- [33] J. Breguet, R. Perez, A. Bergander, C. Schmitt, R. Clavel and H. Bleuler, "Piezoactuators for motion control from centimeter to nanometer," in *IEEE/RSJ International Conference on Intelligent Robots and Systems (IROS 2000)*, Takamatsu, Japan, 2000.
- [34] M. Hochwallner, "On Motion Control of Linear Incremental Hydraulic Actuators. pp.Linköping Studies in Science and Technology," Dissertations, , 2017.
- [35] J. Li, H. Liu and H. Zhao, "A Compact 2-DOF Piezoelectric-Driven Platform Based on “Z-Shaped” Flexure Hinges," *Micromachines*, vol. 8, no. 8, p. 245, 2017.
- [36] C. Oh, J. Choi, H. Nam, J. Bu and S. Kim, "Ultra-compact, Zero-power Magnetic Latching Piezoelectric Inchworm Motor with Integrated Position Sensor," *Sensors & Actuators*, vol. 158, no. 2, pp. 306-312, 2010.
- [37] S. Kim and S. Kim, "Precise rotary motor by inchworm motion using dual wrap belts," *Review of Scientific Instruments*, vol. 70, no. 5, pp. 2546-2550, 1999.
- [38] A. Ashkin, "Acceleration and Trapping of Particles by Radiation Pressure," *Physical Review Letters*, vol. 24, no. 4, pp. 156-159, 1970.

- [39] Y. Li, Z. Guo and S. Qu, "Living cell manipulation in a microfluidic device by femtosecond optical tweezers," *Optics and Lasers in Engineering*, vol. 55, no. C, pp. 150-154, 2014.
- [40] E. Flores-Flores, R. Páez, S. A. Torres-Hurtado, U. Ruiz, G. Beltrán-Pérez, S. L. Neale, J. C. Ramirez-San-Juan and R. Ramos-García, "Trapping and manipulation of microparticles using laser-induced convection currents and photophoresis," *Biomedical Optics Express*, vol. 6, no. 10, p. 4079, 2015.
- [41] J. M. E. Melzer, "Fundamental Limits of Optical Tweezer Nanoparticle Manipulation Speeds," *ACS Nano*, vol. 12, no. 3, pp. 2440-2447, 2018.
- [42] J. Kuo, H. Huang, S. Tung and Y. Yang, "A hydrogel-based intravascular microgripper manipulated using magnetic fields," *Sensors and Actuators A: Physical*, vol. 211, pp. 121-130, 2014.
- [43] H. O. Fatoyinbo, "Microfluidic devices for cell manipulation," in *Microfluidic Devices for Biomedical Applications*, Woodhead Publishing Limited, 2013, pp. 283-350.
- [44] A. Lenshof, C. Magnusson and T. Laurell, "Acoustofluidics 8: Applications of acoustophoresis in continuous flow microsystems," *Lab on a Chip*, vol. 12, no. 7, pp. 1210 - 1223, 2012.
- [45] N. Harris, M. Hill, R. Townsend, N. White and S. Beeby, "Performance of a micro-engineered ultrasonic particle manipulator," *Sensors and Actuators B: Chemical*, vol. 111, pp. 481-486, 2005.
- [46] X. Wang and H. Junhui, "An ultrasonic manipulator with noncontact and contact-type nanowire trapping functions," *Sensors and Actuators A: Physical*, vol. 232, pp. 13-19, 2015.
- [47] A. Neild, S. Oberti, F. Beyeler, J. Dual and B. Nelson, "A micro-particle positioning technique combining an ultrasonic manipulator and a microgripper," *Journal of Micromechanics and Microengineering*, vol. 16, no. 8, pp. 1562-1570, 2006.
- [48] A. Delettre, G. Laurent and N. L. Fort-Piat, "2-DOF Contactless Distributed Manipulation Using Superposition of Induced Air Flows," in *RSJ*

*International Conference on Intelligent Robots and Systems*, San Francisco, CA, USA, 2011.

- [49] A. Delettre, G. Laurent and N. Fort-Piat, "A New Contactless Conveyor System for Handling Clean and Delicate Products Using Induced Air Flows," in *IEEE/RSJ International Conference on Intelligent Robots and Systems*, Taipei, Taiwan, 2010.
- [50] H. V. Brussel, J. Peirs, D. Reynaerts, A. Delchambre, G. Reinhart, N. Roth, M. Weck and Z. E. "Assembly of Microsystems.," *CIRP Annals - Manufacturing Technology*, vol. 49, no. 2, pp. 451-72, 2000.
- [51] G. Fantoni and M. Santochi, "A modular contactless feeder for microparts," *CIRP Annals*, vol. 54, no. 1, pp. 23-26, 2005.
- [52] V. Sariola, V. Liimatainen, T. Tolonen, U. R. and Q. Zhou, "Silicon capillary gripper with self-alignment capability," in *IEEE International Conference on Robotics and Automation*, Shanghai, 2011.
- [53] G. Fantoni, H. H. and M. Santochi, "A new capillary gripper for mini and micro parts," *CIRP Annals*, vol. 62, no. 1, pp. 17-20, 2013.
- [54] A. Vasudev and J. Zhe, "An electrowetting based microgripper," in *51st Midwest Symposium on Circuits and Systems*, Knoxville, TN, 2008.
- [55] A. Vasudev and J. Zhe, "An electrowetting based microgripper," *Applied Physics Letters*, vol. 93, no. 10, p. 103503, 2008.
- [56] W. Rong, Z. Fan, L. Wang, H. Xie and L. Sun, "A vacuum microgripping tool with integrated vibration releasing capability," *Review of Scientific Instruments*, vol. 85, no. 8, p. 085002, 2014.
- [57] X. Huang, Liu Chang and M. Wang, "An automatic vacuum microgripper," in *8th World Congress on Intelligent Control and Automation*, Jinan,, 2010.
- [58] D. Petrovic, G. Popovic, E. Chatzitheodoridis, O. Del Medico, A. Almansa, F. Sumecz, W. Brenner and H. Detter, "ripping tools for handling and assembly of microcomponents," in *23rd International Conference on Microelectronics*, Nis, Yugoslavia, 2002.

- [59] Arai and T. Fukuda, "Adhesion-type micro end effector for micromanipulation," in *International Conference on Robotics and Automation*, Albuquerque, NM,, 1997.
- [60] F. Arai, D. Ando, T. Fukuda, Y. Nonoda and T. Oota, "Micro manipulation based on micro physics-strategy based on attractive force reduction and stress measurement," in *IEEE/RSJ International Conference on Intelligent Robots and Systems*, Pittsburgh, PA, 1995.
- [61] J. T. Feddema, P. Xavier and R. Brown, "Micro-assembly planning with van der Waals force," in *IEEE International Symposium on Assembly and Task Planning (ISATP'99)*, Porto, Portugal, 1999.
- [62] B. LÓpez-Walle, M. Gauthier and N. Chaillet, "Principle of a Submerged Freeze Gripper for Microassembly," *IEEE Transactions on Robotics*, vol. 24, no. 4, pp. 897-902, 2008.
- [63] R. Šafarič and D. Lukman, "One-finger gripper based on the variable van der Waals force used for a single nano/micro-sized object," *Journal of Micromechanics and Microengineering*, vol. 24, no. 8, p. 085012, 2014.
- [64] J. Hesselbach, J. Wrege and A. Raatz, "Micro Handling Devices Supported by Electrostatic Forces," *CIRP Annals*, vol. 56, no. 1, pp. 45-48, 2007.
- [65] S. Büttgenbach, A. Burisch and J. Hesselbach, *Design and manufacturing of active microsystems*, Berlin: Springer, 2011.
- [66] J. Escareno, M. Rakotondrabe and D. Habineza, "Backstepping-based robust-adaptive control of a nonlinear 2-DOF piezoactuator," *Control Engineering Practice*, vol. 41, no. August, pp. 57-71, 2015.
- [67] J. Inoue, K. Kanda and M. K. Fujita F., "Thin-film piezoelectric bimorph actuators with increased thickness using double Pb[Zr,Ti]O<sub>3</sub> layers," *Journal of Micromechanics and Microengineering*, vol. 25, no. 5, p. 055001, 2015.
- [68] L. Kang, "A study on the piezoelectric actuation performance of prestressed piezoelectric unimorph actuators," *Journal of Intelligent Material Systems and Structures*, vol. 25, no. 5, pp. 585-595, 2014.

- [69] I. A. Ivan, D. A. Ciubotariu, C. Clévy, P. Lutz and N. Chaillet, "Duo-bimorph actuator made of PMN-PT [011]: 3D modeling, development and characterization," in *IEEE/ASME International Conference on Advanced Intelligent Mechatronics*, Wollongong, NSW, 2013.
- [70] S. Khadraoui, M. Rakotondrabe and P. Lutz, "Interval Force/position Modeling and Control of a Microgripper Composed of Two Collaborative Piezoelectric Actuators and Its Automation," *International Journal of Control, Automation and Systems*, vol. 12, no. 2, pp. 358-71, 2014.
- [71] D. Piyabongkarn, Y. Sun, R. Rajamani, S. A. and B. Nelson, "Travel range extension of a MEMS electrostatic microactuator," *IEEE Transactions on Control Systems Technology*, vol. 13, no. 1, pp. 138-145, 2005.
- [72] A. Beiser, *Applied physics*, New York: McGraw-Hill, 2003.
- [73] D. Burns and V. Bright, "Nonlinear flexure for stable deflection of an electrostatically actuated micromirror," *Microelectronics Structures and MEMS for Optical Processing*, vol. 3226, p. 125–135, 1997.
- [74] J. Seeger and S. Crary, "Stabilization of electrostatically actuated mechanical devices," in *International Solid State Sensors & Actuators Conference*, 1997.
- [75] M. Hamed, P. Salimi and M. Vismeh, "Simulation and experimental investigation of a novel electrostatic microgripper system," *Microelectronic Engineering*, vol. 98, pp. 467-471, 2012.
- [76] C. Kim, A. Pisano and R. Muller, "Silicon-processed overhanging microgripper," *Journal of Microelectromechanical Systems*, vol. 1, no. 1, pp. 31-36, 1992.
- [77] F. Beyeler, A. Neild, S. Oberti, D. Bell, Y. Sun, D. J. and B. Nelson, "Monolithically Fabricated Microgripper With Integrated Force Sensor for Manipulating Microobjects and Biological Cells Aligned in an Ultrasonic Field," *Journal of Microelectromechanical Systems*, vol. 16, no. 1, pp. 7-15, 2007.

- [78] Y. Jia, J. M. and Q. Xu, "A Dual-Axis Electrostatically Driven MEMS Microgripper," *International Journal of Advanced Robotic Systems*, vol. 11, no. 11, 2014.
- [79] V. Despa, A. Catagiu, I. Ivan, G. V. and M. Ardeleanu, "Modelling and Control of a Microgripper Based on Electromagnetic Actuation," *The Scientific Bulletin of VALAHIA University – MATERIALS and MECHANICS*, vol. 12, no. 9, pp. 131-136, 2014.
- [80] I. Giouroudi, H. Hötzenborfer, J. Kosel, A. D. and W. Brenner, "Development of a microgripping system for handling of microcomponents," *Precision Engineering*, vol. 32, no. 2, pp. 148-152, 2008.
- [81] D. Pugal, K. Jung, A. A. and K. Kim, "Ionic polymer-metal composite mechanoelectrical transduction: review and perspectives," *Polymer International*, vol. 59, no. 3, pp. 279-289, 2010.
- [82] B. Bhandari, L. G. and S. Ahn, "A review on IPMC material as actuators and sensors: Fabrications, characteristics and applications," *International Journal of Precision Engineering and Manufacturing*, vol. 13, no. 1, pp. 141-163, 2012.
- [83] C. Gonzalez and R. Lumia, "An IPMC microgripper with integrated actuator and sensing for constant finger-tip displacement," *Smart Mater. Struct.*, vol. 24, no. 5, p. 055011, 2015.
- [84] A. Sun, D. Bajon, J. Moschetta, B. E. and C. Thipyopas, "Integrated static and dynamic modeling of an ionic polymer-metal composite actuator," *Journal of Intelligent Material Systems and Structures*, vol. 26, no. 10, pp. 1164-1178, 2014.
- [85] H. Park, S. Lee, S. D. and J. Jho, "Highly Enhanced Force Generation of Ionic Polymer–Metal Composite Actuators via Thickness Manipulation," *ACS Appl. Mater. Interfaces*, vol. 7, no. 30, pp. 16659-16667, 2015.
- [86] B. Simon Mun, J. Yoon, S. Mo, K. Chen, N. Tamura, C. Dejoie, M. Kunz, Z. Liu, C. Park, M. K. and H. Ju, "Role of joule heating effect and bulk-surface

- phases in voltage-driven metal-insulator transition in VO<sub>2</sub> crystal," *Applied Physics Letters*, vol. 103, no. 6, p. 061902, 2013.
- [87] K. Chopra, B. L. and M. Francombe, "Electrical Resistivity of Thin Single-Crystal Gold Films," *J. Appl. Phys.*, vol. 34, no. 6, p. 1699, 1963.
  - [88] Ma W. and X. Zhang, "Study of the thermal, electrical and thermoelectric properties of metallic nanofilms," *International Journal of Heat and Mass Transfer*, vol. 58, no. 1-2, pp. 639-651, 2013.
  - [89] M. Hamed, V. M. and P. Salimi, "Design, analysis and fabrication of silicon microfixture with electrothermal microclamp cell," *Microelectronic Engineering*, vol. 111, pp. 160-165, 2013.
  - [90] A. Pasumathy, A. Dwivedi and A. Islam, "Optimized design of Au-polysilicon electrothermal microgripper for handling micro objects," in *International Conference on Electrical, Electronics, Signals, Communication & Optimization (EESCO)*, 2015.
  - [91] Z. Wang, Shen X. and X. Chen, "Design, modeling, and characterization of a MEMS electrothermal microgripper," *Microsystem Technologies*, vol. 21, no. 11, pp. 2307-2314, 2015.
  - [92] H. Kim, E. Nilsen, T. Huang, A. Kim, M. Ellis, G. Skidmore and J. Lee, "Metallic microgripper with SU-8 adaptor as end-effectors for heterogeneous micro/nano assembly applications," *Microsystem Technologies*, vol. 10, no. 10, pp. 689-693, 2004.
  - [93] K. Andersen, K. Carlson, D. Petersen, K. Mølhave, V. Eichhorn, S. Fatikow and P. Bøggild, "Electrothermal microgrippers for pick-and-place operations," in *Micro- and Nano-Engineering 2007 Conference MNE*, 2007.
  - [94] K. Colinjivadi, J. Lee and R. Draper, "Viable cell handling with high aspect ratio polymer chopstick gripper mounted on a nano precision manipulator," *Microsystem Technologies*, vol. 14, no. 9-11, pp. 1627-1633, 2008.

- [95] J. Chu, R. Zhang and Z. Chen, "A novel SU-8 electrothermal microgripper based on the type synthesis of the kinematic chain method and the stiffness matrix method," *J. Micromech. Microeng.*, vol. 21, no. 5, p. 054030, 2011.
- [96] R. Zhang, J. Chu and Z. Chen, "A novel SU-8 electrothermal microgripper based on type synthesis of kinematic chain method," in *16th International Solid-State Sensors, Actuators and Microsystems Conference, TRANSDUCERS'11.*, 2015.
- [97] R. Zhang, J. Chu, H. Wang and Z. Chen, "A multipurpose electrothermal microgripper for biological micro-manipulation," *Microsystem Technologies*, vol. 19, no. 1, pp. 89-97, 2012.
- [98] N. Chronis and L. Lee, "Electrothermally activated SU-8 microgripper for single cell manipulation in solution," *Journal of Microelectromechanical Systems*, vol. 14, no. 4, pp. 857-863, 2005.
- [99] B. Solano, A. Gallant and D. Wood, "Design and Optimisation of a Microgripper: Demonstration of Biomedical Applications Using the Manipulation of Oocytes," in *Symposium on Design, Test, Integration & Packaging of MEMS/MOEMS*, 2009.
- [100] B. Solano and D. Wood, "Design and testing of a polymeric microgripper for cell manipulation," *Microelectronic Engineering*, vol. 84, no. 5-8, pp. 1219-1222, 2007.
- [101] N. Nguyen, S. Ho and C. Low, "A polymeric microgripper with integrated thermal actuators," *J. Micromech. Microeng.*, vol. 14, no. 7, pp. 969-974, 2004.
- [102] O. Sardan, D. Petersen, K. Mølhave, O. Sigmund and P. Bøggild, "Topology optimized electrothermal polysilicon microgrippers," *Microelectronic Engineering*, vol. 85, no. 5-6, pp. 1096-1099, 2008.
- [103] T. Chu Duc, G. Lau, J. Creemer and P. Sarro, "Electrothermal Microgripper With Large Jaw Displacement and Integrated Force Sensors," *Journal of Microelectromechanical Systems*, vol. 17, no. 6, pp. 1546-1555, 2008.



- [104] B. Solano, J. Merrell, A. Gallant and D. Wood, "Modelling and experimental verification of heat dissipation mechanisms in an SU-8 electrothermal microgripper," *Microelectronic Engineering*, vol. 124, pp. 90-93, 2014.
- [105] L. Dodd, S. Ward, M. Cooke and D. Wood, "The static and dynamic response of SU-8 electrothermal microgrippers of varying thickness," *Microelectronic Engineering*, vol. 145, pp. 82-85, 2015.
- [106] J. Luo, R. Huang, J. He, Y. Fu, A. Flewitt, S. Spearing, N. Fleck and W. Milne, "Modelling and fabrication of low operation temperature microcages with a polymer/metal/DLC trilayer structure," *Sensors and Actuators A: Physical*, vol. 132, no. 1, pp. 346-353, 2006.
- [107] J. Ok, Y. Lu and C. Kim, "Pneumatically Driven Microcage for Microbe Manipulation in a Biological Liquid Environment," *Journal of Microelectromechanical Systems*, vol. 15, no. 6, p. 15, 1499-1505.
- [108] A. Alogla, P. Scanlan, S. W. and R. Reuben, "A Scalable Syringe-Actuated Microgripper for Biological Manipulation," *Procedia Engineering*, vol. 74, pp. 882-885, 2012.
- [109] S. Bütefisch, V. Seidemann and S. Büttgenbach, "Novel micro-pneumatic actuator for MEMS," *Sensors and Actuators A: Physical*, Vols. 97-98, pp. 638-645, 2002.
- [110] J. Hesselbach, R. Tutsch, S. Büttgenbach, G. Pokar, S. Bütefisch and M. Berndt, "Assembly and measuring technique for the manufacturing of active micro systems," *Microsystem Technologies*, vol. 10, no. 3, pp. 182-186, 2004.
- [111] V. Seidemann, S. Bütefisch and S. Büttgenbach, "Fabrication and investigation of in-plane compliant SU8 structures for MEMS and their application to micro valves and micro grippers," *Sensors and Actuators A: Physical*, Vols. 97-98, pp. 457-461, 2002.
- [112] A. Cao, J. Kim and L. Lin, "Bi-directional electrothermal electromagnetic actuators," *J. Micromech. Microeng.*, vol. 17, no. 5, pp. 975-982, 2007.

- [113] C. Lee, Z. Chen, H. Chang, C. C. and C. Wen, "Design and fabrication of a novel micro electromagnetic actuator," in *Design, Test, Integration & Packaging of MEMS/MOEMS*, Nice, 2008.
- [114] D. Kim, M. Lee, K. B. and Y. Sun, "A superelastic alloy microgripper with embedded electromagnetic actuators and piezoelectric force sensors: a numerical and experimental study," *Smart Mater. Struct.*, vol. 14, no. 6, pp. 1265-1272, 2005.
- [115] D. Lagoudas, *Shape memory alloys*, New York: Springer, 2008.
- [116] J. Kyung, B. Ko and G. Ha Y. Chung, "Design of a microgripper for micromanipulation of microcomponents using SMA wires and flexible hinges," *Sensors and Actuators A: Physical*, vol. 141, no. 1, pp. 144-150, 2008.
- [117] K. Houston, C. Eder, A. Sieber, A. C. M. Meneiassi and P. Dario, "Polymer sensorised microgrippers using SMA actuation," in *IEEE International Conference on Robotics and Automation, ICRA'07*, 2015.
- [118] I. Roch, P. Bidaud, D. Collard and L. Buchaillot, "Fabrication and characterization of an SU-8 gripper actuated by a shape memory alloy thin film," *J. Micromech. Microeng.*, vol. 13, no. 3, pp. 330-336, 2003.
- [119] S. Nah and Z. Zhong, "A microgripper using piezoelectric actuation for micro-object manipulation," *Sensors and Actuators A: Physical*, vol. 133, no. 1, pp. 218-224, 2007.
- [120] H. Choi, D. Lee, S. Kim and C. Han, "The development of a microgripper with a perturbation-based configuration design method," *J. Micromech. Microeng.*, vol. 15, no. 6, pp. 1327-1333, 2005.
- [121] R. Panepucci and J. A. Martinez, "Waveguide Microgripper with Optical Feedback for Microassembly," in *17th Biennial University/Government/Industry Micro/Nano Symposium*, Louisville, KY, 2008.
- [122] R. Panepucci and J. Martinez, "Novel SU-8 optical waveguide microgripper for simultaneous micromanipulation and optical detection,"

*Journal of Vacuum Science & Technology B: Microelectronics and Nanometer Structures*, vol. 26, no. 6, pp. 2624-2627, 2008.

- [123] J. Martinez and R. Panepucci, "Design, Fabrication, and Characterization of a Microgripper Device, FCRAR 2007,," in *Florida Conference on Recent Advances in Robotics*, Florida, 2007.
- [124] Y. Ma, Y. Xia, J. Liu, S. Zhang, J. Shao, L. B. and Y. Chen, "Processing study of SU-8 pillar profiles with high aspect ratio by electron-beam lithography," *Microelectronic Engineering*, vol. 149, pp. 141-144, 2016.
- [125] MicroChem, "MicroChem," MicroChem, [Online]. Available: [http://www.microchem.com/pdf/SU-82000DataSheet2000\\_5thru2015Ver4.pdf](http://www.microchem.com/pdf/SU-82000DataSheet2000_5thru2015Ver4.pdf). [Accessed 7 12 2015].
- [126] A. Soma, S. Iamoni, R. Voicu, R. Muller, M. H. M. Al-Zandi and C. Wang, "Design and experimental testing of an electro-thermal microgripper for cell manipulation," *Microsyst Technology*, no. 24, pp. 1053-1060, 2018.
- [127] M. Mousavi, J. De Pasquale, A. Soma and E. Brusa, "A novel SU-8 microgripper with external actuator for biological cells manipulation," in *Design, Test, Integration & Packaging of MEMS/MOEMS (DTIP)*, Aix-en-Provence, 2011.
- [128] H. Lorenz, M. Despont, N. Fahrni, N. LaBianca, P. Renaud and P. Vettiger, "SU-8: a low-cost negative resist for MEMS," *J. Micromech. Microeng.*, vol. 7, no. 3, pp. 121-124, 1997.
- [129] J. Shaw, J. Gelorme, N. LaBianca, W. Conley and S. Holmes, "Negative photoresists for optical lithography," *IBM Journal of Research and Development*, vol. 41, no. 12, pp. 81-94, 1997.
- [130] S. Chung and S. Park, "Effects of the temperature on mechanical properties of SU-8 photoresist material," *J. Mech.Sci. Technol*, vol. 27, no. 9, pp. 2701-2707, 2013.
- [131] L. R. e. a. Viannie, "Fabrication and nonlinear thermomechanical analysis of SU8 thermal," *J. of Microelectromech*, vol. 25, no. 1, pp. 125-133, 2016.

- [132] V. Rodica-Cristina, A. Z. Muaiyd, M. Raluca and W. Changhai, "Nonlinear numerical analysis and experimental testing for an electrothermal SU-8 microgripper with reduced out-of-plane displacement," in *28th Micromechanics and Microsystems Europe Workshop*, 2017.
- [133] L. Dellmann, S. Roth, C. Beuret, G.-A. Racine, H. Lorenz, M. Despont, P. Renaud, P. Vettiger and N. d. Rooij, "Fabrication process of high aspect ratio elastic structures for piezoelectric motor applications," in *Proceedings of International Solid State Sensors and Actuators Conference (Transducers '97)*, Chicago, IL, USA, USA, 1997.
- [134] C. J. Robin, A. Vishnoi and K. N. Jonnalagadda, "Mechanical Behavior and Anisotropy of Spin-Coated SU-8 Thin Films for MEMS," *JOURNAL OF MICROELECTROMECHANICAL SYSTEMS*, vol. 23, no. 1, pp. 168-180, 214.
- [135] R. Feng and R. J. Farris, "Influence of processing conditions on the thermal and mechanical properties of SU8 negative photoresist coatings," *Journal of Micromechanics and Microengineering*, vol. 13, no. 1, p. 80–88, 2003.
- [136] R. Feng and R. J. Farris, "The characterization of thermal and elastic constants for an epoxy photoresist SU8 coating," *JOURNAL OF MATERIALS SCIENCE*, vol. 37, no. 22, p. 4793 – 4799, 2003.

## Appendix I Software Code

### GUI Software (VC++)

```
#pragma once
#include <Windows.h>

#pragma comment(lib, "shell32.lib")

namespace CppCLR_WinformsProjekt {

    using namespace System;
    using namespace System::Diagnostics;
    using namespace System::ComponentModel;
    using namespace System::Collections;
    using namespace System::Windows::Forms;
    using namespace System::Data;
    using namespace System::Drawing;
    using namespace System::Net::Sockets;
    using namespace System::Text;
    using namespace System::Timers;
    using namespace System::Threading;

    /// <summary>
    /// Zusammenfassung f r Form1
    /// </summary>
    public ref class Form1 : public System::Windows::Forms::Form
    {
    public:
        Form1(void)
        {
            InitializeComponent();
            //
            //TODO: Konstruktorcode hier hinzuf gen.
            //
        }

    protected:
        /// <summary>
        /// Verwendete Ressourcen bereinigen.
        /// </summary>
        ~Form1()
        {
            if (components)
            {
                delete components;
            }
        }
    }
```

```

    }
    private: System::Windows::Forms::Button^ connectbtn;
    protected:

    private: System::Windows::Forms::Button^ RunInterfacebtn;
    private: System::Windows::Forms::GroupBox^ groupBox1;
    private: System::Windows::Forms::Label^ voltaselbl;
    private: System::Windows::Forms::TextBox^ voltagetxt;
    private: System::Windows::Forms::Button^ setbtn;
    private: System::Windows::Forms::Button^ Startbtn;
    private: System::Windows::Forms::ProgressBar^ progress;
    private: System::Windows::Forms::Label^ processlbl;
    private: System::Windows::Forms::GroupBox^ groupBox2;
    private: System::Windows::Forms::Label^ label5;
    private: System::Windows::Forms::Button^ button1;
    private: System::Windows::Forms::TextBox^ repeattxt;
    private: System::Windows::Forms::Label^ label4;
    private: System::Windows::Forms::TextBox^ ontxt;
    private: System::Windows::Forms::TextBox^ offtxt;
    private: System::Windows::Forms::Label^ label3;
    private: System::Windows::Forms::Label^ label1;
    private: System::Windows::Forms::Label^ label2;
    private: System::Windows::Forms::GroupBox^ groupBox3;
    private: System::Windows::Forms::Button^ stopbtn;

private:
    /// <summary>
    /// Erforderliche Designervariable.
    /// </summary>
    System::ComponentModel::Container ^components;

#pragma region Windows Form Designer generated code
    /// <summary>
    /// Erforderliche Methode für die Designerunterstützung.
    /// Der Inhalt der Methode darf nicht mit dem Code-
    Editor geändert werden.
    /// </summary>
    void InitializeComponent(void)
    {
        this->connectbtn = (gcnew System::Windows::Forms::Button());
        this->RunInterfacebtn = (gcnew System::Windows::Forms::Button());
        this->groupBox1 = (gcnew System::Windows::Forms::GroupBox());
        this->voltaselbl = (gcnew System::Windows::Forms::Label());
        this->voltagetxt = (gcnew System::Windows::Forms::TextBox());
    }

```

```

        this->setbtn = (gcnew System::Windows::Forms::Button());
        this->processlbl = (gcnew System::Windows::Forms::Label());
        this->Startbtn = (gcnew System::Windows::Forms::Button());
        this-
>progress = (gcnew System::Windows::Forms::ProgressBar());
        this->groupBox2 = (gcnew System::Windows::Forms::GroupBox());
        this->stopbtn = (gcnew System::Windows::Forms::Button());
        this->label5 = (gcnew System::Windows::Forms::Label());
        this->button1 = (gcnew System::Windows::Forms::Button());
        this->repeattxt = (gcnew System::Windows::Forms::TextBox());
        this->label4 = (gcnew System::Windows::Forms::Label());
        this->ontxt = (gcnew System::Windows::Forms::TextBox());
        this->offtxt = (gcnew System::Windows::Forms::TextBox());
        this->label3 = (gcnew System::Windows::Forms::Label());
        this->label1 = (gcnew System::Windows::Forms::Label());
        this->label2 = (gcnew System::Windows::Forms::Label());
        this->groupBox3 = (gcnew System::Windows::Forms::GroupBox());
        this->groupBox1->SuspendLayout();
        this->groupBox2->SuspendLayout();
        this->groupBox3->SuspendLayout();
        this->SuspendLayout();
        //
        // connectbtn
        //
        this->connectbtn->ForeColor = System::Drawing::Color::Black;
        this->connectbtn->Location = System::Drawing::Point(6, 23);
        this->connectbtn->Name = L"connectbtn";
        this->connectbtn->Size = System::Drawing::Size(75, 23);
        this->connectbtn->TabIndex = 0;
        this->connectbtn->Text = L"Connect";
        this->connectbtn->UseVisualStyleBackColor = true;
        this->connectbtn-
>Click += gcnew System::EventHandler(this, &Form1::connectbtn_Click);
        //
        // RunInterfacebtn
        //
        this->RunInterfacebtn-
>ForeColor = System::Drawing::Color::Black;
        this->RunInterfacebtn-
>Location = System::Drawing::Point(257, 23);
        this->RunInterfacebtn->Name = L"RunInterfacebtn";
        this->RunInterfacebtn->Size = System::Drawing::Size(99, 23);
        this->RunInterfacebtn->TabIndex = 2;
        this->RunInterfacebtn->Text = L"Run Interface";
        this->RunInterfacebtn->UseVisualStyleBackColor = true;
        this->RunInterfacebtn-
>Click += gcnew System::EventHandler(this, &Form1::RunInterfacebtn_Click)
;
        //
        // groupBox1

```

```

//
this->groupBox1->Controls->Add(this->voltagelbl);
this->groupBox1->Controls->Add(this->voltagegettxt);
this->groupBox1->Controls->Add(this->setbtn);
this->groupBox1->Controls->Add(this->connectbtn);
this->groupBox1->Controls->Add(this->RunInterfacebtn);
this->groupBox1->Location = System::Drawing::Point(12, 3);
this->groupBox1->Name = L"groupBox1";
this->groupBox1->Size = System::Drawing::Size(362, 85);
this->groupBox1->TabIndex = 3;
this->groupBox1->TabStop = false;
//
// voltagelbl
//
this->voltagelbl->AutoSize = true;
this->voltagelbl-
>Font = (gcnew System::Drawing::Font(L"Microsoft Sans Serif", 9, System::
Drawing::FontStyle::Bold, System::Drawing::GraphicsUnit::Point,
    static_cast<System::Byte>(0)));
this->voltagelbl->ForeColor = System::Drawing::Color::Red;
this->voltagelbl->Location = System::Drawing::Point(83, 55);
this->voltagelbl->Name = L"voltagelbl";
this->voltagelbl->Size = System::Drawing::Size(167, 15);
this->voltagelbl->TabIndex = 2;
this->voltagelbl->Text = L"Running Voltage in (mV):";
//
// voltagegettxt
//
this->voltagegettxt->Location = System::Drawing::Point(256, 54);
this->voltagegettxt->Name = L"voltagegettxt";
this->voltagegettxt->Size = System::Drawing::Size(100, 20);
this->voltagegettxt->TabIndex = 1;
this->voltagegettxt->Text = L"100";
//
// setbtn
//
this->setbtn->ForeColor = System::Drawing::Color::Black;
this->setbtn->Location = System::Drawing::Point(6, 52);
this->setbtn->Name = L"setbtn";
this->setbtn->Size = System::Drawing::Size(75, 23);
this->setbtn->TabIndex = 0;
this->setbtn->Text = L"Set";
this->setbtn->UseVisualStyleBackColor = true;
this->setbtn-
>Click += gcnew System::EventHandler(this, &Form1::Setbtn_Click);
//
// processlbl
//
this->processlbl-
>BorderStyle = System::Windows::Forms::BorderStyle::FixedSingle;

```



```

        this->processlbl-
>Font = (gcnew System::Drawing::Font(L"Monotype Corsiva", 11.25F, static_
cast<System::Drawing::FontStyle>((System::Drawing::FontStyle::Bold | Syst
em::Drawing::FontStyle::Italic)),
        System::Drawing::GraphicsUnit::Point, static_cast<System:
:Byte>(0)));
        this->processlbl->Location = System::Drawing::Point(12, 264);
        this->processlbl->Name = L"processlbl";
        this->processlbl->Size = System::Drawing::Size(362, 23);
        this->processlbl->TabIndex = 4;
        this->processlbl->Text = L"Status";
        //
        // Startbtn
        //
        this->Startbtn->ForeColor = System::Drawing::Color::Black;
        this->Startbtn->Location = System::Drawing::Point(175, 14);
        this->Startbtn->Name = L"Startbtn";
        this->Startbtn->Size = System::Drawing::Size(75, 23);
        this->Startbtn->TabIndex = 3;
        this->Startbtn->Text = L"Start";
        this->Startbtn->UseVisualStyleBackColor = true;
        this->Startbtn-
>Click += gcnew System::EventHandler(this, &Form1::Startbtn_Click);
        //
        // progress
        //
        this->progress->Location = System::Drawing::Point(12, 290);
        this->progress->Name = L"progress";
        this->progress->Size = System::Drawing::Size(362, 23);
        this->progress->TabIndex = 4;
        //
        // groupBox2
        //
        this->groupBox2->Controls->Add(this->stopbtn);
        this->groupBox2->Controls->Add(this->label5);
        this->groupBox2->Controls->Add(this->button1);
        this->groupBox2->Controls->Add(this->repeattxt);
        this->groupBox2->Controls->Add(this->label4);
        this->groupBox2->Controls->Add(this->ontxt);
        this->groupBox2->Controls->Add(this->offtxt);
        this->groupBox2->Controls->Add(this->label3);
        this->groupBox2->Controls->Add(this->label1);
        this->groupBox2->ForeColor = System::Drawing::Color::Black;
        this->groupBox2->Location = System::Drawing::Point(12, 147);
        this->groupBox2->Name = L"groupBox2";
        this->groupBox2->Size = System::Drawing::Size(362, 105);
        this->groupBox2->TabIndex = 5;
        this->groupBox2->TabStop = false;
        //
        // stopbtn

```

```

        //
        this->stopbtn-
>Font = (gcnew System::Drawing::Font(L"Microsoft Sans Serif", 11, System:
:Drawing::FontStyle::Bold, System::Drawing::GraphicsUnit::Point,
        static_cast<System::Byte>(0)));
        this->stopbtn->ForeColor = System::Drawing::Color::Red;
        this->stopbtn->Location = System::Drawing::Point(269, 68);
        this->stopbtn->Name = L"stopbtn";
        this->stopbtn->Size = System::Drawing::Size(75, 31);
        this->stopbtn->TabIndex = 8;
        this->stopbtn->Text = L"STOP";
        this->stopbtn->UseVisualStyleBackColor = true;
        this->stopbtn-
>Click += gcnew System::EventHandler(this, &Form1::stopbtn_Click);
        //
        // label5
        //
        this->label5->AutoSize = true;
        this->label5-
>Font = (gcnew System::Drawing::Font(L"Microsoft Sans Serif", 9, System::
Drawing::FontStyle::Bold, System::Drawing::GraphicsUnit::Point,
        static_cast<System::Byte>(0)));
        this->label5->ForeColor = System::Drawing::Color::Red;
        this->label5->Location = System::Drawing::Point(197, 43);
        this->label5->Name = L"label5";
        this->label5->Size = System::Drawing::Size(53, 15);
        this->label5->TabIndex = 7;
        this->label5->Text = L"Cycling";
        //
        // button1
        //
        this->button1->Location = System::Drawing::Point(269, 39);
        this->button1->Name = L"button1";
        this->button1->Size = System::Drawing::Size(75, 23);
        this->button1->TabIndex = 7;
        this->button1->Text = L"Start";
        this->button1->UseVisualStyleBackColor = true;
        this->button1-
>Click += gcnew System::EventHandler(this, &Form1::button1_Click);
        //
        // repeattxt
        //
        this->repeattxt->Location = System::Drawing::Point(110, 42);
        this->repeattxt->Name = L"repeattxt";
        this->repeattxt->Size = System::Drawing::Size(76, 20);
        this->repeattxt->TabIndex = 6;
        this->repeattxt->Text = L"10";
        //
        // label4
        //

```

```

this->label4->AutoSize = true;
this->label4->Location = System::Drawing::Point(6, 45);
this->label4->Name = L"label4";
this->label4->Size = System::Drawing::Size(88, 13);
this->label4->TabIndex = 5;
this->label4->Text = L"Repeat (Number)";
//
// ontxt
//
this->ontxt->Location = System::Drawing::Point(86, 13);
this->ontxt->Name = L"ontxt";
this->ontxt->Size = System::Drawing::Size(86, 20);
this->ontxt->TabIndex = 4;
this->ontxt->Text = L"3";
//
// offtxt
//
this->offtxt->Location = System::Drawing::Point(269, 13);
this->offtxt->Name = L"offtxt";
this->offtxt->Size = System::Drawing::Size(86, 20);
this->offtxt->TabIndex = 3;
this->offtxt->Text = L"3";
//
// label3
//
this->label3->AutoSize = true;
this->label3->Location = System::Drawing::Point(182, 16);
this->label3->Name = L"label3";
this->label3->Size = System::Drawing::Size(81, 13);
this->label3->TabIndex = 2;
this->label3->Text = L"Time OFF (Sec)";
//
// label1
//
this->label1->AutoSize = true;
this->label1->Location = System::Drawing::Point(6, 16);
this->label1->Name = L"label1";
this->label1->Size = System::Drawing::Size(77, 13);
this->label1->TabIndex = 0;
this->label1->Text = L"Time ON (Sec)";
//
// label2
//
this->label2->AutoSize = true;
this->label2-
>Font = (gcnew System::Drawing::Font(L"Microsoft Sans Serif", 9, System::
Drawing::FontStyle::Bold, System::Drawing::GraphicsUnit::Point,
    static_cast<System::Byte>(0)));
this->label2->ForeColor = System::Drawing::Color::Red;
this->label2->Location = System::Drawing::Point(6, 14);

```

```

        this->label2->Name = L"label2";
        this->label2->Size = System::Drawing::Size(127, 15);
        this->label2->TabIndex = 6;
        this->label2->Text = L"Start Dynamic Test";
        //
        // groupBox3
        //
        this->groupBox3->Controls->Add(this->label2);
        this->groupBox3->Controls->Add(this->Startbtn);
        this->groupBox3->Location = System::Drawing::Point(12, 94);
        this->groupBox3->Name = L"groupBox3";
        this->groupBox3->Size = System::Drawing::Size(362, 43);
        this->groupBox3->TabIndex = 7;
        this->groupBox3->TabStop = false;
        //
        // Form1
        //
        this->AutoScaleDimensions = System::Drawing::SizeF(6, 13);
        this->AutoScaleMode = System::Windows::Forms::AutoScaleMode::Font;
        this->ClientSize = System::Drawing::Size(384, 325);
        this->Controls->Add(this->groupBox2);
        this->Controls->Add(this->processlbl1);
        this->Controls->Add(this->progress);
        this->Controls->Add(this->groupBox1);
        this->Controls->Add(this->groupBox3);
        this->ForeColor = System::Drawing::Color::Red;
        this->Name = L"Form1";
        this->Text = L"Dynamic & Cycling Test";
        this->Load += gcnew System::EventHandler(this, &Form1::Form1_Load);
        this->groupBox1->ResumeLayout(false);
        this->groupBox1->PerformLayout();
        this->groupBox2->ResumeLayout(false);
        this->groupBox2->PerformLayout();
        this->groupBox3->ResumeLayout(false);
        this->groupBox3->PerformLayout();
        this->ResumeLayout(false);
    }
#pragma endregion
#pragma region Global Variable
    Timers::Timer^ TDynamic = gcnew Timers::Timer(1000);

    Timers::Timer^ TCycling = gcnew Timers::Timer(1000);
    UINT TimeCount = 0;
    int Repeat;
    bool CycleEn = false;

    int TimeON;

```

```

int TimeOFF;
int RepeatCount;

delegate void del(int i);
delegate void del2(String^ s);

Int32 Port = 25;
String^ Server = "137.195.53.122";
TcpClient^ Client;
NetworkStream^ Stream;
array<Byte>^ SendBytes;
array<Byte>^ data = gcnew array<Byte>(256);
String^ ResponseData = String::Empty;
Int32 bytes;
#pragma endregion

#pragma region Functions
//User functions
void DynamicTest(Object^ source, System::Timers::ElapsedEventArgs
^ e) {
    TimeCount++;
    if (TimeCount == 122) {
        TimeCount = 0;
        TDynamic->Close();
        StatUpdate("Test has been finished");
        ProcessUpdate(0);
        CloseNet();
        return;
    }
    else if (TimeCount == 1) {
        TimerFunc("T\r\n");
        StatUpdate("Test whith power ON");
    }
    else if (TimeCount == 62) {
        TimerFunc("Q\r\n");
        StatUpdate("Test with Power off");
    }
    if (TimeCount % 12 == 0)
        ProcessUpdate((float)TimeCount/12.0*10);
}

void CyclingTest(Object^ source, System::Timers::ElapsedEventArgs
^ e) {
    if (TimeCount == 6) {
        TimeCount = 0;
        if (RepeatCount == 0) {
            TCycling->Close();
            CloseNet();
            StatUpdate("Cycling Finished");
            ProcessUpdate(0);

```

```

        return;
    }
}

switch (TimeCount) {
case(0):
    TimerFunc("C0\r\n");
    RepeatCount -= 1;
    StatUpdate("Cycle Number : " + Convert::ToString(Repeat -
RepeatCount));
    ProcessUpdate(100 * (Repeat - RepeatCount) / Repeat);
    break;
case(3):
    TimerFunc("CF\r\n");
    break;
}
TimeCount += 1;
}

void TimerFunc(String^ state) {
    SendBytes = Encoding::UTF8->GetBytes(state);
    Stream = Client->GetStream();
    Stream->Write(SendBytes, 0, SendBytes->Length);
}

void ProcessUpdate(int i) {
    if (progress->InvokeRequired == false) {
        progress->Value = i;
    }
    else {
        del^ delcall = gcnew del(this, &Form1::ProcessUpdate);
        this->Invoke(delcall, i);
    }
}

void StatUpdate(String^ a) {
    if (processlbl->InvokeRequired == false) {
        processlbl->Text = a;
    }
    else {
        del2^ delcall = gcnew del2(this, &Form1::StatUpdate);
        this->Invoke(delcall, a);
    }
}

void CloseNet() {
    SendBytes = Encoding::UTF8->GetBytes("End\r\n");
    Stream = Client->GetStream();
    Stream->Write(SendBytes, 0, SendBytes->Length);
    Client->Close();
}

```

```

    }
    // Form Functions
    private: System::Void Form1_Load(System::Object^ sender, System::EventArgs^ e) {
        TDynamic-
        >Elapsed += gcnew Timers::ElapsedEventHandler(this, &Form1::DynamicTest);
        TCycling-
        >Elapsed += gcnew Timers::ElapsedEventHandler(this, &Form1::CyclingTest);
        //ShellExecuteW(NULL, L"open", L"C:\\Users\\User\\Desktop\\SerialCom.lnk\\", NULL, NULL, SW_SHOW);
    }
    private: System::Void connectbtn_Click(System::Object^ sender, System::EventArgs^ e) {
        try {
            Client = gcnew TcpClient;
            Client->Connect(Server, Port);

            SendBytes = Encoding::UTF8->GetBytes("Start\r\n");
            Stream = Client->GetStream();
            Stream->Write(SendBytes, 0, SendBytes->Length);

        }
        catch(Exception^ exception){
            MessageBox::Show("Port Connection Failed\n" + exception);
        }
    }

    private: System::Void RunInterfacebtn_Click(System::Object^ sender, System::EventArgs^ e) {
        ShellExecuteW(NULL, L"open", L"C:\\Users\\User\\Desktop\\SerialCom.lnk\\", NULL, NULL, SW_SHOW);
    }
    private: System::Void Setbtn_Click(System::Object^ sender, System::EventArgs^ e) {
        SendBytes = Encoding::UTF8->GetBytes("S\r\n");
        Stream = Client->GetStream();
        Stream->Write(SendBytes, 0, SendBytes->Length);

        Thread::Sleep(100);

        SendBytes = Encoding::UTF8->GetBytes(voltagetxt->Text + "\r\n");
        Stream->Write(SendBytes, 0, SendBytes->Length);
    }
    private: System::Void Startbtn_Click(System::Object^ sender, System::EventArgs^ e) {
        if (TDynamic->Enabled == false) {
            TimeCount = 0;
            TDynamic->Start();
        }
    }
}

```

```

        private: System::Void button1_Click(System::Object^ sender, System::
EventArgs^ e) {
            TimeON = Convert::ToInt64(ontxt->Text);
            TimeOFF = Convert::ToInt64(offtxt->Text);
            Repeat = Convert::ToInt64(repeattxt->Text);
            RepeatCount = Repeat;
            //CycleEn = true;
            if (TCycling->Enabled == false) {
                TimeCount = 0;
                TCycling->Start();
            }
        }
        private: System::Void stopbtn_Click(System::Object^ sender, System::
EventArgs^ e) {
            RepeatCount = 1;
        }
#pragma endregion
};
}

```

## Arduino Firmware (C)

### *Header.h File*

```

#ifndef _Header__h_
#define _Header__h_

#include <SPI.h>
#include <DAC_MCP49xx.h>

#define SS_PIN 10
DAC_MCP49xx dac(DAC_MCP49xx::MCP4921, SS_PIN);

//Required definition and include for the ADC
//For soft I2C
#define SDA_PORT PORTD
#define SDA_PIN 6
#define SCL_PORT PORTD
#define SCL_PIN 7

#define RELAY 5

#define I2C_TIMEOUT 100
#define I2C_NOINTERRUPT 0
#define I2C_SLOWMODE 1
#define FAC 1

#define ADC_Add 0x48

```



```

#define DataRead false
#define RegRead true
#define NewData 0X80

typedef enum {GAIN1,GAIN2,GAIN4,GAIN8} PGA_t;
/*
    Resolution is
    if SPS 240    12 bits
    if SPS 60     14 bits
    if SPS 30     15 bits
    if SPS 15     16 bits
*/
typedef enum {SPS240,SPS60,SPS30,SPS15} DR_t; //SAMPLES PER SECOND
typedef enum {CONTINUOUS,SINGLE} SC_t; //CONVERSION MODE
typedef enum {READ_NEW,START_OLD} ST_t;

typedef union { //ADC REGISTER BITS
    struct{
        uint8_t PGA :2;
        uint8_t DR :2;
        uint8_t SC :1;
        uint8_t NC :2;
        uint8_t ST :1;
    }bits;
    uint8_t REG;
}ADC_ctrl;
typedef union {
    struct{
        uint8_t data_h;
        uint8_t data_l;
    }data_8;
    uint16_t data_16;
}data_adc;

volatile ADC_ctrl ADC_control;
volatile data_adc data_ADC;

#endif

```

### *Main.c*

```

/Required definition and include for the DAC
#include "Header.h"

#include <SPI.h>
#include <DAC_MCP49xx.h>

#include <SoftI2C.h>

```

```

#include <avr/io.h>
#include "Wire.h"

int VOLTAGE_VALUE = 0;
uint16_t Data1[240] , Data2[240];
uint8_t REG, Rs = 0;
uint8_t READ_PER_SEC;

void setup() {
    dac.setSPIDivider(SPI_CLOCK_DIV16);
    Serial.begin(115200);
    i2c_init();
    Wire.begin();
    dac.setPortWrite(true);
    dac.output(0);
    dac.setPortWrite(false);
    pinMode(RELAY,OUTPUT);
    digitalWrite(RELAY,0);

    //SETUP THE ADC REGISTER VALUES
    ADC_control.bits.PGA = GAIN1;
    ADC_control.bits.DR = SPS60;
    ADC_control.bits.SC = CONTINUOUS;
    ADC_control.bits.NC = 0;
    ADC_control.bits.ST = READ_NEW;

    switch(ADC_control.bits.DR){
        case SPS240:
            READ_PER_SEC = 240;
            break;
        case SPS60:
            READ_PER_SEC = 60;
            break;
        case SPS30:
            READ_PER_SEC = 30;
            break;
        case SPS15:
            READ_PER_SEC = 15;
            break;
    }
    i2c_start((ADC_Add<<1)+I2C_WRITE);
    i2c_write(ADC_control.REG);

    Wire.beginTransmission(ADC_Add);
    Wire.write(ADC_control.REG);
    Wire.endTransmission();
}

void loop() {

```

```

}

uint16_t Volt_Code(uint16_t Volt) {
    return (uint16_t)((float)Volt * 4096.0 / 2700.0);
}

void serialEvent() {
    char Com = Serial.read();
    switch(Com){
        case 'S': //set voltage value
            VOLTAGE_VALUE = Serial.parseInt();
            break;
        case 'F': //Turn relay off
            digitalWrite(RELAY,0);
            break;
        case 'O': //Turn relay on
            digitalWrite(RELAY,1);
            break;
        case 'P': //RUN THE VOLTAGE OUT OF DAC TO VOLTAGE_VALUE
            ANALOG_OUT(VOLTAGE_VALUE);
            break;
        case 'Q': //SET THE VOLTAGE OUT OF DAC TO 0
            ANALOG_OUT(0);
            break;
        case 'T': //READ THE A 2 D CONV. FOR A SEC.
            Serial.println("Test");
            for(int x = 0 ; x < READ_PER_SEC ; x++){
                READ_ADC(x);
            }
            Serial.println("Finish");
            break;
        case 'G': //GET SINGLE READING FROM THE ADC
            READ_ADC(0);
            Serial.print(Data1[0]);
            Serial.print(" , ");
            Serial.println(Data2[0]);
            break;
        case 'R': //SEND A SINGLE READING TO COMPUTER
            int i = Serial.parseInt();
            if(i < READ_PER_SEC){
                Serial.print(i);
                Serial.print(" , ");
                Serial.print(Data1[i]);
                Serial.print(" , ");
                Serial.println(Data2[i]);
            }
            break;
    }
}

//SET THE OUTPUT FROM THE DAC TO V

```

```

void ANALOG_OUT(uint16_t V){
    dac.setPortWrite(true);
    dac.output(Volt_Code(V));
    dac.setPortWrite(false);
}
//READ A SINGLE DATA FROM THE TWO ADC
void READ_ADC(int x){

    do{
        i2c_rep_start((ADC_Add<<1)+I2C_READ);
        data_ADC.data_8.data_l = i2c_read(DataRead);
        data_ADC.data_8.data_h = i2c_read(DataRead);
        REG = i2c_read(RegRead);
    }while(REG & NewData);
    i2c_stop();
    Data1[x] = data_ADC.data_16;
    do{
        Wire.requestFrom(ADC_Add, 0x03);
        while(Wire.available()){
            data_ADC.data_8.data_l = Wire.read();
            data_ADC.data_8.data_h = Wire.read();
            REG = Wire.read();
        }
    }while(REG & NewData);
    Data2[x] = data_ADC.data_16;
}

```

### Serial Management (Java Script)

```

function main(){
    var STATIC = 0;
    var R ;
    while(1){
        print("Start new Test");
        while(Net.getState() != "Start\r\n");
        while(Net.getState() == "Start\r\n");
        while(Net.getState() != "End\r\n"){
            if(Net.getState() == "S\r\n"){
                while(Net.getState() == "S\r\n");
                var A = Net.getState();
                Net.setState("");
                Serial.setTarget("S"+A);
                Serial.setTarget("O");
            }else if(Net.getState() == "T\r\n"){
                sleep(1000);
                Serial.setTarget("PT");
                STATIC = 1;
                while(Net.getState() == "T\r\n");
            }else if(Net.getState() == "Q\r\n"){
                Serial.setTarget("Q");
            }
        }
    }
}

```

```

        while(Net.getState() == "Q\r\n");
    }else if(Net.getState() == "CO\r\n"){
        Serial.setTarget("P");
        sleep(1000);
        Serial.setState("G");
        Serial.setTarget("G");
        while(Serial.getState() == "G");
        R = Serial.getState();
        print(R);
        while(Net.getState() == "CO\r\n");
    }else if(Net.getState() == "CF\r\n"){
        Serial.setTarget("Q");
        while(Net.getState() == "CF\r\n");
    }
}
Serial.setTarget("F");
if(STATIC == 1){
    var i = 0;
    for(i; i < 60; i++){
        Serial.setState("Ri");
        Serial.setTarget("R"+ i);
        while(Serial.getState() == "Ri");
        R = Serial.getState();
        print(R);
    }
    STATIC = 0;
}
}
}
}

```

### Image Processing Management (Java Script)

```

function VisionConnector(){

    LeftV.setRequest("Finger_Find.xml");
    LeftV.send();
    LeftV.waitResults();
    L_Data =LeftV.getResults("MATCH");
    while(! L_Data["x"]  && Net.getState() == "Start\r\n"){
        LeftV.waitResults();
        L_Data = LeftV.getResults("MATCH");
        sleep(250);
    }

    RightV.setRequest("Finger_Find.xml");
    RightV.send();
    RightV.waitResults();
    R_Data =RightV.getResults("MATCH");
    while(! R_Data["x"]  && Net.getState() == "Start\r\n"){
        RightV.waitResults();
    }
}

```

```

        R_Data = RightV.getResults("MATCH");
        sleep(250);
    }
}

var countON= 0;
var countOFF = 0;
var Dynamic;
var DataL , DataR;
var Dyn = [];
var cunt;
var S = " , " ;

function ReadVision(){
    if(Dynamic == "ON"){
        cunt = countON;
        countON++;
    }
    else{
        cunt = countON + countOFF;
        countOFF++;
    }
    LeftV.waitForResults();
    DataL = LeftV.getResults("MATCH");

    RightV.waitForResults();
    DataR = RightV.getResults("MATCH");

    Dyn[cunt] = DataL["x"] + S + DataL["y"] + S + DataR["x"] + S + DataR[
"y"] ;
}

function PrintVision(){
    for(var x = 0 ; x < cunt ; x++){
        print(x + " , " + Dyn[x] );
    }
    print("ON: " + countON);
    print("OFF: " + countOFF);
    countON = 0;
    countOFF = 0;
}

var Off , On ;
var a;

function ReadVision2(){
    sleep(1000);
    var Lx = 0, Ly = 0;
    var Rx = 0, Ry = 0;

    for(var i = 0 ; i < 10 ; i++){

```

```

        LeftV.waitForResults();
        L_Data = LeftV.getResults("MATCH");
        Lx = Lx + L_Data["x"] / 10;
        Ly = Ly + L_Data["y"] / 10;

        RightV.waitForResults();
        R_Data = RightV.getResults("MATCH");
        Rx = Rx + R_Data["x"] / 10;
        Ry = Ry + R_Data["y"] / 10;
    }

    if(a == 1)
        On = "O , " + Lx + S + Ly + S + Rx + S + Ry ;
    else
        Off = "F , " + Lx + S + Ly + S + Rx + S + Ry ;
}

function main(){
    while(1){
        print("Start new Test");
        countOn = 0;
        countOff = 0;
        while(Net.getState() != "Start\r\n");
        VisionConnector();
        while(Net.getState() == "Start\r\n");
        while(Net.getState() != "End\r\n"){
            if(Net.getState() == "S\r\n"){
                while(Net.getState() == "S\r\n");
            }else if(Net.getState() == "T\r\n"){
                Dynamic = "ON";
                while(Net.getState() == "T\r\n"){
                    ReadVision();
                }
            }else if(Net.getState() == "Q\r\n"){
                Dynamic = "OFF";
                while(Net.getState() == "Q\r\n"){
                    ReadVision();
                }
            }
            PrintVision();
        }else if(Net.getState() == "CO\r\n"){
            a = 1;
            ReadVision2();
            while(Net.getState() == "CO\r\n");
        }else if(Net.getState() == "CF\r\n"){
            a = 0;
            ReadVision2();
            print(On + " : " + Off);
            while(Net.getState() == "CF\r\n");
        }
    }
}

```

```
        RightV.stop();  
        LeftV.stop();  
    }  
}
```